

1                   The Pennsylvania State University  
2                   The Graduate School  
3                   Eberly College of Science

4   **DEVELOPMENT OF SCALABLE APPROACHES TO NEUTRINO MASS**  
5                   **MEASUREMENT WITH THE PROJECT 8 EXPERIMENT**

6                   A Thesis in  
7                   The Physics Department  
8                   by  
9                   Andrew Douglas Ziegler

10                  © 2023 Andrew Douglas Ziegler

11                  Submitted in Partial Fulfillment  
12                  of the Requirements  
13                  for the Degree of

14                  Doctor of Philosophy

15                  December 2023

<sup>16</sup> The thesis of Andrew Douglas Ziegler was reviewed and approved\* by the following:

Luiz de Viveiros Souza  
Assistant Professor of Physics  
Thesis Advisor  
Chair of Committee

Carmen Carmona  
Assistant Professor of Physics

<sup>17</sup> Doug Cowan  
Professor of Physics and Astrophysics

Xingjie Ni  
Associate Professor of Electrical Engineering

<sup>18</sup> Stephanie Wissel  
Associate Professor of Physics

<sup>19</sup> \*Signatures are on file in the Graduate School.

<sup>20</sup> **Abstract**

<sup>21</sup> Some shit goes here.

# Table of Contents

23	<b>List of Figures</b>	viii
24	<b>List of Tables</b>	viii
25	<b>Acknowledgments</b>	viii
26	<b>Chapter 1</b>	
27	<b>Introduction</b>	1
28	1.1 Summary . . . . .	1
29	1.2 Outline . . . . .	4
30	<b>Chapter 2</b>	
31	<b>Neutrinos and Neutrino Masses</b>	6
32	2.1 Introduction . . . . .	6
33	2.2 Neutrinos and Beta-decay . . . . .	6
34	2.3 Neutrino Oscillations . . . . .	7
35	2.4 Neutrino Masses in the Standard Model . . . . .	10
36	2.5 Neutrino Absolute Mass Scale . . . . .	13
37	2.5.1 Limits from Cosmology . . . . .	13
38	2.5.2 Limits from Neutrinoless Double Beta-decay Searches . . . . .	15
39	2.5.3 Limits from Beta-decay . . . . .	16
40	<b>Chapter 3</b>	
41	<b>Direct Measurement of the Neutrino Mass with Project 8</b>	21
42	3.1 Introduction . . . . .	21
43	3.2 Cyclotron Radiation Emission Spectroscopy and Project 8 . . . . .	22
44	3.2.1 Cyclotron Radiation Emission Spectroscopy — CRES . . . . .	22
45	3.2.2 The Project 8 Collaboration . . . . .	27
46	3.2.3 The Project 8 Phased Development Plan . . . . .	30
47	3.3 Phase II: First Tritium Beta Decay Spectrum and Neutrino Mass Measurement with CRES . . . . .	34
48	3.3.1 The Phase II CRES Apparatus . . . . .	34
49	3.3.2 CRES Track and Event Reconstruction . . . . .	38
50	3.3.3 Results from Phase II . . . . .	42
51	3.4 Phase III R&D: Antenna Array CRES . . . . .	46

53	3.4.1	The Basic Approach . . . . .	47
54	3.4.2	The FSCD: Free-space CRES Demonstrator . . . . .	48
55	3.5	Pilot-scale Experiments . . . . .	53
56	3.5.1	Choice of Frequency . . . . .	53
57	3.5.2	Pilot-scale Experiment Concepts . . . . .	56
58	3.6	Phase IV . . . . .	58

59	<b>Chapter 4</b>		
60	<b>Signal Reconstruction Techniques for Antenna Array CRES and the</b>		
61	<b>FSCD</b>		<b>60</b>
62	4.1	Introduction . . . . .	60
63	4.2	FSCD Simulations . . . . .	61
64	4.2.1	Kassiopeia . . . . .	62
65	4.2.2	Locust . . . . .	66
66	4.2.3	CRESana . . . . .	70
67	4.3	Signal Detection and Reconstruction Techniques for Antenna Array CRES	71
68	4.3.1	Digital Beamforming . . . . .	75
69	4.3.2	Matched Filtering . . . . .	85
70	4.3.3	Machine Learning . . . . .	97
71	4.4	Analysis of Signal Detection Algorithms for the Antenna Array Demonstrator	102
72	4.4.1	Introduction . . . . .	103
73	4.4.2	Signal Detection with Antenna Array CRES . . . . .	105
74	4.4.2.1	Antenna Array and DAQ System . . . . .	105
75	4.4.2.2	Real-time Signal Detection . . . . .	108
76	4.4.3	Signal Detection Algorithms . . . . .	112
77	4.4.3.1	Power Threshold . . . . .	112
78	4.4.3.2	Matched Filtering . . . . .	114
79	4.4.3.3	Machine Learning . . . . .	118
80	4.4.4	Methods . . . . .	120
81	4.4.4.1	Data Generation . . . . .	120
82	4.4.4.2	Template Number and Match Estimation . . . . .	121
83	4.4.4.3	CNN Training and Data Augmentation . . . . .	122
84	4.4.5	Results and Discussion . . . . .	123
85	4.4.5.1	Trigger Classification Performance . . . . .	123
86	4.4.5.2	Computational Cost and Hardware Requirements . . . . .	125
87	4.4.6	Conclusion . . . . .	127

88	<b>Chapter 5</b>		
89	<b>Antenna and Antenna Measurement System Development for the</b>		
90	<b>Project 8 Experiment</b>		<b>129</b>
91	5.1	Introduction . . . . .	129
92	5.2	Antenna Measurements for CRES experiments . . . . .	130
93	5.2.1	Antenna Parameters . . . . .	130
94	5.2.1.1	Radiation Patterns . . . . .	130

95	5.2.1.2	Directivity and Gain . . . . .	131
96	5.2.1.3	Far-field and Near-field . . . . .	132
97	5.2.1.4	Polarization . . . . .	133
98	5.2.1.5	Antenna Factor and Effective Aperture . . . . .	134
99	5.2.2	Antenna Measurement Fundamentals . . . . .	136
100	5.2.2.1	Friis Transmission Equation . . . . .	136
101	5.2.2.2	S-Parameters and Network Analyzers . . . . .	137
102	5.2.2.3	Antenna Array Commissioning and Calibration Measurements . . . . .	138
103	5.2.3	The Penn State Antenna Measurement System . . . . .	140
104	5.3	Development of a Synthetic Cyclotron Antenna (SYNCA) for Antenna Array Calibration . . . . .	143
105	5.3.1	Introduction . . . . .	143
106	5.3.2	Cyclotron Radiation Phenomenology . . . . .	146
107	5.3.3	SYNCA Simulations and Design . . . . .	152
108	5.3.4	Characterization of the SYNCA . . . . .	157
109	5.3.5	Beamforming Measurements with the SYNCA . . . . .	160
110	5.3.6	Conclusions . . . . .	164
111	5.4	FSCD Antenna Array Measurements with the SYNCA . . . . .	165
112	5.4.1	Introduction . . . . .	165
113	5.4.2	Measurement Setups . . . . .	166
114	5.4.2.1	FSCD Array Setup . . . . .	166
115	5.4.2.2	Synthetic Array Setup . . . . .	168
116	5.4.3	Simulations, Analysis, and Results . . . . .	169
117	5.4.3.1	Simulations . . . . .	169
118	5.4.3.2	Phase Analysis . . . . .	170
119	5.4.3.3	Magnitude Analysis . . . . .	175
120	5.4.3.4	Beamforming Characterization . . . . .	177
121	5.4.4	Conclusions . . . . .	180

124	<b>Chapter 6</b>		
125	<b>Development of Resonant Cavities for Large Volume CRES Measurements</b>	<b>182</b>	
126	6.1	Introduction . . . . .	182
127	6.2	Cylindrical Resonant Cavities . . . . .	183
128	6.2.1	General Field Solutions . . . . .	183
129	6.2.2	TE and TM Modes . . . . .	184
130	6.2.3	Resonant Frequencies of a Cylindrical Cavity . . . . .	186
131	6.2.4	Cavity Q-factors . . . . .	188
132	6.3	The Cavity Approach to CRES . . . . .	192
133	6.3.1	A Sketch of a Molecular Tritium Cavity CRES Experiment . . . . .	192
134	6.3.2	Magnetic Field, Cavity Geometry, and Resonant Modes . . . . .	194
135	6.3.3	Trade-offs Between the Antenna and Cavity Approaches . . . . .	197
136	6.4	Single-mode Resonant Cavity Design and Simulations . . . . .	199

138	6.4.1	Open Cylindrical Cavities with Coaxial Terminations . . . . .	199
139	6.4.2	Mode Filtering . . . . .	202
140	6.4.3	Simulations of Open, Mode-filtered Cavities . . . . .	204
141	6.5	Single-mode Resonant Cavity Measurements . . . . .	207
142	6.5.1	Cavities and Setup . . . . .	207
143	6.5.2	Results and Discussion . . . . .	210
144	<b>Chapter 7</b>		
145	<b>Conclusion and Future Prospects</b>		<b>213</b>
146	<b>Bibliography</b>		<b>215</b>

<sup>147</sup> **Acknowledgments**

<sup>148</sup> Shout out to all the haters.

<sup>149</sup> **Dedication**

<sup>150</sup> Something heartfelt.

<sup>151</sup> **Chapter 1** |  
<sup>152</sup> **Introduction**

<sup>153</sup> **1.1 Summary**

<sup>154</sup> Neutrinos are one of the fundamental particles that comprise the standard model of  
<sup>155</sup> particle physics and account for a significant fraction of the matter in the universe.  
<sup>156</sup> Neutrinos are the most abundant fermions in the universe, but due to their weak  
<sup>157</sup> interactions neutrinos seldom interact with other particles. Regardless, neutrinos play a  
<sup>158</sup> unique role in the evolution of the early-universe, therefore, a detailed understanding  
<sup>159</sup> of the properties of the neutrino is important to understanding the cosmology of the  
<sup>160</sup> universe as well as understanding the universe at the fundamental particle physics scale.

<sup>161</sup> Unlike other fermions it was unclear that neutrinos had nonzero mass until neutrino  
<sup>162</sup> flavor oscillations were definitively observed in the late 90's and early 00's. Flavor  
<sup>163</sup> oscillations require that neutrinos experience time so that when acted upon by the  
<sup>164</sup> time-evolution operator the initial neutrino state can evolve to a new flavor state. This  
<sup>165</sup> implies that the neutrino flavor states are really a superposition of at least three separate  
<sup>166</sup> neutrino states with well-defined masses. Measurements of neutrino oscillations that have  
<sup>167</sup> taken place over the past couple of decades have measured the differences between  
<sup>168</sup> neutrino mass eigenstates with increasing precision. However, oscillation measurements  
<sup>169</sup> cannot tell us the mass scale of the neutrinos, which is required in order to measure the  
<sup>170</sup> absolute neutrino masses.

<sup>171</sup> The neutrino mass scale remains an unknown quantity in the standard model of  
<sup>172</sup> particle physics. The value of the neutrino mass influences the evolution of the early  
<sup>173</sup> universe and is likely relevant to the energy-scale of new physics responsible for the factor  
<sup>174</sup> of  $10^{-6}$  difference between the neutrino and electron masses. A model-independent way  
<sup>175</sup> to measure the neutrino mass is to measure the tritium beta-decay spectrum near its  
<sup>176</sup> endpoint. Energy conservation requires that the neutrino mass carry away some kinetic  
<sup>177</sup> energy from the beta-decay electron in the form of its mass, which causes a distortion in

178 the shape of the tritium beta-decay spectrum near the endpoint. The isotope tritium has  
179 many advantages for this measurement, and has been used by the KATRIN collaboration  
180 to perform the most sensitive direct neutrino mass measurement to date.

181 KATRIN represents the state-of-the-art experiment in the current generation of  
182 neutrino mass direct measurement experiments and has a final projected sensitivity to  
183 neutrino masses  $m_\nu < 200$  meV. This sensitivity does not fully exhaust the allowed  
184 parameter space of neutrino masses under the normal and inverted neutrino mass  
185 ordering scenarios, which motivates the development of a next generation of neutrino  
186 mass measurement experiments.

187 The Project 8 collaboration is developing a next-generation neutrino mass direct  
188 measurement experiment designed to be sensitive to  $m_\nu < 40$  meV. This sensitivity  
189 is sufficient to exhaust the range of neutrino masses allowed under the inverted mass  
190 ordering regime. Project 8 intends to achieve its sensitivity goal utilizing two technologies  
191 that are novel to the space of direct neutrino mass measurement — atomic tritium and  
192 cyclotron radiation emission spectroscopy (CRES). Atomic tritium is required in order to  
193 avoid systematic broadening the tritium beta-decay spectrum caused by the final state  
194 of the  ${}^3\text{He}^+ \text{-T}$  molecule, and the CRES technique enables a differential measurement of  
195 the tritium spectrum that is background-free and able to be directly integrated with the  
196 atomic tritium source.

197 The Project 8 collaboration is currently engaged in a research and development  
198 program intended to simultaneously develop the atomic tritium and CRES technologies  
199 so that they can be combined in a next-generation experiment. This past year (2022)  
200 Project 8 has used the CRES technique to measure the molecular tritium beta-decay  
201 spectrum and place an upper limit on the neutrino mass:  $m_\beta \leq 152$  eV. This measurement,  
202 while not competitive scientifically, represents the first proof-of-principle that the CRES  
203 technique can be used to measure the neutrino mass.

204 The future goals of the Project 8 collaboration are to develop the technologies  
205 and techniques necessary to scale-up the volumes in which CRES measurements can  
206 be performed. Project 8's first neutrino mass measurement with CRES utilized a  
207 measurement volume on the cubic-centimeter scale, however, sensitivity calculations  
208 estimate that an experiment sensitive to neutrino masses of 40 meV will require several  
209 tens of cubic-meters of experiment volume filled with atomic tritium. Developing a new  
210 approach to performing CRES measurements that can be successfully scaled to these  
211 volumes is a necessary step towards Project 8's neutrino mass measurement goal, and is  
212 the primary topic of my dissertation research.

213 A parallel development is the technology necessary to produce, cool, trap, and  
214 recirculate a supply of atomic tritium that is compatible with CRES measurements. The  
215 atomic tritium system is equally important as the large-volume CRES measurement  
216 technology, but it will not be the focus of this dissertation since I did not contribute  
217 significantly to this effort.

218 The Project 8 collaboration has identified two scalable approaches to neutrino mass  
219 measurement using the CRES technique. One approach is to use an array of antennas  
220 that surrounds a volume of trapped atomic tritium that can perform CRES measurements  
221 by collection the cyclotron radiation emitted by beta-decay electrons into free-space. The  
222 other approach uses a resonant cavity filled with atomic tritium to perform CRES by  
223 measuring the excitation of resonant cavity modes caused by the motion of electrons  
224 trapped inside the cavity volume.

225 The cavity and antenna approaches to CRES have been studied in detail over the past  
226 five years, and, while both approaches offer a physically viable path towards a 40 meV  
227 neutrino mass measurement the collaboration has elected to pursue the cavity approach  
228 for the foreseeable future. The major advantage of the cavity approach is a significant  
229 reduction in the cost and complexity of the experiment design and data analysis, which  
230 provides a less risky path towards Project 8’s scientific goals.

231 In this dissertation I summarize my most impactful contributions to the research and  
232 development of antenna array and cavity CRES. In short these contributions are

- 233 • the development and analysis of signal reconstruction algorithms for antenna array  
234 CRES, which provided key inputs to sensitivity analyses of antenna array CRES  
235 experiments,
- 236 • the development of a specialized antenna designed to synthesize fake CRES radia-  
237 tion, which enabled bench-top testing and validation of the antenna array CRES  
238 technique,
- 239 • the development of an open-cavity design for CRES measurement whose mode  
240 structure can be tuned using perturbations that modify the impedance of the cavity  
241 walls. The development of this cavity concept was one of many developments that  
242 eventually lead to the adoption of cavities as the CRES technology of choice for  
243 the future of Project 8.

## <sup>244</sup> 1.2 Outline

<sup>245</sup> The outline of this dissertation is as follows. In Chapter 2 I provide an introduction to  
<sup>246</sup> the basic physics of neutrinos and beta-decay, which provides context for a discussion of  
<sup>247</sup> various methods to measure the neutrino absolute mass scale.

<sup>248</sup> Chapter 3 is an overview of the CRES technique and the Project 8 collaboration.  
<sup>249</sup> I highlight the Project 8 Phase II experiment, which was the first measurement of  
<sup>250</sup> the tritium beta-decay spectrum with CRES, and I discuss the planned research and  
<sup>251</sup> development for an antenna array CRES experiment in Phase III of the Project 8  
<sup>252</sup> collaboration’s experiment plan. I end Chapter 3 with a discussion of the pilot-scale and  
<sup>253</sup> Phase IV experiments, that will combine a scalable CRES measurement technology with  
<sup>254</sup> atomic tritium and measure the neutrino mass with 40 meV sensitivity.

<sup>255</sup> Chapter 4 discusses the first of the contributions mentioned above, which is the  
<sup>256</sup> development of signal reconstruction techniques for antenna array CRES and an antenna  
<sup>257</sup> array demonstrator experiment called the FSCD. I discuss the important tools that Project  
<sup>258</sup> 8 uses to simulate antenna array CRES before introducing three signal reconstruction  
<sup>259</sup> algorithms that can be used to detect CRES signals using the array. I end Chapter 4  
<sup>260</sup> with a paper that summarizes a detailed analysis and comparison of the signal detection  
<sup>261</sup> performance of each algorithm.

<sup>262</sup> Chapter 5 describes my contributions to the development of antennas and an antenna  
<sup>263</sup> measurement system for Project 8, which is the second major contribution of this  
<sup>264</sup> dissertation. I begin with a general overview of basic principle of antennas and antenna  
<sup>265</sup> measurements, before including a paper that describes the development of unique antenna  
<sup>266</sup> designed to mimic the cyclotron radiation emitted by electrons in free-space when trapped  
<sup>267</sup> in a magnetic field. I call this antenna the synthetic cyclotron radiation antenna (SYNCA)  
<sup>268</sup> and its main purpose is to serve a fake electron for laboratory validation measurements  
<sup>269</sup> of Project 8’s antenna array CRES simulations. Chapter 5 ends with an overview  
<sup>270</sup> of laboratory measurements of a prototype antenna array that were compared with  
<sup>271</sup> simulations to provide upper bounds on reconstruction errors caused by imperfections in  
<sup>272</sup> real-life measurements.

<sup>273</sup> Chapter 6 discusses the cavity approach to CRES, which was adopted as the preferred  
<sup>274</sup> CRES technology for Phase IV late into my dissertation work. The chapter stars by  
<sup>275</sup> discussing resonant cavities in general before introducing the operating principles of the  
<sup>276</sup> cavity approach to CRES. I end the chapter by discussing a study of and open-cavity  
<sup>277</sup> design that could be used for CRES measurements and integrated with atomic tritium

<sup>278</sup> and an electron gun calibration source for the pilot-scale and Phase IV experiments.

<sup>279</sup> Finally, in Chapter 7 I conclude by briefly discussing the future directions of the  
<sup>280</sup> Project 8 collaboration as we continue towards a direct measurement of the neutrino  
<sup>281</sup> mass.

<sup>282</sup> **Chapter 2 |**

<sup>283</sup> **Neutrinos and Neutrino Masses**

<sup>284</sup> **2.1 Introduction**

<sup>285</sup> In this chapter I provide a cursory overview of background information relevant to  
<sup>286</sup> neutrinos and neutrino mass measurements.

<sup>287</sup> In Section 2.2 I provide some background information on the history of neutrinos and  
<sup>288</sup> beta-decay. In Section 2.3 I describe the discover of neutrino oscillations, which proved  
<sup>289</sup> unambiguously that neutrinos have non-zero masses. In Section 2.4 I discuss the current  
<sup>290</sup> state of the theoretical understanding of neutrino masses in the standard model. Lastly,  
<sup>291</sup> in Section 2.5 I discuss methods for measuring the absolute scale of the neutrino mass.

<sup>292</sup> **2.2 Neutrinos and Beta-decay**

<sup>293</sup> Late in the 19th century the phenomena of radioactivity was first observed in experiments  
<sup>294</sup> performed by Henri Becquerel with uranium, and further studied using thorium and  
<sup>295</sup> radium by Marie and Pierre Currie [1, 2]. Early work in radioactivity classified different  
<sup>296</sup> forms of radiation based on it's ability to penetrate different materials. Rutherford was  
<sup>297</sup> the first to separate radioactive emissions into two types, alpha and beta radiation [3].  
<sup>298</sup> Alpha rays can be easily stopped by a piece of paper or thin foil of metal, whereas beta  
<sup>299</sup> radiation could penetrate metals several millimeters thick. Later a third form of radiation  
<sup>300</sup> was identified by Villard [4], which was still more penetrating, and was eventually termed  
<sup>301</sup> gamma radiation by Rutherford.

<sup>302</sup> When these forms of radioactivity were first discovered it was unclear what physically  
<sup>303</sup> constituted an alpha, beta, or gamma particle. Experiments with radioactivity in  
<sup>304</sup> magnetic fields was eventually able to identify the charge composition of different forms  
<sup>305</sup> of radiation. In particular, experiments by Becquerel identified that beta radiation had

306 an identical charge-to-mass ratio to the electron discovered by Thompson in his work on  
307 cathode rays [5]. This was strongly suggestive that beta particles were indeed electrons.

308 Further studies of beta radiation lead to the discovery that radioactivity resulted in  
309 the transmutation of elements [6] caused by the decay of a heavier nucleus to a lighter  
310 species. One feature of beta radiation, which we now properly call beta-decay, that  
311 was different from alpha-decays and gamma radiation is that the electrons produced by  
312 beta-decay have a continuous spectrum of kinetic energies, whereas, alpha and gamma  
313 particles are emitted with discrete energies. This feature of beta-decay was first observed  
314 by Chadwick in 1914 [7], and was extremely puzzling at the time since the continuous  
315 spectrum apparently violates energy conservation [8].

316 Famously, in 1930 Pauli proposed the existence of a new neutral particle, which he  
317 termed the "neutron", that was also produced during beta-decay in order to resolve the  
318 missing energy problem posed by the beta-decay spectrum [9]. Because this particle  
319 carried no charge, it was hypothesized at the time that it had simply not been observed  
320 in any experiments up to that time. This "neutron", which was initially estimated to  
321 have a mass no larger than that of an electron, was eventually renamed the "neutrino" by  
322 Fermi [10] after the discovery of the neutron by Chadwick in 1932 [11]. Later, in 1933,  
323 Fermi developed a quantum mechanical theory for beta-decay in which both an electron  
324 and neutrino are produced by the decay of a neutron to a proton inside the radioactive  
325 nucleus [12].

326 Little more than a speculation when first introduced, indirect evidence for the existence  
327 of neutrinos was obtained in 1938 by the simultaneous observation of the electron and  
328 recoiling nucleus in cloud chambers by Crane and Halpern [13]. However, it wasn't  
329 until the Cowan-Reines experiment [14] in 1956 that direct evidence for the existence of  
330 neutrinos was observed by detecting the inverse beta-decays caused by neutrinos from a  
331 nuclear reactor interacting with protons contained in water molecules. The difficulty in  
332 detecting neutrinos is caused by their weak interactions with other particles. Further,  
333 experiments revealed that different types of neutrinos existed based on the nature of the  
334 leptons produced in neutrino charged-current interactions [15], but the existence of a  
335 neutrino mass remained an open question that would take more than 40 year to resolve.

## 336 **2.3 Neutrino Oscillations**

337 The first hint of neutrino flavor transitions or neutrino oscillations was indicated by  
338 the solar neutrino problem, which referred to discrepancies between the predicted flux

339 of  $\nu_e$  from the standard solar model and measurements of the solar neutrino flux such  
 340 as the famous experiment at the Homestake mine by Ray Davis Jr. and collaborators  
 341 in the 1960's [16]. Essentially, fewer electron-type neutrinos than expected were being  
 342 observed from the sun. Finally, in the early 2000's the SNO experiment was able to  
 343 resolve the solar neutrino problem by identifying neutrino oscillations as the cause of the  
 344 observed deficit [17]. Furthermore, measurements of the atmospheric flux of neutrinos by  
 345 the Super-Kamiokande experiment and others revealed that fewer muon-type neutrinos  
 346 survived passage through the earth than expected providing strong evidence for neutrino  
 347 oscillations for both flavors [18].

348 The origin of neutrino oscillations is that the weak eigenstates are distinct from the  
 349 mass eigenstates [19]. The neutrino mass eigenstates represent physical particles in the  
 350 sense that they are solutions to the free-particle Hamiltonian, whereas, the neutrino weak  
 351 eigenstates correspond to the neutrino states that interact via the weak charged-current  
 352 interaction. The neutrino weak eigenstates are a linear superposition of the neutrino  
 353 mass eigenstates

$$\nu_\ell = \sum_i U_{\ell i} \nu_i, \quad (2.1)$$

354 where  $\ell = e, \mu, \tau$  and  $i = 1, 2, 3$ . The matrix elements  $U_{\ell i}$  are the elements of the  
 355 Pontecorvo-Maki-Nakagawa-Sakata (PMNS) matrix that describes the mixing between  
 356 the neutrino flavor and mass states.

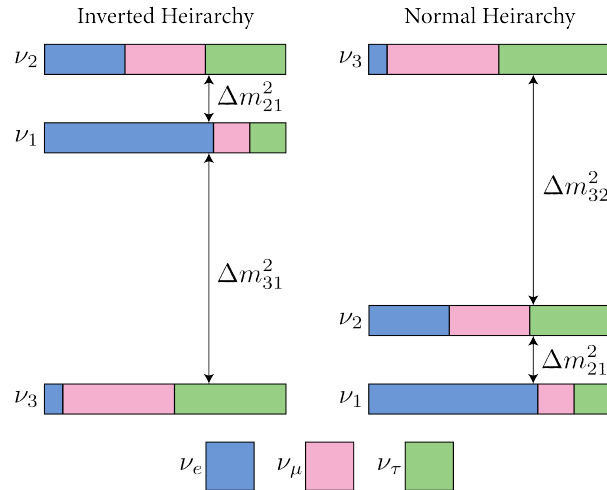


Figure 2.1: A diagram of two different neutrino mass ordering scenarios. In the inverted hierarchy (inverted mass ordering) the lightest neutrino mass is  $m_3$ , whereas, in the normal hierarchy (normal mass ordering)  $m_1$  is the lightest neutrino. What cannot be measured by neutrino oscillations is the neutrino absolute mass scale, which is essentially the mass of the lightest neutrino mass eigenstate.

357 One standard parameterization of the PMNS matrix is

$$\begin{aligned}
U_{PMNS} &= \begin{bmatrix} U_{e1} & U_{e2} & U_{e3} \\ U_{\mu 1} & U_{\mu 2} & U_{\mu 3} \\ U_{\tau 1} & U_{\tau 2} & U_{\tau 3} \end{bmatrix} \\
&= \begin{bmatrix} 1 & 0 & 0 \\ 0 & c_{23} & s_{23} \\ 0 & -s_{23} & c_{23} \end{bmatrix} \begin{bmatrix} c_{13} & 0 & s_{13}e^{-i\delta} \\ 0 & 1 & 0 \\ -s_{13}e^{i\delta} & 0 & c_{13} \end{bmatrix} \begin{bmatrix} c_{12} & s_{12} & 0 \\ -s_{12} & c_{12} & 0 \\ 0 & 0 & 1 \end{bmatrix} \\
&\quad \times \begin{bmatrix} e^{i\alpha_1/2} & 0 & 0 \\ 0 & e^{i\alpha_2/2} & 0 \\ 0 & 0 & 1 \end{bmatrix}, \tag{2.2}
\end{aligned}$$

358 where  $c_{ij} = \cos \theta_{ij}$  and  $s_{ij} = \sin \theta_{ij}$ . The parameters  $\alpha_1$  and  $\alpha_2$  are only included in the  
359 PNMS matrix if neutrinos are Majorana particles, something which represents a current  
360 area of research in neutrino physics. The phase  $\delta$  quantifies the degree of CP-violation  
361 in the neutrino sector. Including the Majorana phases the PMNS matrix contains six  
362 independent parameters. In addition, neutrino oscillation probabilities depend on the  
363 squared mass differences between neutrino mass eigenstates

$$\Delta m_{ij}^2 = m_i^2 - m_j^2, \tag{2.3}$$

364 where  $ij = 12, 32, 31$  respectively. Because  $\Delta m_{32}^2 = \Delta m_{31}^2 - \Delta m_{21}^2$ , this adds an additional  
365 two parameters that must be constrained by neutrino oscillations.

366 A giant experimental effort over the past couple of decades has greatly contained the  
367 majority of parameters in the PMNS matrix, many to relative uncertainties of only a  
368 few percent. However, some parameters still remain relatively unconstrained, which is  
369 the origin of the current uncertainty in the ordering of the neutrino masses (see Figure  
370 2.1). The neutrino masses can be organized by their relative mass. The current neutrino  
371 oscillation data can confirm that  $m_2 > m_1$ , however, the sign of  $\Delta m_{32}^2$  is still unknown.  
372 This leads to two scenarios where neutrino masses follow the ordering  $m_3 > m_2 > m_1$ ,  
373 which is called the normal mass ordering (NMO), or alternatively neutrino masses may  
374 be ordered  $m_2 > m_1 > m_3$ , which is called the inverted mass ordering (IMO). Next-  
375 generation neutrino oscillation experiments such as JUNO [20], Hyper-Kamiokande [21],  
376 and DUNE [22] are poised to resolve this ambiguity in the coming years.

377 Neutrino oscillation probabilities are only sensitive to the neutrino masses via the  
378 squared mass differences. Therefore, oscillation probabilities are unaffected by the

absolute scale of the neutrino mass. However, oscillations can be used to obtain a lower bound on the neutrino masses by setting the mass of the lightest neutrino mass state to zero. This results in different lower limits depending on the ordering of the neutrino mass states. Current best-fit values [23] with  $1\sigma$ -uncertainties for the squared mass differences are

$$\Delta m_{21}^2 = (7.42^{+0.21}_{-0.20}) \times 10^{-5} \text{ eV}^2, \quad (2.4)$$

$$\Delta m_{31}^2 = (2.5176^{+0.026}_{-0.028}) \times 10^{-3} \text{ eV}^2 \text{ (NMO)}, \quad (2.5)$$

for the normal mass ordering, and in the case of the inverted ordering we have

$$\Delta m_{32}^2 = (-2.498^{+0.028}_{-0.028}) \times 10^{-3} \text{ eV}^2 \text{ (IMO).} \quad (2.6)$$

By letting the lightest neutrino mass in each ordering scenario ( $m_{\text{least}}$ ) take on a range of values one can visualize the relative masses of the neutrinos as a function of  $m_{\text{least}}$  (see Figure 2.2).

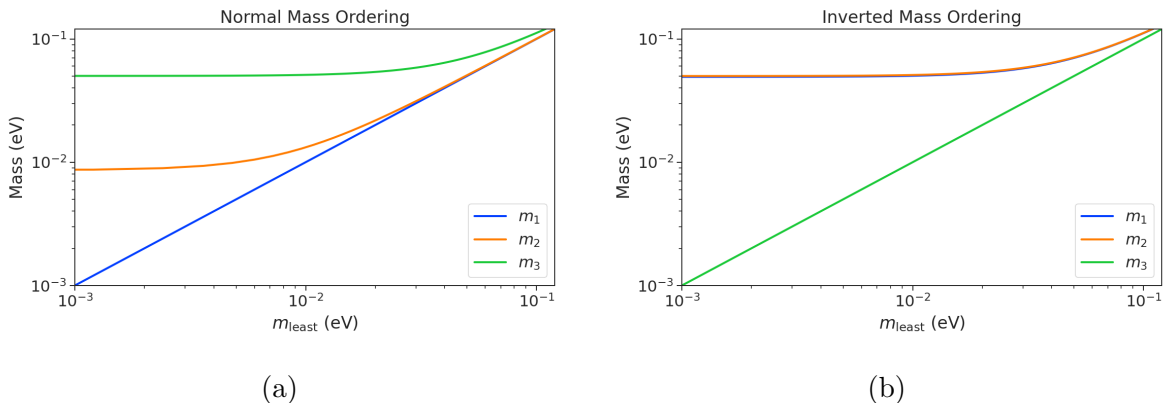


Figure 2.2: The masses of the neutrinos as a function of the lightest neutrino mass in both the normal (a) and inverted (b) mass ordering regimes.

## 2.4 Neutrino Masses in the Standard Model

In this section, I briefly summarize the current theoretical understanding of neutrino masses in the standard model [24–26]. Neutrinos are spin 1/2 particles, which are described using the Dirac equation.

$$(i\hbar\gamma^\mu\partial_\mu - mc)\psi(x) = 0, \quad (2.7)$$

392 where the field that describes the particle is denoted as  $\psi(x)$ . In the standard model  
 393 fermions acquire mass through the Yukawa interaction, which add to the standard model  
 394 Lagrangian terms of the form

$$\mathcal{L}_{\text{Yukawa}} = -Y_{ij}^\ell \bar{L}_{Li} \phi E_{Rj} + \text{h.c.}, \quad (2.8)$$

395 where  $Y_{ij}^\ell$  is an element of the  $3 \times 3$  Yukawa coupling matrix for leptons,  $L_{Li}$  is the  
 396 left-handed lepton doublet for generation  $i$ ,  $\phi$  is the Higgs doublet, and  $E_{Rj}$  is the  
 397 right-handed lepton field for generation  $j$ . Neutrinos are represented only as left-handed  
 398 neutrinos and right-handed antineutrinos in the standard model, which is consistent  
 399 with experimental observations. Since there are no right-handed neutrino singlet fields,  
 400 there are no Yukawa interaction terms, thus neutrinos in the standard model are strictly  
 401 massless. Therefore, non-zero neutrino mass is evidence for physics beyond the standard  
 402 model.

403 For the charged leptons, the Yukawa interaction leads to masses of the form

$$m_{ij}^\ell = Y_{ij}^\ell \frac{v}{\sqrt{2}}, \quad (2.9)$$

404 where  $v$  is the Higgs vacuum expectation value. The observation of massive neutrinos  
 405 motivates the extension of the standard model to explain the origin of neutrino masses,  
 406 which can be approached in different ways, but all approaches add additional degrees of  
 407 freedom to the standard model. One approach is to introduce to the standard model a  
 408 right-handed neutrino field that allows one to include Yukawa terms of the form

$$\mathcal{L}_{\nu \text{Yukawa}} = -Y_{ij}^\ell \bar{L}_{Li} \phi \nu_{Rj} + \text{h.c.} \quad (2.10)$$

409 where  $\nu_{Rj}$  is the right-handed neutrino singlet. Because experimental evidence strongly  
 410 predicts only three active neutrinos, these additional neutrinos are sterile and do not in-  
 411 teract via the strong, weak, or electromagnetic interactions. After spontaneous symmetry  
 412 breaking, the Yukawa interaction leads to mass terms given by

$$\mathcal{L}_D = -M_{Di} \bar{\nu}_{Ri} \nu_{Lj} + \text{h.c.}, \quad (2.11)$$

413 which is called a Dirac mass term. One of the issues with constructing neutrino masses  
 414 in this way is that the required Yukawa couplings are at least a factor of  $10^6$  smaller than  
 415 that of an electron, which begs the question: why are the Yukawa couplings so small for

<sup>416</sup> the neutrinos?

<sup>417</sup> An alternative approach is to allow the neutrinos to have a Majorana mass, which is  
<sup>418</sup> possible because neutrinos are electrically neutral particles. The Majorana mass terms  
<sup>419</sup> for the neutrino have the form

$$\mathcal{L}_M = -\frac{1}{2}(M_{Rij}\bar{\nu}_{Ri}\nu_{Rj}^c M_{Lij}\bar{\nu}_{Li}\nu_{Lj}^c) + \text{h.c.}, \quad (2.12)$$

<sup>420</sup> where  $M_{Rij}$  and  $M_{Lij}$  are right-handed and left-handed Majorana mass matrices. A  
<sup>421</sup> consequence of neutrinos being Majorana particles is lepton number violation, which  
<sup>422</sup> predicts the occurrence of neutrino-less double beta-decay at a rate proportional to the  
<sup>423</sup> neutrino mass.

<sup>424</sup> In the most general case neutrinos have both Dirac and Majorana mass terms, which  
<sup>425</sup> allows one to generate neutrino masses with Yukawa couplings similar to the rest of  
<sup>426</sup> the standard model. Considering just one generation of neutrinos for illustration, the  
<sup>427</sup> combined Lagrangian can be written as

$$\mathcal{L}_{D+M} = -m_D\bar{\nu}_R\nu_L - \frac{1}{2}(m_L\bar{\nu}_L\nu_L^c + m_R\bar{\nu}_R\nu_R^c) + \text{h.c.}, \quad (2.13)$$

<sup>428</sup> or equivalently,

$$\mathcal{L}_{D+M} = -\frac{1}{2} \begin{bmatrix} \bar{\nu}_L & \bar{\nu}_R^c \end{bmatrix} \begin{bmatrix} m_L & m_D \\ m_D & m_R \end{bmatrix} \begin{bmatrix} \nu_L^c \\ \nu_R \end{bmatrix} + \text{h.c..} \quad (2.14)$$

<sup>429</sup> An example mass generation mechanism with this approach is the Type-I see-saw  
<sup>430</sup> mechanism [27], in which we take  $m_L = 0$  and  $m_R \gg m_D$ . By diagonalizing Equation  
<sup>431</sup> 2.14 one obtains the mass eigenvalues that represent the physical masses of the neutrinos.  
<sup>432</sup> The light neutrino mass eigenstate, which represents the observed neutrino mass, has a  
<sup>433</sup> mass given by

$$m_1 \approx \frac{m_D^2}{m_R}, \quad (2.15)$$

<sup>434</sup> and the heavy neutrino mass eigenstate, which represents the unobserved sterile neutrino,  
<sup>435</sup> has a mass

$$m_2 \approx m_R. \quad (2.16)$$

<sup>436</sup> For  $m_D$  similar to the other quark or lepton masses, one obtains physical neutrino masses  
<sup>437</sup> consistent with observations from sterile neutrino masses of  $m_R \approx O(10^{15})$  GeV. This  
<sup>438</sup> mass scale is well beyond the capabilities of modern particle accelerators.

## <sup>439</sup> 2.5 Neutrino Absolute Mass Scale

<sup>440</sup> The neutrino absolute mass scale or simply "neutrino mass" cannot be probed with  
<sup>441</sup> neutrino oscillations, since oscillation probabilities are determined by the squared mass  
<sup>442</sup> differences between neutrino mass eigenstates, therefore, alternative techniques are needed  
<sup>443</sup> to perform an effective measurement of the neutrino mass.

### <sup>444</sup> 2.5.1 Limits from Cosmology

<sup>445</sup> The  $\Lambda$ CDM model summarizes our current cosmological understanding of our universe [28].  
<sup>446</sup>  $\Lambda$ CDM predicts that the universe originated from a single expansion event colloquially  
<sup>447</sup> called the "Big Bang". During the Big Bang, the universe originated as a hot spacetime  
<sup>448</sup> singularity, which abruptly experienced rapid expansion in a process known as inflation.  
<sup>449</sup> After expansion the inflationary field eventually decayed into a population of quarks,  
<sup>450</sup> gluons, leptons, and photons, which were kept in thermal equilibrium by the high-  
<sup>451</sup> temperatures of the early universe.

<sup>452</sup> As the universe continued to expand its density and temperature decreased until  
<sup>453</sup> the formation of neutral atoms, primarily hydrogen, was possible. At which point the  
<sup>454</sup> population of photons produced during the Big Bang thermally decoupled. A direct  
<sup>455</sup> prediction of the  $\Lambda$ CDM model is that this population of photons should still be present,  
<sup>456</sup> but with a significantly reduced temperature due to the expansion of the universe. This  
<sup>457</sup> is consistent with the observation of the CMB (cosmic microwave background), which is  
<sup>458</sup> a population of microwave radiation with a blackbody temperature of 2.7 K. The CMB  
<sup>459</sup> is extremely uniform in all directions with slight anisotropies that can be analyzed to  
<sup>460</sup> study the evolution of the early universe. A series of experiments have measured the  
<sup>461</sup> CMB with increasing levels of precision, which has lead to a significant increase in our  
<sup>462</sup> current understanding of cosmology.

<sup>463</sup> In addition to the CMB, inflation predicts the existence of a  $C\nu B$  (cosmic neutrino  
<sup>464</sup> background) [29], which are the remnant neutrinos produced during the Big Bang. Since  
<sup>465</sup> neutrinos only interact via the weak force, they decouple from the hot Big Bang plasma  
<sup>466</sup> at an earlier time than the CMB radiation. The temperature at which the  $C\nu B$  decouples  
<sup>467</sup> depends on the neutrino rest mass. Neutrinos play a unique role in the  $\Lambda$ CDM model,  
<sup>468</sup> due to the fact that neutrinos act as radiation early in the universe but as matter in the  
<sup>469</sup> late universe. This leads to specific signatures that impact the expected anisotropies  
<sup>470</sup> of the CMB as well as the distribution of matter in the universe [30]. By combining  
<sup>471</sup> measurements of the CMB with measurements of the large-scale structure (LSS) of the

universe one can constrain the neutrino mass scale by fitting these datasets with the  $\Lambda$ CDM model. This analysis results in some of the most stringent constraints on the neutrino mass. Recent analyses [28] have been able to constrain the neutrino mass scale to

$$\Sigma_{m_\nu} \equiv \sum_i m_i < 0.11 \text{ eV}, \quad (2.17)$$

where  $m_i$  are the neutrino mass eigenstates.

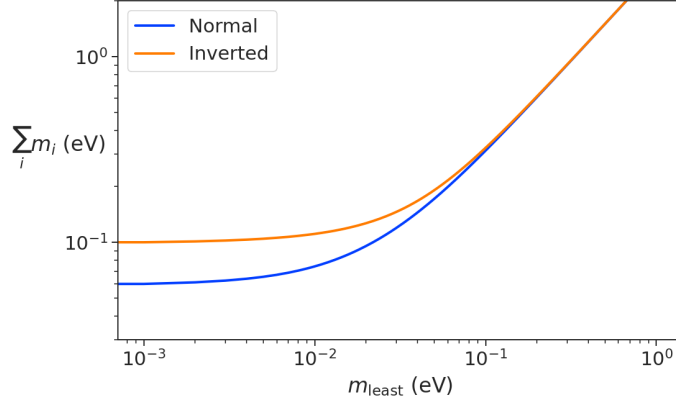


Figure 2.3: The neutrino mass observable measured by cosmology as a function of the lightest neutrino mass eigenstate.

The observable  $\Sigma_{m_\nu}$  constrains the neutrino mass by setting the mass of the lightest neutrino mass eigenstate ( $m_{\text{least}}$ ). In the normal mass ordering  $\Sigma_{m_\nu}$  can be rewritten in the form

$$\Sigma_{m_\nu} = m_{\text{least}} + \sqrt{\Delta m_{21}^2 + m_{\text{least}}^2} + \sqrt{\Delta m_{32}^2 + m_{\text{least}}^2}, \quad (2.18)$$

where it is clear that a measurement of  $\Sigma_{m_\nu}$  effectively sets the neutrino mass scale through  $m_{\text{least}}$ . The analogous formula for the inverted mass ordering is

$$\Sigma_{m_\nu} = m_{\text{least}} + \sqrt{-\Delta m_{32}^2 + m_{\text{least}}^2} + \sqrt{-\Delta m_{31}^2 + m_{\text{least}}^2}. \quad (2.19)$$

In figure 2.3 we plot the observable  $\Sigma_{m_\nu}$  as a function of  $m_{\text{least}}$ .

Upcoming experiments [31] are planned to refine measurements of the CMB, LSS, and other cosmological observables. With this additional data it is possible that in the near future cosmological measurements will be able to positively constrain the neutrino absolute mass scale. However, the strength of these limits strictly depend on the accuracy of the  $\Lambda$ CDM model, which highlights the need for direct experimental measurements of the neutrino mass to confirm the predictions of cosmology and to fix the neutrino mass

<sup>489</sup> parameter in future cosmological analyses.

### <sup>490</sup> 2.5.2 Limits from Neutrinoless Double Beta-decay Searches

<sup>491</sup> If neutrinos are Majorana fermions, then the neutrino is equivalent to its own antiparticle  
<sup>492</sup> and lepton conservation is not an exact law of nature [32]. Limits on the rate of  
<sup>493</sup> neutrinoless double beta-decay ( $0\nu\beta\beta$ ), are some of the most powerful current tests of  
<sup>494</sup> lepton number conservation [28]. If  $0\nu\beta\beta$  were observed it would direct evidence that  
<sup>495</sup> neutrinos are Majorana fermions, and provide a method for measuring the neutrino mass  
<sup>496</sup> scale.

<sup>497</sup> Standard double beta-decay occurs when two neutrons contained in the nucleus  
<sup>498</sup> spontaneously decay into two protons, which results in the production of two electrons  
 and two neutrinos (see Figure 2.4). However, during  $0\nu\beta\beta$  the two neutrinos self-annihilate

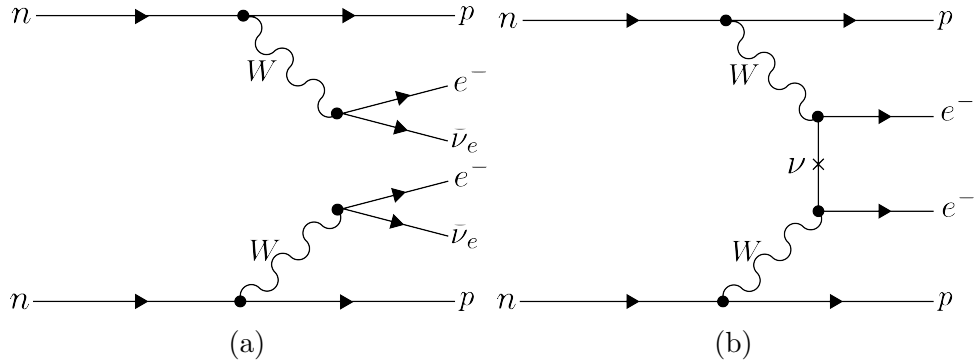


Figure 2.4: Feynman diagrams for double beta-decay (a) and  $0\nu\beta\beta$ (b).

<sup>499</sup>  
<sup>500</sup> producing only two electrons, which violates lepton number by two.

<sup>501</sup> Assuming that the exchange of two Majorana neutrinos is the dominant channel for  
<sup>502</sup>  $0\nu\beta\beta$ , then a measurement of the  $0\nu\beta\beta$  half-life for a particular isotope can be used to  
<sup>503</sup> set the neutrino absolute mass scale [33]. The half-life is written in terms of the effective  
<sup>504</sup> neutrino mass for  $0\nu\beta\beta$  ( $m_{\beta\beta}$ ) using the equation

$$T_{1/2}^{0\nu} = \frac{1}{G|\mathcal{M}|^2 m_{\beta\beta}^2}, \quad (2.20)$$

<sup>505</sup> where  $G$  is the phase-space factor for the decay and  $\mathcal{M}$  is the relevant nuclear matrix  
<sup>506</sup> element.  $m_{\beta\beta}$  is given by an incoherent sum of the neutrino mass eigenstates weighted

507 by the PMNS mixing matrix parameters,

$$m_{\beta\beta} = \left| \sum_i U_{ei}^2 m_i \right|. \quad (2.21)$$

508 The information provided from  $0\nu\beta\beta$  on the neutrino mass scale can be visualized  
 509 by expressing the value of  $m_{\beta\beta}$  in terms of  $m_{\text{least}}$  and two relative Majorana phases [34].  
 510 The allowed regions for  $m_{\beta\beta}$  as a function of  $m_{\text{least}}$  are shown in Figure 2.5 as the regions  
 511 bounded by the black curves overlayed with the discovery probabilities of future  $0\nu\beta\beta$   
 decay experiments based on current neutrino data.

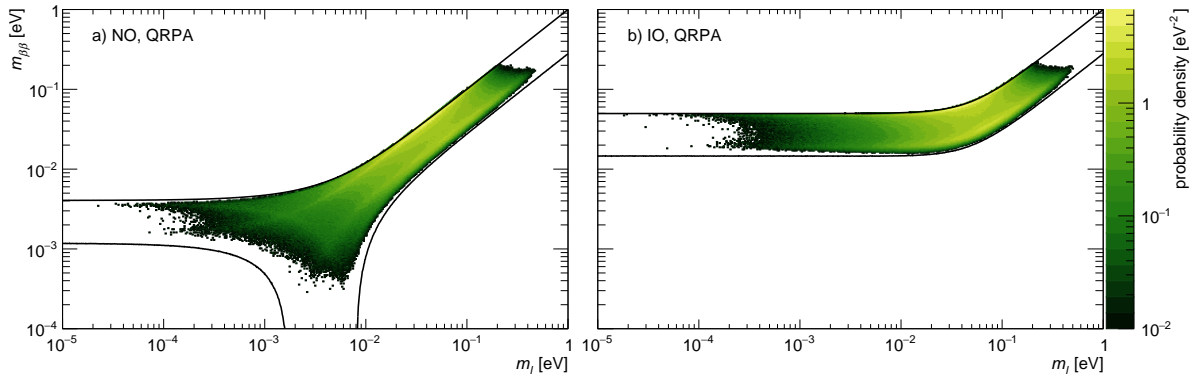


Figure 2.5: The discovery probabilities for the future generation of  $0\nu\beta\beta$  experiments as a function of  $m_{\beta\beta}$  and  $m_{\text{least}}$ . Figure from [34].

512  
 513 Because of the possibility of cancellation due to the unknown Majorana phases  
 514 included in the sum specified by Equation 2.21, the information gained is necessarily  
 515 imperfect. Additionally, theoretical uncertainties in the calculation of the nuclear matrix  
 516 elements complicates the calculation of  $m_{\beta\beta}$  from a measurement of  $0\nu\beta\beta$  half-life. Similar  
 517 to cosmology, there is a high degree of complementarity between direct measurements  
 518 of the neutrino mass and  $0\nu\beta\beta$ . In particular, a measurement of  $m_{\text{least}}$  to less than  
 519 than 0.1 eV sensitivity provides significant information for  $0\nu\beta\beta$  searches based of the  
 520 discovery probabilities of Figure 2.5.

### 521 2.5.3 Limits from Beta-decay

522 Certain processes involving neutrinos, in particular beta-decay (see Figure 2.6), have  
 523 initial states with well-defined total energies and final states that can be measured with  
 524 high accuracy and precision. Beta-decay involves the decay of an unstable isotope where  
 525 a neutron spontaneously converts to a proton and emits and electron and anti-neutrino

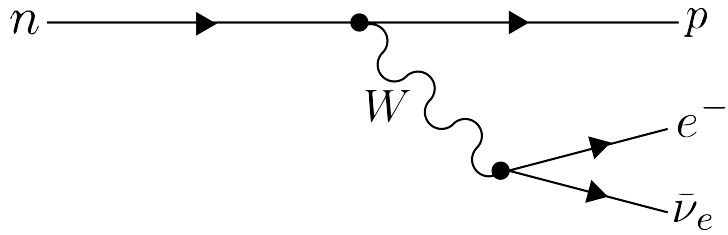


Figure 2.6: A Feynman diagram of beta decay

526 ("neutrino" for brevity) to conserve charge and lepton number [1]. Therefore, by applying  
 527 the principles of energy and momentum conservation, a measurement of the kinematics  
 528 of the final state can be used to constrain the neutrino mass [35].

529 Using beta-decay to measure the neutrino mass can be tied back to Fermi's original  
 1934 theory of nuclear beta-decay [12] (see Figure 2.7). Because the constraints on the

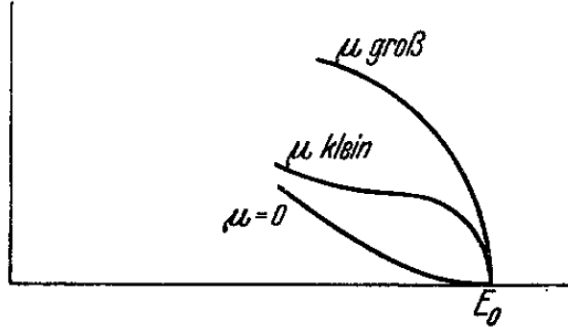


Figure 2.7: A figure from Fermi's 1934 paper on a theory of beta-decay depicting the kinetic energy spectrum of the emitted electron. The effect of the neutrino mass, written as  $\mu$ , is to distort the shape of the spectrum near the endpoint from the zero-mass spectrum.

530 neutrino mass from beta-decay depend only on the final state measurement capabilities  
 531 and the principles of energy and momentum conservation, neutrino mass measurements  
 532 with beta-decay are sometimes called direct measurements. A direct measurement like  
 533 beta-decay contrasts with other neutrino mass measurements approaches that are model-  
 534 dependent such as cosmology and  $0\nu\beta\beta$ , which provide complementary ways to study  
 535 the physics of massive neutrinos.

537 The isotope of choice for direct neutrino mass measurements with beta-decay has  
 538 been tritium ( ${}^3H_2$ ) for many decades, because it conveniently fulfills many experimental  
 539 requirements. Of upmost importance is a decay with a low Q-value, which is the available  
 540 kinetic energy based on the mass difference between the initial and final states. The

541 effect of a massive neutrino on the shape of the spectrum is magnified for low Q-values  
 542 and tritium decays have an unusually low Q-value of 18.6 keV.

543 Additionally, tritium beta-decay is a super-allowed decay, which results in a relatively  
 544 short half-life of 12.3 years. Therefore, it is relatively easy to obtain a high-activity  
 545 using a small source mass. High-activity is desirable because of the low-activity near  
 546 the tritium spectrum endpoint. For tritium beta-decays only a factor of  $3 \times 10^{-13}$  of  
 547 the decays occur in the last 1 eV of the spectrum. Isotopes with Q-values lower than  
 548 tritium are known [35], but this is outweighed by exceedingly long half-lives leading to  
 549 unobtainable source masses.

550 The measurement involves quantifying the effect of the neutrino's mass on shape of  
 551 the electron's kinetic energy spectrum near the endpoint. The shape of the kinetic energy  
 552 spectrum (see Figure 2.8) is given by

$$\frac{d\Gamma}{dE} = \frac{G_F^2 |V_{ud}|^2}{2\pi^3} (G_V^2 + 3G_A^2) F(Z, \beta) \beta (E + m_e)^2 (E_0 - E) \\ \times \sum_{i=1,2,3} |U_{ei}|^2 [(E_0 - E)^2 - m_i^2]^{1/2} \Theta(E_0 - E - m_i), \quad (2.22)$$

553 where  $G_F$  is the Fermi coupling constant,  $V_{ud}$  is an element of the CKM matrix,  $E$  is  
 554 the kinetic energy of the electron,  $\beta$  is the velocity of the electron divided by the speed  
 555 of light,  $E_0$  is the endpoint energy assuming zero neutrino mass,  $F(Z, \beta)$  is the Fermi  
 556 function, and  $\Theta(E_0 - E - m_i)$  is the Heaviside function, which enforces energy conservation.  
 557 One can see that the decay spectrum is actually a combination of three spectra with  
 558 different endpoints based on the actual values of the neutrino mass eigenstates,  $m_i$ . This  
 559 results in "kinks" in the spectrum shape due to the overlapping spectra, but such an  
 560 effect would likely be impossible to resolve given the finite energy resolution of a real  
 561 experiment and low statistics.

562 The neutrino mass scale variable measured by beta-decay is given by

$$m_\beta^2 = \sum_i |U_{ei}|^2 m_i^2, \quad (2.23)$$

563 where  $m_\beta$  is the electron-weighted neutrino mass or simply "neutrino mass" for brevity.  
 564  $m_\beta$  corresponds to a particular weighted sum of the neutrino masses, which is distinct  
 565 from effective neutrino masses such as  $m_{\beta\beta}$  [35]. Assuming unitarity, the neutrino mass  
 566 can be expressed in terms of the PMNS matrix elements, squared mass differences, and

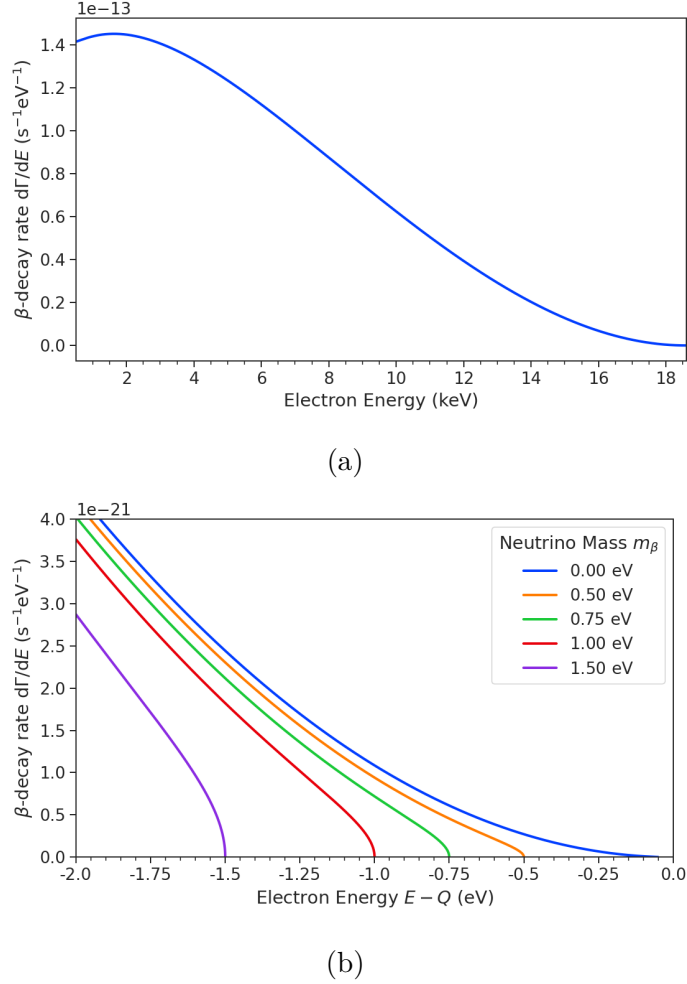


Figure 2.8: The tritium beta-decay spectrum. The affect of a massive neutrino on the spectrum is to change it's shape near the endpoint by an amount proportional to the size of the neutrino mass. This suggests that a sufficiently high-statistic and high-resolution measurement of the spectrum endpoint would be able to measure the neutrino mass.

<sup>567</sup> the lightest neutrino mass eigenstate. For the normal mass ordering the equation is

$$m_\beta^2 = m_{\text{least}}^2 + |U_{e2}|^2 \Delta m_{21}^2 + |U_{e3}|^2 \Delta m_{31}^2, \quad (2.24)$$

<sup>568</sup> and for the inverted ordering the equation is

$$m_\beta^2 = m_{\text{least}}^2 + |U_{e1}|^2 (-\Delta m_{32}^2 - \Delta m_{21}^2) + |U_{e2}|^2 (-\Delta m_{32}^2). \quad (2.25)$$

<sup>569</sup> Therefore, a measurement of the neutrino mass in combination with neutrino mixing  
<sup>570</sup> parameters is effectively a measurement of  $m_{\text{least}}$ .

571        Since the neutrino mass is small ( $< 1$  eV), it's effect on the spectrum is limited to  
572        the endpoint region. The affect of a non-zero neutrino mass on the endpoint spectrum is  
573        plotted for the reader in Figure 2.8. Resolving the small changes in the spectrum shape  
574        requires an experimental technique with high statistics, excellent energy resolution, and  
575        low background activity.

576 **Chapter 3** |

577 **Direct Measurement of the Neutrino Mass**

578 **with Project 8**

579 **3.1 Introduction**

580 A promising technique for direct measurements of the neutrino mass beyond the projected  
581 limit of the ongoing KATRIN experiment [36] is tritium beta-decay spectroscopy with an  
582 atomic tritium source [37]. Atomic tritium, combined with a large-volume, high-resolution  
583 energy measurement technique, is capable of measuring the neutrino mass with sensitivity  
584 below the 50 meV limit allowed by neutrino oscillations.

585 Cyclotron Radiation Emission Spectroscopy or CRES is a high-resolution energy  
586 measurement technique compatible with atomic tritium production and storage that can  
587 enable the next-generation of neutrino mass direct measurement experiments [38]. The  
588 Project 8 collaboration is currently engaged in a program of research and development  
589 (R&D) aimed at developing the technology necessary for a 40 meV sensitivity measurement  
590 of the neutrino mass using CRES and atomic tritium [39].

591 In Section 3.2 I provide an introduction to the basics of the CRES technique as well as  
592 the goals of the Project 8 experiment. Additionally, I sketch out the phased experiment  
593 development plan being implemented by Project 8 to build towards a next-generation  
594 neutrino mass experiment.

595 In Section 3.3 I give a brief overview of Phase II of the Project 8 experiment [40, 41],  
596 which completed early in 2023. Although the bulk of the work presented in this thesis is  
597 relevant to designs of future Project 8 experiments, a description of the work in Phase II  
598 provides useful context for the rest of the work.

599 In Section 3.4 I introduce a CRES measurement concept based on antenna arrays [42],  
600 which could be the basis for the ultimate Project 8 neutrino mass experiment. A  
601 significant portion of the R&D efforts of Project 8 in Phase III were directed towards

602 simulating and modeling this experimental concept in order to understand the achievable  
603 sensitivity to the neutrino mass.

604 Lastly, in Section 3.5 I introduce conceptual designs of pilot-scale experiments and  
605 Phase IV that combine atomic CRES with a large-volume CRES detection technique.  
606 This includes a design concept for an antenna array based experiment, but also a design  
607 for a resonant cavity based experiment. Resonant cavities are discussed in more depth in  
608 Chapter 6 and have become the default choice for the Phase IV experiment.

## 609 **3.2 Cyclotron Radiation Emission Spectroscopy and Project** 610 **8**

### 611 **3.2.1 Cyclotron Radiation Emission Spectroscopy — CRES**

612 Time and frequency are two of the most precisely measured quantities in physics. It is  
613 often advantageous to convert measurements of other physical quantities like mass or  
614 length into frequency measurements due to the digital nature of frequency measurements  
615 that make them immune to many sources of noise. Atomic clocks, which operate by  
616 measuring the frequencies of various atomic transitions, have been used to measure  
617 time with astounding relative uncertainties of  $10^{-18}$  seconds [43]. The extreme precision  
618 possible with frequency measurements is often summarized using the a quote from the  
619 Physicist Arthur Schawlow who said advise his students to "Never measure anything but  
620 frequency!" [44].

621 Neutrino mass measurements using tritium beta-decay require us to measure pertur-  
622 bations of the 18600 eV tritium endpoint to a precision as low as 0.1 eV, therefore, a  
623 spectroscopic technique with extremely high resolution is required for this measurement.  
624 The intuitive explanation for why frequency measurements are capable of such high reso-  
625 lutions is that they are essentially counting measurements, which average the number of  
626 oscillations of a physical system over time. By observing a rapidly oscillating system over  
627 a sufficient length of time one can obtain essentially arbitrary precision on a frequency  
628 limited only by the time available for measurement and the SNR of the system.

629 What is required is that one translate the kinetic energy of the electron into a frequency,  
630 and a straightforward way to accomplish this is to place a gaseous supply of tritium into  
631 a magnetic field. When an atom decays the resulting electron will immediately begin  
632 to orbit around a magnetic field line at the cyclotron frequency, which is proportional  
633 to its kinetic energy (see Figure 3.1). The acceleration caused by the orbit leads to the

634 emission of cyclotron radiation that can be detected using an array of antennas or a  
 635 different RF sensor such as a resonant cavity. The frequency of the radiation gives the  
 636 electron's kinetic energy, which is used to build the beta-decay spectrum and measure  
 637 the neutrino mass. The name for this measurement technique is Cyclotron Radiation  
 638 Emission Spectroscopy or CRES [38].

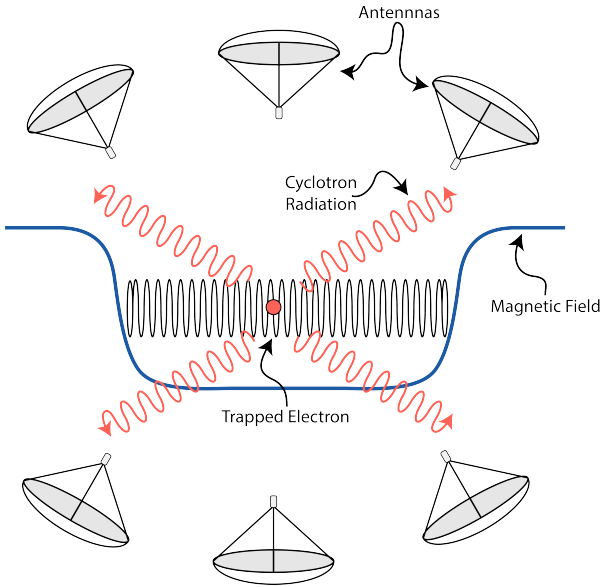


Figure 3.1: A cartoon illustration of the CRES technique. An electron is contained in a magnetic trap so that its cyclotron radiation can be detected by an array of antennas. Detecting the cyclotron radiation allows us to measure its cyclotron frequency and determine its kinetic energy.

639 For non-relativistic particles the cyclotron frequency is simply a function of the  
 640 charge-to-mass ratio of the particle, however, from the relativistic form of the cyclotron  
 641 frequency

$$f_c = \frac{qB}{2\pi m_e \gamma} = \frac{1}{2\pi} \frac{qB}{m_e + E_{\text{kin}}/c^2}, \quad (3.1)$$

642 one can see that the kinetic energy ( $E_{\text{kin}}$ ) of the electron is directly proportional to the  
 643 inverse of the cyclotron frequency ( $f_c$ ). Electrons with kinetic energies of 18.6 keV are in  
 644 the weakly relativistic regime with  $\beta = \frac{v}{c} = 0.263$  and  $\gamma = 1.036$ .

645 The required frequency resolution needed for neutrino mass measurement can be  
 646 obtained by differentiating Equation 3.1,

$$\frac{df_c}{dE_{\text{kin}}} = \frac{1}{2\pi} \frac{-qBc^2}{(m_e c^2 + E_{\text{kin}})^2}, \quad (3.2)$$

647 from which we can obtain the relationship between fractional differences in energy and  
648 frequency,

$$\frac{df_c}{f_c} = \frac{1 - \gamma}{\gamma} \frac{dE_{\text{kin}}}{E_{\text{kin}}}. \quad (3.3)$$

649 Therefore, an energy precision of 1 eV for an 18.6 keV electron requires a frequency  
650 precision of approximately 2 ppm.

651 The minimum observation time required to achieve this resolution can be estimated  
652 using the uncertainty principle as formulated by Gabor [45]. Electrons from tritium  
653 beta-decay experience random collisions with the background gas particles, which limits  
654 the uninterrupted radiation lifetime. The time between collision events, referred to  
655 as track length in the context of CRES measurements, is an exponentially distributed  
656 variable. Differences in the track lengths of a population of mono-energetic electrons leads  
657 to uncertainty or broadening in the distribution of measured frequencies proportional to  
658 the mean track length,  $\tau_\lambda$ . The resulting frequency distribution has a Lorentzian profile,  
659 whose width is given by the Gabor limit,

$$\tau_\lambda \Delta f_c = \frac{1}{2\pi} \implies \Delta f_c = \frac{1}{2\pi\tau_\lambda}. \quad (3.4)$$

660 The cyclotron frequency for a 18.6-keV electron in a 1 T field is approximately  
661 27 GHz, from which one can estimate the minimum observation time for 2 ppm frequency  
662 resolution at approximately 3  $\mu$ sec. The Gabor limit is not the true lower bound on the  
663 frequency resolution for a CRES signal, since it is based on the details of the Fourier  
664 representation of a time-series with a fixed length. If one takes the approach of fitting  
665 the CRES signal in the time-domain, then one finds that the limit on frequency precision  
666 is given by the Cramér-Rao lower bound (CRLB) [46], which depends on the track length  
667 and SNR. The CRLB allows for better precision on the cyclotron frequency, however,  
668 the Gabor limit provides an intuitive limit with the correct order of magnitude.

669 Ensuring that an electron remains under observation long enough so that its frequency  
670 can be precisely measured requires a magnetic trap. A magnetic trap is a local minimum  
671 in a background magnetic field generated an appropriate configuration of electromagnetic  
672 coils. Since magnetic fields can do no work, there is no danger of the magnetic trap  
673 affecting the kinetic energy electron after it is emitted from the beta-decay. One common  
674 approach to creating a magnetic trap is the "bathtub" trap configuration, which in it's  
675 simplest form consists of two high magnetic field pinch coils aligned on a central axis  
676 that are well separated (see Figure 3.2). This configuration produces a trap with a flat  
677 uniform bottom and relatively steep walls, which is ideal for CRES measurements.

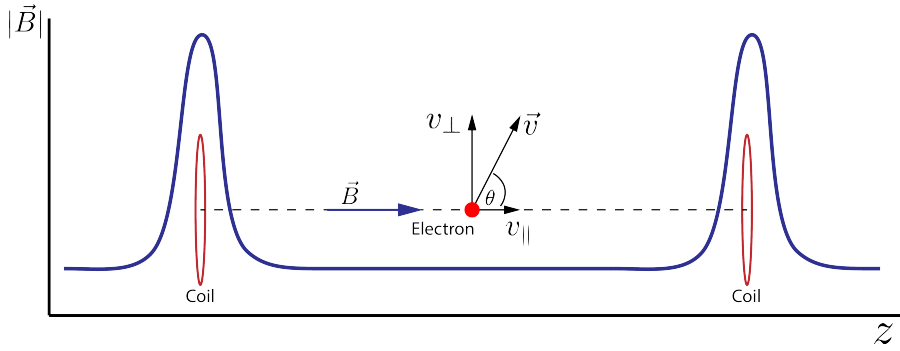


Figure 3.2: An illustration of an electron in a bathtub magnetic trap generated by two well-separated coils.

678     Electrons produced in the trap oscillate back and forth between the trap walls at  
 679     a frequency that depends upon the pitch angle, unless they are produced with pitch  
 680     angles too small to be contained in the trap. Pitch angle is defined as the angle between  
 681     the component of the electron's velocity perpendicular to the magnetic field and the  
 682     component parallel to the magnetic field,

$$\tan \theta = \frac{v_{\perp}}{v_{\parallel}}. \quad (3.5)$$

683     The axial motion of the electron leads to variation in the cyclotron frequency due to  
 684     the changing value of the magnetic fields. This leads to frequency modulation that  
 685     generate sidebands in the cyclotron radiation spectrum. Resolving these sideband  
 686     frequency components is necessary for a complete reconstruction of the CRES signal in  
 687     the experiment.

688     Electrons trapped in a cylindrically symmetric trap have three primary components of  
 689     motion (see Figure 3.3). The dominant component, typically with the highest frequency,  
 690     is the electron's cyclotron orbit, which encodes information on the electron's kinetic  
 691     energy. Axial motion from the electron's pitch angle leads to frequency modulation but  
 692     also a shift in the average magnetic field experienced by an electron. This leads to a  
 693     correlation between the kinetic energy of the electron and the pitch angle depending on  
 694     the particular shape of the magnetic trap, which can negatively impact energy resolution.  
 695     To reduce this correlation one must engineer the trap to have a flat bottom with very  
 696     steep wall both of which are more easily achieved with a small aspect ratio bathtub trap.  
 697     Radial gradients in the trap leads to a third component of motion called grad-B drift [47].

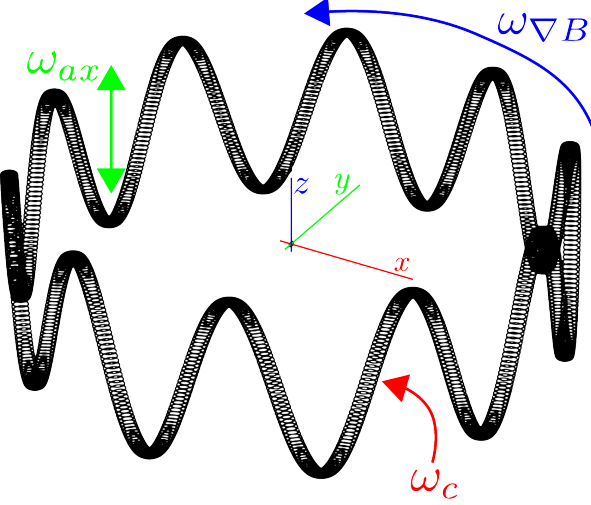


Figure 3.3: A plot of the main components of an electron's trajectory in a cylindrically symmetric trap.

<sup>698</sup> The equation for the drift velocity is

$$\mathbf{v}_{\nabla B} = \frac{m_e v_\perp^2}{2qB} \frac{\mathbf{B} \times \nabla B}{B^2}. \quad (3.6)$$

<sup>699</sup> These additional components of motion all influence the shape of the CRES signal so  
<sup>700</sup> modeling their effects is critical to proper measurement of the kinetic energy.

<sup>701</sup> The total power of the radiation emitted by an electron in a free-space environment  
<sup>702</sup> is given by the Larmor equation [48]

$$P(\gamma, \theta_p) = \frac{1}{4\pi\epsilon_0} \frac{2}{3} \frac{q^2 \omega_c^2}{c} (\gamma^2 - 1) \sin^2 \theta_p, \quad (3.7)$$

<sup>703</sup> where  $\omega_c$  is the cyclotron frequency multiplied by  $2\pi$  and  $\theta_p$  is the pitch angle to distinguish  
<sup>704</sup> it from the spherical angle coordinate. A single electron with a 90° pitch angle and  
<sup>705</sup> 18.6 keV of kinetic energy in a 1 T magnetic field emits a total radiation power of 1.2 fW,  
<sup>706</sup> which is quite small compared with typical RF systems, furthermore, one is typically  
<sup>707</sup> only able to receive a fraction of this total power with an antenna or other detection  
<sup>708</sup> system. Therefore, RF systems in CRES experiments must be operated at cryogenic  
<sup>709</sup> temperatures to limit the noise power such that adequate SNR can be achieved for signal  
<sup>710</sup> detection and reconstruction. Alternatively, longer tracks enable detection of weaker  
<sup>711</sup> signals due to the increase in the total signal energy available for the detection algorithm.

### **712 3.2.2 The Project 8 Collaboration**

713 The Project 8 collaboration<sup>1</sup> is a group of institutions in the United States and Germany  
714 aiming to measure the neutrino mass by developing a novel spectrometer technology  
715 based on CRES. In the ultimate Project 8 experiment the CRES technique will be used  
716 to measure the beta-decay spectrum using a large source of atomic tritium sufficient to  
717 achieve the required statistics in the last  $O(10)$  eV of the decay spectrum. Project 8 is  
718 targeting a neutrino mass sensitivity below 50 meV [49], which exhausts the range of  
719 possible neutrino masses under the inverted hierarchy and is a factor of four less than  
720 sensitivity projections for the ongoing KATRIN experiment.

721 Project 8's proposed experiment requires the development of two novel technologies:  
722 the production and trapping of a source of atomic tritium on cubic-meter scales and  
723 technology to enable CRES measurements of individual electrons in the same volume.

### **724 Atomic Tritium**

725 Previous measurements of the tritium beta-decay spectrum for neutrino mass measure-  
726 ments have relied on sources of molecular tritium for their measurements [36, 50, 51] due  
727 to the technical challenges associated with the production and storage of atomic tritium.

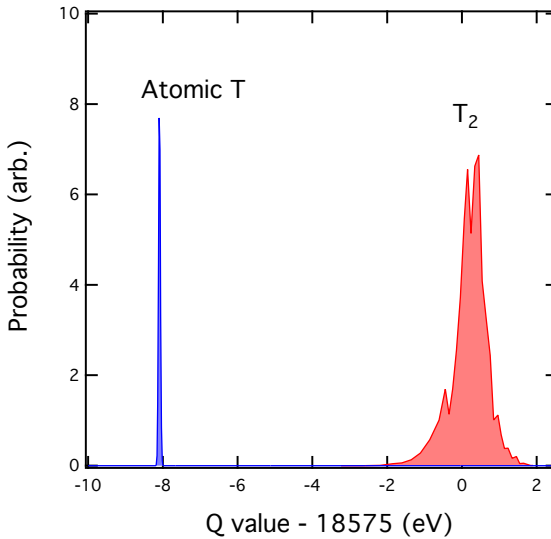


Figure 3.4: A plot of the final state distributions of atomic and molecular tritium. The final state distribution provides the primary contribution to the width of the molecular spectrum whereas thermal doppler broadening is responsible for the width of the atomic spectrum.

---

<sup>1</sup><https://www.project8.org/>

728 One must supply sufficient energy to the tritium molecules to break the molecular  
729 bond and create atomic tritium. Common approaches to this include the use of hot  
730 coaxial filament atom crackers as well as plasma atom sources. Both involve heating the  
731 tritium atoms to temperatures of  $> 2500$  K, which must then be cooled to temperatures  
732 on the order of a few mK so that the tritium atoms can be trapped. Cooling the atoms  
733 requires the construction of a large tritium infrastructure and cooling system that can  
734 supply a source of cold atoms to the trap.

735 Once cold tritium atoms are produced they cannot make contact with any surfaces  
736 to avoid recombination of the atoms to molecules. Therefore, a magnetic trap is required  
737 to store the atoms for a sufficient length of time that they have a chance to decay before  
738 escaping the trap. Trapping the atoms requires the construction of a large and complex  
739 magnet system that must be cooled to cryogenic temperatures.

740 The significant experimental complexity caused by atomic tritium makes a molecular  
741 source the obvious choice from practical considerations. However, the drawback of  
742 molecular tritium for neutrino mass measurement is the irreducible broadening in the  
743 electron's kinetic energy due to the final state spectrum of molecular tritium (see Figure  
744 3.4). The broadening of the final state spectra has a RMS amplitude of 436 meV [52, 53]  
745 caused by variation in the final vibrational state of the daughter molecule. For atomic  
746 tritium the primary sources of broadening in the final state spectrum are magnetic  
747 hyperfine splittings (magnitude of  $O(10^{-5})$  eV) and thermal Doppler broadening caused  
748 by the motion of the trapped atom. For atomic tritium at a temperature of 1 mK thermal  
749 broadening is the dominant contribution, providing about 1 meV RMS of broadening to  
750 the electron's kinetic energy.

751 The larger energy broadening with molecular tritium leads to an irreducible statistical  
752 uncertainty that limits the achievable sensitivity to approximately 100 meV at 90%  
753 confidence. For previous direct measurements of the neutrino mass this uncertainty is an  
754 insignificant contribution to the overall uncertainty budget, however, for experiments  
755 like Project 8 atomic tritium is a key component to the success of the experiment.

## 756 **CRES for Neutrino Mass Measurement**

757 Several features of the CRES technique make it an attractive choice for a next generation  
758 neutrino mass measurement experiment. For example, with a CRES experiment the  
759 volume of the source gas can be the same as the volume of the CRES spectrometer.  
760 This is due to the fact that CRES is a remote-sensing technique that can observe the  
761 energy of the electron without altering its trajectory or directly interacting with the

762 electron. Given that tritium gas is transparent to cyclotron radiation the kinetic energies  
763 of electrons can be measured with an appropriate sensing technology, such as a cavity or  
764 antenna array, located directly outside the atom trapping volume.

765 The current state-of-the-art tritium beta-decay spectroscopy experiment, KATRIN,  
766 utilizes the magnetic adiabatic collimation with an electrostatic filter (MAC-E filter)  
767 technique to measure the beta-decay spectrum of molecular tritium. In this approach,  
768 a source of molecular tritium is located outside the spectrometer. When a beta-decay  
769 occurs the electron must exit the tritium source and travel through the MAC-E filter  
770 before it can be detected on the other side of the filter using a charge sensor. The  
771 measurement statistics of the MAC-E filter are limited by the transverse areas of the  
772 tritium source and the filter due to the need to travel through the experiment without  
773 scattering. This scaling is less favorable than the volumetric scaling of CRES due to the  
774 ability to co-locate source and detector.

775 Another promising aspect of the CRES technique is the inherently high precision  
776 of frequency based measurements. The endpoint of the molecular tritium beta-decay  
777 spectrum is approximately 18.6 keV, which dwarfs the neutrino mass scale of  $< 1 \text{ eV}/c^2$   
778 by at least a factor of  $10^5$ . Measuring the effect of such a small mass on a high energy  
779 electron requires excellent energy resolution. Since frequency measurements are essentially  
780 counting measurements they are intrinsically quite accurate due to the ability to measure  
781 the cyclotron frequency by effectively averaging over millions of cyclotron orbits. Using  
782 off-the-shelf RF components its is possible to achieve part-per-million accuracy on the  
783 kinetic energy with the CRES technique.

784 CRES is also nearly immune to typical sources of backgrounds that plague other  
785 experiments. Since CRES operates via non-destructive measurements of the electron's  
786 cyclotron frequency potential sources of background electrons are effectively filtered out  
787 by limiting the frequency bandwidth of the measurement. The fiducial volume of the  
788 experiment is free from any surfaces that could introduce stray electrons and electrons  
789 from sources outside the fiducial volume can be prevented from entering the experiment.

## 790 Neutrino Mass Sensitivity Goals

791 Project 8's ultimate goal is to combine CRES with atomic tritium to measure the neutrino  
792 mass with 40 meV sensitivity at the 90% confidence level (see Figure 3.5). This sensitivity  
793 is sufficient to fully exhaust the range of allowable neutrino masses under the inverted  
794 neutrino mass ordering regime and is approximately an order of magnitude less than the  
795 projected final sensitivity of the KATRIN experiment. Excluding the full neutrino mass

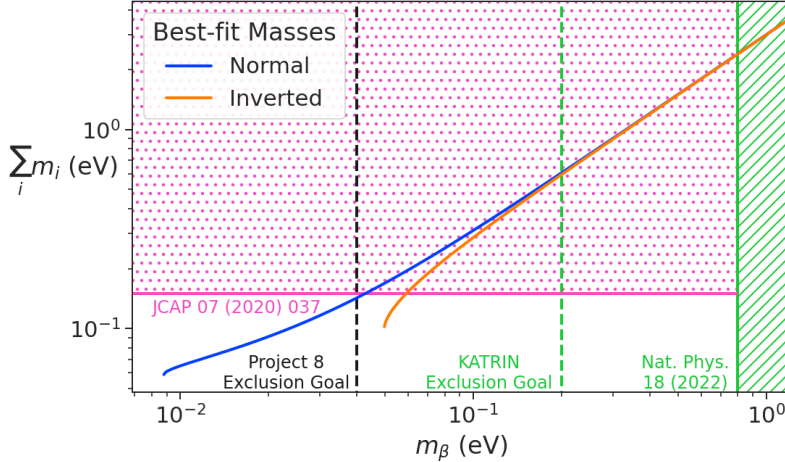


Figure 3.5: Neutrino mass exclusion plot including limits from cosmological measurements and the KATRIN experiment. Allowed ranges for neutrino masses under the normal and inverted hierarchies are shown as the blue and orange lines respectively. The black dashed line shows Project 8’s goal neutrino mass sensitivity for the Phase IV experiment.

796 parameter space would require a sensitivity an order of magnitude lower than what is  
 797 proposed by Project 8, which would require an experiment whose size and complexity  
 798 are currently well beyond proposals for the next-generation of neutrino mass direct  
 799 measurement experiments.

### 800 3.2.3 The Project 8 Phased Development Plan

801 Reaching 40 meV sensitivity requires the simultaneous development and eventually  
 802 combination of CRES and atomic tritium. These technologies require a significant up-  
 803 front research and development (R&D) investment to build-out the required capabilities  
 804 for a 40 meV CRES experiment. Therefore, Project 8 is following a phased experiment  
 805 plan in which incremental progress can be made towards the ultimate goal of a 40 meV  
 806 neutrino mass measurement with CRES.

#### 807 Phase I and II: Proof of Principle and First Tritium Measurements

808 The earlier phases of the Project 8 experiment, Phase I and II, were focused on demon-  
 809 stration and development of the CRES technique itself as well as a proof-of-principle  
 810 measurement of the neutrino mass using the CRES technique.

811 In Phase I, Project 8 performed a proof-of-principle measurement of the  $^{83m}\text{Kr}$

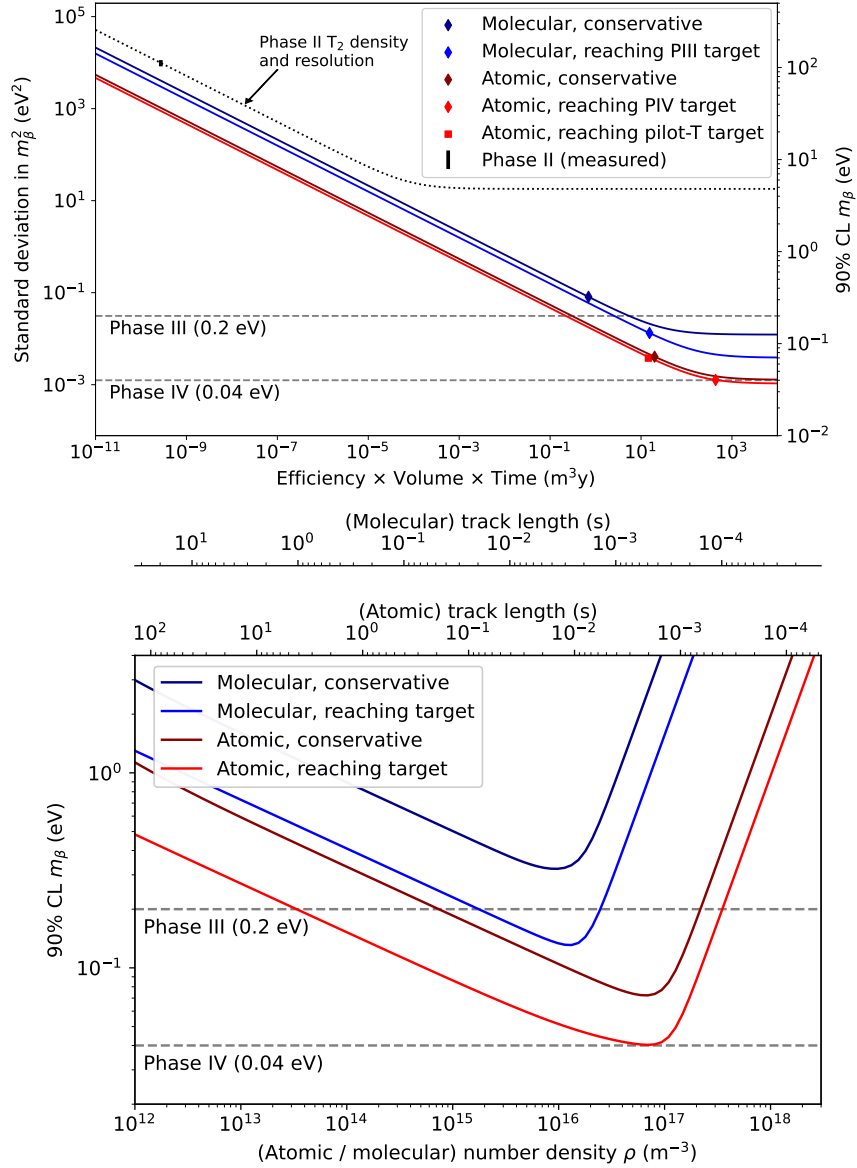


Figure 3.6: Sensitivity calculations for a cavity based CRES experiment that demonstrate the neutrino mass measurement goals of the Project 8 collaboration throughout the phased development plan. The blue curves indicate molecular tritium sources and the red curves indicate atomic tritium sources. In the current plan Phase III contains two tritium experiments. The first is the Low-frequency Apparatus (LFA) which is a molecular tritium experiment and the second is the atomic tritium pilot-scale experiment that ends Phase III. The sensitivity of these experiments is primarily a function of statistics, however, there is a critical density beyond which CRES electrons do not have enough time to radiate between collisions for a high-resolution frequency measurement leading to worse sensitivity.

spectrum using CRES, which marked the first ever energy spectrum measurement with CRES. The experiment included all of the main components expected for the full-scale version of the experiment. An electron source consisting of a gas of  $^{83m}\text{Kr}$  was supplied to a waveguide gas cell constructed out of a segment of WR-42 waveguide and sealed with Kapton windows at the top and bottom. A magnetic trapping region was created in the waveguide cell using a single electromagnetic coil wrapped around the waveguide which provided a trapping volume on the order of a few cubic-millimeters. Detection of the cyclotron radiation was performed by connecting the waveguide cell to an additional segment of waveguide that transmitted the radiation to a cryogenic amplifier.

Success in Phase I was achieved with the 2014 publication of the measured  $^{83m}\text{Kr}$  conversion spectrum [54], which contains a mono-energetic 17.8-keV as well as several other conversion lines at higher energies. Publication of this result marked the official end of Phase I and the start of Phase II in which Project 8 shifted its focus to the demonstration of the first tritium beta-decay spectrum using CRES. Phase II successfully concluded in 2023 with the submission of the papers demonstrating the first tritium beta-decay spectrum endpoint and neutrino mass measurement using CRES. For more information on Phase II please see Section 3.3.

### Phase III: Research and Development and a Pilot-scale Experiment

After Phase II Project 8 has shifted focus to R&D towards the construction of an experiment that demonstrates all the technologies required for a 40 meV measurement of the neutrino mass. The goal for this pilot-scale experiment is to successfully retire all technological and engineering risks associated with the Phase IV experiment, while being a scientifically interesting experiment in its own right that has sensitivity to neutrino masses on par with KATRIN’s final projected sensitivity.

Phase III R&D is divided into two equally important efforts — atomic tritium and CRES detection techniques. Atomic tritium development in Phase III includes the development of all aspects of the tritium system. This includes the production of tritium atoms, atomic cooling and recirculation systems, purity and isotope concentration monitoring, and atom trapping. Currently, Project 8 is operating small scale demonstrator systems developing atom crackers to show that atom production at the estimated rates needed for Phase IV is achievable. Future efforts will continue the current developments on atom production and expand to include demonstrations of atomic cooling with an evaporative beam line as well as atom trapping using Halbach magnet arrays.

The need for new CRES detection techniques is driven by the drastic increase in scale

846 from Phase II to the Phase IV and the pilot-scale experiments. The physical volume  
847 used for CRES in Phase II was on the order of a few cubic-centimeters, and achieving  
848 Project 8’s sensitivity target of 40 meV requires an experiment volume on the multi-cubic  
849 meter scale. Therefore, the waveguide gas cell CRES detection technique used in Phase  
850 II is not a feasible option for the future of Project 8 due to it’s inability to scale to the  
851 required size.

852 Two alternative CRES detection techniques have been proposed for the pilot-scale  
853 experiment — antenna arrays and resonant cavities (see Section 3.4 and Chapter 6).  
854 Both approaches have relative advantages and disadvantages, however, the improved  
855 understanding of the antenna array and cavity approaches to CRES in the recent years  
856 has led to cavities being the preferred technology for the pilot-scale experiment and  
857 Phase IV due to the estimated reduced cost and complexity of this approach. Since a  
858 large degree of the work presented in this thesis is focused on the development of the  
859 antenna array CRES technique as well as the design of demonstrator experiments, we  
860 described the proposed R&D plan for antenna array CRES in Phase III in Section 3.4.

861 Cavity CRES R&D in Phase III consists of a series of demonstrator experiments  
862 intended to demonstrate cavity CRES at a variety of scales and magnetic fields using  
863 electrons from  $^{83m}\text{Kr}$ , an electron gun, and potentially molecular tritium sources. The  
864 near-term cavity effort in Project 8 is the cavity CRES apparatus (CCA), which is a  
865 small-scale cavity experiment operating near 26 GHz, that will perform the first CRES  
866 measurements using a small cavity. This experiment will pave the way towards larger  
867 scale cavity experiments in preparation for the eventual pilot-scale tritium experiment.

868 The pilot-scale experiment is the first experiment, which will combine atomic tritium  
869 and large-volume CRES detection in the same experiment. It will directly demonstrate  
870 all the technologies required for Phase IV such that no technical risks remain for scaling  
871 the experiment to required scale. A robust approach to scaling the pilot-scale experiment  
872 is to simply build multiple copies of it for the Phase IV experiment.

### 873 **Phase IV: Project 8’s Ultimate Neutrino Mass Experiment**

874 The design of Phase IV should be a direct extension of the pilot-scale CRES experiment  
875 that marks the official end of Phase III (see Section 3.5). The Phase IV experiment  
876 represents the final experiment in the Project 8 neutrino mass measurement experiment  
877 plan and will have sensitivity to neutrino masses of 40 meV.

878 **3.3 Phase II: First Tritium Beta Decay Spectrum and**  
879 **Neutrino Mass Measurement with CRES**

880 In Phase II Project 8 demonstrated the first ever measurement of the tritium beta-decay  
881 spectrum endpoint using the CRES technique, which lead to the first neutrino mass  
882 measurement by the Project 8 collaboration. This milestone was made possible by many  
883 improvements in the CRES technique and in the understanding of CRES systematics,  
884 which takes an important first step towards larger scale measurements of the tritium  
885 beta-decay spectrum with CRES. In this section, I briefly describe some important  
886 elements of the Phase II experiment, with the goal of contextualizing the research and  
887 development efforts for Phases III and IV of Project 8. For more complete descriptions of  
888 the work that lead to Project 8’s Phase II results please refer to the relevant publications  
889 by the collaboration [40, 41].

890 **3.3.1 The Phase II CRES Apparatus**

891 **Magnet and Cryogenics**

892 The magnetic field for the the Phase II experiment is provided by a nuclear magnetic  
893 resonance (NMR) spectroscopy magnet with a central bore diameter of 52 mm (see Figure  
894 3.7). The magnet produces a background magnetic field with an average value of 0.959 T  
895 and a 10 ppm variation across the bore diameter achieved using several shim coils built  
896 into the magnet. Using an external NMR field probe the variation of the magnetic field  
897 along the vertical axis of the magnet bore was measured to obtain an accurate model of  
898 the magnetic field so that the CRES cell could be positioned for optimal magnetic field  
899 uniformity.

900 An external solenoid magnet was installed inside the magnet bore to provide the  
901 ability to shift the magnitude of the background magnetic field by values on the order of  
902 a few mT. The solenoid has inside diameter of 46 mm and a length of 350 mm, which  
903 terminates in a vacuum flange that allows it to be inserted into the NMR magnet bore  
904 from the bottom. By shifting the value of the magnetic field by a few mT, the cyclotron  
905 frequencies of electrons produced by the 17.8 keV  $^{83m}\text{Kr}$  internal-conversion line [55]  
906 can be shifted over a range of frequencies on the order of 100 MHz. This allows one to  
907 study the frequency dependent behavior of multiple CRES systematics such as detection  
908 efficiency that directly affect the measured shape of the tritium spectrum.

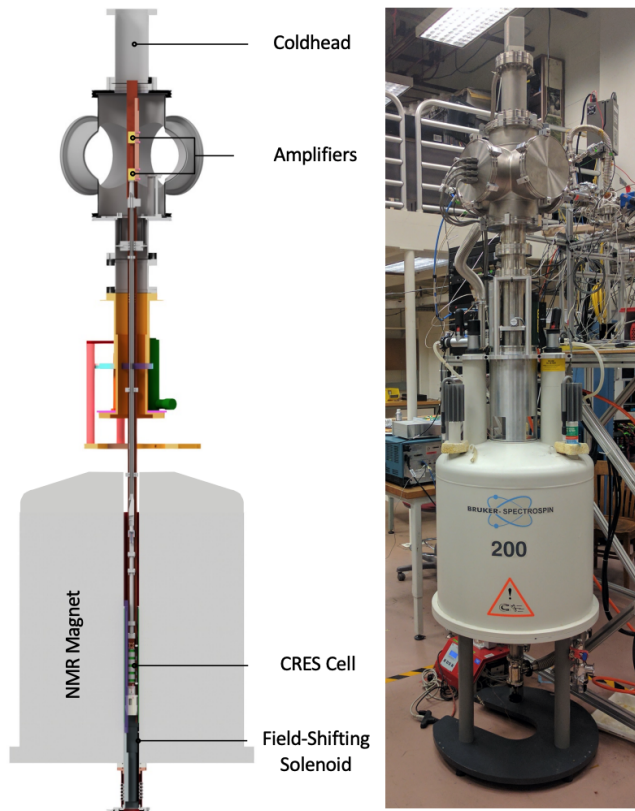


Figure 3.7: The Phase II CRES apparatus used to perform the first measurement of the tritium beta-decay spectrum using CRES.

909       The inside of the magnet bore diameter was pumped down to a vacuum of less than  
 910      10  $\mu\text{torr}$  using a turbomolecular pump, which allows for cryogenic cooling of the CRES  
 911      cell and RF system. Cooling power was supplied to the Phase II apparatus using a  
 912      cryopump with its coldhead mounted above the primary magnet and CRES cell. This  
 913      arrangement allowed for sufficient cooling power to be delivered to the amplifiers to cool  
 914      them to a temperature of  $\approx 40$  K, while keeping the amplifiers far enough from the  
 915      magnet so as not to be damaged by the large field strength. Thermal contact between  
 916      the coldhead, amplifiers, RF system, and CRES cell is achieved using a copper bar that  
 917      runs the full length of the apparatus. To prevent freeze-out of  $^{83m}\text{Kr}$  on the walls of the  
 918      CRES cell a separate heater was installed to keep the CRES cell near a temperature of  
 919      85 K during the operation of the experiment.

920    **CRES Cell**

921    Located in the most uniform region of the magnetic field is the CRES cell, which is the  
922    region of the apparatus where radioactive decays of  $^{83m}Kr$  and  $T_2$  emit electrons that can  
be trapped and measured using CRES (see Figure 3.8). The CRES cell is manufactured

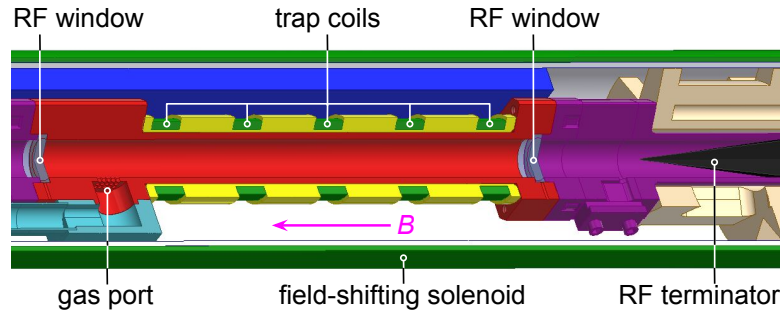


Figure 3.8: Diagram of the CRES cell portion of the Phase II apparatus.

923  
924    from a segment of cylindrical waveguide designed to operate at K-band frequencies  
925    near 26 GHz. The diameter of the waveguide determines which resonant modes of the  
926    waveguide will couple to the electron and transmit its radiation to the amplifiers. For  
927    Phase II a waveguide diameter of 1 cm was selected, which allows electrons to couple to  
928    the TE<sub>11</sub> and TM<sub>01</sub> cylindrical waveguide modes. To reduce complexity in modeling and  
929    analyzing the CRES data, it is ideal to select a diameter that prevents electrons from  
930    coupling to higher-order waveguide modes beyond the fundamental TE and TM modes.

931    Around the exterior of the cylindrical waveguide are several magnetic coils used to  
932    produce magnetic traps inside the CRES cell volume. Without a magnetic trap electrons  
933    produced from decays inside the CRES cell quickly impact the cell wall, which prevents  
934    a measurement of their cyclotron frequency using CRES. Each coil along the length of  
935    the waveguide produces a separate trap that is approximately harmonic in shape. By  
936    independently controlling the currents provided to each coil the traps can be configured  
937    to have equal values of the magnetic field at the trap bottom despite a non-uniform field  
938    from the NMR magnet.

939    Two primary magnetic trap configurations were used during the Phase II experiment.  
940    The first was a shallow trap configuration used primarily for it's high energy resolution to  
941    study systematics using  $^{83m}Kr$  decays, and the second was a deeper trap that could trap a  
942    higher percentage of pitch angles. The trade-off with this trap is that the higher trapping  
943    efficiency comes at the cost of lower energy resolution due to the greater variation in pitch  
944    angle. The deep trap was the trap used to measure the tritium beta-decay spectrum in  
945    Phase II.

946        The source gases were delivered into the CRES cell through a gas port located near the  
 947 top end of the cylindrical waveguide. To prevent the gases from escaping the cell, vacuum  
 948 tight RF transparent windows are needed to contain the tritium and krypton source  
 949 gas across a 1 atm pressure differential, while still transmitting the cyclotron radiation  
 950 without distortion. The crystalline material,  $\text{CaF}_2$ , which has a thermal expansion  
 951 coefficient similar to that of copper, was used for this purpose in the CRES cell. Two  
 952 windows, each 2.4 mm thick, were used to seal off the ends of the CRES cell. The  
 953 thickness of 2.4 mm corresponds to half of a cyclotron wavelength when one accounts for  
 954 the permittivity of  $\text{CaF}_2$ .

955 **RF System**

956        The RF system in the Phase II apparatus transferred the cyclotron radiation from the  
 957 CRES cell to the receiver chain. The receiver chain performs the down-conversion and  
 958 digitization required to obtain signals that can be analyzed to determine the cyclotron  
 frequencies of electrons in the CRES cell (see Figure 3.9).

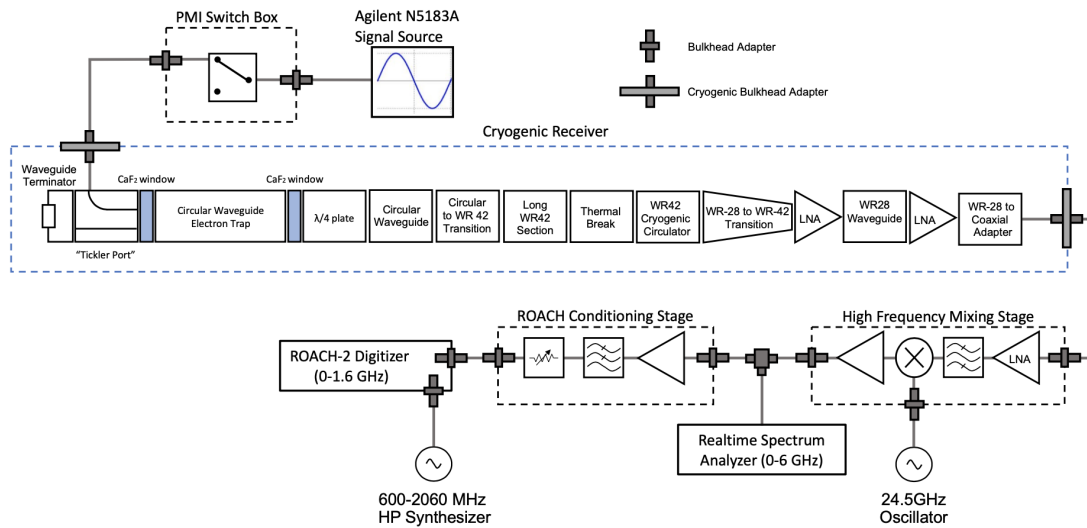


Figure 3.9: RF system diagram for the Phase II apparatus.

959  
 960        Below the CRES cell, at the bottom of the Phase II apparatus, is a tickler port and  
 961 waveguide terminator. The tickler port is used to inject signals into the CRES cell and  
 962 RF system for testing and calibration purposes. The waveguide terminator is designed to  
 963 absorb cyclotron radiation emitted by electrons that transmits out of the bottom of the  
 964 CRES cell. This lowers the total power received from electrons in the CRES cell, since all  
 965 the energy radiated downwards is absorbed into the terminator. Earlier iterations of the

966 Phase II apparatus used an RF short in this location that reflected this power up towards  
967 the amplifiers, however, interference between the upward traveling and reflected radiation  
968 led to a disappearance in the signal carrier that made reconstruction impossible.

969 Radiation traveling upward passes through the  $\text{CaF}_2$  window passes through a  $\lambda/4$  plate,  
970 which transforms the circularly polarized cyclotron radiation into linear polarization.  
971 The linearly polarized fields next travel through a segment of circular waveguide that  
972 transitions into a long segment of WR-42 waveguide that carries the fields out of the  
973 high magnetic field region. A thermal break segment is included, which consists of a  
974 segment of gold-plated stainless steel WR-42 waveguide, to help thermally isolate the  
975 relatively warm CRES cell from the colder amplifiers. The radiation then passes through  
976 a cryogenic circular, which prevents signals reflected from the amplifiers from interfering  
977 with the CRES cell before a WR-42 to WR-28 transition connects the waveguide to the  
978 first of the cryogenic amplifiers. The radiation passes through two cryogenic amplifiers  
979 before being coupled to a coaxial termination at the top of the Phase II apparatus.

980 The coaxial cable transfers the cyclotron radiation signals to a high-frequency mixing  
981 stage that performs an analog frequency down-conversion using a 24.5 GHz LO. Two forms  
982 of digitization can be used at this stage to readout the CRES data. One is a real-time  
983 spectrum analyzer that digitizes the CRES signal data in time-domain and computes the  
984 frequency spectrum in real-time, which allows for direct visualization of CRES signal  
985 spectrograms as the experiment is running. The real-time spectrum analyzer is most  
986 useful for taking small amount of streamed data for debugging and analysis of the system.  
987 The other method, which was used to collect the majority of the CRES data in Phase II,  
988 is a ROACH-2 FPGA and digitizer system. The ROACH system consists of a fast ADC  
989 that samples the CRES signal data at 3.2 GSps. Internal digital down-conversion stages  
990 implemented in the FPGA perform a mixing operation that reduces the bandwidth of the  
991 CRES signals to 100 MHz. The FPGA implements a 8192 sample FFT and packetizes  
992 time and frequency domain records in parallel. The packetized data is then transferred  
993 from the ROACH to be analyzed by the data-processing pipeline.

### 994 **3.3.2 CRES Track and Event Reconstruction**

#### 995 **Time-Frequency Spectrogram**

996 The online data-processing is intended to identify interesting data that could contain  
997 CRES signals using a software real-time triggering algorithm. Interesting segments of  
998 data identified by this algorithm are collected into files that are transferred to a server for

offline processing and analysis. The data files contain a continuous series of time-domain samples, broken into a set of records, which are 4096 samples long. The time-series is made up of 8-bit IQ samples acquired at 100 MHz.

Each time-series record is accompanied by an associated frequency spectrum consisting of 4096 frequency bins approximately 24.4 kHz wide, which is represented as a power spectral density. The individual frequency spectra can be organized temporally to create a time-frequency spectrogram that represents the evolution of the cyclotron frequency spectrum over the course of the CRES event (see Figure 3.10). The time-frequency

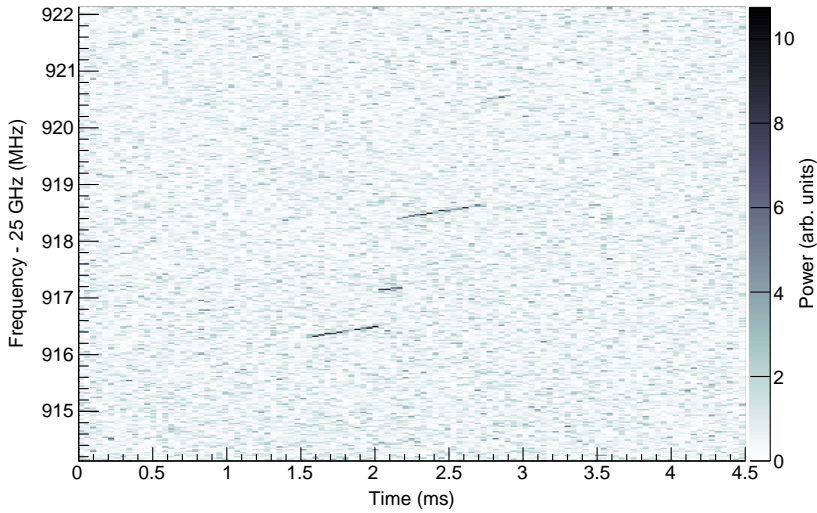


Figure 3.10: The time-frequency spectrogram of a tritium CRES event in the Phase II apparatus.

spectrogram is represented as a two-dimensional image where the color of each pixel is proportional to the power spectral density. Each vertical slice of pixels in the image represents a frequency spectrum, therefore, each horizontal bin represents the data obtained over a duration of  $4096 \times 0.01 \text{ MHz}^{-1} = 40.96 \mu\text{sec}$ .

### CREST Event Data Features

Phenomenologically, a CRES signal appears as a sinusoidal signal whose frequency slowly increases ("chirps") over time. Axial motion of the electron in the trap leads to the formation of frequency sidebands that surround the more powerful carrier frequency, due to Doppler modulation of the electron's frequency as it bounces between the walls of the magnetic trap. The critical piece of information that must be extracted from the track and event reconstruction procedure is the carrier frequency, since it is this frequency

1018 that gives the cyclotron frequency and thus the kinetic energy. While axial motion from  
1019 non- $90^\circ$  pitch angles does change the average magnetic field experienced by an electron  
1020 and, therefore, changes the cyclotron frequency. Because of low-SNR sidebands were  
1021 unable to be observed in Phase II, so a correction for the effect of the pitch angle on the  
1022 cyclotron frequency was not possible.

1023 In the time-frequency spectrogram representation the chirping carrier frequency  
1024 appears as a linear track of high-power frequency bins (see Figure 3.10). The vertical  
1025 slope of the tracks is caused by the emission of energy from the electron in the form of  
1026 cyclotron radiation, therefore, the size of the slope parameter is directly proportional  
1027 to the Larmour power. The continuous track is periodically interrupted by random  
1028 jumps to higher frequency and lower energy caused by random inelastic collisions with  
1029 background gas molecules. The length of a track is an exponentially distributed variable  
1030 whose mean value is inversely proportional to the gas density. The size of the frequency  
1031 discontinuities is directly proportional to the energies of the rotational and vibrational  
1032 states of background gas molecules.

1033 A CRES event refers to the collection of tracks produced by a trapped electron until  
1034 it inevitably scatters into a pitch angle that can no longer be trapped. The goal of track  
1035 and event reconstruction is to first identify the set of tracks present in a time-frequency  
1036 spectrogram that represents a segment of data acquired in the Phase II apparatus. These  
1037 tracks must then be clustered into events from which we can determine the first track  
1038 produced by the electron and thus estimate it's starting cyclotron frequency and kinetic  
1039 energy.

## 1040 Track Reconstruction

1041 The first step in CRES event reconstruction is the identification of tracks in the time-  
1042 frequency spectrogram, which is essentially an image processing task. Track finding  
1043 starts by normalizing the power spectral density based on the average noise power.  
1044 Next a power threshold is applied to the normalized spectrogram where only bins that  
1045 have a signal-to-noise ratio greater than five are selected to build tracks. In this case  
1046 signal-to-noise ratio is defined as the ratio between the normalized, unitless power of a  
1047 bin divided by the average normalized power across the full frequency spectrum.

1048 The sparse spectrogram produced by this power cut consists only of a sparse collection  
1049 of high-power frequency bins that could be part of a CRES signal track (see Figure  
1050 3.11). In this form is it much easier to identify tracks "by eye", however, for the Phase II  
1051 analysis Project 8 developed its own custom-made track finding algorithm, called the

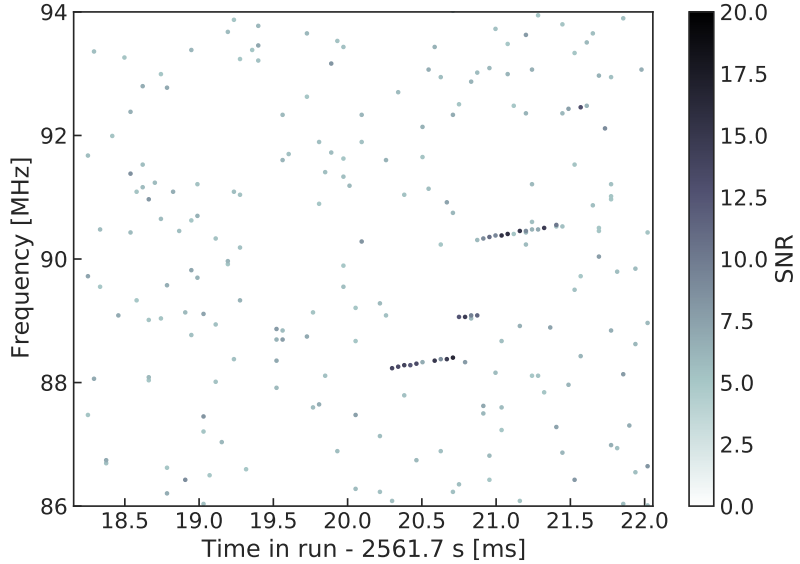


Figure 3.11: The sparse spectrogram obtained by placing a power cut on the raw spectrogram shown in Figure 3.10.

1052 sequential track finder (STF).

1053 The STF algorithm processes the sparse spectrogram in sequential fashion, processing  
 1054 each time-slice one-by-one until the end of the spectrogram is reached. Tracks are found  
 1055 by searching for points in the sparse spectrogram that appear to fall on a straight line.  
 1056 Multiple configurable parameters are built into the STF algorithm that allow the user to  
 1057 tune the criteria for adding a point to an existing track or creating a new track. These  
 1058 include parameters such as maximum time and frequency differences between subsequent  
 1059 points in a track as well as minimum SNR values for the start and endpoints of the track.  
 1060 Additionally, tracks are required to have a minimum length and slope to be considered  
 1061 potential CRES tracks rather than random noise fluctuations.

1062 The resulting output of the STF is a collection of track objects that consist of the track  
 1063 point objects and their properties. The final step is to calculate track-level properties  
 1064 and apply cuts to reject false tracks found by the STF. This involves the fitting of a  
 1065 line to the collection of track points as well as the total and average power of the track  
 1066 obtained by computing the sum and mean of the points powers. The starting frequency  
 1067 of the track is determined by calculating the time coordinate that intersects with the  
 1068 linear fit. A cut is performed to remove all tracks that do not have a specified average  
 1069 power over their duration, which helps to remove the majority of noise fluctuations that  
 1070 have passed all previous cuts up to this point.

1071 **Event Reconstruction**

1072 After track reconstruction comes event reconstruction where the identified tracks are  
1073 grouped into events that correspond to the trajectory of a single electron in the trap. This  
1074 procedure attempts to match tracks head to tail by checking if the start and end times  
1075 of a pair of tracks falls within a certain tolerance. This tolerance is a configurable  
1076 parameter that can be tuned to an optimal value using Monte Carlo simulations of events  
1077 in the Phase II apparatus.

1078 After the event building procedure has completed there remains a small likelihood  
1079 that false tracks have made it through to the event reconstruction stage. Typically, cuts  
1080 at the track level are able to remove 95% of the false tracks identified by the STF, which  
1081 leads to a significant number of false tracks at the event building stage. However, the  
1082 additional event-level information makes it possible to reject events that contain these  
1083 false tracks with a high degree of confidence.

1084 Two event level features are associated with events caused by real electrons — the  
1085 duration of the first track as well as the number of tracks in the event. Real electrons  
1086 tend to have event structures with longer first tracks and a higher number of total tracks.  
1087 Based on the values of these two criteria, a minimum threshold on the average power in  
1088 the first track was configured to reject false events. The average power in the first track  
1089 was chosen due to the critical nature of the starting frequency of the first track in an  
1090 event to the krypton and tritium spectrum analyses.

1091 **3.3.3 Results from Phase II**

1092 The main result from Phase II was the measurement of the tritium beta-decay spectrum  
1093 using CRES, which lead to the first neutrino mass limit with CRES. However, Phase  
1094 II also included a significant  $^{83m}\text{Kr}$  measurement campaign to understand important  
1095 systematics relevant to the tritium spectrum measurement, but also to understanding the  
1096 fundamentals of the CRES technique itself. This required high-resolution measurements  
1097 of the  $^{83m}\text{Kr}$  internal-conversion spectrum [55], which is an interesting science result in  
1098 its own right.

1099 The results from Phase II represents a significant effort from the entire Project 8  
1100 collaboration over several years. Because the focus of my contributions to Project 8 is  
1101 directed towards the research and development efforts for the Phase III experiments, the  
1102 goal in this section is not to provide a detailed description of the analyses that lead to  
1103 the Phase II results. Rather, I will provide brief descriptions of a few plots representative

1104 of the main results from Phase II.

1105 **Measurements with Krypton**

1106 Measurements with krypton were a key calibration tool for Phase II of the experiment and  
1107 will continue to be useful in Phase III. In the context of Project 8 krypton measurements  
1108 refers to CRES measurements of the internal-conversion spectrum of the metastable state  
1109 of krypton-83,  $^{83m}\text{Kr}$ , produced by electron capture decays of  $^{83}\text{Rb}$ . A supply of  $^{83}\text{Rb}$   
1110 was built into the Phase II apparatus gas system that supplied the CRES cell with  $^{83m}\text{Kr}$   
1111 via emanation.

1112 The  $^{83m}\text{Kr}$  internal-conversion spectrum consists of several lines based on the orbital  
1113 of the electron ejected during the decay. The conversion lines useful to Project 8 are  
1114 those that emit electrons with kinetic energies that fall inside the detectable frequency  
1115 bandwidth of the Phase II apparatus. These are the K; L2 and L3; M2 and M3; and N2  
1116 and N3 lines with kinetic energies of 17.8 keV,  $\approx$  30.4 keV,  $\approx$  31.9 keV, and  $\approx$  32.1 keV,  
1117 respectively. The different energies of the lines allow a onw to test the linearity of the  
1118 relationship between kinetic energy and frequency across the range of frequencies covered  
1119 by the continuous tritium spectrum.

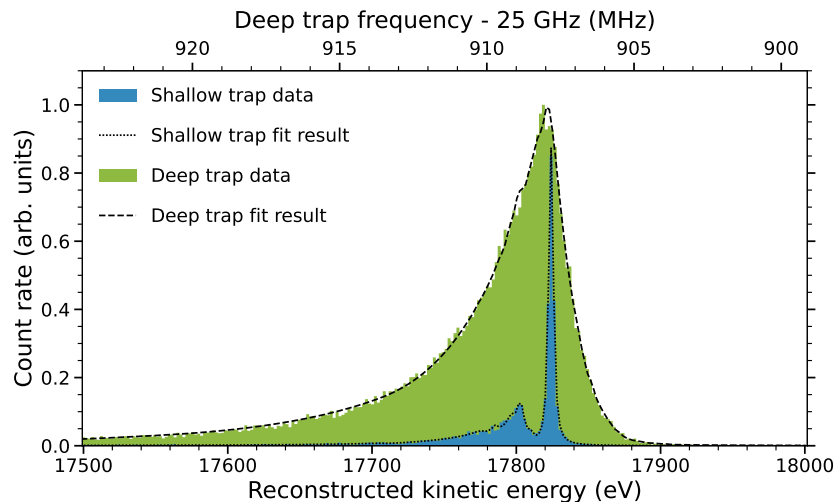


Figure 3.12: Fits to the measured 17.8-keV  $^{83m}\text{Kr}$  conversion line using the deep and shallow trap configurations.

1120 Numerous detector related effects relevant to the tritium analysis can be characterized  
1121 by measuring the shape of the krypton spectrum. Specific examples include variations  
1122 in the magnetic field as a function of the radial position of the electron, variation in  
1123 the magnetic field caused by the trap shape, variation in the average magnetic field for

1124 electrons with different pitch angles, and the effect of missing tracks due to scattering.  
1125 These spectrum shape measurements focused on the 17.8-keV krypton line and utilized  
1126 different trap geometries based on the particular goal of the dataset (see Figure 3.12).

1127 Krypton measurements with a shallow trap allow for high energy resolution, since  
1128 variation in frequency due to pitch angle differences is sharply reduced in the shallow  
1129 trap configuration. With this trap the main 17.8-keV peak of the conversion spectrum is  
1130 clearly visible along with additional satellite peaks at lower energy, which correspond to  
1131 the shakeup/shakeoff spectrum of the decay. The high accuracy of the fit demonstrates a  
1132 high degree of understanding of the CRES systematics.

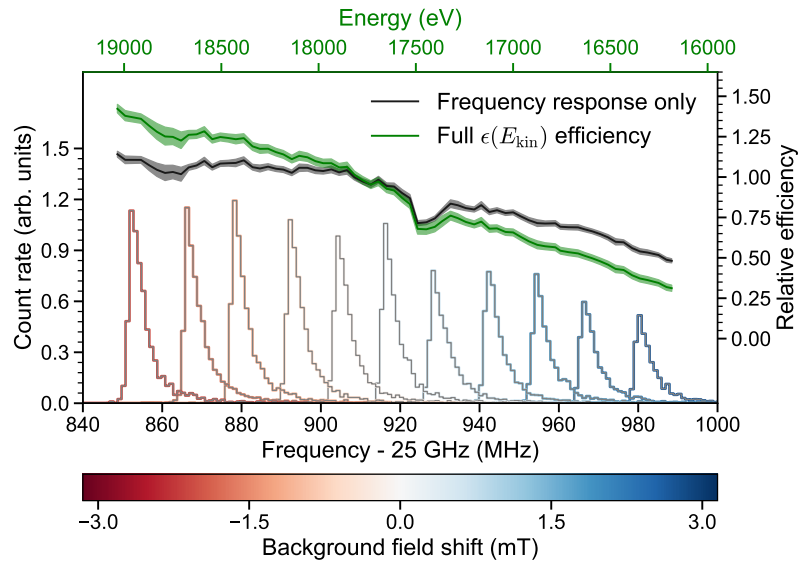


Figure 3.13: Measurements of the 17.8-keV  $^{83m}\text{Kr}$  line using the deep trap configuration for different values of the magnetic field from the field shifting solenoid.

1133 The broadening of the krypton spectrum seen for the deeper track is due to the large  
1134 range of electron pitch angles that can be trapped. Furthermore, with a deeper trap  
1135 there is a larger parameter space of electron that could be produced with pitch angles  
1136 that are trappable but not visible in the time-frequency spectrogram. These electrons  
1137 live in the trap and can scatter multiple times before randomly scattering to a visible  
1138 pitch angle. This leads to one or more missing tracks earlier in the event, which leads to  
1139 a misreconstruction of the true starting frequency. By measuring the krypton spectrum  
1140 shape in the same trap used to detect tritium events, the effect this has on the spectrum  
1141 shape can be characterized to mitigate its impact on the tritium measurements.

1142 Changes in the Krypton spectrum shape as a function of CRES frequency were

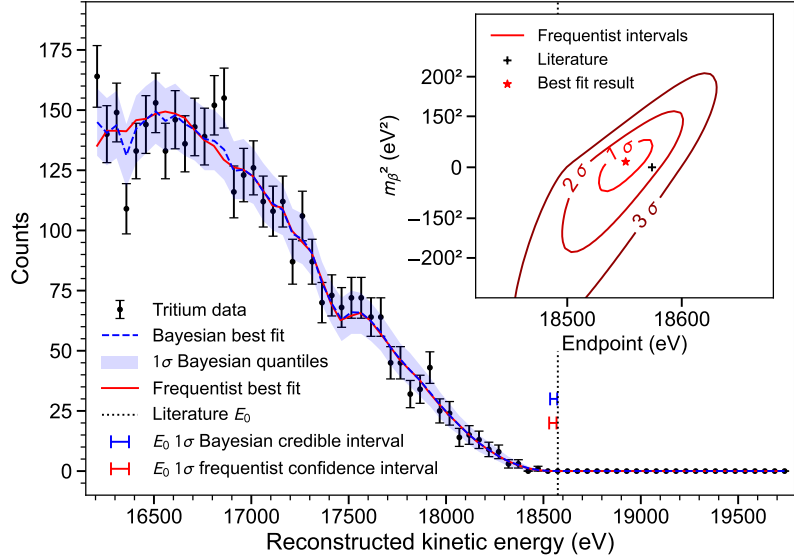


Figure 3.14: The measured tritium spectrum from Phase II with Bayesian and frequentist fits.

used to study the detection efficiency of the Phase II apparatus. Variations in the detection efficiency as a function of frequency directly influences the measured shape of the continuous tritium spectrum, which can lead to errors in the neutrino mass estimate if not modeled appropriately. Using the field shifting solenoid the cyclotron frequency of the krypton 17.83 keV line was shifted across the full frequency range of the tritium spectrum data (see Figure 3.13). Variations in the deep trap krypton spectrum shape can be used to infer the detection efficiency as a function of frequency and correct for this affect in the tritium measurements.

### 1151 Tritium Spectrum and Neutrino Mass Results

1152 The tritium measurement campaign resulted in the collection of 82 days of detector  
 1153 live time during which 3770 total tritium events were detected. The track and event  
 1154 reconstruction analysis extracted the starting frequencies of these tritium events, which  
 1155 were used to build a frequency spectrum of tritium beta-decays. The resulting frequency  
 1156 spectrum was then converted to an energy spectrum using the information gleaned from  
 1157 the krypton measurement campaign to obtain the tritium beta-decay spectrum (see  
 1158 Figure 3.14).

1159 CRES is inherently a very low background technique with the dominant source of  
 1160 noise being random RF fluctuations. Monte Carlo simulations backed validated using

1161 measurements of the RF noise background were used to set track and event cuts to  
1162 guarantee that zero false events would occur over the duration of the experiment with  
1163 90% confidence. Notably, the measured spectrum has zero events beyond the tritium  
1164 spectrum endpoint, which allows us to constrain the background rate in the Phase II  
1165 apparatus to less than  $3 \times 10^{-10}$  counts/ev/s. Achieving a low background is critical for  
1166 future neutrino mass experiments that seek to measure the neutrino mass with less than  
1167 100 meV sensitivity.

1168 Bayesian and frequentist based fits to the measured tritium spectrum, incorporating  
1169 information gained about CRES systematics from the krypton measurements, were  
1170 performed to extract upper limits on the tritium beta-decay spectrum endpoint as well as  
1171 the neutrino mass. The estimated spectrum endpoints are  $18553^{+18}_{-19}$  eV for the Bayesian  
1172 analysis and  $18548^{+19}_{-19}$  eV for the frequentist analysis. The quoted uncertainties are  
1173  $1-\sigma$ , and both results are within  $2-\sigma$  of the literature endpoint value of 15574 eV. The  
1174 estimated neutrino mass for both results is consistent with  $m_\beta^2 = 0$ . The 90% confidence  
1175 upper limits for the Bayesian analysis is  $m_\beta < 155$  eV/c<sup>2</sup> and  $m_\beta < 152$  eV/c for the  
1176 frequentist analysis.

1177 Though the neutrino mass results from Phase II are not competitive with KATRIN  
1178 the experiment was a promising first step towards the development of more precise  
1179 neutrino mass measurements using CRES. The low-background and high-resolution  
1180 achievable with krypton measurements are promising features of the technique that were  
1181 demonstrated with the Phase II apparatus. As new technologies are developed to enable  
1182 CRES measurements in larger volume, many of the lessons learned from Phase II will  
1183 continue to influence the operation and design of future experiments.

### 1184 **3.4 Phase III R&D: Antenna Array CRES**

1185 The goal of Phase III in the Project 8 experimental program is to develop the technologies  
1186 and expertise required to build an experiment that uses CRES to measure the neutrino  
1187 mass with a target sensitivity of 40 meV. One of the key technologies is a method for  
1188 performing high resolution CRES measurements in a large volume, which allows one to  
1189 observe a sufficient quantity of tritium to measure the low-activity endpoint region of  
1190 the tritium spectrum.

### 1191 3.4.1 The Basic Approach

1192 One possible approach, suggested in the original CRES publication [38], is to use many  
1193 antennas to surround a volume of tritium gas in a magnetic field (see Figure 3.15). When  
1194 a decay occurs the electron will begin to emit cyclotron radiation that can be collected  
by the array and used to perform CRES. Each antenna in the array collects only a small

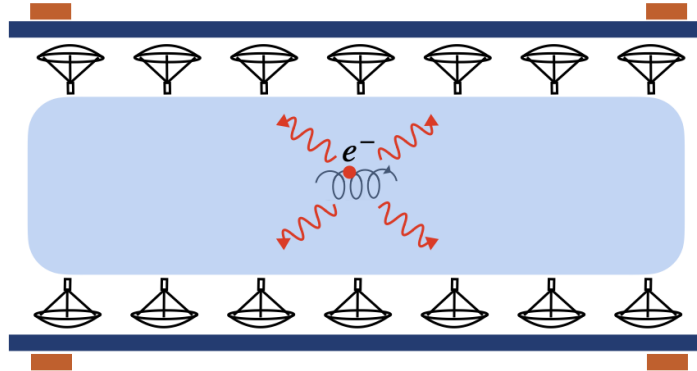


Figure 3.15: A cartoon illustration of the basics of the antenna array CRES technique.

1195  
1196 fraction of the electron's signal power, which is less than 1 fW for a 18.6 keV kinetic  
1197 energy electron in a 1 T magnetic field. Scaling to large volumes with the antenna  
1198 array approach is accomplished by increasing the number of antennas in the array, which  
1199 increases the volume under observation proportionally, so that a sufficient population of  
1200 tritium atoms can be observed to measure the tritium spectrum endpoint shape.

1201 Several features of the antenna array approach make it an attractive candidate technol-  
1202 ogy for a large volume experiment. One example is the accurate position reconstruction  
1203 made possible by the multichannel nature of the array. Using techniques like digital  
1204 beamforming it is possible to estimate the radial and azimuthal positions of the electron  
1205 in the magnetic trap with a precision significantly less than the size of the cyclotron  
1206 wavelength. This capability allows one to perform event-by-event estimations of the  
1207 magnetic field experienced by an electron, which is crucial to achieving high energy  
1208 resolution with the CRES technique.

1209 The easy availability of position information with the antennas array approach  
1210 is potentially a unique advantage that provides significant flexibility in the magnetic  
1211 field uniformity requirements compared to other proposed approaches to large volume  
1212 CRES (see Chapter 6). Spatial discrimination using digital beamforming leads to pileup  
1213 reduction, which helps to reduce the potential of background events caused by missing  
1214 tracks or by incorrectly clustering a group of tracks into an event. Limits on the

1215 background rate for a neutrino mass measurement with 40 meV sensitivity are stringent  
1216 and the total activity of the tritium source for such an experiment is gigantic relative to  
1217 the activity near the endpoint. Thus, pileup discrimination could be an important tool  
1218 for a large scale CRES experiment.

1219 Another beneficial quality of the antenna array approach is that the volume of the  
1220 experiment can be scaled independent of frequency by simply adding more antennas to  
1221 the array (see Figure 3.19). Resonant cavities, the proposed alternative large volume  
1222 CRES technology, are ideally operated in magnetic fields that cause electrons to move  
1223 with cyclotron frequencies near the fundamental cavity resonance, to avoid complex  
1224 coupling of the electron to many cavity modes simultaneously. This leads to a coupling  
1225 between the cavity volume and the magnetic field magnitude, which forces one to lower  
1226 the magnetic field in order to increase the experiment scale. Whereas, for antenna arrays,  
1227 in principle there is no physical limitation on the size of the antenna array that can be  
1228 used at a particular magnetic field. However, the nature of scaling an antenna array  
1229 based experiment leads to rapidly increasing cost and complexity due to the large number  
1230 of antennas, amplifiers, and data streams that require substantial computer processing  
1231 power to effectively analyze.

### 1232 **3.4.2 The FSCD: Free-space CRES Demonstrator**

1233 The complexity of the antenna array CRES technique requires the construction of a  
1234 small scale demonstration experiment to develop an understanding of technique itself and  
1235 relevant systematics. Without a demonstrator experiment it is not possible to sufficiently  
1236 retire the technical risks associated with the full-scale experiment. Therefore, Phase  
1237 III of the Project 8 experimental program is primarily focused on the development and  
1238 operation of demonstrator experiments to inform the design of the Phase IV experiment.

1239 The demonstrator experiment developed for antenna array CRES in Phase III is called  
1240 the Free-space CRES Demonstrator or FSCD. The FSCD is intended as a demonstration  
1241 of antenna array CRES, but is also a capable neutrino mass measurement experiment  
1242 in its own right, with a target neutrino mass sensitivity of a few eV using a molecular  
1243 tritium source.

#### 1244 **Magnetic Field**

1245 The background magnetic field for the FSCD is provided by a hospital-grade MRI magnet  
1246 (see Figure 3.16). The magnet produces a magnetic field of approximately 0.958 T, which

corresponds to a tritium spectrum endpoint frequency of approximately 25.86 GHz. The



Figure 3.16: An image of the MRI magnet installed in the Project 8 laboratory at the University of Washington, Seattle.

1247  
1248 magnet is installed in the Project 8 laboratory located at the University of Washington,  
1249 Seattle, and is shimmed to produce a uniform magnetic field with variations on the  
1250 ppm-level. Measurements of the magnetic field non-uniformities are performed using a  
1251 NMR probe and rotational gantry to capture measurements of the magnetic field around  
1252 an elliptical surface in the center of the MRI magnet. During the operation of the FSCD  
1253 an array of Hall or NMR magnetometers would be used to periodically measure the  
1254 magnetic field to monitor its time stability.

1255 Inside the field of the MRI magnet additional electromagnets would be installed that  
1256 provide the capability to shift the value of the background magnetic field and produce  
1257 a magnetic trap. Shifting the background magnetic field by a few  $\mu$  T lets one control  
1258 the cyclotron frequencies of electrons with a fixed kinetic energy, which is key to an  
1259 effective calibration of the FSCD. The preferred calibration method for the FSCD is  
1260 a mono-energetic electron gun that can inject electrons into the magnetic trap with a  
1261 known kinetic energy. In combination with the field shifting magnet, one can vary the  
1262 cyclotron frequencies of the electrons to measure the response of the antenna array as a  
1263 function of the radiation frequency and electron position. This procedure characterizes  
1264 the response of the antenna array and provides further information on magnetic field  
1265 uniformity, which important to achieving good energy resolution.

1266 The design of the magnetic trap is absolutely critical to the success of a CRES  
1267 experiment. The ideal shape is the perfect magnetic box, which has a flat bottom and

1268 step function walls. Any variation in the average magnetic field experienced by an  
1269 electron leads to changes in the cyclotron frequency that can make determining the true  
1270 starting kinetic energy more difficult. This includes changes in the magnetic field caused  
1271 by the walls of the magnetic trap as well as radial magnetic field variations.

1272 The ideal box trap is completely uniform and has infinitely steep walls that cause  
1273 no change in the electron's cyclotron frequency as it is reflected from the trap wall,  
1274 however, such a trap cannot be made from any combination of magnetic coils since it  
1275 violates Maxwell's equations. One of the goals of magnetic trap design is to identify the  
1276 configuration of coils that produces a trap that approximates the perfect box trap as  
1277 closely as possible.

1278 **Antenna Array**

1279 The canonical antenna array design for CRES is a uniform cylindrical array of antennas  
1280 that surrounds the magnetic trap volume. Since the FSCD is a demonstrator experiment,  
1281 the antenna array design is the simplest form of the uniform cylindrical array, which is a  
single circular ring of antennas with a diameter of 20 cm (see Figure 3.17). Along this

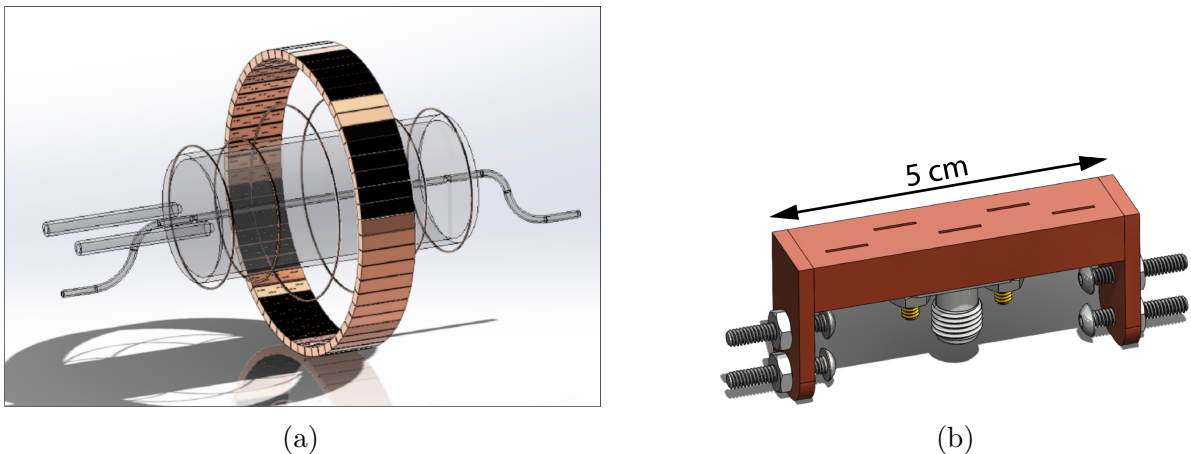


Figure 3.17: (a) A model of the FSCD antenna array, magnetic trap, and tritium containment vessel design.(b) A more detailed model of a prototype design for the 5-slot waveguide antenna design.

1282  
1283 circle are sixty slotted waveguide antennas that fully populate the available space around  
1284 the array circumference. In order to maximize the power collected from each electron  
1285 it is optimal to cover as large a fraction of the solid angle around the magnetic trap as  
1286 possible.

1287 The distance between antennas around the circumference of the array is proportional

1288 to the wavelength of the cyclotron radiation. Therefore, maximizing the solid angle  
1289 coverage of the array, while minimizing channel count to keep the hardware and data  
1290 acquisition costs manageable, biases one towards smaller array diameters. Antenna  
1291 near-field effects limit the minimum diameter of the array for a given antenna design  
1292 since the radiation from electrons that are too close to the array cannot be detected  
1293 due to destructive interference caused by path-length differences from the electron to  
1294 different points on the antenna surface.

1295 Slotted waveguide antennas are used in the FSCD antenna array due to their high  
1296 efficiency and low loss, which comes from the lack of dielectric materials in the antenna  
1297 structure. Coupling to the waveguide can be performed with a coaxial cable connected  
1298 at the center or on either end of the waveguide. One of the drawbacks of waveguide  
1299 antennas is the large amount of space required to fit them inside the limited MRI magnet  
1300 volume. Alternative antenna designs, constructed from microstrip printed circuit boards  
1301 require significantly less space at the cost of slightly higher energy loss in the antenna  
1302 structure.

1303 The FSCD antenna design is a 5 cm long segment of WR-34 waveguide with 5 vertical  
1304 slots cut into the side. The distance between slots along the length of the waveguide is  
1305 a half wavelength for optimal power combination between the individual antenna slots.  
1306 Each slot is offset from the center of the antenna face a small distance in order to most  
1307 effectively couple the slot to waveguide modes inside the antenna.

1308 The passive power combination achieved by placing 5 slots in a single waveguide is a  
1309 compromise intended to reduce the cost and complexity of the antenna array system.  
1310 Each additional channel in the array requires it's own cryogenic amplifier and also increase  
1311 the required computer power to process the raw data collected by digitizing each channel.  
1312 Passive summation, achieved by combining antennas into arrays axially, reduces the array  
1313 channel count at the cost of losses from imperfect passive combination. Imperfect passive  
1314 combination is caused by effects such as re-radiation of energy from and destructive  
1315 interference between slots in the waveguide antenna.

1316 Interference and re-radiation eventually limit the achievable the axial extent of passive  
1317 power combination. The 5-slot designed developed for the FSCD is optimized to minimize  
1318 the impact of these losses while achieving the maximum amount of axial coverage with a  
1319 single ring of antennas. Scaling beyond the volume covered by a single ring of antennas is  
1320 achieved by stacking additional rings of antennas together to cover a larger trap volume  
1321 for a higher statistics measurement of the tritium spectrum endpoint region. A likely  
1322 scenario for the FSCD experiment involves a staged experiment approach, where first

1323 a series of measurements is performed using only a single ring of antennas followed by  
1324 experiments that add additional rings to the FSCD. The goal would be to first understand  
1325 the principles of antenna array CRES using the simplest possible experiment, before  
1326 attempting to scale the technique by expanding the antenna array size.

### 1327 **Tritium Source**

1328 While the primary purpose of the FSCD is as a technology demonstrator, it is unlikely  
1329 for the collaboration to gain the required confidence in the antenna array CRES tech-  
1330 nique to perform neutrino mass measurements at the 40 meV sensitivity level without  
1331 an intermediate scale measurement of the neutrino mass using antenna array CRES.  
1332 Therefore, the FSCD has an additional scientific goal of measuring the neutrino mass  
1333 with a rough sensitivity goal of a few eV. This level of precision is achievable using a  
1334 source of molecular tritium with a volume of approximately 1 L at a density comparable  
1335 to potential Phase IV scenarios.

1336 Unlike previous CRES experiments, where the tritium source could be co-located  
1337 with the receiving antenna inside a waveguide transmission line, the tritium source  
1338 in the FSCD is thermally isolated from the antenna array to avoid freeze-out of the  
1339 tritium molecules. The tiny radiation power emitted by electrons requires a system noise  
1340 temperature of  $\approx 10$  K or less, in order to detect events at a high enough efficiency to  
1341 reach the neutrino mass sensitivity goals of the experiment. Achieving a system noise of  
1342 10 K requires that the antenna array and amplifiers operate at cryogenic, liquid helium  
1343 temperatures of  $\approx 4$  K, which significantly lowers the vapor pressure of molecular tritium.  
1344 By keeping the molecular tritium isolated in an RF-transparent vessel the tritium gas can  
1345 be kept at a relatively warmer temperature in the range of 30 K to avoid the accumulation  
1346 of tritium on the experiment surfaces.

### 1347 **Data Acquisition and Reconstruction**

1348 A fundamental change in the data acquisition system for the FSCD is the shift from  
1349 single to multi-channel reconstruction. This transition results in a significant increase in  
1350 the data-generation rate, which is linearly related to the number of independent channels  
1351 in the array. The larger data volume coincides with an increased demand for computer  
1352 processing power based on the need for more precise signal reconstruction algorithms  
1353 driven by the FSCD and Phase IV sensitivity goals. Therefore, the data acquisition  
1354 system for the FSCD is likely to represent a significantly larger fraction of the experiment  
1355 cost and complexity than previous CRES experiments.

1356        Each antenna in the array is connected to a cryogenic amplifier and down-converted  
1357 from the 26 GHz CRES frequency using an IQ-mixer to reduce the size of the analysis  
1358 window in which the tritium spectrum is measured. Using an LO with a frequency of  
1359 approximately 25.80 GHz the antenna array signals can be digitized at a rate of 200 MHz,  
1360 which is sufficient bandwidth to resolve the complete sideband spectrum produced by  
1361 axial oscillations of electrons in the FSCD magnetic trap.

1362        Direct storage of the raw FSCD antenna array data is undesirable, since the estimated  
1363 amount of raw data generated is  $O(1)$  exabyte per year. The management and storage  
1364 of such a large dataset is infeasible for a demonstrator experiment on the scale of the  
1365 FSCD and would represent a large fraction of the budget for a Phase IV scale antenna  
1366 array based CRES experiment. Therefore, a sub-goal of the FSCD experiment is the  
1367 development of real-time reconstruction methods that could reduce the raw data volume  
1368 by detecting and reconstructing CRES events in real-time. The ultimate goal would be  
1369 a complete real-time reconstruction pipeline that takes raw voltages samples from the  
1370 antenna array and returns estimates for the starting kinetic energies of CRES events in  
1371 the data.

1372        The feasibility of a real-time reconstruction pipeline rests on the development of  
1373 computationally efficient algorithms that can be implemented without the need for  
1374 enormous computing resources. One challenge with the antenna array approach is that  
1375 the small radiation power of a single electron is distributed between each channel in  
1376 the array, such that reconstruction using only the information in a single channel is not  
1377 possible. Therefore, the simply performing the initial step in reconstruction — signal  
1378 detection — requires orders of magnitude more computational power than previous CRES  
1379 experiments. This operation will then be followed by other, potentially more expensive,  
1380 reconstruction steps that are required in order to determine the kinetic energy of the  
1381 electron.

## 1382        **3.5 Pilot-scale Experiments**

### 1383        **3.5.1 Choice of Frequency**

1384        The optimal CRES frequency for Project 8 is that which can reach our target sensitivity  
1385 of 40 meV, while minimizing the cost and complexity of the overall experiment. The  
1386 magnitude of the background magnetic field determines the cyclotron frequency, which  
1387 affects the entirety of the CRES detection system design, specifying the operating

frequency of the CRES experiments is one of the first steps towards developing a full design.

## Scaling Laws

The Phase I and II experiments utilized a background magnetic field of 0.959 T provided by an NMR magnet. This magnetic field was selected primarily for convenience, however, the cyclotron frequencies for electrons near the tritium endpoint in a 0.959 T field ranges from 25 to 26 GHz, which is within the standard RF Ka-band. Therefore, microwave electronics specialized for these frequencies are easily obtainable for relatively low cost. The operating frequency for the large-scale experiments must be selected in a more rigorous manner due to the increased scale and complexity of the systems as well as the requirements of the 40 meV neutrino mass science goal.

There is a bias towards lower frequencies in a large-volume experiment, due to the direct relationship between wavelength and the physical size of the compatible RF components like antennas and cavities. With a longer wavelength more volume can be surrounded by an array with fewer antennas, which reduces hardware and data-processing costs. Additionally, the size of a cavity experiment is directly proportional to the wavelength since this sets the physical dimensions of the cavity. Furthermore, it is easier to engineer a magnet that provides a uniform magnetic field across several cubic-meters of space at lower magnetic fields, which provides advantages in terms of cost-reduction and field uniformity.

A concern with lower magnetic fields and frequencies is the scaling of the Larmour power equation, which is proportional to the square of the frequency. Naively, one would predict that the SNR would decrease with lower fields, however, two additional scaling laws that affect the noise power also come into play. Noise power is directly proportional to the required bandwidth, which decreases linearly with the magnetic field. Furthermore, at lower frequencies it is possible to purchase amplifiers with lower noise temperatures until approximately 300 MHz at which point this relationship tends to flatten. Therefore, it is expected that the SNR remains approximately constant as the frequency decreases.

The SNR directly impacts the overall efficiency of the experiment through its effects on signal detection and energy resolution. Thus, the expectation that SNR remains the same at lower frequencies clearly biases large-scale experiments in this direction. One drawback of lower magnetic fields is the increased influence of external magnetic fields on the experiment. This includes magnetic fields from the building materials as well as variations in the earth's magnetic field. To deal with these affects a suitable magnetic

<sup>1422</sup> field correction system will need to be devised, which includes constant monitoring of  
<sup>1423</sup> external fields.

## <sup>1424</sup> Atomic Tritium Considerations

<sup>1425</sup> The pilot-scale experiments will be the first Project 8 experiments to combine CRES with  
<sup>1426</sup> atomic tritium, therefore, the optimal frequency should take into account the affect of the background magnetic field on the atom trap. The primary influence of the background

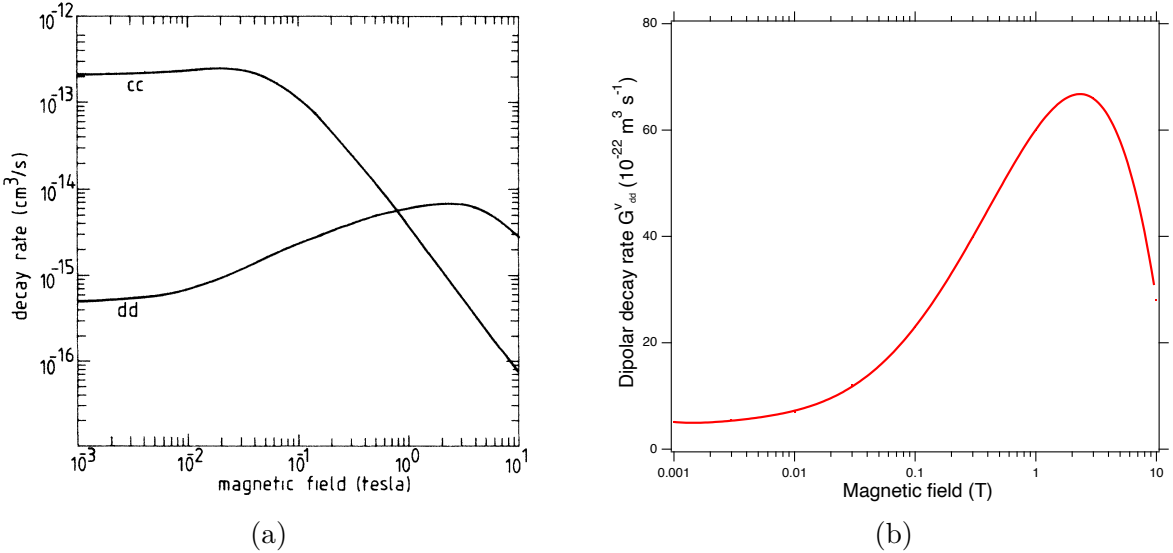


Figure 3.18: (a) A plot of the decay rate for the two-body dipolar spin exchange interaction for cc and dd state. (b) A plot of the decay rate of the dipolar spin exchange interaction for d+d states as a function of magnetic field magnitude. Lowering the magnetic field is key for reducing the losses from this interaction.

<sup>1427</sup>

<sup>1428</sup> field magnitude is through the rate of dipolar spin-flips caused by a spin exchange  
<sup>1429</sup> interaction between trapped atoms [56].

<sup>1430</sup> Atomic tritium is a simple quantum system with a hyperfine structure given by the  
<sup>1431</sup> addition of the nuclear and atomic spins. The addition of two spins leads to a hyperfine  
<sup>1432</sup> structure with four states in the  $(m_s, m_I)$  basis [57]. The states with atomic spins directed  
<sup>1433</sup> anti-parallel to the magnetic field have  $m_s = -1/2$  and are labeled as the a and b states.  
<sup>1434</sup> The a and b states are colloquially known as high-field seeking states, since their energy is  
<sup>1435</sup> minimized when in regions of higher magnetic field. This leads to losses in the magnetic  
<sup>1436</sup> trap as these atoms are drawn to higher fields away from the trap center. Alternatively,  
<sup>1437</sup> the c and d states, with atomic spin  $m_s = +1/2$ , minimize their energy in low magnetic  
<sup>1438</sup> fields because of the parallel alignment between spin and the magnetic field. Therefore,

1439 these low-field seeking states tend to stay trapped significantly longer than the high-field  
1440 seeking states.

1441 It would be advantageous to prepare tritium atoms in purely c and d states before  
1442 trapping, however, even in this case losses still occur due to dipolar interactions between  
1443 pairs of c and d states leading to flipped atomic spins and subsequent losses from high-field  
1444 seeking atoms. The rate of these interactions depends on the magnitude of the background  
1445 magnetic field and is maximal for dd interactions around 1 T (see Figure 3.18). The rate  
1446 of losses from these interactions at 1 T requires atomic tritium production at a rate two  
1447 orders of magnitude larger than at 0.1 T, thus, requirements on the whole atomic tritium  
1448 system are significantly relaxed at lower magnetic fields, which provides an additional  
1449 argument for transitioning to lower frequencies with the pilot-scale experiments.

1450 **3.5.2 Pilot-scale Experiment Concepts**

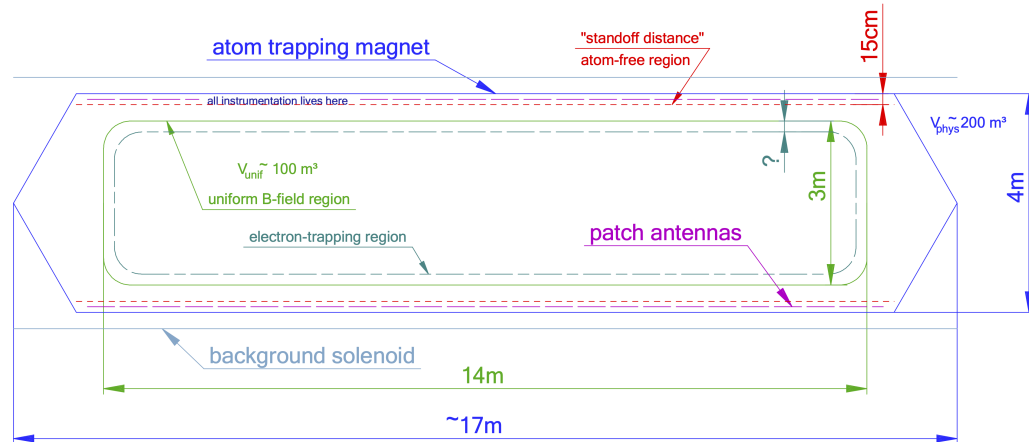


Figure 3.19: A conceptual sketch of a large-volume antenna array based CRES experiment to measure the neutrino mass.

1451 While the pilot-scale experiments are still in the early stages, enough is known to  
1452 sketch the general features of these experiments at the conceptual level.

1453 **Pilot-scale Antenna Array CRES Experiment Concept**

1454 A conceptual design for an antenna-based CRES experiment is shown in Figure 3.19.  
1455 A large solenoid magnet provides a uniform background magnetic field less than 0.1 T  
1456 in magnitude. Inside this region is the atom trapping magnet that generates a high  
1457 magnetic field at the walls, which decays exponentially towards the central region. Known

<sup>1458</sup> magnet designs that produce suitable atom trapping fields include Ioffe-Prichard traps,  
<sup>1459</sup> which use conducting coils, as well as a Halbach array made from permanent magnets.  
<sup>1460</sup> Either magnet choice produces a region of high magnetic fields, which excludes atoms  
<sup>1461</sup> and allows for the placement of antennas inside the experiment.

<sup>1462</sup> Inside this region an array of microstrip patch antennas is inserted to collect the  
<sup>1463</sup> cyclotron radiation without providing a surface for atomic tritium recombination. Due  
<sup>1464</sup> to the lower frequency of cyclotron radiation antennas of a larger size can be used,  
<sup>1465</sup> which lowers the total number of antennas required to observe the experiment volume.  
<sup>1466</sup> Because of this scaling, the lower frequency experiment uses a similar number of antennas  
<sup>1467</sup> compared to a much smaller demonstrator experiment with a 1 T magnetic field.

<sup>1468</sup> The atomic tritium beamline that supplies fresh tritium atoms to the experiment is  
<sup>1469</sup> not shown in the figure. The general configuration would matches the one shown for the  
<sup>1470</sup> pilot-scale cavity experiment (see Figure 3.20).

## <sup>1471</sup> Pilot-scale Cavity CRES Experiment Concept

<sup>1472</sup> The pilot-scale cavity experiment includes both an atomic tritium system and cavity  
<sup>1473</sup> CRES system. The atomic system consists of a thermal atom cracker located at the  
<sup>1474</sup> start of an evaporatively cooled atomic beamline. The atomic tritium system provides a  
<sup>1475</sup> supply of tritium atoms to the trap with temperatures on the order of a few mK. Atoms  
<sup>1476</sup> at this temperature can be trapped magneto-gravitationally, which is the reason for the  
<sup>1477</sup> vertical orientation of the cavity. At these low magnetic fields the trapping requirements  
<sup>1478</sup> for electrons and atoms differ enough such that it is advantageous to decouple the the  
<sup>1479</sup> trapping potentials to avoid radioactive heating of the tritium atoms from excess trapped  
<sup>1480</sup> electrons. Electron trapping is provided by a set of magnetic pinch coils at the top and  
<sup>1481</sup> bottom of the cavity and a multi-pole Ioffe or Halbach magnet serves to contain the  
<sup>1482</sup> atoms.

<sup>1483</sup> The cavity design for the pilot-scale experiment consists of a large cylindrical cavity  
<sup>1484</sup> with a TE011 resonance of 325 MHz. Such a cavity is truly enormous, with a diameter  
<sup>1485</sup> of approximately 1.2 m and a height of 11 m. When an electron is produced inside  
<sup>1486</sup> the cavity with a cyclotron frequency that matches the TE011 resonant frequency it's  
<sup>1487</sup> cyclotron orbit couples the electron to the TE011, which drives a resonance in the cavity.  
<sup>1488</sup> These resonant fields can be read-out using an appropriate cavity coupling mechanism  
<sup>1489</sup> located at the center of the cavity. For more information on the cavity approach to  
<sup>1490</sup> CRES see Chapter 6.

<sup>1491</sup> The bottom of the cavity has a cone termination to match the contour of the atom

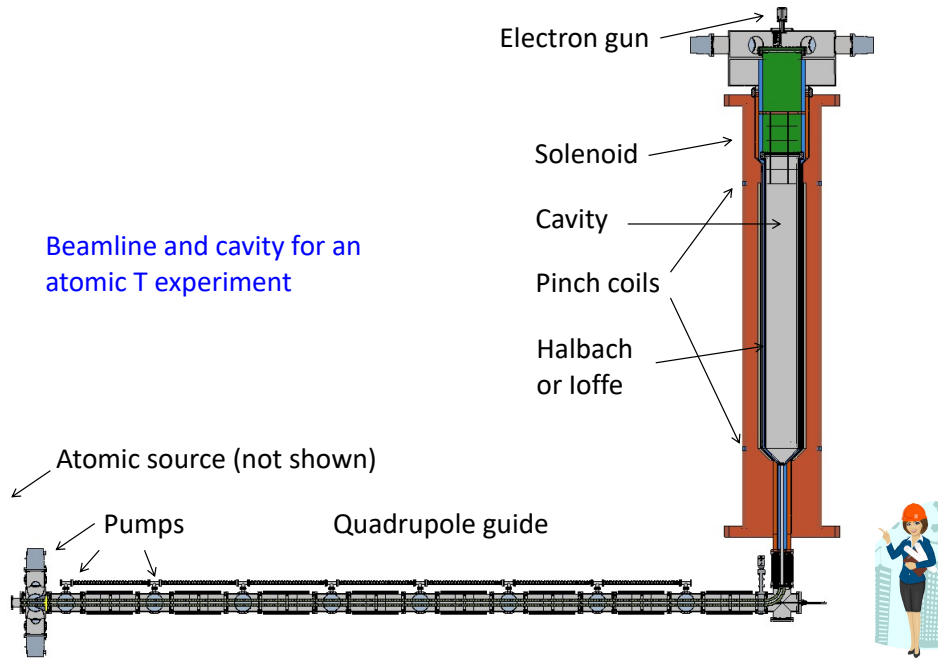


Figure 3.20: A conceptual sketch of a pilot-scale cavity CRES experiment with an atomic tritium beamline.

1492 trapping magnet. This shape still allows for TE011 resonances with high internal Qs,  
 1493 which are required for good SNR in the cavity experiment. A small opening in the bottom  
 1494 of the cone serves as an entry point for the tritium atoms. To allow for calibration of  
 1495 the magnetic field inhomogeneities with an electron gun, the top of the cavity is left  
 1496 nearly completely open. Normally, this would drastically lower the Q-factor of the TE011  
 1497 mode, but a specially configured coaxial partition is inserted at the top. This termination  
 1498 scheme is designed to act as a perfect short for the TE011 mode since the circular shape  
 1499 of the partition matches the electric field boundary conditions for the TE011 mode.  
 1500 Simulations with HFSS have confirmed that this design results in a high quality TE011  
 1501 resonance despite the nearly completely open end.

## 1502 **3.6 Phase IV**

1503 The baseline CRES technology being pursued by the Project 8 collaboration are resonant  
 1504 cavities, which, due to their geometric properties, simple CRES signal structure, and low  
 1505 channel count, appear to be the better option for Phase IV. The current knowledge of the  
 1506 antenna array CRES approach reveals no technical obstacles that would preclude it as a  
 1507 baseline technology for Phase IV though it would most certainly be significantly more

1508 expensive. Therefore, antenna arrays represent a fallback approach if resonant cavities  
1509 prove infeasible.

1510 The sensitivity of the pilot-scale atomic tritium experiment is estimated to be on  
1511 the order of 0.1 eV, which means that increasing the sensitivity to reach the Phase IV  
1512 goal will require an even larger experiment. Because of the direct coupling between the  
1513 RF characteristics of a cavity and its geometry, the baseline plan is to build multiple  
1514 copies of the pilot-scale experiment (see Figure 3.21) to obtain the required amount of  
1515 volume rather than increase the size of the cavity beyond the pilot-scale. The built-in  
1516 redundancy of this approach is useful in the sense that the experiment has no single  
1517 point of failure, additionally, building several copies of the a pilot-scale experiment will  
1518 minimize new engineering and design effort.

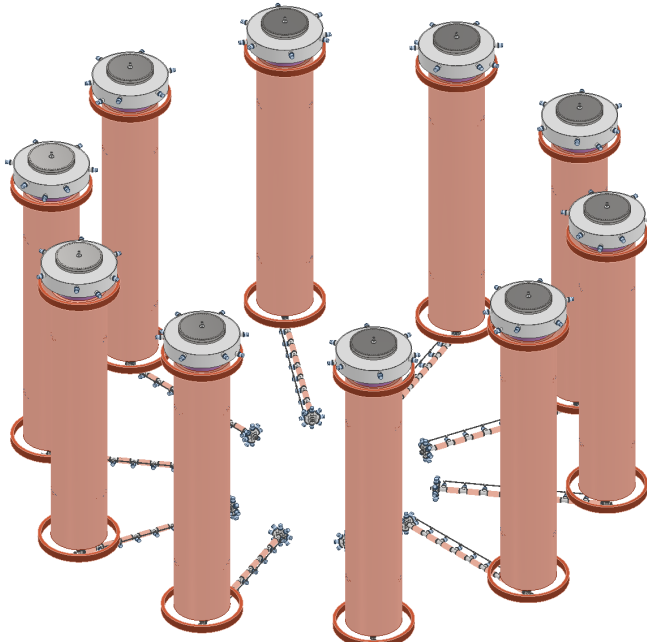


Figure 3.21: An illustration of a possible arrangement of ten pilot-scale cavity experiments for Phase IV. The experiments are arranged in a circle with an approximate diameter of 50 meters. Each atomic beamline connected to the bottom of each cavity is approximately 10 m in length. The cavities themselves are designed to operate at 325 MHz and are approximately 11 m tall. The circular arrangement of cavities has some advantages when it comes to cancellation of fringe fields from neighboring magnets, which is important due to the small magnetic field magnitudes consistent with these CRES frequencies. The advantage of ten independent atomic sources and cavities is that there is no single point of failure for the experiment. If an experiment goes down for repairs the other nine may continue running. Figure courtesy of Michael Huehn at UW-Seattle.

# **Chapter 4**

## **Signal Reconstruction Techniques for Antenna Array CRES and the FSCD**

### **4.1 Introduction**

The transition from a waveguide CRES experiment to an antenna array CRES experiment introduces new challenges related to data acquisition, signal detection, and signal reconstruction caused by the multi-channel nature of the data. The development of signal reconstruction algorithms is crucial to the design of antenna array based experiments like the FSCD, because these algorithms directly influence the detection efficiency and energy resolution of the CRES experiment. In this Chapter I summarize my contributions to the development and analysis of signal reconstruction and detection algorithms for the FSCD experiment.

In Section 4.2 I discuss the primary tool for this work, which is the Locust simulations package developed by the Project 8 experiment. Locust is used to simulate CRES events in the detector. Locust uses Kassiopeia to calculate particle trajectory solutions for electrons in the magnetic trap. The trajectories are then used to calculate the response of the antenna array to the cyclotron radiation produced by the electron, which results in signals that can be used to analyze the performance of different signal reconstruction algorithms. More recently, Project 8 has developed CREsana, which is a new simulations package that takes a more analytical approach to CRES signal simulations for antenna arrays. Although CREsana signals were not used for the signal reconstruction algorithm development detailed here, we introduce the software as it plays a role in the antenna array measurements presented in Section 5.4.

In Section 4.3 I discuss the signal reconstruction and detection approaches analyzed for the FSCD experiment. In general there are two steps to signal reconstruction — detection and parameter estimation. With signal detection one is primarily concerned

1545 only with distinguishing between data that contains a signal versus data that contains only  
1546 noise, whereas, with parameter estimation one is interested in extracting the kinematic  
1547 parameters of the electron encoded in the cyclotron radiation signal shape. Due to  
1548 the low signal power of electrons near the spectrum endpoint in the FSCD experiment,  
1549 signal detection is a non-trivial problem. This is magnified by the need to maximize the  
1550 detection efficiency of the experiment in order to achieve the neutrino mass sensitivity  
1551 goals. My contributions to signal reconstruction analysis for the FSCD are focused on  
1552 this signal detection component of reconstruction.

1553 After the discussion of various signal detection approaches, in Section 4.4 I present a  
1554 more detailed analysis of the detection performance of three algorithms, which could be  
1555 used to signal detection in the FSCD. This section was originally prepared for publication  
1556 in JINST as a separate paper. The algorithms include a digital beamforming algorithm,  
1557 a matched filter algorithm, and a neural network algorithm, which I analyze in terms of  
1558 classification accuracy and estimated computational cost.

## 1559 **4.2 FSCD Simulations**

1560 Antenna array CRES and the FSCD requires a combination of different capabilities  
1561 not often found in a single simulation tool. First of all, accurate calculations of the  
1562 magneto-static fields produced by current-carrying coils are required in order to accurately  
1563 model the magnetic trap and background magnets. The resulting magnetic fields must  
1564 then be used to calculate the exact relativistic trajectory of electrons, which is required  
1565 in order to calculate the electro-magnetic (EM) fields produced by the acceleration of  
1566 the electron. Finally, the simulation has to model the interaction of the antenna and  
1567 RF receiver chain with these EM-fields in order to produce the simulated voltage signals  
1568 produced by the antenna array during the CRES event. At the time when Project 8 was  
1569 developing this simulation capability, no single available simulation tool was known to  
1570 adequately perform this suite of calculations, which prompted the development of custom  
1571 simulation framework to simulate the FSCD. This simulation framework includes custom  
1572 simulation tools developed by Project 8 as well as other open-source and proprietary  
1573 software developed by third-parties.

1574 **4.2.1 Kassiopeia**

1575 Kassiopeia<sup>1</sup> is a particle tracking and static EM-field solver developed by the KATRIN  
1576 collaboration for simulations of their spectrometer based on magnetic adiabatic collimation  
1577 with an electrostatic filter [58]. Due to the measurement technique employed by the  
1578 KATRIN collaboration, Kassiopeia is not designed to solve for the EM-fields produced by  
1579 electrons in magnetic fields. However, it does provide efficient solvers for static electric  
1580 and magnetic fields and charged particle trajectory solvers. Because of this, Project 8  
1581 has incorporated parts of Kassiopeia into its own simulation framework.

1582 **Magnetostatic Field Solutions**

1583 The solutions to the electric and magnetic fields generated by a static configuration of  
1584 charges and currents is given by Maxwell's equations in the limit where the time-dependent  
1585 terms go to zero. In their static form Maxwell's equations [47] are

$$\nabla \cdot \mathbf{E} = \frac{\rho}{\epsilon_0} \quad (4.1)$$

$$\nabla \times \mathbf{E} = 0 \quad (4.2)$$

$$\nabla \cdot \mathbf{B} = 0 \quad (4.3)$$

$$\nabla \times \mathbf{B} = \mu_0 \mathbf{J}, \quad (4.4)$$

1586 where we can see that the electric and magnetic fields are now completely decoupled  
1587 from each other. The solution for the magnetic field in this boundary value problem is  
1588 given by the Biot-Savart law

$$\mathbf{B}(\mathbf{r}) = \frac{\mu_0}{4\pi} \int dr' \frac{r'^3 \mathbf{J}(\mathbf{r}') \times (\mathbf{r} - \mathbf{r}')}{|\mathbf{r}' - \mathbf{r}|^3}, \quad (4.5)$$

1589 which Kassiopeia uses a variety of numeric integration techniques to solve for a user  
1590 defined current distribution.

1591 **Kassiopeia Simulation of the FSCD Magnetic Trap**

1592 The trap developed for the FSCD experiment utilizes six current carrying coils, which  
1593 surround a cylindrical tritium containment vessel (see Figure 4.1). Some critical aspects  
1594 of the trap design include the total trapping volume, the maximum trap depth, the

---

<sup>1</sup><https://github.com/KATRIN-Experiment/Kassiopeia>

steepness of the trap walls, as well as the radial and azimuthal uniformity of the magnetic fields.

The volume of the FSCD trap is a cylindrically shaped region with a radius of 5 cm and a length of 15 cm resulting in a roughly 1 L total trap volume. The trap volume is an important design feature, because it sets the volume of the experiment that is potentially usable for CRES measurements. Trapping a larger volume allows one to observe a larger number of tritium atoms, which increases the statistical power and sensitivity of the neutrino mass measurement. Due to the cost of constructing magnets with large and uniform magnetic fields it is important that the trap use as much of the available volume as possible to limit the overall cost of the experiment.

Coil	Radius (mm)	Z Pos. (mm)	Current (A × Turns)
1	50.0	-92.3	750.0
2	50.1	-56.9	-220.3
3	68.5	-19.5	-250.0
4	68.5	19.5	-250.0
5	50.1	56.9	-220.3
6	50.0	92.3	750.0

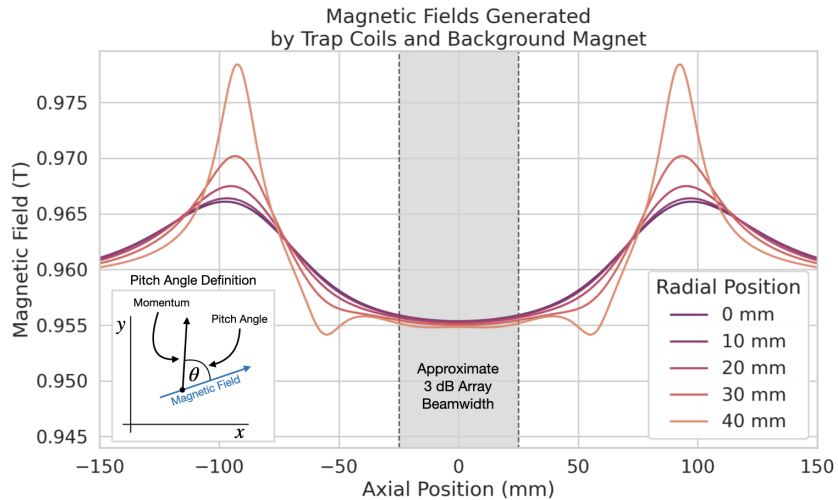
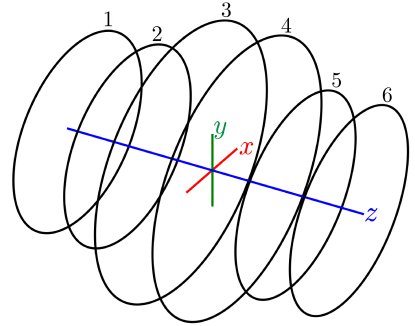


Figure 4.1: The geometry and parameters of the coils used to simulate the FSCD magnetic trap in Kassiopeia. Some axial profiles of the magnetic trap at different radial positions are show to demonstrate the shape of the magnetic field and trap depth as a function of position. Calculation of the magnetic field profiles was graciously done by René Reimann.

The depth of the FSCD trap is approximately 10 mT when measured along the central axis, which is sufficient to trap electrons with pitch angles as small as  $84^\circ$ . The

1607 trap depth factors into the efficiency of the experiment by directly controlling the range  
1608 of electron pitch angles that can be trapped. If a higher fraction of pitch angles are  
1609 trapped then, in principle, more decay events can be observed. However, the signals from  
1610 electrons with small pitch angles are typically significantly harder to detect than larger  
1611 pitch angles when using an antenna array, which increases the likelihood of not detecting  
1612 the first track of the CRES event and harms the energy resolution of the experiment.

1613 The steepness of the trap walls as well as any non-uniformities in the magnetic  
1614 field contribute to the total energy resolution of the CRES measurement by causing  
1615 uncertainty in the relationship between an electron's kinetic energy and it's cyclotron  
1616 frequency. When an electron is trapped, it oscillates back and forth along the trap z-axis  
1617 (see Figure 4.1) unless it is produced with a pitch angle of exactly 90° [59]. As the  
1618 electron is reflected from the trap walls it experiences a change in the total magnetic  
1619 field, which causes a modulation in the cyclotron frequency. This change in magnetic  
1620 field from the trap introduces a correlation between the pitch angle and kinetic energy  
1621 parameters of the electron that can reduce energy resolution. In order to mitigate this  
1622 effect it is important to make the trap walls as steep as possible.

## 1623 Particle Trajectory Solutions

1624 The magnetic fields solved by direct integration of the electron's current density can  
1625 be used by Kassiopeia to solve for the trajectory of electrons based on user specified  
1626 initial conditions. Various distributions are available within Kassiopeia that can be  
1627 sampled in order to replicate realistic event statistics, including uniform, Gaussian, and  
1628 Lorentzian among others. In general, an electron has six kinematic parameters that define  
1629 its trajectory, which are the three-dimensional coordinates of the initial position and the  
1630 three components of the electron's momentum vector. However, when simulating CRES  
1631 events it is more common to parameterize the electron's trajectory in terms of it's initial  
1632 position, the kinetic energy, the pitch angle, and the initial direction of the component  
1633 of the electron's momentum perpendicular to the magnetic field. This parameterization  
1634 is completely equivalent to specify each component of the electrons initial position and  
1635 momentum vectors.

1636 From the initial parameters of the electron and the magnetic field, Kassiopeia solves  
1637 for the trajectory of the electron. The direct approach proceeds by solving the motion of  
1638 the electron using the Lorentz force equation, which takes the form of a set of differential

1639 equations

$$\frac{d\mathbf{r}}{dt} = \frac{\mathbf{p}}{\gamma m} \quad (4.6)$$

$$\frac{d\mathbf{p}}{dt} = e(\mathbf{E} + \frac{\mathbf{p} \times \mathbf{B}}{\gamma m}), \quad (4.7)$$

1640 where  $\mathbf{r}$  is the position of the electron,  $\mathbf{p}$  is the electron's momentum,  $e$  is the charge of  
1641 the electron,  $m$  is the electron's mass, and  $\gamma$  is the relativistic Lorentz term. To account  
1642 for kinetic energy losses from radiation Kassiopeia includes an additional term in the  
1643 momentum differential equation, which calculates the change in the electron's momentum  
1644 induced by synchrotron radiation. Kassiopeia solves this pair of differential equations  
1645 using numerical integration, however, the exact trajectory can be computationally  
1646 intensive to solve. If the adiabatic approximation can be applied, then Kassiopeia can  
1647 make use of a simpler set of equations that can be more readily solved numerically.

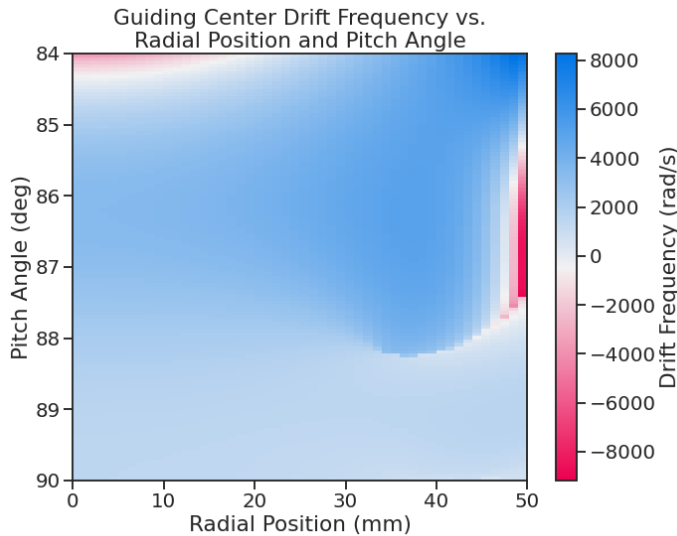


Figure 4.2: A map of the average  $\nabla B$ -drift frequency for electrons trapped in the prototype FSCD trap shown in Figure 4.1. Negative drift frequencies indicate electrons that are drifting opposite to the standard direction, which means that they are close to escaping the magnetic trap.

1648 Even though Kassiopeia is not directly capable of simulating the cyclotron radiation,  
1649 it is still an invaluable CRES simulation tool, due to the accurate trajectory solutions  
1650 for electrons in magnetic traps. With Kassiopeia it is possible to test the efficiency of a  
1651 particular trap design and analyze features of the electron trajectories that are important  
1652 to the position, track, and event reconstruction algorithms (see Section 4.3). One example

of this for the FSCD is the analysis of the average  $\nabla B$ -drift frequency as a function of  
 the electrons radial position and pitch angle in the magnetic trap (see Figure 4.2). Radial  
 gradients in the trap cause the guiding center of the electron to drift around the center of  
 the magnetic trap with an average frequency on the order of  $10^3$  rad/s. This frequency,  
 while slow compared to the length of a typical CRES time-slice, is large enough to cause  
 a significant loss in efficiency of certain signal reconstruction algorithms. Therefore, it is  
 important to model the drift of the electron in the reconstruction algorithm in order to  
 mitigate the effects of this motion on the reconstruction.

### 4.2.2 Locust

The Locust<sup>2</sup> software package [60] is the primary simulation tool developed and used  
 by the Project 8 collaboration for CRES experiments. Locust simulates the responses  
 of antennas and receiver electronics chain to rapidly time-varying electric fields using  
 a flexible approach that allows one to choose from a variety of electric field sources  
 and antennas. Similarly, one can simulate the receiver chain using a series of modular  
 generators that include standard signal processing operations such as down-mixing and  
 fast Fourier transforms (FFT). Since the primary focus of this chapter is the application  
 of Locust to analyses of the FSCD, we shall describe only the most relevant aspects of  
 the software rather than provide a comprehensive description.

### Cyclotron Radiation Field Solutions

Simulating CRES events in the FSCD requires that we calculate the electric fields  
 produced by the acceleration of the electron. In the general case, this can be a complicated  
 question to answer, due to back-reaction forces on the electron from its own electric fields  
 that occur when the electron is surrounded by conductive material such as a waveguide  
 or cavity. However, in the case of the FSCD it is possible to ignore such effects and  
 approximate the electron as radiating into a free-space environment.

The equations that describe the electromagnetic fields from a relativistic moving  
 point particle are the Liénard-Wiechert field equations [61, 62], which are obtained by  
 differentiating the Liénard-Wiechert potentials. In their full form the Liénard-Wiechert  
 field equations are

$$\mathbf{E} = e \left[ \frac{\hat{n} - \boldsymbol{\beta}}{\gamma^2(1 - \boldsymbol{\beta} \cdot \hat{n})^3 |\mathbf{R}|^2} \right]_{t_r} + \frac{e}{c} \left[ \frac{\hat{n} \times [(\hat{n} - \boldsymbol{\beta}) \times \dot{\boldsymbol{\beta}}]}{(1 - \boldsymbol{\beta} \cdot \hat{n})^3 |\mathbf{R}|} \right]_{t_r} \quad (4.8)$$

---

<sup>2</sup>[https://github.com/project8/locust\\_mc/tree/master](https://github.com/project8/locust_mc/tree/master)

$$\mathbf{B} = [\hat{n} \times \mathbf{E}]_{t_r}, \quad (4.9)$$

where  $e$  is the charge of the particle,  $\hat{n}$  is the unit vector pointing from the particle to the position where the fields are calculated,  $\beta$  and  $\dot{\beta}$  are the velocity and acceleration of the particle divided by the speed of light ( $c$ ),  $\mathbf{R}$  is the distance from the particle to the field calculation position, and  $\gamma$  is the relativistic Lorentz term. The subscript  $t_r$  indicates that the equations must be evaluated at the retarded time so that the time-delay from the travel time of the electromagnetic radiation is correctly accounted for.

The only required input to calculate the electric field at the position of an FSCD antenna is the velocity and acceleration of the electron, which can be obtained from Kassiopeia simulations. Therefore, when simulating a CRES event Locust first runs a Kassiopeia simulation of the electron and calculates the electric field incident on the antenna. The only difficulty with this approach is the determination of the retarded time. The retarded time corresponds to the time that a photon, which has just arrived at an antenna at the space-time position  $(t, \mathbf{r})$ , was actually emitted by the electron at the space-time position of  $(t_r, \mathbf{r}_e(t_r))$ . Defined in this way, finding the retarded time requires solving

$$c(t - t_r) = |\mathbf{r} - \mathbf{r}_e(t_r)|, \quad (4.10)$$

where the distance traveled by the photon between the measurement and retarded times is equal to the distance between the antenna and the electron at the retarded time. Locust solves Equation 4.10 using a built-in root finding algorithm to find the retarded time, and thus the electric field produced by the electron at the position of each antenna in the FSCD array.

## Antenna Response Modeling

With the electric field it is possible, in principle, to calculate the resulting voltages produced in the antenna. However, direct simulation of the antenna itself is computationally expensive since it would require the modeling of complex interactions of the electron's electric fields with charge carriers in the conductive elements of the antenna. Direct simulation of the antenna in Locust can be avoided by modeling the antenna response using the antenna factor, or antenna transfer function, approach. The antenna factor defines the voltage produced in the antenna terminal for an incident electric field [63],

$$A_F = \frac{V}{|\mathbf{E}|}, \quad (4.11)$$

1710 where  $V$  is the voltage and  $|\mathbf{E}|$  is the magnitude of the incident electric field. To obtain the  
 1711 antenna factor for the antennas developed for the FSCD Project 8 employs Ansys HFSS.  
 1712 HFSS is a commercially available finite element method electromagnetic solver widely  
 1713 used throughout the antenna engineering industry [64]. HFSS is capable of calculating  
 1714 the antenna factor and gain patterns for complex antenna designs and outputting the  
 1715 resulting quantities in the form of a text file that can be used as an input to the Locust  
 1716 simulation.

1717 The antenna factor defines the steady-state response of the antenna to electromagnetic  
 1718 plane waves and is a function of the frequency of the radiation. Therefore, in order to  
 1719 apply the transfer function for the calculation of the antenna voltage response in the  
 1720 time domain, Locust models the antenna as a linear time-invariant system [65]. In this  
 1721 formalism the response of the system to the driving force is given by

$$y[n] = h * x = \sum_k h[k]x[n - k], \quad (4.12)$$

1722 where  $y[n]$  is the discretely sampled response,  $x$  is the driving force stimulus, and  $h$  is  
 1723 the finite impulse response (FIR) filter. When applied to the FSCD array, this formalism  
 1724 calculates the voltage time-series produced in each antenna by convolving the electric  
 1725 field time-series with the antenna FIR filter, which is obtained by performing a inverse  
 1726 Fourier transform on the transfer function from HFSS.

## 1727 Radio-frequency Receiver and Signal Processing

1728 After obtaining the voltage time-series by computing the electron trajectory and antenna  
 1729 response, Locust simulates the signal processing associated with the radio-frequency  
 1730 receiver chain. The standard receiver chain used in Locust simulations of the FSCD  
 1731 attempts to mimic the operations that would actually occur in hardware (see Figure 4.3).

1732 Frequency down-conversion is used in the FSCD to reduce the digitization bandwidth  
 1733 required to read-out CRES data. According to the Nyquist sampling theorem [66], the  
 1734 minimal sampling rate that guarantees no information loss for a signal with a bandwidth  
 1735  $\Delta f$  is given by

$$f_{\text{Nyq}} = 2\Delta f. \quad (4.13)$$

1736 The total bandwidth of CRES signal frequencies from tritium beta-decay ranges from 0  
 1737 to 26 GHz in a 0.95 T magnetic field, therefore, direct digitization of CRES signals from  
 1738 the FSCD would require sampling frequencies greater than 50 GHz, which is infeasible for

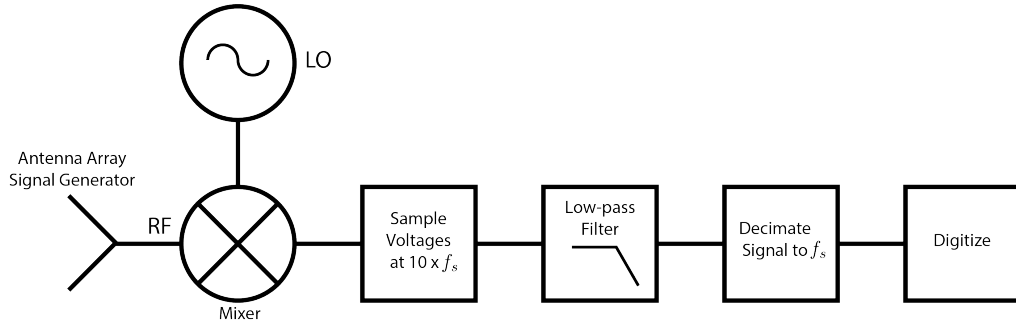


Figure 4.3: The receiver chain used by Locust when simulating CRES events in the FSCD.

1739 a real experiment. However, for the purposes of neutrino mass measurement we are only  
 1740 interested in measuring the shape of the spectrum in the last 100 eV, which corresponds  
 1741 to a frequency bandwidth of 5 MHz. Down-conversion is a technique for reducing the  
 1742 base frequencies of signals in a bandwidth given by  $[f_{\text{LO}}, f_{\text{LO}} + \Delta f]$  to the bandwidth  
 1743  $[0, \Delta f]$ , by performing the following multiplication

$$x(t) \rightarrow x(t)e^{-2\pi f_{\text{LO}} t}. \quad (4.14)$$

1744 In down-conversion the signal ( $x(t)$ ) is multiplied by a sinusoidal signal with frequency  
 1745  $f_{\text{LO}}$  to reduce the absolute frequencies of the signals in the bandwidth. In the FSCD this  
 1746 allows us to detect events in the last 100 eV of the tritium spectrum while sampling the  
 1747 data far below 50 GHz. The standard bandwidth used in the FSCD is 200 MHz, which  
 1748 allows for higher frequency resolution than the minimum sampling frequency for 100 eV  
 1749 of energy bandwidth.

1750 Trying to directly simulate down-conversion with a frequency multiplication in Locust  
 1751 would require the sampling of the electric fields at each antenna in the FSCD array with  
 1752 a period of  $\approx 20$  ps, which is extremely slow computationally. To avoid this Locust  
 1753 performs the down-conversion by intentionally under-sampling the electric fields with  
 1754 a frequency of 2 GHz. Sampling below the Nyquist limit causes the higher frequency  
 1755 components of the CRES signal to alias, however, Locust can remove these aliased  
 1756 frequency peaks using a combination of low-pass filtering and decimation to recreate  
 1757 frequency down-conversion. After filtering and decimation, Locust simulates digitization  
 1758 by an 8-bit digitizer at a sampling frequency of 200 MHz to recreate the conditions of  
 1759 the FSCD. The voltage offset and the digitizer range must be configured by the user  
 1760 based on the characteristics of the simulation.

1761 **Data**

1762 The output of Locust simulations for the FSCD primarily consists of two data files. The  
1763 first is the electron trajectory information calculated by Kassiopiea, which is output in  
1764 the form of a `.root` file [67]. This file contains important kinematic information about  
1765 the electron such as it's position and pitch angle as a function of time. The other file is  
1766 produced by Locust and it contains the digitized signals acquired from each antenna in  
1767 the FSCD array. The Locust output files conform to the Monarch specification developed  
1768 by Project 8, which is based on the commonly used HDF5 file format, and matches the  
1769 format of the files produced by the Project 8 data acquisition software. This makes it  
1770 possible to use the same data analysis code to analyze both simulated and real data.

1771 **4.2.3 CRESana**

1772 Locust is the primary simulation tool used by Project 8 in the development and simulation  
1773 of the FSCD. However, simulations of CRES events in larger antenna arrays ( $\geq 100$   
1774 antennas) using Locust can take several hours to complete, which is prohibitively long  
1775 when one is performing a sensitivity analysis for a large scale antenna experiment. One  
1776 of the reasons for Locust's slow operation is that the electric fields from the electron  
1777 must be solved numerically for each time-step for each of the antennas in the array.  
1778 These numerical solutions allow Locust to accurately simulate the electric fields from  
1779 arbitrarily complicated electron trajectories at the cost of more computations and slower  
1780 simulations. Therefore, an additional simulation tool that sacrifices some accuracy for  
1781 computational efficiency would be extremely useful simulations and sensitivity analyses  
1782 of larger antenna array experiments.

1783 To fill this need, Project has developed a new simulations package called CRESana<sup>3</sup>,  
1784 specifically designed to perform analytical simulations of antenna array based CRES  
1785 experiments. CRESana is not as flexible as Locust, but it provides a significant increase  
1786 in simulation speed. It does this by using well-justified analytical approximations of the  
1787 electrons motion in the magnetic field and the resulting electric fields from the electron's  
1788 acceleration. The electric fields and signals generated by CRESana are consistent with  
1789 theoretical calculations of the electron's radiation, and are test for accuracy using  
1790 well-known test-case simulations and consistency checks.

---

<sup>3</sup><https://github.com/MCFlowMace/CRESana>

## **4.3 Signal Detection and Reconstruction Techniques for Antenna Array CRES**

### **Antenna Array CRES Signal Reconstruction**

A robust set of FSCD simulation tools are vital to the development of the analysis algorithms necessary for antenna array CRES to succeed. In order to perform CRES measurements using an antenna array, one must develop an algorithm that uses the multi-channel time-series obtained by digitizing the array to estimate the starting kinetic energies of electrons produced in the magnetic trap. This procedure consists of a multi-stage process of detecting a CRES signal then estimating the parameters of the electron that produced and is often referred to as simply CRES signal reconstruction.

Compared with the signal reconstruction approaches of the Phase I and II CRES experiments, antenna array CRES requires a significantly different approach to signal reconstruction. In Phase I and II, CRES was performed using a waveguide gas cell that could be directly connected to a waveguide transmission line. The transmission line efficiently transmits the cyclotron radiation along its length to an antenna at either end of the waveguide. However, with an antenna array the electron is essentially radiating into free-space, therefore, the cyclotron radiation power collected by the array is directly proportional to the solid angle surrounding the electron that is covered with antennas. Because it is not practical to fully surround the magnetic trap with antennas, some of the cyclotron radiation power that would have been collected by the waveguide escapes into free-space. Furthermore, the power that is collected by the antenna array is split between every channel in the antenna array, which significantly lowers the signal-to-noise ratio (SNR) of CRES signals in a single antenna channel compared to a waveguide apparatus. Therefore, a suite of completely new signal reconstruction techniques are needed in order to perform CRES in the FSCD.

Changes to the approach to CRES signal reconstruction are also motivated by the more ambitious scientific goals of the FSCD experiment. A measurement of the tritium beta-decay spectrum that is sensitive to neutrino masses as small as 40 meV requires that we measure the kinetic energies of individual electrons with a total energy broadening of 115 meV [68]. This resolution includes all sources of uncertainty in the electron's kinetic energy such as magnetic field inhomogeneities. This level of energy resolution is compatible only with an event-by-event signal reconstruction approach where the kinetic energies, pitch angles, and other parameters of the CRES events are estimated before

1824 constructing the beta-decay spectrum.

1825 The event-by-event approach is distinct from the analysis done for the Phase I and  
1826 Phase II experiments where only the starting cyclotron frequency of the event was  
1827 estimated by analyzing the tracks formed by the carrier frequency in the time-frequency  
1828 spectrogram. These frequencies were then combined into a frequency spectrogram, which  
1829 was converted to the beta-decay energy spectrum using an ensemble approach that  
1830 averaged over all other event parameters. The ensemble approach to signal reconstruction  
1831 results in poor energy resolution because other kinematic parameters such as pitch angle  
1832 change the cyclotron carrier frequency due to changes in the average magnetic field  
1833 experience by the electron, and it is therefore incompatible with the future goals of the  
1834 Project 8 collaboration.

### 1835 Components of Reconstruction: Signal Detection and Parameter Estimation

1836 CRES signal reconstruction can be viewed as a two-step procedure consisting of signal  
1837 detection followed by parameter estimation. In the former, one is concerned with  
1838 identifying CRES signals in the data regardless of the signal parameters, whereas, in the  
1839 latter one operates under the assumption that a signal is present and then estimates its  
1840 parameters.

1841 More formally, signal detection is essentially a binary hypothesis test between the  
1842 signal and noise data classes and parameter estimation describes a procedure of fitting a  
1843 model to the observed data. While both of these processes are required for a complete  
1844 reconstruction (see Figure 4.4), the focus of my work and this chapter is on the signal  
1845 detection aspect of antenna array CRES signal reconstruction.

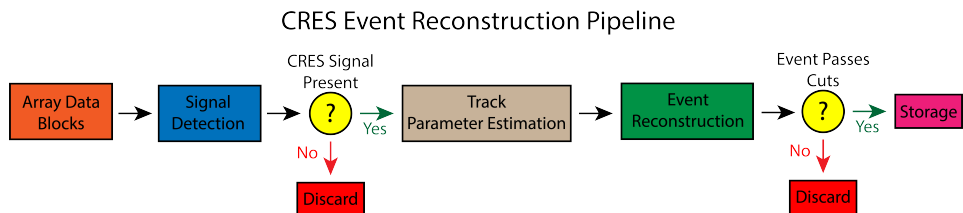


Figure 4.4: A high-level diagram depicting the process of CRES event reconstruction. The first step consists of identifying the presence of a signal in the data. This step is necessary to avoid the danger of performing a reconstruction of a false event, which would constitute a background contribution to the tritium spectrum measured by CRES.

1846 **Detection Theory**

1847 The problem of signal detection can be posed as a statistical hypothesis test [69]. For  
1848 CRES signals, which are essentially vectors with added white Gaussian noise (WGN),  
1849 one needs to choose between two hypotheses

$$\mathcal{H}_0 : \mathbf{y} = \boldsymbol{\nu} \quad (4.15)$$

$$\mathcal{H}_1 : \mathbf{y} = \mathbf{x} + \boldsymbol{\nu}, \quad (4.16)$$

1850 where  $\mathbf{y}$  is the CRES data vector,  $\boldsymbol{\nu}$  is a sample of WGN, and  $\mathbf{x}$  represents the CRES  
1851 signal. The hypothesis that the data contains only noise is labeled  $\mathcal{H}_0$  and the hypothesis  
1852 that the data contains a signal is labeled  $\mathcal{H}_1$ .

1853 For illustrative purposes one can examine the case where one the first sample of  
1854 data is used to distinguish between  $\mathcal{H}_0$  and  $\mathcal{H}_1$ . The value of the first data sample is  
1855 distributed according to two gaussian distributions corresponding to  $\mathcal{H}_0$  and  $\mathcal{H}_1$  (see  
1856 Figure 4.5). By setting a decision threshold on the value of this sample, one can choose  
1857 the correct hypothesis with a probability given by the areas underneath the probability  
1858 distribution curves. A true positive corresponds to correctly identifying that the data  
1859 contains signal, whereas, a true negative means that one has correctly identified the data  
1860 as noise. The rate at which the detector performs a true positive classification is given  
1861 by the green region underneath  $p(\mathbf{y}[0]; \mathcal{H}_0)$ , and the rate at which the detector performs  
1862 a true negative classification is given by the orange region underneath  $p(\mathbf{y}[0]; \mathcal{H}_1)$ . Two  
1863 types of misclassifications are possible. Either we declare noise data as signal, which is  
1864 call a false positive, or we declare signal data as noise, which is a false negative. Note  
1865 that it is only possible to trade off these two types of errors by tuning the detection  
1866 threshold. One cannot simultaneously reduce the rate of false positives without also  
1867 increasing the rate of false negatives.

1868 The approach taken with CRES signals is to fix the rate of false positives by setting  
1869 a minimum value for a detection threshold. The rate of false positives that is acceptable  
1870 at the detection stage depends upon the rate of background events compatible with the  
1871 sensitivity goals of the experiment. The ultimate goal of a neutrino mass measurement  
1872 with 40 meV sensitivity in general has strict requirements on the number of background  
1873 events, which requires a relatively high detection threshold to achieve. Consequently,  
1874 the ideal signal detection algorithm is the one that achieves the maximum rate of true  
1875 positives for a fixed rate of false positives, so that the detection efficiency of the experiment  
1876 is maximized and potential sources of background are kept to a minimum.

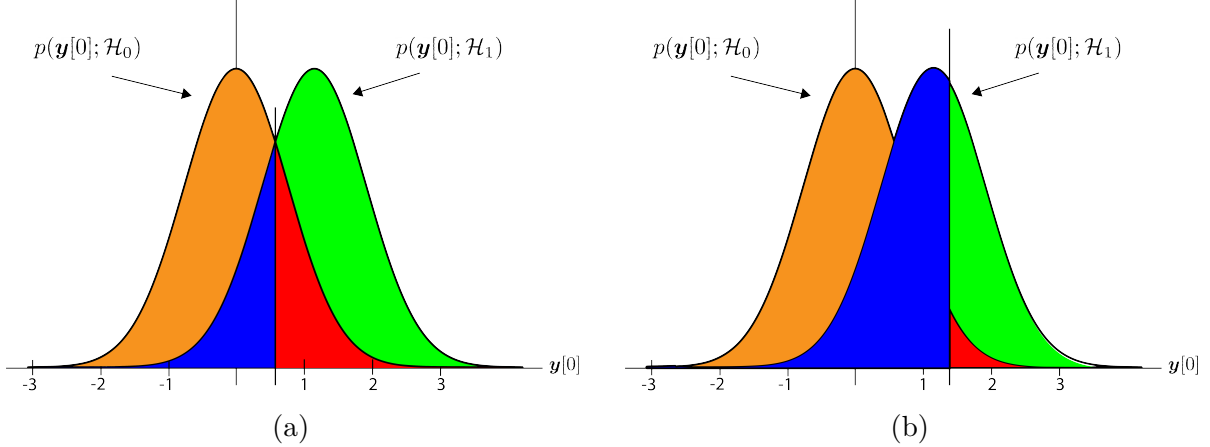


Figure 4.5: An illustration of two PDFs associated with a binary hypothesis test. The decision threshold is represented by the vertical line that partitions both distributions. The orange and red areas correspond to the true negative and false positive probabilities and the blue and green areas correspond to the false negative and true positive probabilities respectively. To decide between the two hypotheses we perform the likelihood ratio test specified by the Neyman-Pearson theorem. This approach achieves the highest true positive probability for a given false positive probability.

According to the Neyman-Pearson theorem [70], the statistical hypothesis test that maximizes the probability of detection for a fixed rate of false positives is the likelihood ratio test, which is formed by computing the ratio of the signal likelihood to the noise likelihood,

$$L(x) = \frac{P(\mathbf{y}; \mathcal{H}_1)}{P(\mathbf{y}; \mathcal{H}_0)} > \gamma. \quad (4.17)$$

Here, the likelihood of the hypotheses  $\mathcal{H}_0$  and  $\mathcal{H}_1$  are described by the probability distributions  $P(\mathbf{y}; \mathcal{H}_0)$  and  $P(\mathbf{y}; \mathcal{H}_1)$  respectively, and  $\gamma$  is the threshold for deciding  $\mathcal{H}_1$ . The decision threshold is determined by integrating  $P(\mathbf{y}; \mathcal{H}_0)$  such that

$$P_{\text{FP}} = \int_{\gamma}^{\infty} P(\tilde{\mathbf{y}}; \mathcal{H}_0) d\tilde{\mathbf{y}} = \alpha, \quad (4.18)$$

where  $\alpha$  is the desired false positive detection rate given by the red colored areas shown in Figure 4.5. The true positive detection rate is given by the similar integral

$$P_{\text{TP}} = \int_{\gamma}^{\infty} P(\tilde{\mathbf{y}}; \mathcal{H}_1) d\tilde{\mathbf{y}}, \quad (4.19)$$

which corresponds to the green areas in Figure 4.5.

Changing the decision threshold allows one to trade-off between  $P_{\text{TP}}$  and  $P_{\text{FP}}$  as

appropriate for the given situation. It is common to summarize the relationship between  $P_{\text{TP}}$  and  $P_{\text{FP}}$  using the receiver operating characteristic (ROC) curve, which is obtained by evaluating the true positive and false positive probabilities as a function of the decision threshold value (see Figure 4.6). The ROC curve provides a convenient way to compare

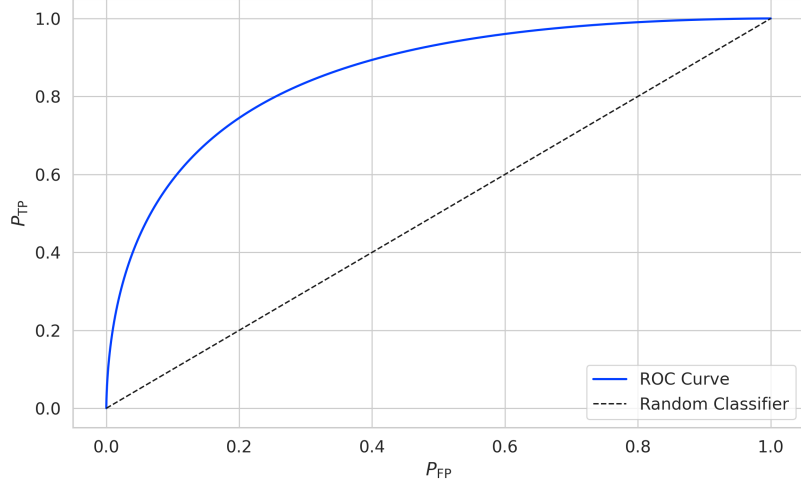


Figure 4.6: An example ROC curve formed by computing the  $P_{\text{FP}}$  and the  $P_{\text{TP}}$  for a given likelihood ratio test. As the decision threshold is increased  $P_{\text{FP}}$  decreases at the expense of a lower  $P_{\text{TP}}$ . The black dashed line indicates the lower bound ROC curve obtained by randomly deciding between  $\mathcal{H}_0$  and  $\mathcal{H}_1$ .

the performance of different signal detection algorithms. In general, a classifier with a higher the  $P_{\text{TP}}$  as a function of  $P_{\text{FP}}$  is desirable, which corresponds to a larger area underneath the respective ROC curve. A perfect classifier has an area underneath the curve of 1.0, however, such a classifier is almost never achievable in practice.

### 4.3.1 Digital Beamforming

#### Introduction to Beamforming

Beamforming refers to a suite of antenna array signal processing techniques that are designed to enhance the radiation or gain of the array in certain directions and suppress it in other direction [63]. Beamforming is of interest to Project 8 as a first level of signal reconstruction for the FSCD and other antenna array CRES experiments, which operates at the signal detection stage of reconstruction.

Beamforming is accomplished by performing a phased summation of the signals received by the antenna array. The beamforming phases are chosen such that the signals

1905 emitted by the array will constructively interfere at the point of interest (see Figure  
 1906 4.7). As a consequence of the principle of reciprocity [71], when the array is operating in  
 1907 receive mode, the signals emitted from a source at the same point will constructively  
 interfere when summed. The origin of the phase delays in beamforming is the path-

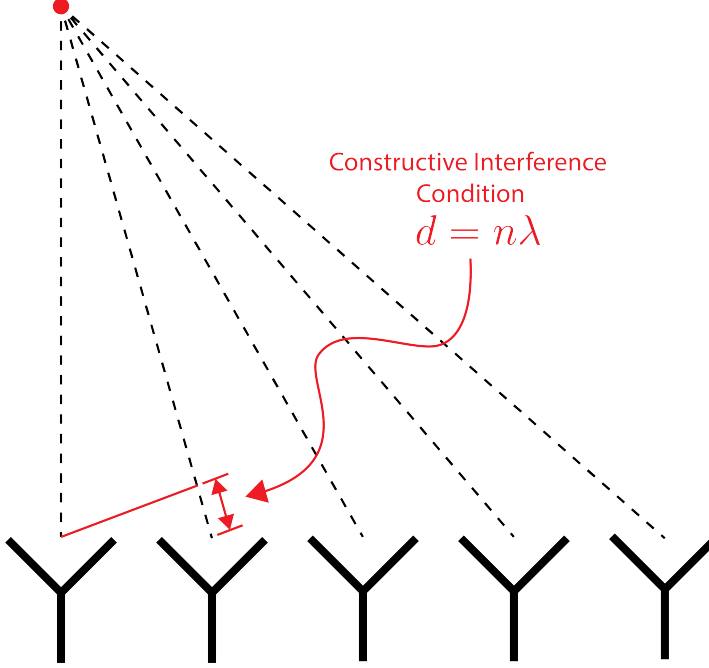


Figure 4.7: An illustration of the constructive interference condition which is the operating principle of digital beamforming using a uniform linear array as an example.

1908  
 1909 length difference to the beamforming point between different antennas in the array. The  
 1910 relationship between the phase delay and the path-length difference is given by the  
 1911 familiar equation

$$\phi = \frac{2\pi d}{\lambda}, \quad (4.20)$$

1912 where  $\phi$  is the phase delay,  $d$  is the path-length difference, and  $\lambda$  is the wavelength of  
 1913 the radiation. In practice, one chooses the values of  $d$  by specifying the beamforming  
 1914 positions of interest and then calculates the beamforming phases using Equation 4.20,  
 1915 which is guaranteed to follow the constructive interference condition shown in Figure 4.7.

1916 Beamforming can be neatly expressed mathematically using the vector equation

$$y[n] = \Phi^T[n] \mathbf{x}[n], \quad (4.21)$$

1917 where  $\mathbf{x}[n]$  is the array snapshot vector,  $\Phi[n]$  is a vector of beamforming shifts, and  
 1918  $y[n]$  is the resulting summed signal. The beamforming shifts consist of a set of complex

1919 numbers that contain the beamforming phase shift and an amplitude weighting factor,

$$\Phi[n] = [A_0[n]e^{-2\pi i \phi_0[n]}, A_1[n]e^{-2\pi i \phi_1[n]}, \dots, A_{N-1}[n]e^{-2\pi i \phi_{N-1}[n]}], \quad (4.22)$$

1920 where the set of magnitudes  $A_i[n]$  are amplitude weighting factors and  $\phi_i[n]$  are the phase  
1921 shifts from the path-length differences. The index  $i$  is used to denote the antenna channel  
1922 number. The amplitude weighting factor is the relative magnitude of the signal received  
1923 by a particular antenna to the other antennas in the array, such that the antennas that  
1924 receive signals with higher amplitude, due to being closer to the source, have more  
1925 weight in the beamforming summation. The input and outputs signals beamforming  
1926 are naturally expected to be functions of time as indicated by the index  $[n]$ , however, it  
1927 is also possible to use time dependent beamforming phases that shift the beamforming  
1928 position of the array over time.

1929 Digital beamforming is the type of beamforming algorithm of interest to Project 8 for  
1930 CRES. Specifically, digital beamforming means that the beamforming phases are applied  
1931 to the array signals in software rather than employing fixed beamforming phase shifts in  
1932 the receiver chain hardware. The advantage of digital beamforming is that for a given  
1933 series of array snapshots one can specify a large number of beamforming positions and  
1934 effectively search for electrons by performing the beamforming summation associated  
1935 with each point and applying a signal detection algorithm to identify the presence of a  
1936 CRES signal.

1937 One of the most attractive features of digital beamforming is the spatial filtering  
1938 effect, which is a direct consequence of the constructive interference condition used to  
1939 define the beamforming phases. Spatial filtering allows for signals from multiple electrons  
1940 at different positions in the trap to be effectively separated, because the constructive  
1941 interference condition will force the signals from electrons at positions different from the  
1942 beamforming position to cancel. This helps to reduce signal pile-up that could become  
1943 an issue for large scale CRES experiments using a dense tritium source.

1944 The digital beamforming positions can be specified with arbitrary densities limited  
1945 only by the available computational resources. This provides a very straight-forward way  
1946 to estimate the position of the electron in the trap by using a dense grid of beamforming  
1947 positions and maximizing the output power of the beamforming summation over this  
1948 grid. This natural approach to position reconstruction is attractive due the requirements  
1949 of an event-by-event signal reconstruction, which needs an accurate estimation of the  
1950 exact magnetic field experienced by the electron in order to correctly estimate it's kinetic

1951 energy. Combined with an accurate map of the magnetic field inhomogeneities of the  
1952 trap obtained from calibrations, beamforming allows one to apply this magnetic field  
1953 correction with a spatial resolution that is a fraction of the cyclotron wavelength.

1954 **Laboratory Beamforming Demonstrations**

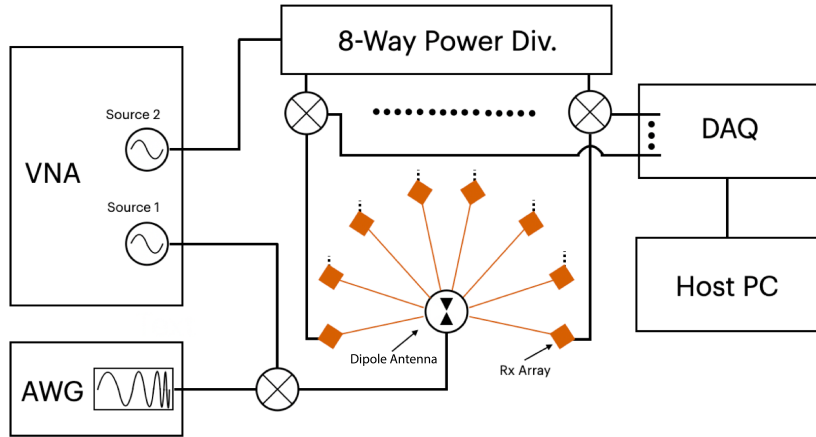


Figure 4.8: System level diagram of the laboratory setup used for beamforming demonstrations at Penn State. For more information on this system see Chapter 5. Signals near 26 GHz are fed to a dipole antenna using an arbitrary waveform generator (AWG) and vector network analyzer (VNA), which drive a mixer. The dipole radiation is collected by an array of antennas connected to the digitizer data acquisition (DAQ) system.

1955 As part of the development of antenna array CRES for the FSCD, an antenna  
1956 measurement setup was constructed at Penn State to serve as a testbed for antenna  
1957 prototypes and to perform laboratory validations of array simulations. This system  
1958 is discussed in more detail in Chapter 5. Early versions of the antenna measurement  
1959 system (see Figure 4.8 and Figure 4.9) were used to perform beamforming reconstruction  
1960 studies of a simple probe antenna to better understand the principles of beamforming  
1961 and confirm the estimated beamforming performance of Locust.

1962 Signals from an arbitrary waveform generator were up-converted to 26 GHz using a  
1963 mixer and a high-frequency source from a vector network analyzer and fed to the dipole  
1964 antenna through a balun. The radiation from the dipole antenna was received by an  
1965 array of horn antennas. The signals from the horn antennas were then down-converted  
1966 to baseband using a collection of mixers and an 8-way power divider. The signals were  
1967 then digitized and saved to a host computer for analysis.

1968 The data collected using the dipole and horn antenna array is reconstructed using the

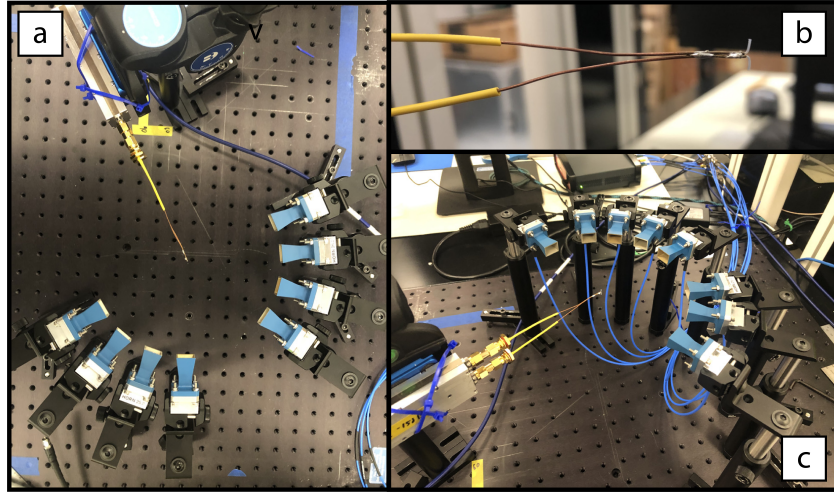


Figure 4.9: Photographs of the beamforming demonstration setup. In (a) I show a top-down view of the dipole antenna and the array of eight horn antennas. Manual repositioning of the horn antennas allows one to synthesize a full-circular antenna array. The dipole antenna is mounted on a camera tripod mount that allows for manual position tuning. (b) is a close up image of the dipole, which is manufactured from two segments of semi-rigid coaxial cable. (c) is another image of the dipole and array.

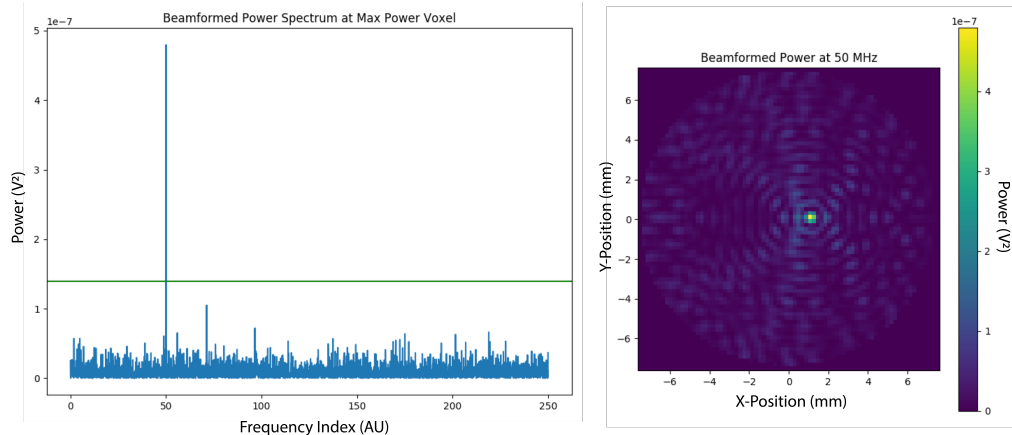


Figure 4.10: An example of digital beamforming reconstruction of a dipole antenna using a synthetic array of horn antennas. The beamforming image on the right is constructed by computing the time-averaged power of the summed signals for a two-dimensional grid of beamforming positions. In the image one can see a clear maximum that corresponds to the position of the dipole antenna. On the left I show the frequency spectrum of the time-series at the maximum power pixel. White gaussian noise is added to the signal to mimic a more realistic signal-to-noise-ratio. The signal emitted by the dipole is clearly visible as the high power peak in the frequency spectrum.

beamforming reconstruction approach specified in Section 4.3.1. A two-dimensional grid of xy-positions is defined and the beamforming phase shifts for each of these positions is calculated. The phased summation can be visualized by plotting the time-averaged power for each of the summations as a pixel in the resulting beamforming image (see Figure 4.10). White Gaussian noise (WGN) can be added to the data at this stage to simulate more realistic signal-to-noise ratios (SNR) if desired. The beamforming peak maxima is expected to have a Bessel function shape due to the circular symmetry of the array, and by analyzing the size of the beamforming maxima one can confirm that the beamforming reconstruction measurement has similar position resolution as expected from Locust simulations. Additionally, signal detection rates can be estimated from the data by comparing the magnitude of the beamforming signal peak in the frequency spectra to simulation.

## FSCD Beamforming Simulations

Using Locust simulations of the FSCD one can perform beamforming reconstruction studies using the simulated CRES signal data. As we mentioned in the previous section, the beamforming procedure beings by specifying a set of beamforming positions and corresponding beamforming shifts. The beamforming positions form a grid that covers the region of interest in the field of view of the antenna array. There are effectively an infinite number of ways to specify the grid positions, however, uniform square grids are the most commonly used due to their simplicity. In the FSCD experiment the number and pattern of the grid positions would be optimized to cover the most important regions of the trap volume to maximize detection efficiency while minimizing superfluous calculations.

The beamforming grids used for signal reconstruction with the FSCD consist of a set of points that cover a region of the two-dimensional plane formed by the perimeter of the antenna array. The axial dimension is left out of the beamforming grid because the electrons are assumed to occupy only an average axial position, which corresponds to the center of the magnetic trap. This is because it is impossible to resolve the axial position of the electron as a function of time due to the rapid axial oscillation frequencies of trapped electrons relative to the FSCD time-slice duration.

After beamforming, a summed time-series is obtained for each beamforming position that can be evaluated for the presence of a signal using a detection algorithm. A beamforming image is a visualization method that is equivalent to arranging the beamforming grid points according to their physical locations to form a three-dimensional matrix where the first two dimensions encode the XY-position of the beamforming point and

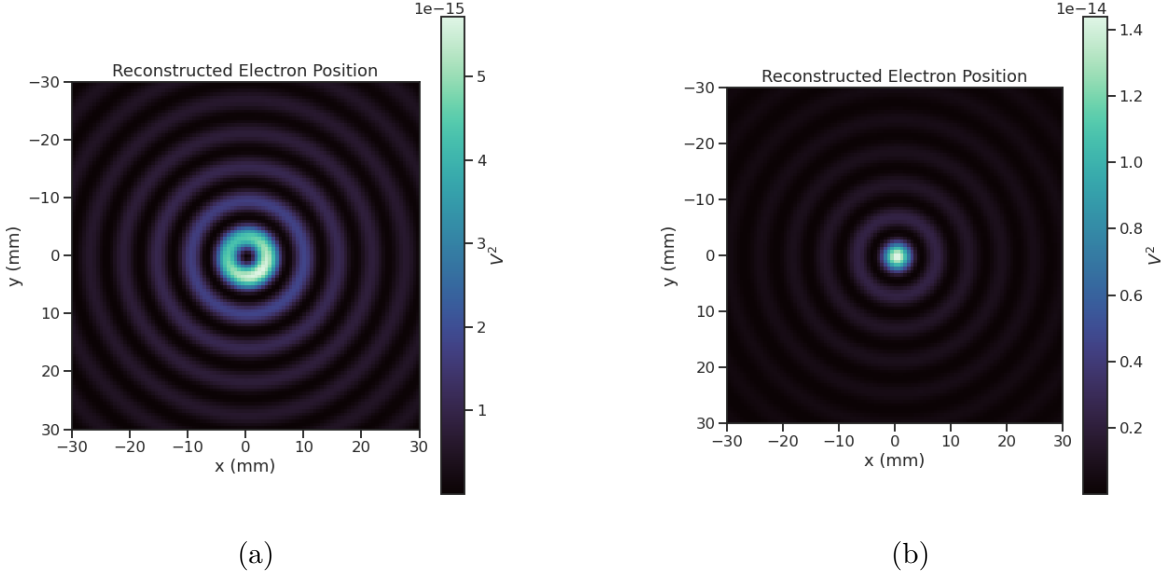


Figure 4.11: Beamforming images visualizing the reconstruction of an electron without (a) and with (b) the cyclotron phase correction. The images were generated using data from Locust simulations. The cyclotron phase refers to a phase offset equal to the relative azimuthal position of an antenna in the array. This phase offset is caused by the circular electron orbit and must be corrected for during reconstruction.

2003 the third dimension contains the summed time-series. The image is formed by taking the  
 2004 time-averaged power (see Figure 4.11). Beamforming images are purely for the purposes  
 2005 of visualization and are not particularly useful for signal detection or reconstruction.

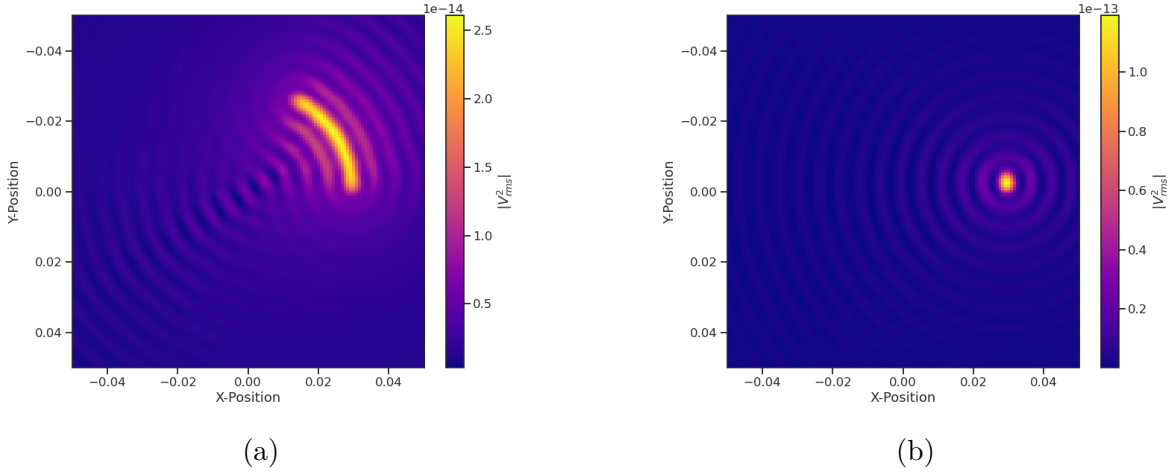
2006 If the beamforming phases consist only of the spatial phase component from Equation  
 2007 4.20, then the resulting beamforming image contains a relatively high-power ring-shaped  
 2008 region that is centered on the position of the electron (see Figure 4.11a). The origin  
 2009 of this shape is an additional phase offset particular to a cyclotron radiation source.  
 2010 Essentially, the circular motion that produces the cyclotron radiation introduces a relative  
 2011 phase offset to the electric fields that is equal to the azimuthal position of the field  
 2012 measurement point. For example, if we have two antennas, one located at an azimuthal  
 2013 position of  $0^\circ$  and another located at an azimuthal position of  $90^\circ$ , then the CRES signals  
 2014 received by these antennas will be out of phase by  $90^\circ$ , which is the difference in their  
 2015 azimuthal positions. This phase offset can be corrected by adding an additional term to  
 2016 the beamforming phase equation that is equal to the azimuthal position of the antenna  
 2017 relative to the electron,

$$\phi_i[n] = \frac{2\pi d_i[n]}{\lambda} + \Delta\varphi_i[n], \quad (4.23)$$

2018 where  $\Delta\varphi_i$  is difference between the azimuthal position of the electron and the  $i$ -th

2019 antenna channel. Using the updated beamforming phases in the summation changes the  
 2020 ring feature into a Bessel function peak whose maximum corresponds to the position of  
 2021 the electron. Including this cyclotron phase correction significantly improves the signal  
 2022 detection and reconstruction capabilities of beamforming by more than doubling the  
 2023 summed signal power and shrinking the beamforming maxima feature size.

2024 The beamforming image examples in Figure 4.11 were produced using an electron  
 2025 located on the central axis of the magnetic trap, which do not experience  $\nabla B$ -drift.  
 2026 However, for electrons produced at non-zero radial position the beamforming phases  
 2027 must be made time-dependent in order to track the position of the electron's guiding  
 2028 center over time. Without this correction the  $\nabla B$ -drift causes the electron to move  
 2029 between beamforming positions, which effectively spreads the cyclotron radiation power  
 over a wider area in the beamforming image (see Figure 4.12). This effect significantly



2030  
 2031 Figure 4.12: Beamforming images visualizing the reconstruction of an electron located  
 2032 off the central axis of the FSCD trap. In (a) we performing beamforming without the  
 $\nabla B$ -drift correction, and in (b) we include the  $\nabla B$ -drift correction.

2033 reduces the power of the beamforming maxima and increases the size of the beamforming  
 2034 features, simultaneously harming detection efficiency and position reconstruction.

2035 The  $\nabla B$ -drift correction simply adds a circular time-dependence to the beamforming  
 2036 positions as a function of time,

$$r[n] = r_0 \quad (4.24)$$

$$\varphi[n] = \varphi_0 + \omega_{\nabla B} t[n], \quad (4.25)$$

2037 where  $\omega_{\nabla B}$  is the drift frequency and  $t[n]$  is the time vector. In the ideal case the  $\nabla B$ -drift

2036 frequencies from Figure 4.2 for the correct pitch angle and radial position would be used,  
2037 however, it is not possible to know the electron’s pitch angle a priori. In principle, one  
2038 could perform multiple beamforming summations for a given beamforming position using  
2039 different drift frequencies and choose the one that maximizes the summed power, but  
2040 this approach leads to a huge computational burden that would be impractical for a  
2041 real FSCD experiment. A compromise is to use an average value of  $\omega_{\nabla B}$  obtained by  
2042 averaging over the drift frequencies for electrons of different pitch angle at a particular  
2043 radius. This approach keeps the computational cost of time-dependent beamforming to a  
2044 minimum while still providing a significant increase in the detection efficiency of digital  
2045 beamforming.

2046 **Signal Detection with Beamforming and a Power Threshold**

2047 Up to this point we have neglected any specific discussion of how digital beamforming is  
2048 used for signal detection and reconstruction. This is because, strictly speaking, digital  
2049 beamforming consists only of the phased summation of the array signals and cannot  
2050 be used alone for signal detection. The example beamforming images shown in Figure  
2051 4.11 and Figure 4.12 were produced using simulated data that contained no noise, which  
2052 significantly degrades the utility of analyzing the beamforming images for signal detection  
2053 and reconstruction.

2054 Digital beamforming as a detection algorithm is understood to mean digital beam-  
2055 forming plus a detection threshold placed on the amplitude of the frequency spectrum  
2056 obtained by applying a fast Fourier transform (FFT) to the summed time-series (see  
2057 Figure 4.13). This approach is most similar to the time-frequency spectrogram analysis  
2058 employed in previous CRES experiments, however, in principle any signal detection  
2059 algorithm could be used after the beamforming procedure. In Section 4.4 I analyze the  
2060 signal detection performance of the power threshold approach in detail.

2061 From the example frequency spectra in Figure 4.13 it is clear that without a re-  
2062 construction technique that coherently combines the signals from the full antenna our  
2063 ability to detect CRES signals will be drastically reduced. Because the CRES signals are  
2064 in-phase at the correct beamforming position the summed power increases as a function  
2065 of  $N^2$  compared to a single antenna channel, where  $N$  is the number of antennas. It  
2066 is true that the noise power is also increased by beamforming, but, because the noise  
2067 is incoherent, its power only increases linearly. Consequently, the signal-to-noise ratio  
2068 (SNR) of the CRES signal increases linearly with the number of antennas, which greatly  
2069 improves detection efficiency compared to using only the information in a single antenna.

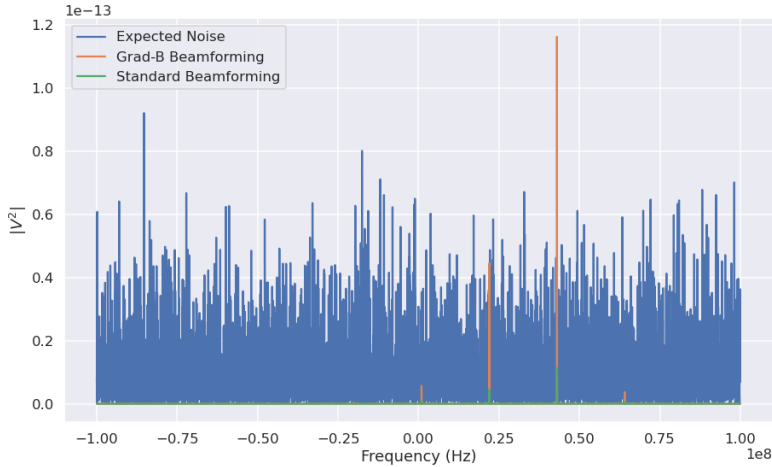


Figure 4.13: A plot of a typical frequency spectrum obtained by applying a Fourier transform to the time-series obtained from beamforming. The frequency spectra are plotted without noise on top of an example of a typical noise spectrum to visualize a realistic signal-to-noise ratio. In the example we see that without beamforming it would not be possible to detect anything since the signal amplitudes would be reduced by a factor of sixty relative to the noise. Additionally, we see that the  $\nabla B$ -drift correction is needed to detect this electron since it comes from a simulation of an electron with a significant off-axis position.

2070     The power threshold detection algorithm searches for high-power frequency bins that  
 2071     should correspond to a frequency component of the CRES signal. In order to prevent  
 2072     random noise fluctuations from being mistaken as CRES signals the power threshold  
 2073     must be set high enough so that it is unlikely that random noise could be responsible. A  
 2074     consequence of this is that many electrons that can be trapped will go undetected because  
 2075     the modulation caused by axial oscillations leads to the cyclotron carrier power to falling  
 2076     below the decision threshold. The time-dependent beamforming used to correct for the  
 2077      $\nabla B$ -drift increases the volume of the magnetic trap where electrons can be detected,  
 2078     but it is ineffective at increasing the range of detectable pitch angles (see Figure 4.14).  
 2079     Fundamentally, this is because the power threshold only uses a fraction of the signal  
 2080     power to detect electrons and ignores the power present in the frequency sidebands. In  
 2081     the subsequent sections I examine two other signal detection algorithms that seek to  
 2082     improve the detection efficiency of the FSCD by utilizing the more of the signal shape to  
 2083     compute the detection test statistics.

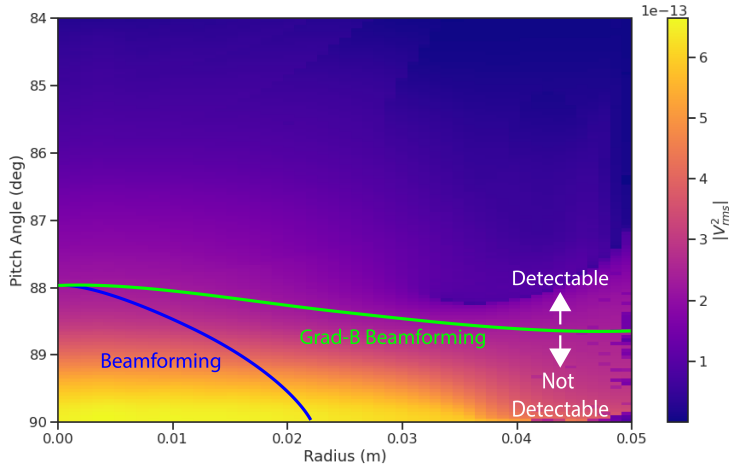


Figure 4.14: A plot of the total signal power received by the FSCD array from trapped electrons with different radial positions and pitch angles generated using Locust simulations. The lines on the plot indicate a 10 dB detection threshold above the mean value of the noise in the frequency spectrum. With static beamforming electrons with radial positions larger than about two centimeters are undetectable due to the change in the electron's position over time causing losses from beamforming phase mismatch. This is corrected by including  $\nabla B$ -drift frequencies in the beamforming phases. Both beamforming techniques fail to detect electrons below  $\approx 88.0^\circ$ , since these signal are composed of several relatively weak sidebands that are comparable to the noise.

### 2084 4.3.2 Matched Filtering

#### 2085 Introduction to Matched Filtering

2086 The problem of CRES signal detection is the problem of detecting a signal buried in  
 2087 WGN, which has been examined at great depth in the signal processing literature [69].  
 2088 For a fully known signal in WGN the optimal detector is the matched filter, which means  
 2089 that it achieves the highest true positive rate for a fixed rate of false positives. The  
 2090 matched filter test statistic is calculated by taking the inner product of the data with  
 2091 the matched filter template

$$\mathcal{T} = \left| \sum_n h^\dagger[n] y[n] \right|, \quad (4.26)$$

2092 where  $h[n]$  is the matched filter template and  $y[n]$  is the data. The matched filter test  
 2093 statistic defines a binary hypothesis test in which the data vector is assumed to be an  
 2094 instance of two possible data classes. By setting a decision threshold on the value of  $\mathcal{T}$ ,  
 2095 one can classify a given data vector as belonging to two distinct hypotheses. Under the  
 2096 first hypothesis the data is composed of pure WGN, and under the second hypothesis the

2097 data is composed of the known signal with additive WGN. The matched filter template  
 2098 is obtained by rescaling the known signal in the following way

$$h[n] = \frac{x[n]}{\sqrt{\tau \sum_n x^\dagger[n]x[n]}}, \quad (4.27)$$

2099 where  $\tau$  is the variance of the WGN and  $x[n]$  is the known signal. Strictly speaking,  
 2100 Equation 4.27 is only true for noise with a diagonal covariance matrix, however, in the  
 2101 context of the FSCD we are justified in assuming this to be true. Defining the matched  
 2102 filter templates in this way guarantees that the expectation value of  $\mathcal{T}$  is equal to one  
 2103 when the data contains only noise, which is the standard matched filter normalization in  
 2104 the signal processing literature.

2105 Although matched filters are canonically formulated in terms of a perfectly known  
 2106 signal, it is still possible to apply the matched filter technique given imperfect information  
 2107 about the signal provided that the signal is deterministic. From our discussion of CRES  
 2108 simulation tools for the FSCD (see Section 4.2) we know that the shape of CRES signals  
 2109 are completely determined by the initial parameters of the electron. The random collisions  
 2110 with background gas molecules which cause the formation of signal tracks are the only  
 2111 stochastic component of the CRES event after the initial beta-decay, therefore, it is  
 2112 possible to develop a matched filter for the detection of CRES signal tracks which are fully  
 2113 determined by the parameters of the electron after the initial beta-decay or subsequent  
 2114 collision events.

2115 The matched filter test statistic for CRES signals is a modified version of Equation  
 2116 4.26

$$\mathcal{T} = \max_{\mathbf{h}, m} |\mathbf{h} * \mathbf{y}| = \max_{\mathbf{h}, m} \left| \sum_k h^\dagger[k]x[m - k] \right|, \quad (4.28)$$

2117 where the matched filter inner product has been replaced with a convolution operation  
 2118 and a maximization over the template and convolution delay ( $m$ ). Replacing the inner  
 2119 product with a convolution accounts for the fact that the start time of the CRES signal is  
 2120 now an unknown parameter, in addition, we now perform a maximization of the matched  
 2121 filter convolution over a number of different templates. Because the shape of the signal is  
 2122 unknown we are forced to guess a number of different signal shapes to create a template  
 2123 bank with which we can identify unknown signals by performing an exhaustive search.

2124 The template bank approach to matched filtering, while quite powerful, can quickly  
 2125 become computationally intractable. This is especially true in the case of the FSCD  
 2126 because of the large amount of raw data produced by the array that must be analyzed.

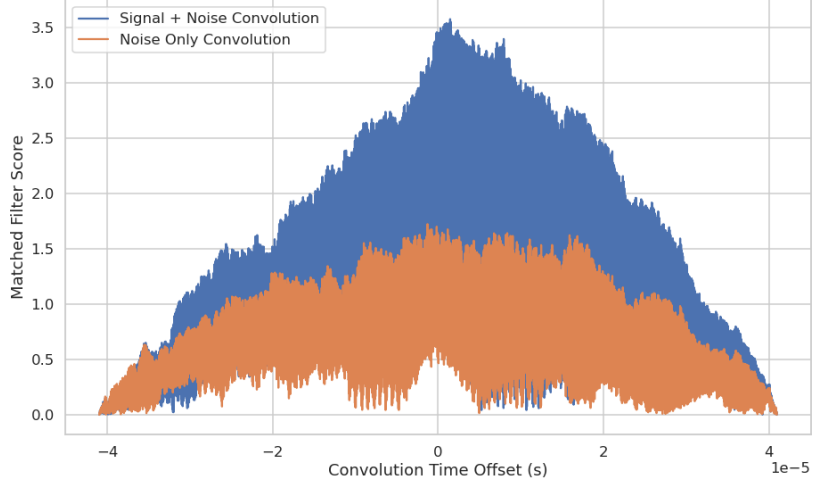


Figure 4.15: Example of a convolution of a CRES signal template with a segment of noisy data. A simulated CRES signal was simulated using Locust and normalized to create a matched filter template. When this template is convolved with noisy data the contains the matching signal the convolution output increases dramatically compared to data with only noise. The decreasing convolution output as the time offset of the convolution increases is caused by zero-padding of the data and template.

2127 Specifically, the time-domain convolution specified by Equation 4.28 is particularly  
 2128 computationally intensive and is a major barrier towards the implementation of a  
 2129 matched filter for signal detection in an experiment like the FSCD. This can be avoided  
 2130 by using the convolution theorem to replace the time-domain convolution with an inner  
 2131 product in the frequency domain.

2132 The convolution theorem states that

$$\mathbf{f} * \mathbf{g} = \mathcal{F}^{-1}(\mathbf{F} \cdot \mathbf{G}) \quad (4.29)$$

2133 where  $\mathbf{f}$  and  $\mathbf{g}$  are discretely sampled time-series,  $\mathbf{F}$  and  $\mathbf{G}$  are the respective discrete  
 2134 Fourier transforms, and  $\mathcal{F}^{-1}$  is the inverse discrete Fourier transform operator. The  
 2135 convolution theorem allows us to perform the matched filter convolution by first com-  
 2136 puting the Fourier transform of the template and data, then performing a point-wise  
 2137 multiplication of the two frequency series, and finally performing the inverse Fourier  
 2138 transform to obtain the convolution output. Because discrete Fourier transforms can be  
 2139 performed extremely efficiently, the convolution theorem is almost always used in lieu of  
 2140 directly computing the convolution.

2141 One thing to note here is that the convolution theorem for discrete sequences shown

here, is technically valid only for circular convolutions, which is not directly specified in Equation 4.28. However, because typical CRES track lengths are much longer than the Fourier analysis window and also that the frequency chirp rates are small compared to the time-slice duration, it is relatively safe to use circular convolutions to evaluate matched filter scores for CRES signals, which allows us to apply the convolution theorem to compute matched filter scores using the frequency representation of the data and matched filter template.

## Matched Filter Analysis of the FSCD

The optimality provided by the matched filter makes it a useful algorithm for analysis of CRES experiment designs for sensitivity analyses, since it indicates the best possible detection efficiency achievable by an experiment configuration. The standard approach to performing these studies involves generating a large number of simulated electron signals that span the kinematic parameter space of electrons in the magnetic trap. In general, electrons have six kinematic parameters along with an additional start time parameter.

In order to limit the number of simulations required to evaluate the detection efficiency the standard approach is to fix the starting axial position, starting azimuthal position, starting direction of the perpendicular component of the electron's momentum, and event start time to reduce the parameter space to starting radial position, starting kinetic energy, and starting pitch angle. The fixed variables are true nuisance parameters that do not affect the detection efficiency estimates for the FSCD design, because they manifest as phases which are marginalized during the calculation of the matched filter score.

Across radial position, kinetic energy, and pitch angle one defines a regular grid of parameters and uses Locust to simulate the corresponding signals (see Figure 4.16). This grid of simulated signals can be used to estimate the likelihood of detecting signals, because the matched filter score specifies the shape of the PDF that defines the detection probability and the size of the template bank influences the likelihood of a good match between a template and a random signal.

The matched filter approach can also be used to estimate the achievable energy resolution of the experiment by using a dense grid of templates generated with parameters close to the unknown signal (see figure 4.17). Because matched filter templates with similar parameters have signal shapes that are also similar, templates with incorrect parameters can have nearly identical matched filter scores as the correct template. Since only one sample of noise is included in a sample of real data, one cannot guarantee that the best matching template corresponds to the ground truth parameters of the signal.

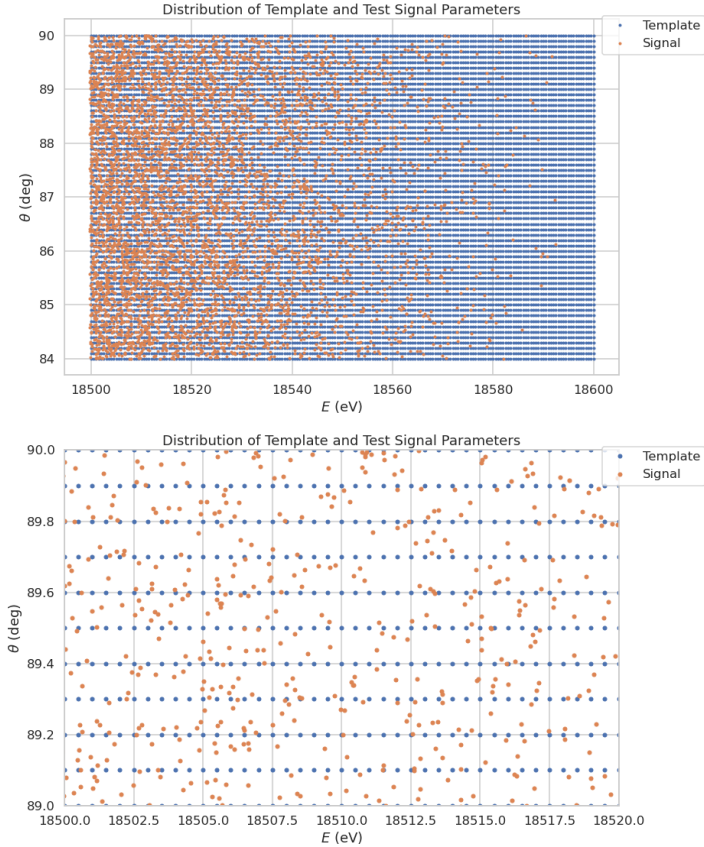


Figure 4.16: An example two-dimensional parameter distribution of a matched filter template bank and random test signals.  $\theta$  refers to the pitch angle of the electron and  $E$  is the kinetic energy. The template bank forms a regular grid of in pitch angle and energy, whereas, the test signals are uniformly distributed in pitch angle and follow the tritium beta-decay kinetic energy distribution. This is why there are fewer test signals at higher energies. The need for high match across the full parameter space prevents one from reducing the density of templates in this low activity region. A zoomed in version of the template bank illustrates the relative density of templates and signals needed for match  $> 90\%$ .

This introduces uncertainty into the signal parameter estimation that manifests as an energy broadening. Dense grids of matched filter templates allows one to quantify this broadening by analyzing the parameter space of templates with matched filter scores close to the ground truth. This approach is analogous to maximum likelihood estimation and is one key component of a complete sensitivity analysis for an antenna array CRES experiment.

A key parameter for describing the performance of a matched filter template bank at signal detection is match, which we define as the average ratio of the highest matched

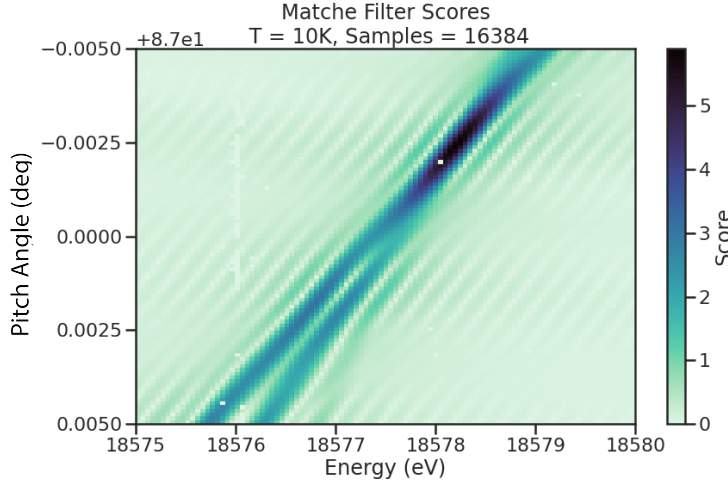


Figure 4.17: The matched filter scores of a dense grid of templates in pitch angle energy space. Dense template grids allow one to estimate the kinetic energy of the electron by identifying the best matching template. The uncertainty on this value is proportional to the space of templates that also match the test signal well. In the worst case matched filter templates can be completely degenerate where templates with different parameters match a signal with equal likelihood.

2184 filter score for a random signal to the matched filter score for a perfectly matching  
2185 template. In equation form this is

$$\text{Match} \equiv \Gamma = \frac{\mathcal{T}_{\text{best}}}{\mathcal{T}_{\text{ideal}}}, \quad (4.30)$$

2186 where  $\mathcal{T}_{\text{best}}$  is the matched filter score of the best fitting template in the bank and  $\mathcal{T}_{\text{ideal}}$  is  
2187 the hypothetical matched filter score one would measure if the signal perfectly matched  
2188 the template. Generally, one desires an average match as close to one as possible, however,  
2189 the average match value is an exponential function of the number of templates in the  
2190 template bank (see Figure 4.18). This behavior is observed for dense matched filter grids  
2191 like the one in Figure 4.17. A dense grid was used to calculate the average value of match  
2192 for different template bank sizes shown in Figure 4.18.

2193 The exponential relationship between match and template bank size is also evident  
2194 for template banks that cover a wide range of parameters, such as the template bank  
2195 visualized in Figure 4.16. Since no prior knowledge of the signal parameters is available,  
2196 one has no choice but to use a template bank that covers a large range of parameters for  
2197 signal detection. Achieving a high average match in this scenario can easily overwhelm  
2198 the available computational resources, so in practice only a limited number of templates

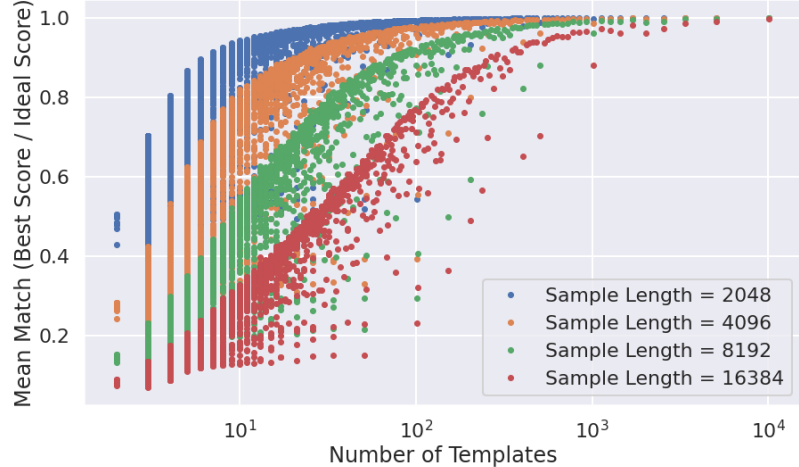


Figure 4.18: The mean match of the dense template grid shown in Figure 4.17 for different numbers of templates. Grids of different sizes were obtained by decimating a dense grid of templates and the average match for each grid was computed using the same set of randomly distributed test signals. Plotting the mean match against the size of the grid allows one to visualize the exponential relationship between match and template bank size. The noise in each curve is caused by sampling effects from the decimation algorithm. In general, longer templates are harder to than shorter templates.

2199 could be used at the detection stage. Therefore, accurately modeling the effects of match  
2200 is key to correct sensitivity calculations.

2201 The effect of match on the detection efficiency of the matched filter template bank can  
2202 be summarized using the ROC curve (see Figure 4.19). A single ROC curve is obtained  
2203 by averaging over the PDFs that describe the detection probabilities of each individual  
2204 template. The matched filter score for a template follows a Rician distribution with a  
2205 mean value equal to the matched filter score multiplied by the match ratio between the  
2206 template and signal. Therefore, the distribution that describes the average matched filter  
2207 score when there is a signal in the data is obtained by averaging over the distributions  
2208 for every template, whose expectation values are multiplied by the average match ratio.

2209 The distribution of the matched filter score when there is no signal in the data follows  
2210 a Rayleigh distribution. Therefore, a trials penalty, which is the statistical penalty one  
2211 pays for randomly checking many templates in order to avoid a random match between  
2212 noise and a template, is included by computing the joint distribution of  $N_{\text{template}}$  Rayleigh  
2213 distributions, where  $N_{\text{template}}$  is the size of the template bank. For more information on  
2214 the calculation of matched filter template bank ROC curves please refer to Section 4.4.

2215 An alternative way to visualize the detection performance for each algorithm is to

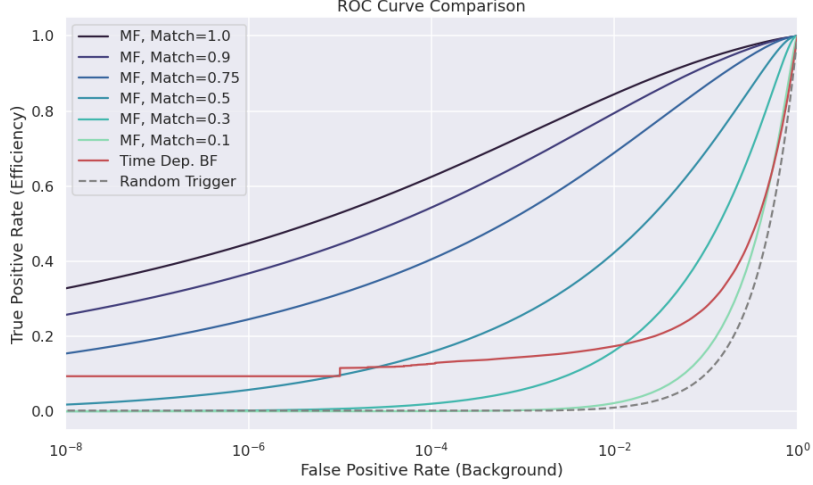


Figure 4.19: Matched filter template bank ROC curves as a function of mean match. One can see that for low match a matched filter is on average worse than the more straight forward beamforming detection approach.

2216 specify a minimum acceptable false positive rate at the trigger level. This is equivalent  
 2217 to specifying a minimum threshold on the value of the matched filter score or the size of  
 2218 a frequency peak for a beamforming power threshold trigger. One can then draw regions  
 2219 of detectable signals as a function of the electron's pitch angle and radial position (see  
 2220 Figure 4.20). A kinetic energy shift is equivalent to an overall frequency shift of the  
 2221 signal and should have no effect on the detection probability assuming sufficient density  
 2222 of matched filter templates in the energy dimension. A electron is declared "detectable"  
 2223 for the regions in Figure 4.20 if the signal has at least 50% probability of falling above the  
 2224 decision threshold of the respective classifier. One can see that the parameter space of  
 2225 detectable signals is greatly expanded beyond the beamforming power threshold trigger  
 2226 with a matched filter (MF) or deep neural network (DNN) (see Section 4.3.3). Plots such  
 2227 as Figure 4.20 are useful for visualization, but, since the handling of detection likelihood  
 2228 is not sufficiently rigorous, the detection probability boundaries are not well-suited to  
 2229 sensitivity estimates.

2230 **Optimized Matched Filtering Implementation for the FSCD**

2231 The biggest practical obstacle to the implementation of a matched filter template bank  
 2232 detection approach is oftentimes the computational cost associated with exhaustively  
 2233 calculating the matched filter scores of the template bank, and the FSCD is no exception  
 2234 in this regard. At a basic level computing a matched filter score requires the convolution

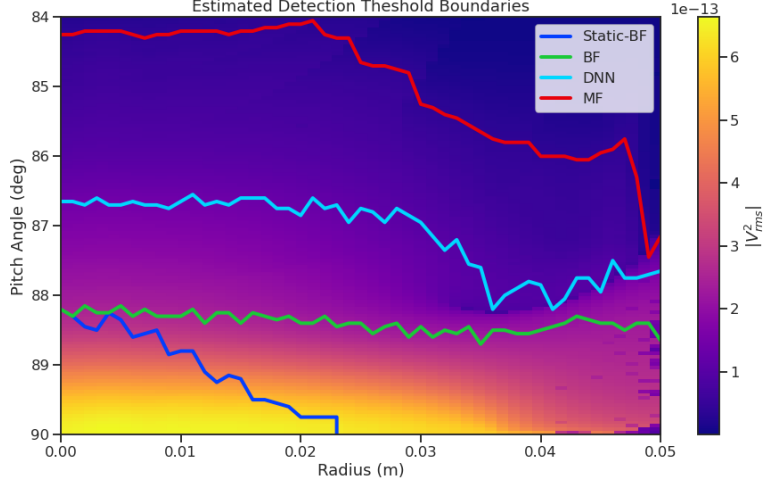


Figure 4.20: Boundaries of detectable electrons in pitch angle kinetic energy space for a series of different signal detection algorithms. A detectable signal is defined as a signal that is above a consistent decision with at least 50% probability. This non-rigorous treatment of detection probability is primarily useful for the visualization the relative increases in detection performance provided by the different algorithms. The static beamforming (Static-BF) algorithm is the digital beamforming algorithm introduced above without the  $\nabla B$ -drift correction. The DNN algorithm refers to a convolutional neural network classifier trained to detect CRES signals (see Section 4.3.3).

of two vectors, which can be performed very efficiently by computers if the convolution theorem and fast Fourier transforms (FFT) are utilized. Furthermore, one can consider applying digital beamforming as a pre-processing step to reduce the dimensionality of the data before the matched filter is applied. In order to understand the relative gain in computational efficiency offered by these optimizations we analyze the total number of floating-point operations (FLOP) of several matched filter implementations in big  $O$  notation that utilize different combinations of optimizations.

A direct implementation of a matched filter as specified by Equation 4.28 involves the convolution of  $N_{\text{ch}}$  signals of length  $N_s$  with template signals of length  $N_t$ . As a uniform metric we shall compare the FLOP of the various matched filter implementations on a per-template basis, since each implementation scales linearly with the number of templates. The direct convolution approach to matched filtering costs

$$O(N_{\text{ch}}) \times O(N_s \times N_t) \quad (4.31)$$

FLOP per-template, whose cost is dominated by the  $O(M \times N)$  convolution operation. The computational cost of the direct matched filter approach can be significantly

2249 reduced by exploiting the convolution theorem and FFT algorithms. If we restrict  
 2250 ourselves to signals and templates that contain equal numbers of samples then the  
 2251 convolution can be calculated by Fourier transforming both vectors, performing the  
 2252 point-wise multiplication, and then performing the inverse Fourier transform to obtain  
 2253 the convolution result. The FFT algorithm is able to compute the Fourier transform  
 2254 utilizing only  $O(N \log N)$  operations compared to  $O(N^2)$  for a naive Fourier transform  
 2255 implementation. This optimization results in a computational cost per-template of

$$O(N_{\text{ch}}) \times O(N_s \log N_s) \quad (4.32)$$

2256 A typical signal vector in the FSCD contains  $O(10^4)$  samples in which case the FFT  
 2257 reduces the computational cost of the matched filter by a factor of  $O(10^3)$ . This large  
 2258 reduction in computational cost implies that a direct implementation of a matched filter  
 2259 is completely infeasible in the FSCD due to resource constraints.

2260 Rather than relying solely on the matched filter it is tempting to consider using  
 2261 digital beamforming as an initial step in the signal reconstruction for the purposes of  
 2262 data reduction. The primary motivation is to reduce the dimensionality of the data by  
 2263 a factor of  $N_{\text{ch}}$  by combining the array outputs coherently into a single channel. One  
 2264 can view the beamforming operation as a partial matched filter, in the sense that the  
 2265 matched filter convolution contains the beamforming phased summation along with a  
 2266 prediction of the signal shape. By separating beamforming from the signal shape one  
 2267 hopes to reduce the overall computational cost by effectively shrinking the number of  
 2268 templates and reducing the number of operations required to check each one.

2269 The nature of this optimization requires that we account for the number of templates  
 2270 used for pure matched filtering versus the hybrid approach. To first order, the total  
 2271 number of templates at the trigger stage is a product of the number of guesses for each  
 2272 of the electron's parameters

$$N_T = N_E \times N_\theta \times N_r \times N_\varphi, \quad (4.33)$$

2273 where  $N_E$  is the number of kinetic energies,  $N_\theta$  is the number of pitch angles,  $N_r$  is the  
 2274 number of starting radial positions, and  $N_\varphi$  is the number of starting azimuthal positions.  
 2275 The starting axial position and cyclotron motion phase are not necessary to include in  
 2276 the template bank since these parameters manifest themselves as the starting phase of  
 2277 the signal, which is effectively marginalized when using a FFT to compute the matched  
 2278 filter convolution. Therefore, the total number of operations required by a matched filter

2279 to detect a signal in a segment of array data is on the order of

$$O(N_T) \times O(N_{ch}) \times O(N_s \log N_s) \quad (4.34)$$

2280 With the hybrid approach we attempt to remove the spatial parameters from the  
2281 template bank by using beamforming to combine the array signals into a single channel.  
2282 Beamforming explicitly assumes a starting position, which allows us to only use matched  
2283 filter templates that span the two-dimensional space of kinetic energy and pitch angle.  
2284 The total computational cost of the hybrid method is directly proportional to the number  
2285 of beamforming positions. For the time-dependent beamforming defined in Section 4.3.1,  
2286 the number of beamforming positions is given by

$$N_{BF} = N_r \times N_\varphi \times N_{\omega_{\nabla B}}, \quad (4.35)$$

2287 where  $N_r$  and  $N_\varphi$  are the same spatial parameters encountered in the pure matched  
2288 filter template bank and  $N_{\omega_{\nabla B}}$  is the number of  $\nabla B$ -drift frequency assumptions. If a  
2289 unique drift frequency is used for each pitch angle then the hybrid approach is effectively  
2290 equivalent to a pure matched filter in the number of operations. The key efficiency gain  
2291 of the hybrid approach is to exploit the relatively small differences in  $\omega_{\nabla B}$  for electrons  
2292 of different pitch angles by using only a small number of average drift frequencies.

2293 The total number of operations for the hybrid approach can be expressed as a sum of  
2294 the operations required by the beamforming and matched filtering steps,

$$O(N_{BF}) \times O(N_{ch} N_s) + O(N_{BF}) \times O(N_E N_\theta) \times O(N_s \log N_s). \quad (4.36)$$

2295 The first product in the sum is the number of operations required by beamforming,  
2296 which is simply the number of beamforming points times the computational cost of the  
2297 beamforming matrix multiplication, and the second product is the computational cost  
2298 of matched filtering the summed signal generated by each beamforming position. To  
2299 compare this to pure matched filtering we take the ratio of Equations 4.34 and 4.36 to  
2300 obtain

$$\Gamma_{BFMF} = \frac{O(N_{\omega_{\nabla B}})}{O(N_E N_\theta) \times O(\log N_s)} + \frac{O(N_{\omega_{\nabla B}})}{O(N_{ch})}. \quad (4.37)$$

2301 This expression can be simplified by observing that  $O(N_E N_\theta) \times O(\log N_s) \gg O(N_{ch})$ ,

2302 which means that the ratio of computational cost for the two methods can be reduced to

$$\Gamma_{\text{BFMF}} \approx \frac{O(N_{\omega_{\nabla B}})}{O(N_{\text{ch}})}. \quad (4.38)$$

2303 If we limit ourselves to a number of estimated drift frequencies of  $O(1)$  then we see that  
2304 the estimated computational cost reduction of the hybrid approach is of  $O(N_{\text{ch}})$ . This is  
2305 quite a large reduction considering that the FSCD antenna array contains sixty antennas  
2306 in the baseline design.

2307 The main drawback of the hybrid approach is that the limited number of allowed  
2308 drift frequency guesses can lead to detection efficiency loss due to phase mismatch. The  
2309 degree of phase error from an incorrect drift frequency is proportional to the length of  
2310 the array data vector used by the signal detection algorithm. For signals with lengths  
2311 equal to the baseline FSCD Fourier analysis window of 8192 samples, typical phase errors  
2312 from using an average versus the exact  $\nabla B$ -drift frequency are on the order of a few  
2313 percent in terms of the signal energy. This has a relatively small impact on the overall  
2314 detection efficiency, however, future experiments with antenna array CRES will want to  
2315 balance optimizations such as these during the design phase to keep experiment costs to  
2316 a minimum while still achieving scientific goals.

## 2317 Kinetic Energy and Pitch Angle Degeneracy

2318 More accurate modeling of a matched filter requires that we consider the effects of  
2319 mismatched signals and template, since this more accurately reflects the real-world usage  
2320 of a matched filter where many incorrect templates are convolved with the data until the  
2321 matching template is found. One way to study this is to use the grid of simulated signals  
2322 to compute the matched filter scores between mismatched signals and templates and  
2323 evaluate the matched filter scores under this scenario. What one finds when performing  
2324 this analysis is that templates for kinetic energies and pitch angles that do not match  
2325 the underlying signal can have matched filter scores that are indistinguishable from the  
2326 matched filter score of the correct template (see Figure 4.21 and Figure 4.21).

2327 This degeneracy in matched filter score is the result of correlations between the kinetic  
2328 energy of the electron and the pitch angle caused by changes in the average magnetic field  
2329 experienced by an electron for different pitch angles. While in principle helpful for the  
2330 purposes of signal detection these correlations are unacceptable since they greatly reduce  
2331 the energy resolution of the experiment by causing electrons with specific kinetic energy  
2332 to templates across a wide range of energies. It is important to emphasize that this

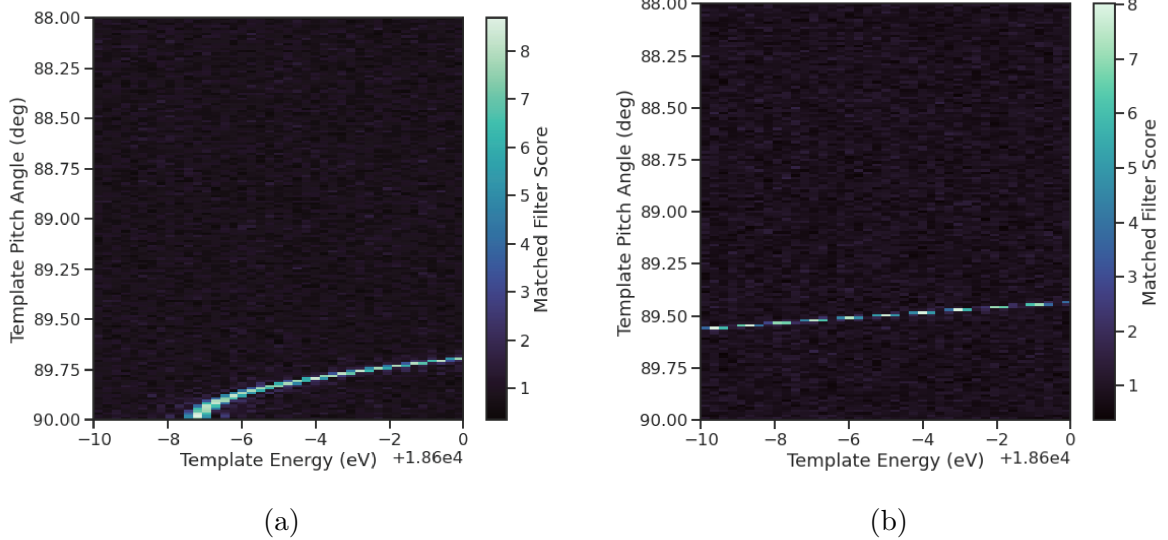


Figure 4.21: Two example illustrations of the correlation between kinetic energy and pitch angle imparted by the shape of the FSCD magnetic trap. The correlations manifest themselves as degeneracies in the matched filter score where multiple matched filter templates have the same matched filter for a particular signal. These degeneracies are a sign that the magnetic trap must be redesigned in order to break the correlation between pitch angle and kinetic energy.

2333 degeneracy cannot be fixed by implementing a different signal reconstruction algorithm.  
2334 As revealed by the matched filter scores the shapes of the signals for different parameters  
2335 are identical. Resolving this degeneracy between pitch angle and energy requires the  
2336 design of a new magnetic trap with steeper walls so that the average magnetic field  
2337 experienced by an electron is less dependent on pitch angle.

### 2338 4.3.3 Machine Learning

2339 Machine learning is a vast and rapidly developing field of research [72]. In this Section  
2340 we shall attempt to provided a brief introduction to some of the concepts and techniques  
2341 of machine learning that were applied to CRES signal detection rather than attempt a  
2342 comprehensive overview.

#### 2343 Introduction to Machine Learning

2344 Digitization of the FSCD antenna array generates large amounts of data that must be  
2345 rapidly processed to enable real-time signal detection and reconstruction. While digital  
2346 beamforming combined with a power threshold is relatively computationally inexpensive,

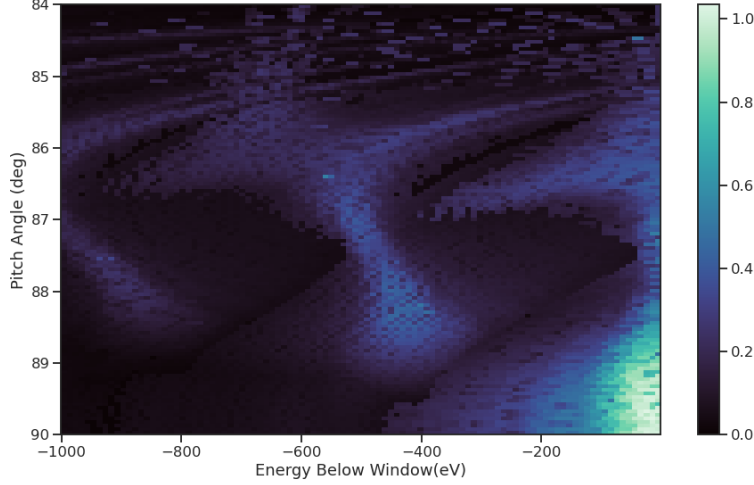


Figure 4.22: A visualization of the correlation between energy and pitch angle in the FSCD magnetic trap. The image is formed by computing the match of the best template from a grid consisting of pitch angles from 84 to 90 degrees in steps of 0.05 degrees, kinetic energies from 17574 to 18574 eV, located at 2 cm from the central axis, and simulated for a length of three FSCD time-slices. The signals used to compute the best matching template consisted of a grid from 84 to 90 degrees in steps of 0.05 degrees, kinetic energies from 18550 to 18575 eV in steps of 0.25 eV, located 2 cm from the central axis, and simulated for three FSCD time-slices. The colored regions of the plot show how well signals with lower energy can match those of higher energy for the FSCD magnetic trap, which is proportional to the achievable energy resolution of the FSCD design.

it is relatively ineffective at detecting CRES signal with small pitch angles, since it relies on a visible frequency peak above the noise. On the other hand, a matched filter is able to detect signals with a significantly larger range of parameters, however, the exhaustive search of matched filter templates can be computationally expensive. Machine learning based triggering algorithms have been used successfully in many different high-energy physics experiments [73] and recent developments have shown success in the detection of gravitational wave signals using machine learning techniques [74, 75] in place of the more traditional matched filtering method. This motivates the exploration of machine learning as a potential CRES signal detection algorithm.

There are several different approaches to machine learning, but the one most important to our discussion here is the supervised learning approach. In supervised machine learning one uses a differentiable model or function that is designed to map the input data to the appropriate label [72]. The data is represented as a multidimensional matrix of floating point values such as an image or a time-series, and the label is generally a class name such as signal or noise for classification problems or a continuous value like kinetic energy

2362 in the case of regression problems.

2363 In supervised learning the model is trained to map from the data to the correct label  
2364 by evaluating the output of the model using a training dataset consisting of a set of  
2365 paired data and labels. To evaluate the difference between the model output and the  
2366 correct label a loss function is used to quantify the error between the model prediction  
2367 and the ground truth. For example, a common loss function in regression problems is the  
2368 squared error loss function, which quantifies error using the squared difference between  
2369 the model output and label.

2370 Using the outputs of the loss function the next step in supervised learning is to  
2371 compute the gradient of error with respect to the model parameters in a process called  
2372 backpropagation. Using the model parameter gradients the last step in the supervised  
2373 learning process is to perform an update of the parameter values in order to minimize  
2374 the error in the model predictions across the whole dataset. This loop is performed many  
2375 times while randomly shuffling the dataset until the error converges to a minimum value  
2376 at which point the training procedure has finished. It is standard practice to monitor  
2377 the training procedure by evaluating the performance of the model using a separate  
2378 validation dataset that matches the statistical distribution of the training data and to  
2379 check the performance of the model after training using yet another dataset called the  
2380 test dataset. These practices help to guard against overtraining which is a concern for  
2381 models with many parameters.

## 2382 Convolutional Neural Networks

2383 A popular class of machine learning models are neural networks. A neural network is  
2384 essentially a function composed of a series of linear operations called layers which take a  
2385 piece of data typically represented as a matrix, multiplies the elements of the data by a  
2386 weight, and then sums these products to produce an output matrix. Neural networks  
2387 composed of purely linear operations are unable to model complex non-linear behavior,  
2388 therefore, non-linear activation functions are applied to the outputs of each of the layers  
2389 to increase the ability of the neural network to model complex relationships between the  
2390 data.

2391 Neural networks are typically composed of at least three layers, but with the present  
2392 capabilities of computer hardware they more often contain many more than this. The  
2393 first layer in a neural network is called the input layer, because it takes the data objects  
2394 as input, and the last layer in a neural network is known as the output layer. The  
2395 output layer is trained by machine learning to map the data to a desired output using

2396 the supervised learning procedure described in Section 4.3.3. In between the input and  
2397 the output layer are typically several hidden layers that receive inputs from and transmit  
2398 outputs to other layers in the neural network model. The term deep neural network  
2399 (DNN) refers to those neural networks that have at least one hidden layer, which have  
2400 proven to be extremely powerful tools for pattern recognition and function approximation.

2401 An important type of DNN are convolutional neural networks (CNN) that typically  
2402 contain several layers which perform a convolution of the input with a set of filters. These  
2403 convolution operations are typically accompanied by layers that attempt to down-sample  
2404 the data along with the standard neural network activation functions. A standard CNN  
2405 is composed of several convolutional layers at the beginning of the network and ends  
2406 with a series of fully-connected neural network layers at the output. Intuitively, one  
2407 can imagine that the convolutional layers are extracting features from the data that  
2408 fully-connected layers use to perform the classification or regression task.

2409 **Deep Filtering for Signal Detection in the FSCD**

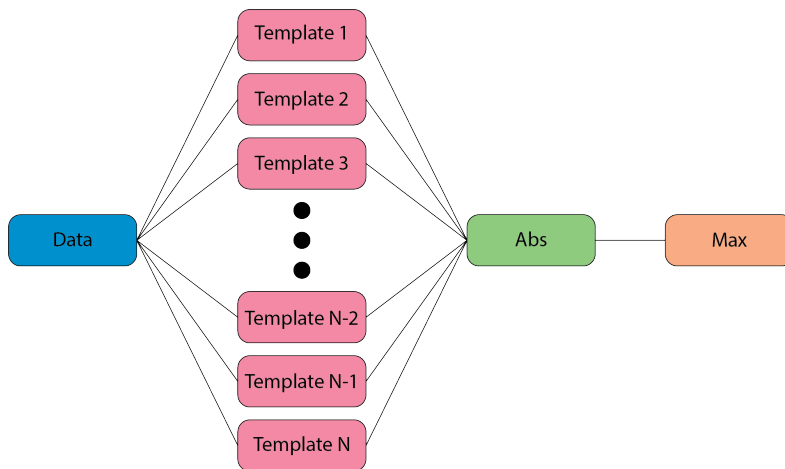


Figure 4.23: A representation of a matched filter template bank as a convolutional neural network. The network has a single layer composed of the templates, which act as convolutional filters. The activation of the neural network is an absolute value followed by a max operator.

2410 CNNs have been extremely influential in the field of computer vision, particularly tasks  
2411 such as image segmentation and classification, but have also been applied in numerous  
2412 experimental physics contexts. Given the particular challenge posed by signal detection  
2413 and reconstruction in the FSCD we are interested in exploring the potential of machine  
2414 learning as an effective algorithm for real-time signal detection, since this application

2415 requires both high efficiency and fast evaluation.

2416 In the machine learning paradigm signal detection is equivalent to a binary classifi-  
2417 cation problem between the signal and noise data classes, and my investigation focuses  
2418 specifically on the application of CNNs to signal detection in the FSCD, which is moti-  
2419 vated by relatively recent demonstrations of CNNs achieving classification accuracies for  
2420 gravitational wave time-series signals comparable to a matched filter template bank. In  
2421 this framework it is possible to interpret the matched filter as a type of CNN composed  
2422 of a single convolutional layer with the templates making up the layer filters (see Figure  
2423 4.23). Since this neural network has no hidden layers, it is not a DNN like we have  
2424 been discussing so far, but we can attempt to construct a proper CNN that attempts to  
2425 reproduce the classification performance of the matched filter network.

2426 The name deep filtering refers to this scheme of replacing a matched filter template  
2427 bank with a DNN. The reason why one might want to do this is that it may be possible to  
2428 exploit redundancies and correlations between templates that may allow one to perform  
2429 signal detection with similar accuracy but with fewer computations, which is important  
2430 for real-time detection scenarios like the FSCD experiment. In Section 4.4 we perform a  
2431 detailed comparison of the signal detection performance of a CNN to beamforming and a  
2432 matched filter template bank.

2433 Deep filtering is conceptually a simple technique. Similar to a matched filter template  
2434 bank a large number of simulated CRES signals are generated and used to train a model  
2435 to distinguish between signal and noise data (see Figure 4.24). In order to reduce the  
2436 dimensionality of the input FSCD data a digital beamforming summation is applied  
2437 to the raw time-series data generated by Locust to compress the 60-channel data to a  
2438 single time-series. CRES signal have a sparse frequency representation and experiments  
2439 training CNN's on time-series and frequency series data found that models trained on  
2440 frequency spectrum data performed significantly better, therefore, an FFT is applied to  
2441 the summed time-series before being normalized and fed to the classification model.

2442 The data used to train the model consists of an equal proportion of signal and noise  
2443 frequency spectra. Unique samples of WGN are generated and added to the signals during  
2444 training time to avoid have to pre-generate and store large samples of noise data. The  
2445 binary cross-entropy loss function combined with the ADAM optimizer proved effective  
2446 at training the models to classify CRES data. A simple hyperparameter optimization  
2447 was performed by manually tuning model, loss function, and optimizer parameters. The  
2448 model and training loops was implemented in python using the PyTorch deep learning  
2449 framework. Standard machine learning best practices were followed when training the

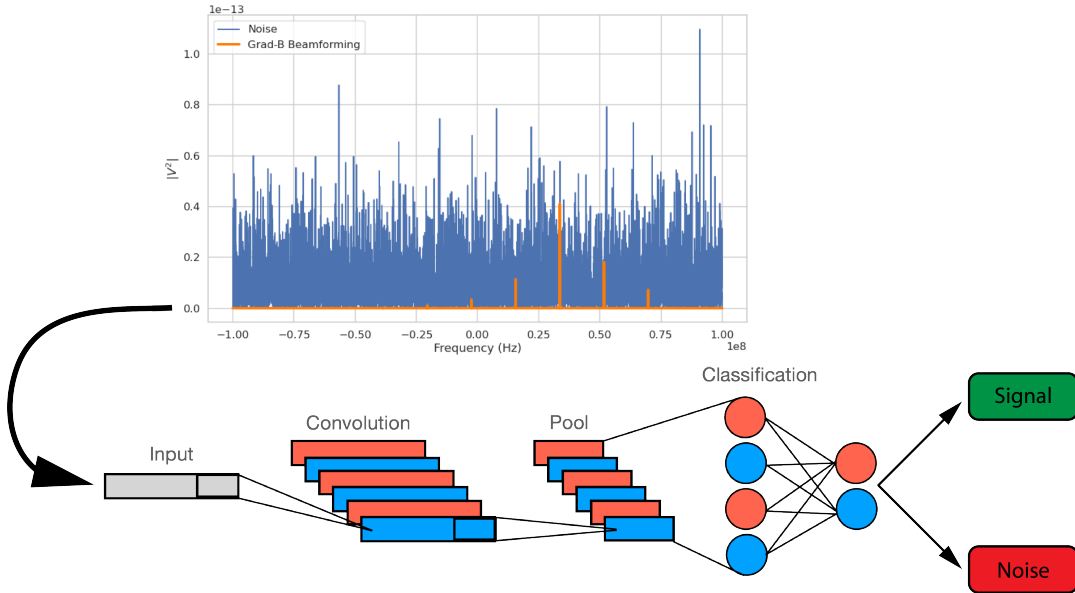


Figure 4.24: A graphical depiction of CRES signal detection using a CNN. A noisy segment of data is converted to a frequency series using digital beamforming and a FFT. The complex-valued frequency series is input into a trained CNN model that classifies the data as signal or noise using a decision threshold on the CNN output.

models, such as overtraining monitoring using a validation dataset. Models were trained until the training loss and accuracy converged and then evaluated using a separate test data set.

The classification results of the test dataset are used to quantify the relationship between the true positive rate and the false positive rate for the model. The true positive rate is analogous to detection efficiency and the false positive rate is a potential source of background in the detector. One can limit the rate of false positives using a sufficiently high threshold on the model output at the cost of a lower detection efficiency (see Figure 4.25 and Figure 4.26). As expected, the performance of the model at signal classification is negatively effected the noise power, which is quantified by the noise temperature.

## 4.4 Analysis of Signal Detection Algorithms for the Antenna Array Demonstrator

This section contains an early version of the manuscript for the triggering paper prepared for publication in JINST. In it I present a relatively detailed analysis of the signal detection performance of the three signal detection approaches discussed so far using a

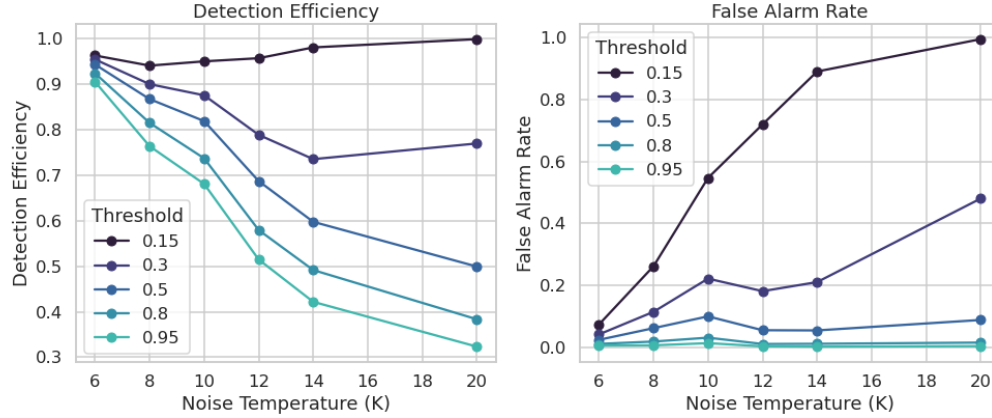


Figure 4.25: The detection efficiency and false alarm rate (false positive rate) as a function of the decision threshold for different values of the noise temperature. The model is trained to output a value close to one for data that contains a signal and outputs a value near zero when the data contains only noise. One sees that a lower decision threshold will have a high detection efficiency at the cost of a high rate of false alarms.

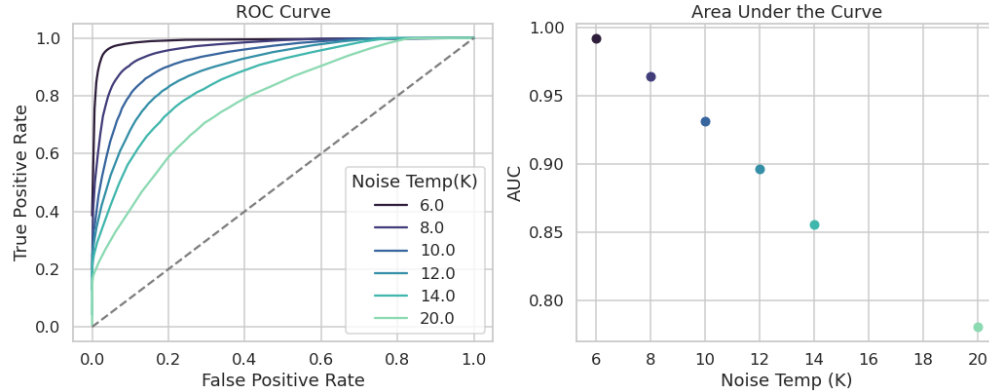


Figure 4.26: ROC curves for a CNN model classifying CRES signals. One can see that the area under the curve, which is a figure of merit that describes the performance of the classifier, is roughly linearly dependent with the noise temperature.

2465 population of simulated CRES signals generated with Locust. The focus of the paper is  
 2466 on the performance of the signal detection algorithms for pitch angles below  $88.5^\circ$  where  
 2467 the beamforming power threshold begins to fail.

#### 2468 4.4.1 Introduction

2469 Cyclotron Radiation Emission Spectroscopy (CRES) is a technique for measuring the  
 2470 kinetic energies of charged particles by observing the frequency of the cyclotron radiation

2471 that is emitted as they travel through a magnetic field [38]. The Project 8 Collaboration  
2472 is developing the CRES technique as a next-generation approach to tritium beta-decay  
2473 endpoint spectroscopy for neutrino mass measurement. Recently, Project 8 has used  
2474 CRES to perform the first ever tritium beta-decay energy spectrum and neutrino mass  
2475 measurement [40, 41].

2476 Previous CRES measurements have utilized relatively small volumes of gas that are  
2477 directly integrated with a waveguide transmission line, which transmits the cyclotron  
2478 radiation emitted by the trapped electrons to a cryogenic amplifier. While this technology  
2479 has had demonstrable success, it is not a feasible option for scaling up to significantly  
2480 larger measurement volumes. In particular, the goal of the Project 8 Collaboration  
2481 is to use CRES combined with atomic tritium to measure the neutrino mass with a  
2482 40 meV sensitivity. Achieving this sensitivity goal will require a multi-cubic-meter scale  
2483 measurement volume in order to obtain the required event statistics in the tritium  
2484 beta-spectrum endpoint region; hence, there is a need for new techniques to enable large  
2485 volume CRES measurements for future experiments.

2486 One approach is to surround a large volume with an array of antennas that together  
2487 collect the cyclotron radiation emitted by trapped electrons [39, 76]. A promising  
2488 array design is an inward-facing uniform cylindrical array that surrounds the tritium  
2489 containment volume. Increasing the size of the antenna array, by adding additional  
2490 rings of antennas along vertical axis, allows one to grow the experimental volume until a  
2491 sufficient amount of tritium gas can be observed by the array. A challenging aspect of  
2492 this approach is that the total radiated power emitted by an electron near the tritium  
2493 spectrum endpoint is on the order of 1 fW or less, which is then distributed between  
2494 all the antennas in the array. Consequently, detecting the presence of a CRES signal  
2495 and determining the electron’s kinetic energy requires reconstructing the entire antenna  
2496 array output over the course of the CRES event, posing a significant data acquisition  
2497 and signal reconstruction challenge.

2498 Project 8 has developed a triggering system to enable real-time identification of CRES  
2499 events using an antenna array [77]. Previous measurements with the CRES technique  
2500 have utilized a threshold on the frequency spectrum formed from a segment of CRES  
2501 time-series data. This algorithm relies on the detection of a frequency peak above the  
2502 thermal noise background, which limits the kinematic parameter space of detectable  
2503 electrons. Due to the limitations of this power threshold, Project 8 has been investigating  
2504 alternative signal identification approaches, including both matched filtering and machine  
2505 learning based classifiers, to improve the detection efficiency of the experiment. In

order to evaluate the relative gains in detection efficiency that come from utilizing these alternative algorithms, we develop analytical models for the power threshold and matched filter signal classifier performance applicable to an antenna array based CRES detector. In addition, we implement and test a basic convolutional neural network (CNN) as a first step towards the development of neural-network based classifiers for CRES measurements. These results allow us to compare the estimated detection efficiencies of each of these methods, which we weigh against the associated computational costs for real-time applications.

The outline of this paper is as follows. In Section 4.4.2 we give an overview of a prototypical antenna array CRES experiment, and describe the major steps involved in the proposed approach to real-time signal identification. In Section 4.4.3 we develop models for the power threshold and matched filter algorithms, and introduce the machine learning approach and CNN architecture. In Section 4.4.4 we describe our process for generating simulated CRES signal data and the details of training the CNN. Finally, in Section 4.4.5 we perform a comparison of the signal classification accuracy of the three approaches and discuss the relevant trade-offs in terms of detection efficiency and computational cost.

## 4.4.2 Signal Detection with Antenna Array CRES

### 4.4.2.1 Antenna Array and DAQ System

In order to explore the potential of antenna array CRES for neutrino mass measurement, the Project 8 Collaboration has developed a conceptual design for a prototype antenna array CRES experiment [39, 76], called the Free-space CRES Demonstrator or FSCD, which could be used as a demonstration of the antenna array measurement technique (see Figure 4.27). The FSCD utilizes a single ring of antennas, which is the simplest form of a uniform cylindrical array configuration, to surround a radio-frequency (RF) transparent tritium gas vessel. A prototype version of this antenna array has been built and tested by the Project 8 collaboration to validate simulations of the array radiation pattern and beamforming algorithms [42]. In the FSCD the antenna array is positioned at the center of the magnetic trap formed by a set of electro-magnetic coils that are designed to produce a magnetic trap with flat central region and steep walls both radially and axially.

When a beta-decay electron is trapped its motion consists of three primary components. The component with the highest frequency is the cyclotron orbit whose frequency is

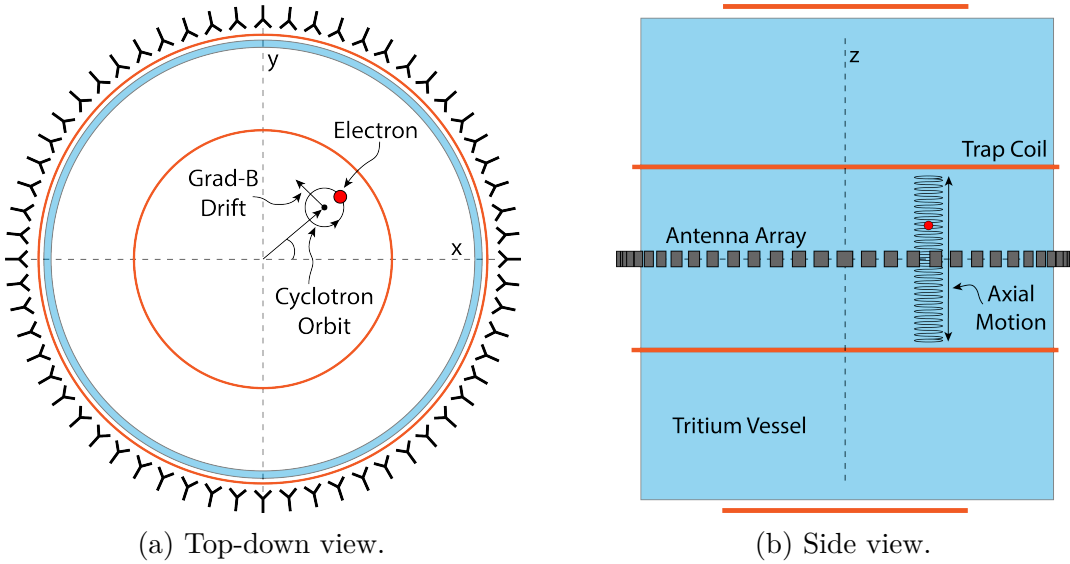


Figure 4.27: An illustration of the conceptual design for an antenna array CRES tritium beta-decay spectrum measurement. The antenna array geometry consists of a 20 cm interior diameter with 60 independent antenna channels arranged evenly around the circumference. The nominal antenna design is sensitive to radiation in the frequency range of 25-26 GHz, which corresponds to the cyclotron frequency of electrons emitted near the tritium beta-spectrum endpoint in a 1 T magnetic field. The array is located at the center of the magnetic trap produced by a set of current-carrying coils. The nominal magnetic trap design is capable of trapping electrons up to 5 cm away from the central axis of the array and traps electrons within an approximately 6 cm long axial region centered on the antenna array.

2539 determined by the size of the background magnetic field. The FSCD design assumes  
 2540 a background magnetic field value of approximately 0.96 T, which results in cyclotron  
 2541 frequencies for electrons with kinetic energies near the tritium beta-spectrum endpoint  
 2542 from 25 to 26 GHz. The component with the next highest frequency is the axial oscillation  
 2543 experienced by electrons with pitch angles of less than  $90^\circ$  [59]. The flat region of the  
 2544 FSCD magnetic trap extends approximately 3 cm above and below the antenna array  
 2545 plane causing electrons to move back and forth as they are reflected from the trap walls.  
 2546 Typical oscillation frequencies are on the order of 10's of MHz, which results in an  
 2547 oscillation period that is  $O(10^3)$  smaller than the duration of a typical CRES event.  
 2548 Therefore, when reconstructing CRES events we treat the electron as occupying only an  
 2549 average axial position at the center of the magnetic trap, since we are not able to resolve  
 2550 the axial position as a function of time. The component of motion with the smallest  
 2551 frequency is  $\nabla B$ -drift caused by radial field gradients in the trap, producing an orbit of  
 2552 the electron around the central axis of the trap with a frequency on the order of a few

2553 kHz, dependent on the pitch angle and the radial position of the electron.

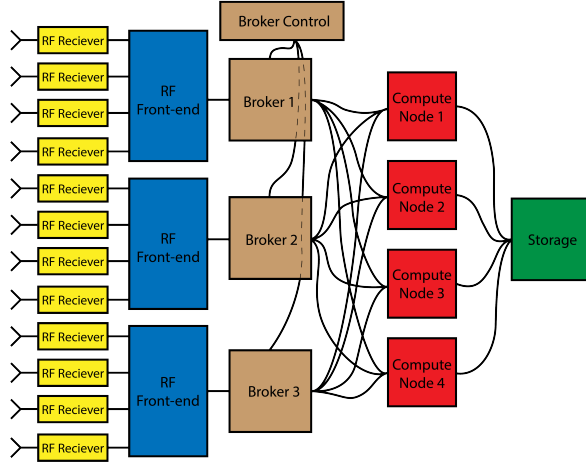


Figure 4.28: A high-level diagram of the DAQ system archctecture envisioned for the FSCD.

2554 The data acquisition (DAQ) system digitizes the signals from the antenna array and  
2555 combines thee data streams into a time-ordered matrix of array snapshots that can be  
2556 used by the reconstruction algorithms. The FSCD DAQ system design [77] is divided into  
2557 three layers 4.28. The first layer is the RF front-end, which includes the antenna array,  
2558 the RF receiver boards, and the digitization electronics. The receiver board contains an  
2559 amplifier, RF mixer, and bandpass filter to enable down-conversion, and is followed by  
2560 the digitization electronics that sample the CRES signals at 200 MHz. In order to achieve  
2561 an adequate signal-to-noise ratio to detect CRES events, the DAQ system for the antenna  
2562 array demonstrator must have a total system noise temperature of  $\approx 10$  K, which we  
2563 can achieve by using low-noise amplifiers and operating at cryogenic temperatures. After  
2564 digitization, the array data must be reorganized from individual data streams sorted  
2565 by channel into array snapshots sorted by time. In order to solve this data transfer  
2566 and networking problem the second layer of the DAQ system consists of a set of broker  
2567 computer nodes that reorganize the array data into time-ordered chunks. This approach  
2568 allows us accommodate different data transfer requirements by scaling the number of  
2569 broker nodes in this layer accordingly. Next, the broker layer distributes these chunks  
2570 of array data to the final layer of the DAQ system, which consists of a set of identical  
2571 reconstruction nodes that perform the calculations required for CRES reconstruction.  
2572 Similar to the broker layer, the number of reconstruction nodes can be increased or  
2573 decreased depending on the amount of computer power required for real-time CRES  
2574 reconstruction.

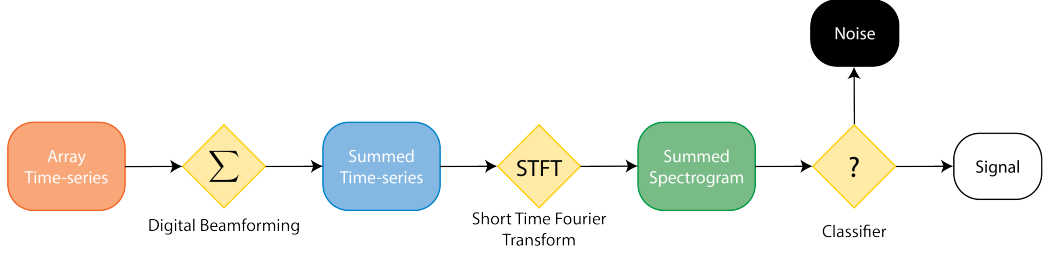


Figure 4.29: A block diagram illustration of the real-time triggering algorithm proposed for antenna array CRES reconstruction.

The design of the FSCD DAQ system is intended to enable a significant portion of the CRES event reconstruction to occur in real-time. The motivation for this comes from the fact that the FSCD antenna array generates approximately 1 exabyte of raw data per year of operation. Therefore, in order to reduce the data-storage requirements, it is ideal to perform at least some of the CRES event reconstruction in real-time so that it is possible to save a reduced form of the data for offline analysis. The first step of the real-time reconstruction would be a real-time signal detection algorithm, which is the focus of this paper. Our approach consists of three main operations performed on the time-series data blocks including digital beamforming, a short time Fourier transform (STFT), and a binary classification algorithm to distinguish between signal and noise data (see Figure 4.29).

#### 4.4.2.2 Real-time Signal Detection

The first step in the real-time detection algorithm is digital beamforming, which is a phased summation of the signals received by individual antennas in the array (see Figure 5.21). The phase shifts correspond to the path length differences between a spatial position and each individual antenna such that, when there is an electron located at the beamforming position, all the signals received by the array constructively interfere. Since we do not know ahead of time where an electron will be produced in the detector, we define a grid of beamforming positions that cover the entire region where electrons can be trapped and perform a phased summation for each of these points for every time-step in the array data block. As we saw in Section 4.4.2.1, the axial oscillation of the electrons prevents us from resolving its position along the Z-axis of the trap, therefore our beamforming grid need only cover the possible positions of the electron in the two-dimensional plane defined by the antenna array.

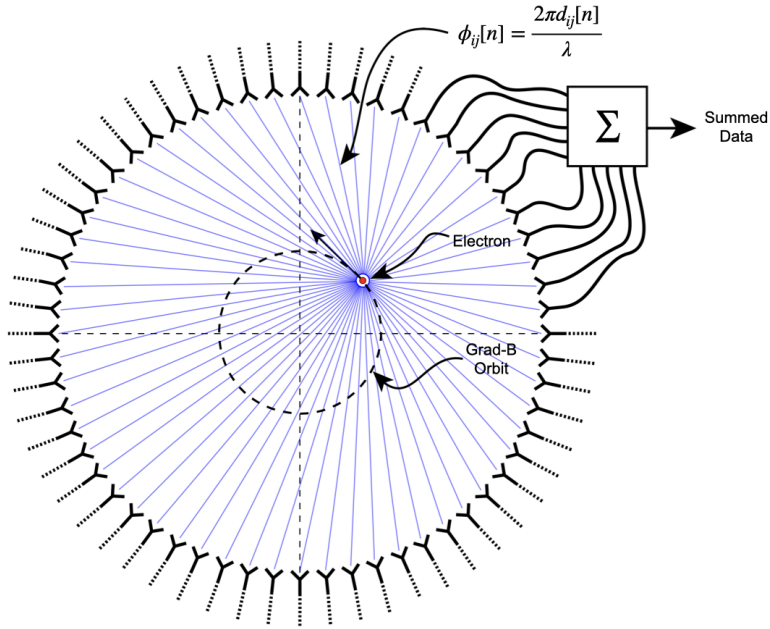


Figure 4.30: An illustration of the digital beamforming procedure. The blue lines indicate the various distances from the beamforming position to the antenna. In the situation depicted the actual position of the electron matches the beamforming position, so we should expect constructive interference when the phase shifted signals are summed. To prevent the electron's  $\nabla B$ -motion from moving the electron off of the beamforming position, the beamforming phase include a time-dependence to follow the trajectory of the electron in the magnetic trap.

2599

The equation defining digital beamforming can be expressed as

$$\mathbf{y}[n] = \Phi^T[n]\mathbf{x}[n], \quad (4.39)$$

2600 where  $\mathbf{x}[n]$  is array snapshot vector at the sampled time  $n$ ,  $\Phi[n]$  is the matrix of  
 2601 beamforming phase shifts, and  $\mathbf{y}[n]$  is summed output vector that contains the voltages  
 2602 for each of the summed channels that correspond to a particular beamforming position.  
 2603 The elements of the beamforming phase shift matrix can be expressed as a weighted  
 2604 complex exponential

$$\Phi_{ij}[n] = A_{ij}[n] \exp(2\pi i \phi_{ij}[n]), \quad (4.40)$$

2605 where the indices  $i$  and  $j$  label the beamforming and antenna positions respectively. The  
 2606 weight  $A_{ij}$  accounts for the relative power increase for antennas that are closer to the  
 2607 position of the electron, and  $\phi_{ij}$  is the total beamforming phase shift for the  $j$ -th antenna  
 2608 at the  $i$ -th beamforming position.

2609 The beamforming phase shift is a sum of two terms

$$\phi_{ij}[n] = \frac{2\pi d_{ij}[n]}{\lambda} + \theta_{ij}[n], \quad (4.41)$$

2610 where the first term is the phase shift originating from the path length difference ( $d_{ij}[n]$ )  
2611 between the beamforming and antenna positions, which are represented by the vectors  
2612  $(r_j, \theta_j)$  and  $(r_i, \theta_i[n])$ , and the second term is the angular separation ( $\theta_{ij}[n]$ ) of the two  
2613 positions. The angular separation enters into the beamforming phase due to an effect  
2614 caused by the circular orbit of the electron that produces radiation whose phase is linearly  
2615 dependent on the relative azimuthal position of the antenna [78,79]. The time-dependence  
2616 of the beamforming phases is intended to correct for the effects of  $\nabla B$ -drift, which cause  
2617 the guiding centers of electrons to orbit the center of the magnetic trap. By including a  
2618 linear time-dependence in the azimuthal beamforming position,

$$\theta_i[n] = \omega_{\nabla B} t[n] + \theta_{i,0}, \quad (4.42)$$

2619 where  $\omega_{\nabla B}$  is the azimuthal grad-B drift frequency,  $t[n]$  is the time vector and,  $\theta_{i,0}$  is the  
2620 starting azimuthal position, we can configure the beamforming phases to effectively track  
2621 the XY-position of the guiding center over the event duration. Predicting accurate values  
2622 of  $\omega_{\nabla B}$  for a specific trap and set of kinematic parameters will be done by simulations,  
2623 which are performed using the Kassiopeia software package [58] by Project 8.

2624 After digital beamforming, we apply a short-time Fourier transform (STFT) to the  
2625 summed time-series to obtain the frequency spectrum representation of the signals (see  
2626 Figure 4.31). From the detection perspective, the frequency representation of the CRES  
2627 data is advantageous compared to the time domain, because the frequency spectra of  
2628 CRES signals are well-approximated by a frequency and amplitude modulated sinusoidal  
2629 whose carrier frequency increases as a linear chirp. The modulation is caused by the axial  
2630 oscillation of the electron in the magnetic trap and produce frequency spectra that are  
2631 well-described by a small number of frequency components. The linear chirp is caused  
2632 by the energy loss due to cyclotron radiation, which results in a relatively slow increase  
2633 in the frequency components of the CRES signal over time. During the standard Fourier  
2634 analysis window for the FSCD of 40.96  $\mu$ sec, we expect a typical CRES signal to increase  
2635 in frequency by approximately 15 kHz, which is smaller than the frequency bin width  
2636 given the 200 MHz sample rate. Therefore when considering a single frequency spectrum  
2637 it is justifiable to neglect the effects of the linear frequency chirp.

2638 In the cases where the electron's pitch angle is  $\gtrsim 88.5^\circ$ , the majority of the signal

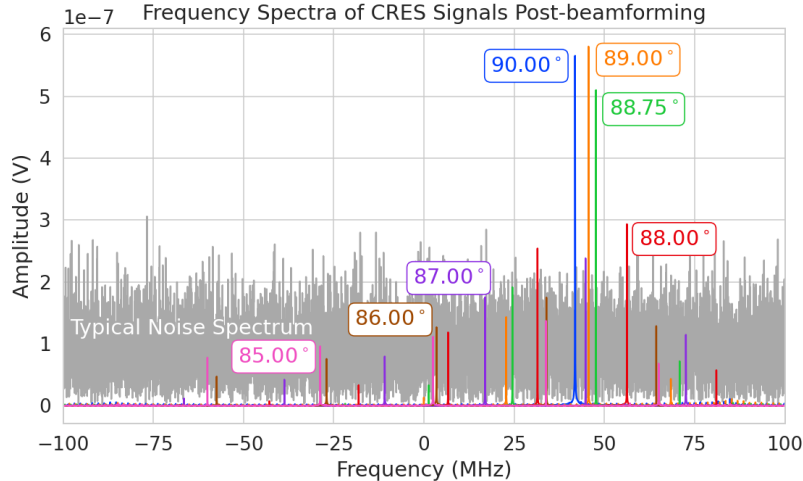


Figure 4.31: Frequency spectra of simulated CRES signals post-beamforming. The signal of a  $90^\circ$  electron consists of a single frequency component that is easy to detect with a power threshold on the frequency spectrum. This power threshold is still effective for signals with relatively large pitch angles such as  $89.0^\circ$  and  $88.75^\circ$ , which are composed of a main carrier and a few small sidebands. Signals with smaller pitch angles, below about  $88.5^\circ$ , tend to be dominated by sidebands such that no single frequency component can be reliably distinguished from the noise with a power threshold.

power is contained in a single frequency component, with the remaining signal power contained in a small number of sidebands proportional to the electron's axial modulation (see Figure 4.31). In these cases detection is relatively straight-forward by implementing a power threshold on the STFT, since the amplitude of the main signal peak is distinct from the thermal noise spectrum. However, as the pitch angle of the electron is decreased below  $88.5^\circ$ , the modulation index of the signal increases causing the maximum amplitude of the frequency spectrum to be comparable to typical noise fluctuations. At this point, the power threshold trigger is no longer able to distinguish between signal and noise leading to a reduction in detection efficiency. The neutrino mass sensitivity of the FSCD is directly linked to the overall detection efficiency. And, because the distribution of electron pitch angles is effectively uniformly distributed across the range of pitch angles that can be trapped, the overall detection efficiency is directly influenced by the range of pitch angles that have detectable signals. Therefore, utilizing a signal detection algorithm that can more effectively identify signals with pitch angles less than  $88.5^\circ$  will improve both detection efficiency and ultimately the neutrino mass sensitivity of the FSCD and other CRES experiments.

Modeling the detection performance of alternative signal detection algorithms for

2656 the FSCD requires that we pose the signal detection problem in a consistent manner.  
2657 The approach we take is to perform a binary hypothesis test on the frequency spectra  
2658 generated by the STFT. Mathematically, this is expressed as,

$$\mathcal{H}_0 : y[n] = \nu[n] \quad (4.43)$$

$$\mathcal{H}_1 : y[n] = x[n] + \nu[n]. \quad (4.44)$$

2659 Where under hypothesis  $\mathcal{H}_0$ , the vector representing the frequency spectrum ( $y[n]$ ) is  
2660 composed of pure white Gaussian noise (WGN) represented by  $\nu[n]$ , and under hypothesis  
2661  $\mathcal{H}_1$  the frequency spectrum is composed of a CRES signal ( $x[n]$ ) with added WGN. The  
2662 dominant source of noise in a FSCD-like experiment is expected to be thermal Nyquist-  
2663 Johnson noise, which is well approximated by a WGN distribution. In order to decide  
2664 between these two hypotheses we follow the standard Neyman-Pearson approach by  
2665 performing a log-likelihood ratio test between the probability distributions of the signal  
2666 classifier output under  $\mathcal{H}_1$  and  $\mathcal{H}_0$  [69]. The output of the log-likelihood ratio test is  
2667 called the test statistic, which is used to assign the data as belonging to the noise ( $\mathcal{H}_0$ )  
2668 or signal ( $\mathcal{H}_1$ ) classes by setting a decision threshold on the value of the test statistic.

2669 In practice, we select the decision threshold by finding the value of the test statistic  
2670 that guarantees an acceptable rate of false positives and then attempt to maximize  
2671 the signal detection probability under that fixed false positive rate. Because the signal  
2672 classifier will be used to evaluate the spectra of  $O(10^2)$  beamforming positions every  
2673 40.96  $\mu$ sec, we will require the signal classifiers to operate with decision thresholds that  
2674 provide false positive rates significantly smaller than 1%. This reduces the burden placed  
2675 on later stages of the CRES reconstruction chain to reject these false positives and  
2676 decreases the overall likelihood of reconstructing a false event. Below, we calculate the  
2677 probability distributions that allow us characterize how different detection algorithms  
2678 will perform for CRES signals in an FSCD experiment.

### 2679 **4.4.3 Signal Detection Algorithms**

#### 2680 **4.4.3.1 Power Threshold**

2681 The power threshold detection algorithm uses the maximum amplitude of the frequency  
2682 spectra as the detection test statistic. To model the performance of this approach,  
2683 consider first the case where the signal is pure WGN. For a single bin in the frequency  
2684 spectrum, the probability that the amplitude falls below a specific threshold value is

2685 given by the Rayleigh cumulative distribution function (CDF),

$$\text{Ray}(x; \tau) = 1 - \exp(-|x|^2/\tau), \quad (4.45)$$

2686 where the complex amplitude of the frequency bin is  $x$ , and  $\tau$  is the WGN variance.  
 2687 Because the noise samples for each frequency bin are independent and identically dis-  
 2688 tributed (IID), the probability that every bin in the frequency spectrum falls below the  
 2689 threshold is the joint CDF formed by the product of each individual frequency bin CDF,

$$F_0(x; \tau, N_{\text{bin}}) = \text{Ray}(x; \tau)^{N_{\text{bin}}}. \quad (4.46)$$

2690 The PDF for the power threshold classifier can then be obtained by differentiating the  
 2691 CDF.

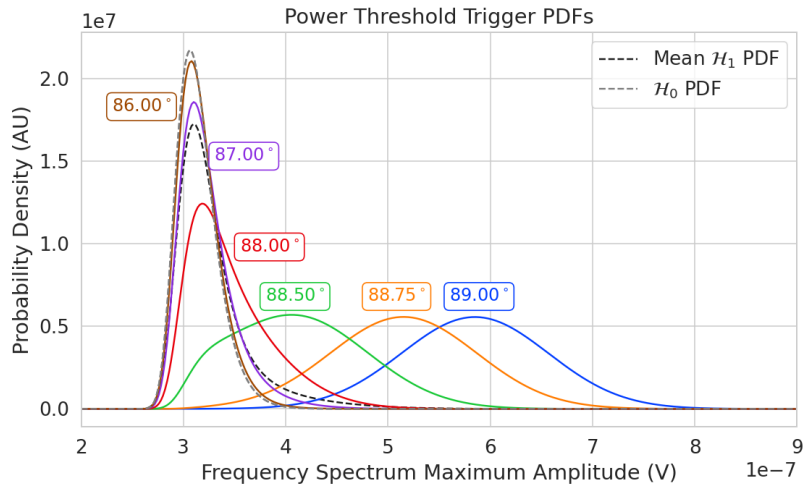


Figure 4.32: PDFs of the power threshold test statistic for CREs signals with various pitch angles as well as the PDF for the noise-only signal case. The average PDF computed for pitch angles ranging from 85.5 to 88.5° is also shown. As the pitch angle is decreased the signal PDF converges towards the noise PDF which indicates that the power threshold trigger is unable to distinguish between small pitch angle signals and noise.

2692 The probability distribution for the power threshold classifier under  $\mathcal{H}_1$  is formed in  
 2693 a similar way, but the frequency bins that contain signal must be treated separately. For  
 2694 a frequency bin that contains both signal and noise we can describe the probability that  
 2695 the amplitude of the bin will fall below our threshold using the Rician CDF,

$$\text{Rice}(x; \tau, \nu) = 1 - Q_1 \left( \frac{|\nu|}{\sqrt{2\tau}}, \frac{|x|}{\sqrt{2\tau}} \right), \quad (4.47)$$

2696 where the parameter  $|\nu|$  defines the noise-free amplitude of the signal and  $Q_1$  is the  
 2697 Marcum Q-function. This time the CDF that describes the probability that the entire  
 2698 spectrum falls below the decision threshold is the product of both signal and noise CDFs,

$$F_1(x; \tau, \nu, N_{\text{bin}}, N_s) = \text{Ray}(x; \tau)^{N_{\text{bin}} - N_s} \prod_{k=0}^{N_s} \text{Rice}(x; \tau, \nu_k). \quad (4.48)$$

2699 The first half of Equation 4.48 is the contribution from the bins in the frequency spectrum  
 2700 that contain only noise, and the second half is the product of the Rician CDFs for the  
 2701 frequency bins that contain signal peaks with a noise-free amplitude of  $|\nu_k|$ . In Figure  
 2702 4.32 we show plots of example PDFs under  $\mathcal{H}_1$  and  $\mathcal{H}_0$ .

#### 2703 4.4.3.2 Matched Filtering

2704 The shape of a CRES signal is completely determined by the initial conditions of the  
 2705 electron as it is emitted from beta-decay, which implies that it is possible to apply  
 2706 matched filtering as a signal detection algorithm. With a matched filter one uses the  
 2707 shape of the known signal, which is called a template, to filter the incoming data by  
 2708 computing the convolution between the signal and the data [69]. For cases where the  
 2709 signal is buried in WGN, the matched filter is the optimal detector in that it achieves  
 2710 the maximum probability of a true detection for a fixed false positive rate. Since CRES  
 2711 signals have an unknown shape but are deterministic, we can apply a matched filter by  
 2712 using simulations to generate a large number of signal templates called a template bank,  
 2713 which spans the parameter space of possible signals. Then at detection time, we use the  
 2714 template bank to identify signals by performing the matched filter convolution for each  
 2715 template in an exhaustive search.

2716 As we saw from the frequency spectra in Figure 4.31, CRES signals are highly periodic  
 2717 in nature. In such cases, it is advantageous to utilize the convolution theorem to replace  
 2718 the matched filter convolution with an inner product in the frequency-domain. With the  
 2719 convolution theorem, the matched filter test statistic that describes the detection of a  
 2720 signal buried in WGN using a matched filter template bank is given by

$$\mathcal{T} = \max_{\mathbf{h}} \left| \sum_{n=0}^{N_{\text{bin}}} h^\dagger[n] y[n] \right|, \quad (4.49)$$

2721 where  $h^\dagger[n]$  is the complex conjugate of the signal template. For the case when our  
 2722 template bank consists of only a single template it is possible to derive an exact analytical

2723 form for the PDF describing the matched filter test statistic. First, we derive PDF under  
 2724 the signal hypothesis, where the equation describing the matched filter test statistic, also  
 2725 known as the matched filter score, becomes

$$\mathcal{T} = \left| \sum_{n=0}^{N_{\text{bin}}} h^\dagger[n] y[n] \right|. \quad (4.50)$$

2726 Each noisy frequency bin represented by  $y[n]$  is the sum between value of the signal  
 2727 at that bin and complex WGN, which means that  $y[n]$  is itself Gaussian distributed.  
 2728 Therefore, the value of the inner product between the template and the data is also a  
 2729 complex Gaussian variable; and, since the matched filter score is the magnitude of this  
 2730 inner product, it must follow a Rician distribution.

2731 We can derive the equation for the Rician PDF by expressing the matched filter  
 2732 template  $\mathbf{h}$  in terms of the corresponding simulated signal, which we write as  $\mathbf{x}_h$  to  
 2733 distinguish from the signal in the data. Using the standard normalization and assuming  
 2734 uncorrelated WGN, the matched filter templates can be written as

$$\mathbf{h} = \frac{\mathbf{x}_h}{\sqrt{\tau |\mathbf{x}_h|^2}} \quad (4.51)$$

2735 where  $\tau$  is the noise variance. Inserting this into Equation 4.49 and expressing the data  
 2736 as a sum between a signal and a WGN vector yields,

$$\mathcal{T} = \frac{1}{\sqrt{\tau |\mathbf{x}_h|^2}} \left| \sum_{n=1}^{N_{\text{bin}}} x_h[n] (x[n] + \nu[n]) \right|. \quad (4.52)$$

2737 Next, we transform the expression by isolating the randomly distributed components  
 2738 giving

$$\mathcal{T} = \frac{\left| \sum_{n=1}^{N_{\text{bin}}} x_h[n] x[n] \right|}{\sqrt{\tau |\mathbf{x}_h|^2}} + \frac{1}{\sqrt{\tau |\mathbf{x}_h|^2}} \left| \sum_{n=1}^{N_{\text{bin}}} x_h[n] \nu[n] \right|. \quad (4.53)$$

2739 The first term of 4.53 can be simplified by using the Cauchy-Schawrz inequality to express  
 2740 the magnitude of the inner product in terms of the magnitudes of the signal and template  
 2741 as well as an orthogonality constant which we call "match" ( $\Gamma$ ). Using this we obtain,

$$\mathcal{T} = |\mathbf{h}| |\mathbf{x}| \Gamma + \frac{1}{\sqrt{\tau |\mathbf{x}_h|^2}} \left| \sum_{n=1}^{N_{\text{bin}}} x_h[n] \nu[n] \right|. \quad (4.54)$$

2742 The second term is a sum of Gaussian distributed variables, which we should expect also  
2743 follows a Gaussian distribution. Each of the samples  $\nu[n]$  is described by

$$\nu[n] \sim \mathcal{N}(0, \tau), \quad (4.55)$$

2744 where  $\mathcal{N}(0, \tau)$  is a complex Gaussian distribution with zero mean and variance  $\tau$ . There-  
2745 fore,

$$\frac{x_h[n]}{\sqrt{\tau|\mathbf{x}_h|^2}}\nu[n] \sim \mathcal{N}\left(0, \frac{x_h[n]^2}{|\mathbf{x}_h|^2}\right), \quad (4.56)$$

$$\sum_{n=1}^{N_{\text{bin}}} \frac{x_h[n]}{\sqrt{\tau|\mathbf{x}_h|^2}}\nu[n] \sim \mathcal{N}\left(0, \frac{\sum_{n=1}^{N_{\text{bin}}} x_h[n]^2}{|\mathbf{x}_h|^2}\right) = \mathcal{N}(0, 1), \quad (4.57)$$

$$|\mathbf{h}||\mathbf{x}|\Gamma + \sum_{n=1}^{N_{\text{bin}}} \frac{x_h[n]}{\sqrt{\tau|\mathbf{x}_h|^2}}\nu[n] \sim \mathcal{N}(|\mathbf{h}||\mathbf{x}|\Gamma, 1). \quad (4.58)$$

2746 We see that  $\mathcal{T}$  is magnitude of a complex variable with mean  $|\mathbf{h}||\mathbf{x}|\Gamma$  and variance one. In  
2747 order to simply the expression a bit further, we define the quantity  $\mathcal{T}_{\text{ideal}} = |\mathbf{h}||\mathbf{x}|\Gamma$ , which  
2748 we call the ideal matched filter score, because it represents the value of the matched  
2749 filter inner product that we would expect if no noise was present in the signal. We can  
2750 write the matched filter test statistic as the magnitude of a two-dimensional vector in  
2751 the complex plane

$$\mathcal{T} = |(\mathcal{T}_{\text{ideal}} + n_r, n_i)|, \quad (4.59)$$

2752 where  $n_r$  and  $n_i$  are the real and imaginary components of the noise each with variance  
2753  $1/2$ , which is modeled by a Rician distribution with shape factor  $\mathcal{T}_{\text{ideal}}$ . Therefore, the  
2754 probability distribution of the matched filter test statistic is given by,

$$P_1(x; \mathcal{T}_{\text{ideal}}) = 2x \exp(- (x^2 + \mathcal{T}_{\text{ideal}}^2)) I_0(2x\mathcal{T}_{\text{ideal}}), \quad (4.60)$$

2755 where  $I_0$  is the zeroth-order modified Bessel function.

2756 The shape of the matched filter score distribution is controlled by the parameter  
2757  $\mathcal{T}_{\text{ideal}}$ , which is effectively the value of the matched filter score if the data contained no  
2758 noise. Without noise, the data vector reduces to the signal,  $\mathbf{x}$ , in which case Equation  
2759 4.50 becomes the magnitude of an inner product between two vectors. We can write  
2760 the magnitude of an inner product in terms of the lengths of the individual vectors and  
2761 a constant that describes the degree of orthogonality between them. Applying this to

2762 Equation 4.50, we obtain

$$\mathcal{T}_{\text{ideal}} = |\mathbf{h}^\dagger \cdot \mathbf{x}| = |\mathbf{h}| |\mathbf{x}| \Gamma \quad (4.61)$$

2763 where  $\Gamma$  describes the orthogonality between  $\mathbf{h}$  and  $\mathbf{x}$ . From the point of view of matched  
2764 filtering, we can interpret  $\Gamma$  as describing how well the template matches the underlying  
2765 signal in the data.

2766 The matched filter score PDF under the noise hypothesis can be readily obtained  
2767 from Equation 4.60 by setting the value of  $\mathcal{T}_{\text{ideal}}$  to zero, since the data contains no signal  
2768 in the noise case. Doing this, we obtain the Rayleigh distribution that describes the  
2769 matched filter score under  $\mathcal{H}_0$ ,

$$P_0(x) = 2x \exp(-x^2). \quad (4.62)$$

2770 Equations 4.60 and 4.62 describe the behavior of the matched filter test statistic  
2771 under  $\mathcal{H}_0$  and  $\mathcal{H}_1$  for a single template. However, defining a PDF that describes the  
2772 matched filter test statistic in the case of multiple templates is in general a mathematically  
2773 intractable problem, since there is no guarantee of orthogonality between matched filter  
2774 templates. This leads to correlations between the matched filter scores of different  
2775 templates because only one sample of noise is used to compute the matched filter scores  
2776 of the template bank. In order to proceed, we need to make the simplifying assumption  
2777 that we can treat the matched filter scores as IID variables, which allows to ignore  
2778 correlations between templates. The overall effect of this will be an underestimate of the  
2779 performance of the matched filter, since we are under counting the number of templates  
2780 that could contribute a detectable score.

2781 For  $\mathcal{H}_0$  we model the probability that the matched filter score falls below our threshold  
2782 using the CDF obtained by integrating Equation 4.62. Because we are assuming that  
2783 the matched filter scores using different templates are independent, the probability that  
2784 the matched filter score for all templates falls below a threshold value is the joint CDF  
2785 formed by multiplying the CDF for each template. Under  $\mathcal{H}_0$  this is

$$F_0(x) = \left(1 - e^{-x^2}\right)^{N_t}, \quad (4.63)$$

2786 where  $x$  is the matched filter score threshold and  $N_t$  is the number of templates. We  
2787 should expect that the distribution describing the matched filter template bank maximum  
2788 score depends on  $N_t$ , because with more templates there is a greater chance of a random  
2789 match between the template and data.

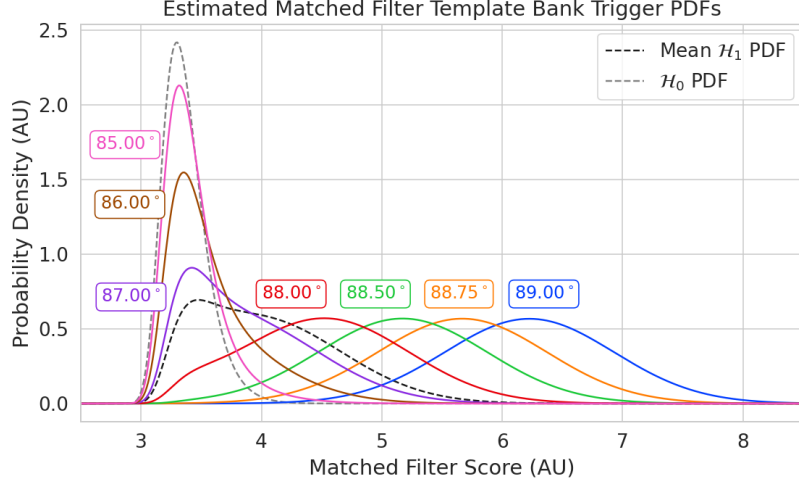


Figure 4.33: Plots of the estimated PDFs for the matched filter template bank test statistic for CRES signals with various pitch angles as well as the estimated PDF for the noise only signal case. We assume an estimated number of templates of  $10^5$  and perfect match between signal and template i.e.  $\Gamma_{\text{best}} = 1$ . The mean PDF includes signals ranging from  $85.5 - 88.5^\circ$  in pitch angle. There is a much larger distinction between the signal PDFs at small pitch angle compared to the power threshold indicating a higher detection efficiency for these signals.

For  $\mathcal{H}_1$ , we start by denoting the CDF of the best matching template as  $F_{\text{best}}(x; \mathcal{T}_{\text{best}})$ , and treat the matched filter scores for all other templates as negligible ( $\mathcal{T}_{\text{ideal}} \approx 0$ ). Then we form the joint CDF by combining the distributions for all templates used during detection. Since we are exhaustively checking the matched filter scores, the number of templates checked will be a randomly distributed variable that ranges from zero to the total number of available templates. If we assume that signals are uniformly distributed across the parameter space spanned by the template bank then on average we check  $(N_t - 1)/2 \approx N_t/2$  templates for each inference. Therefore, the estimated CDF under  $\mathcal{H}_1$  is

$$F_1(x; \mathcal{T}_{\text{best}}) = F_{\text{best}}(x; \mathcal{T}_{\text{best}}) \left(1 - e^{-x^2}\right)^{N_t/2}. \quad (4.64)$$

In Figure 4.33 we show plots of the estimated matched filter template bank classifier PDFs under both  $\mathcal{H}_0$  and  $\mathcal{H}_1$ .

#### 4.4.3.3 Machine Learning

In this paper we focus on Convolutional Neural Networks (CNN) as an example of a machine learning based signal classifier. CNNs are constructed using a series of

2804 convolutional layers, each composed of a set of filters that are convolved with the input  
 2805 data. The individual convolutional filters can be viewed as matched filter templates that  
 2806 are learned from a set of simulated data rather than being directly generated. This opens  
 2807 the possibility of finding a more efficient representation of the matched filter templates  
 2808 during the training process that can potentially reduce computational cost at inference  
 2809 time while still offering good classification performance.

2810 The machine learning approach is distinct from both the power threshold and matched  
 2811 filtering in that we do not attempt to manually engineer a test statistic that is computed  
 2812 from the data for classification. Instead, we attempt calculate the test statistic by  
 2813 constructing a differentiable function that maps the complex frequency series generated  
 2814 by the STFT to a binary classification as either signal or noise. The test statistic for the  
 2815 machine learning classifier can be expressed as

$$\mathcal{T} = G(\mathbf{y}; \boldsymbol{\Omega}) \quad (4.65)$$

2816 where  $\mathbf{y}$  is the noisy data vector and  $G(\mathbf{y}; \boldsymbol{\Omega})$  is the machine learning model parameterized  
 2817 by the weights  $\boldsymbol{\Omega}$ . By using supervised learning on a labeled set of training signals, we  
 2818 can modify the function parameters to learn the mapping from the data to the likelihood  
 2819 of  $\mathbf{y}$  belonging to either  $\mathcal{H}_1$  or  $\mathcal{H}_0$ .

Table 4.1: A summary of the CNN model layers and parameters. The output of each 1D-Convolution and Fully Connected layer is passed through a LeakyReLU activation function and re-normalized using batch normalization before being passed to the next layer in the model. The output of the final Fully Connected layer in the model is left without activation so that the model outputs can be directly passed to the Binary Cross-entropy loss function used during training.

Layer	Type	Input Channels	Output Channels	Parameters
1	1D-Convolution	2	15	( $N_{\text{kernel}} = 4$ , $N_{\text{stride}} = 1$ )
2	Maximum Pooling	15	15	( $N_{\text{kernel}} = 4$ , $N_{\text{stride}} = 4$ )
3	1D-Convolution	15	20	( $N_{\text{kernel}} = 4$ , $N_{\text{stride}} = 1$ )
4	Maximum Pooling	20	20	( $N_{\text{kernel}} = 4$ , $N_{\text{stride}} = 4$ )
5	1D-Convolution	20	25	( $N_{\text{kernel}} = 4$ , $N_{\text{stride}} = 1$ )
6	Maximum Pooling	25	25	( $N_{\text{kernel}} = 4$ , $N_{\text{stride}} = 4$ )
7	Fully Connected	3200	512	NA
8	Fully Connected	512	64	NA
9	Fully Connected	64	2	NA

2820 The CNN architecture used for this work is summarized by Table 4.1. No strategic  
 2821 hyper-parameter optimization approach was implemented beyond the manual testing

2822 of different CNN architecture variations, so this particular model is best viewed as a  
2823 proof-of-concept rather than a rigorously optimized design. Numerous model variations  
2824 were tested, some with significantly more layers and convolutions filters per layer, as  
2825 well as others that were even smaller than the architecture in Table 4.1. Ultimately, the  
2826 model architecture choice was driven by the motivation to find the minimal model whose  
2827 classification performance was still comparable to the larger CNN’s tested, because of  
2828 the importance of minimizing computational cost in real-time applications. It is possible  
2829 that more sophisticated machine learning models could improve upon the classification  
2830 results achieved here, but we leave this investigation for future work.

## 2831 **4.4.4 Methods**

### 2832 **4.4.4.1 Data Generation**

2833 To test the triggering performance of the classifiers, simulated CRES signals were  
2834 generated using the Locust simulations package [60, 78] developed by the Project 8  
2835 collaboration. Locust uses the separately developed Kassiopeia package to calculate the  
2836 magnetic fields produced by a user defined set of current carrying coils along with any  
2837 specified background magnetic fields, resulting in a magnetic trap. Next, Kassiopeia  
2838 calculates the trajectory of an electron in this magnetic field starting from a set of user  
2839 specified initial conditions. The Locust software then uses the electron trajectories from  
2840 Kassiopeia to calculate the resulting electromagnetic fields using the Liénard-Wiechert  
2841 equations, and determine the voltages generated in the antenna array with the antenna  
2842 transfer function. Locust then simulates the down-conversion, filtering, and digitization  
2843 steps resulting in the simulated CRES signals for an electron.

2844 The shape of the received CRES signal is determined by the initial kinematic param-  
2845 eters, including the starting position of the electron, the starting kinetic energy of the  
2846 electron, and the pitch angle. For the studies performed here we constrain ourselves to a  
2847 single initial electron position located at  $(x, y, z) = (5, 0, 0)$  mm, and using this starting  
2848 position we generate two datasets by varying the initial kinetic energy and the starting  
2849 pitch angle. The first dataset consists of a two-dimensional square grid of kinetic energy  
2850 and pitch angle spanning an energy range from 18575-18580 eV with a spacing of 0.1 eV,  
2851 and pitch angles from 85.5-88.5° with a spacing of 0.001°, resulting in 153051 signals with  
2852 a unique energy-pitch angle combination. This dataset is intended to represent a matched  
2853 filter template bank. The second dataset was generated by randomly sampling uniform  
2854 probability distributions covering the same parameter space to produce approximately

2855 50000 signals randomly parameterized in energy and pitch angle. This dataset provides  
2856 the training and test data for the machine learning approach, and acts as a representative  
2857 sample of signals to evaluate the performance of the matched filter template bank.

2858 Each signal was simulated for a duration of  $40.96 \mu\text{s}$ , which is equivalent to 8192  
2859 samples at the FSCD digitization rate, and begins at time  $t = 0 \text{ s}$  for all simulations.  
2860 This duration represents a single frequency spectrum generated by the STFT. The output  
2861 of the Locust simulation is a matrix of array snapshots with size given by the number of  
2862 channels times the event length ( $N_{\text{ch}} \times N_{\text{sample}}$ ), which we pre-process using the digital  
2863 beamforming summation and STFT described in Section 4.4.2.2. The  $\nabla B$ -drift correction  
2864 uses the exact value of  $\omega_{\nabla B}$ , obtained from the Kassiopeia simulation of that electron.  
2865 In practice, an average value for  $\omega_{\nabla B}$  could be used, because there is limited variation in  
2866 drift frequency across this parameter space.

#### 2867 4.4.4.2 Template Number and Match Estimation

2868 The estimated PDF for the matched filter template bank depends on the score of the  
2869 best matching template or equivalently the match of the best template ( $\Gamma_{\text{best}}$ ) as well  
2870 as the number of templates. One expects that with a higher number of templates the  
2871 average value of  $\Gamma_{\text{best}}$  will increase, however, there is a point of diminishing returns at  
2872 which more templates will not significantly increase match, but will still increase the  
2873 likelihood of false positives. Therefore, it is desirable to use the minimum number of  
2874 templates that provide an acceptable mean value of  $\Gamma_{\text{best}}$ .

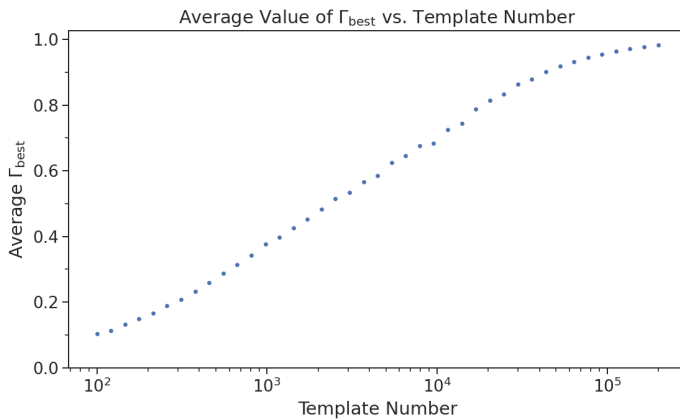


Figure 4.34: The mean match of the matched filter template bank to a test set of randomly parameterized signals as a function of the number or density of templates. The parameter space includes pitch angles from  $85.5 - 88.5^\circ$  and energies from 18575 – 18580 eV.

2874

2875 To quantify the relationship between match and template number, we calculated  
2876 the mean match of the random dataset to a selection of templates obtained from the  
2877 regularly spaced dataset. The results are shown in Figure 4.34, where we find that the  
2878 average value of  $\Gamma_{\text{best}}$  is an exponential function of the number of templates. From this  
2879 plot we select the desired value of mean match at which we would like to evaluate the  
2880 matched filter PDF and can infer the required number of templates.

#### 2881 4.4.4.3 CNN Training and Data Augmentation

2882 To prepare the data for training the model, we split the random dataset in half to create  
2883 distinct training and test datasets. Additionally, a randomly selected 20% of the training  
2884 data is isolated for use as a validation set during the training loop. The size of the  
2885 training, validation, and test datasets are then tripled by appending two additional copies  
2886 of the data to increase the sample size of the dataset after data augmentation. The  
2887 data is loaded with no noise, which is added to each data batch during the training  
2888 phase by generating a new noise sample from a complex WGN distribution. In order to  
2889 ensure an even split between signal and noise data we append to the noise-free signals an  
2890 equal number of empty signals composed of all zeros. Therefore, as the data is randomly  
2891 shuffled during training, on average an equal number of empty signals will be included  
2892 with the training signals. After adding the sample of WGN to the data batch, the empty  
2893 signals represent the noise-only data that the model must distinguish from signal data.

2894 As the training signals are loaded we apply a unique random phase shift as the  
2895 first form of data augmentation. Since the data is generated using the same initial  
2896 axial position and cyclotron orbit phase, the randomization is an attempt to prevent  
2897 overtraining on these features. During each training epoch the data is randomly shuffled  
2898 and split into batches of 2500 signals. Each batch of signals is then circularly shifted  
2899 by a random number of frequency bins to simulate a kinetic energy shift from  $-75$  to  
2900  $20$  eV to simulate a training dataset with a larger energy range. Next, a sample of  
2901 complex WGN, consistent with the expected 10 K Nyquist-Johnson noise expected for  
2902 the FSCD, is generated and added to the signal, which prevents overtraining on noise  
2903 features. As a final step, the data is renormalized by the standard deviation of the noise  
2904 so that the range of values in the data is close to  $[-1, 1]$ , which helps ensure well-behaved  
2905 back-propagation.

2906 The Binary Cross-entropy loss function is used to compute the loss for each batch of  
2907 data and the model weights are updated using the ADAM optimizer with a learning rate  
2908 of  $5 \times 10^{-3}$ . After each training epoch, the loss and classification accuracy of the validation

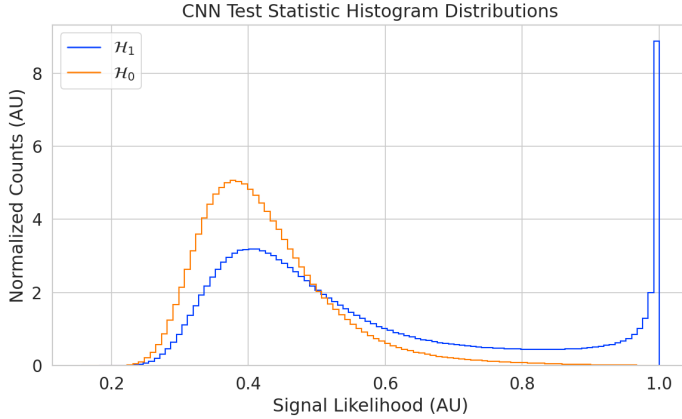


Figure 4.35: Histograms of the trained CNN model output from the test dataset. The blue histogram shows the model outputs for signal data. The oddly shaped peak near the end is the result of the softmax function mapping the long tail of the raw output distribution to the range [0, 1].

dataset are computed to monitor for overtraining. It was noticed that the relatively high noise power and the fact that a new sample of noise was used for each batch together provided a strong form of regularization, since no evidence of over-training was observed even after several thousand epochs. Typically, the loss and classification accuracy of the model converged after a few hundred training epochs, but the training loop was extended to 3000 epochs to attempt to achieve the best possible performance. The training procedure generally took about 24 hrs using a single NVIDIA V100 GPU [80].

After training the model, we use it to classify the test dataset and generate histograms of the model outputs for both classes of data. The data augmentation procedure for the evaluation of the test data mirrors the training procedure without the validation split. Since a random circular shift and a new sample of WGN is added to each batch, the testing evaluation loop is run for 100 epochs to get a representative sample of noise and circular shifts. The model outputs for each batch are passed through a softmax activation and then combined into histograms, which we show in Figure 4.35.

## 4.4.5 Results and Discussion

### 4.4.5.1 Trigger Classification Performance

Using the matched filter and power threshold CDFs, along with the classification results from the CNN, we compare detection performance by computing receiver operating characteristic (ROC) curves. Specifically, we compare the detection performance averaged

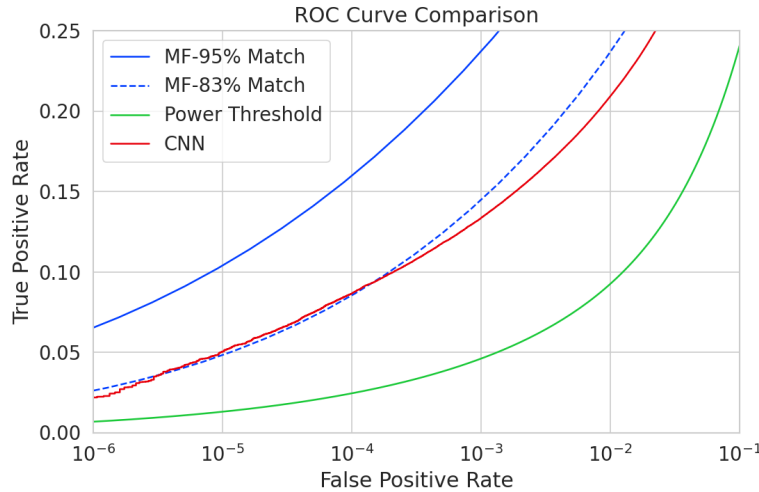


Figure 4.36: ROC curves describing the detection efficiency or true positive rates for the three signal classification algorithms examined in this paper.

over the full signal parameter space in order to get a measure of the overall detection efficiency achieved by each algorithm. For the power threshold and matched filter algorithms, we obtain the mean ROC curve by taking the average over all signals in the regularly spaced dataset. In the case of the matched filter, we examine two cases using different numbers of templates, which have different values of mean match. The ROC curve describing the CNN is obtained by forming a histogram of the network outputs for each class of signal and from this computing the estimated CDFs and ROC curve. In Figure 4.36, we show the ROC curves obtained for each of the detection algorithms, visualized in terms of true positive rate and false positive rate.

The true positive rate of a signal classifier is equivalent to its detection efficiency, and we see that for the population of signals with pitch angles  $< 88.5^\circ$  the power threshold has a consistently lower detection efficiency than the CNN and the matched filter. This result could have been predicted from the visualization of signal spectra in Figure 4.31, where we see that there is no way to distinguish between a noise peak and a signal peak with high confidence at small pitch angles. The CNN offers a significant and consistent increase in detection efficiency over the power threshold approach, with the relative improvement in detection efficiency increasing as the false positive rate decreases. If we compare the CNN to the matched filter, we see that the performance of the tested network is roughly equivalent to a matched filter detector with an average match of about 83%, which uses approximately 20000 matched filter templates. The overall best detection efficiency is achieved by the matched filter classifier if a large enough template

bank is used. We show in the plot the ROC curve for a matched filter template bank with 95% average match, which is achieved with approximately 100000 templates. Since the matched filter is known to be statistically optimal for detecting a known signal in WGN, it is somewhat expected that this algorithm has the highest detection efficiency.

A potentially impactful difference between the matched filter and CNN algorithms is that the CNN relies upon convolutions as its fundamental calculation mechanism, whereas our implementation of a matched filter utilizes an inner product. Since convolution is a translation invariant operation, the detection performance of CNN can be extended to a wider range of CRES event kinetic energies with less cost than the matched filter, a feature that we exploited during the CNN training by including circular translations of the CRES frequency spectra in the training loop. Increasing the range of kinetic energies detectable by a matched filter requires a proportional increase in the number of templates, which directly translates into increased computational and hardware costs. From a practical perspective, the detection algorithm is always limited by the available computational hardware, so estimating the relative costs is a key factor in determining their feasibility. Below we perform a more detailed analysis of the relative costs of each of the detection algorithms.

#### 4.4.5.2 Computational Cost and Hardware Requirements

In the process of investigating triggering approaches for an antenna array CRES experiment, we have uncovered a strong tension between detection efficiency and computational resources. To relate the computational cost estimates to actual costs, we compare the theoretical amount of computer hardware required to implement the signal classifiers for real-time detection in an FSCD experiment. To do this we shall utilize order of magnitude estimates of the theoretical peak performance values for currently available Graphics Processing Units (GPUs) as a metric. This approach will underestimate the amount of required hardware, since it is unlikely that any CRES detection algorithm could reach the theoretical peak performance of the hardware.

Of the three detection algorithms tested, the power threshold classifier is the least expensive. It requires that we check whether the amplitude of each frequency bin in the STFT is below or above our decision threshold. The STFT combined with digital beamforming produces  $N_{\text{bin}}N_b$  frequency bins that must be checked every  $N_{\text{bin}}/f_s$  seconds. This requires approximately  $O(10^{10})$  FLOPS to check in real-time. Current generations of GPUs have peak theoretical performances in the range of  $O(10^{13}) - O(10^{14})$  FLOPS [81], dependent on the required floating-point precision of the computation. Therefore, the

entire computational needs of a real-time triggering system using a power threshold classifier, including digital beamforming and generation of the STFT, could be met by a single high-end GPU or a small number of less powerful GPUs. Since triggering is only one step of the full real-time signal reconstruction approach, limiting the computational cost of this stage is ideal. However, we have seen that the power threshold classifier does not provide sufficient detection efficiency across the entire range of possible signals, which is the primary motivation for exploring more complicated triggering solutions.

As discussed, the computational cost of the matched filter approach requires counting the number of templates that must be checked for each frequency spectra produced by the STFT. Computing the matched filter scores requires  $O(N_b N_t N_{\text{bin}})$  operations, since for each of the  $N_b$  beamforming positions we must multiply  $N_t$  templates with a data vector that has length  $N_{\text{bin}}$ . The time within which we must perform this calculation is equal to  $N_{\text{bin}}/f_s$  to keep up with the data generation rate. To cover the 5 eV kinetic energy range spanned by the template bank, we saw that  $10^4$  to  $10^5$  templates are required in order to match or exceed the detection efficiency of the CNN. If the number of templates scales linearly with the kinetic energy range of interest as expected, then we would require  $10^5$  to  $10^6$  matched filter templates with this more realistic range of energies. Considering this, the estimated computational cost of the matched filter is between  $O(10^{15})$  to  $O(10^{16})$  FLOPS, which is  $O(10^2)$  to  $O(10^3)$  high-end GPUs.

Lastly, we have the CNN classifier. To estimate the computational cost we simply sum the number of convolutions and matrix multiplications specified by the network architecture shown in Table 4.1. Each convolutional layer consists of  $N_{\text{in}} N_{\text{out}} N_{\text{kernel}} L_{\text{input}}$  floating-point operations, where  $N_{\text{in}}$  is the number of input channels,  $N_{\text{out}}$  is the number of output channels,  $N_{\text{kernel}}$  is the size of the convolutional kernel, and  $L_{\text{input}}$  is the length of the input vector, and the fully connected layers each contribute  $N_{\text{in}} N_{\text{out}}$  operations. Summing all the neural network layers we estimate that the CNN would require  $O(10^6)$  floating point operations for each frequency spectra; therefore, the total computation cost of the CNN trigger is this cost times the number of beamforming positions per the data acquisition time, which is  $O(10^{13})$  FLOPS or  $O(10^0)$  GPUs.

Compared with the matched filter approach the CNN requires  $O(100)$  to  $O(1000)$  fewer GPUs to implement, dependent on the exact number of templates used in the template bank. The 100 eV kinetic energy range is motivated by the application of these detection algorithms to an FSCD-like neutrino mass measurement experiment. However, if a significantly larger range of kinetic energies is required, a CNN may be the preferred detection approach despite the lower average detection efficiency due to computational

3018 cost considerations. The low estimated computational cost of the CNN is directly related  
3019 to the small network size.

3020 Additional experiments with larger CNNs, generated by increasing the depth and  
3021 width of the neural network, and we observed that these changes provided minimal  
3022 ( $\lesssim 1\%$ ) improvement in the classification accuracy of the model. A potential reason  
3023 for this could be the sparse nature of the signals in the frequency domain and the low  
3024 SNR which makes for a challenging dataset to learn from. Future work could investigate  
3025 modifications to the neural network architecture such as sparse convolutions, which may  
3026 improve the classification accuracy of the model or further reduce the computational  
3027 costs of this approach. Alternatively, more complicated CNN architectures such as a  
3028 ResNet [82] or VGG model [83] may provide improved classification performance over a  
3029 basic CNN. An additional promising area of investigation are recurrent neural networks,  
3030 which may be able to exploit the time-ordered features of the STFT for more accurate  
3031 signal detection if the electron signals last for multiple Fourier transform windows.

3032 Our estimate of the computational cost of the matched filter is somewhat naive if  
3033 we notice that the majority of the values that make up a CRES frequency spectra are  
3034 zero (see Figure 4.31). Therefore, the majority of operations in the matched filter inner  
3035 product are unnecessary, and we could instead evaluate the matched filter inner product  
3036 using only the  $\lesssim 10$  frequency peaks that make up CRES signal. This optimization  
3037 reduces the number of operations required to check each template by a factor of  $O(100)$   
3038 to  $O(1000)$ , which brings the estimated computational cost of the matched filter in  
3039 line with the CNN. Although this level of sparsity results in a multiplication with very  
3040 low arithmetic complexity, the resulting sparse matched filter algorithm is still likely  
3041 to be constrained by memory access speed rather than compute speed. Ultimately, the  
3042 comparison of the relative computational and hardware costs between the matched filter  
3043 and CNN will depend on the efficiency of the software implementation and hardware  
3044 support for neural network and sparse matrix calculations.

#### 3045 **4.4.6 Conclusion**

3046 Increasing the detection efficiency and overall event rate of the CRES technique represents  
3047 a key developmental path towards new scientific results and broader applications of the  
3048 CRES technique. It is what motivates both the antenna array detection approach and  
3049 the development of real-time signal reconstruction algorithms. We have demonstrated  
3050 that significant gains in the detection efficiency of the CRES technique are achievable  
3051 by utilizing triggering algorithms that account for the specific shape of CRES signals in

3052 the detector. These algorithms emphasize the need for accurate and fast methods for  
3053 CRES simulation, since they directly contribute to the success of matched filter methods  
3054 by providing a way to generate expected signal templates and also serve as a source of  
3055 training data for machine learning approaches.

3056 The improvements in detection efficiency offered by these alternative approaches to  
3057 triggering are crucial to the success of efforts to develop scalable technologies for CRES  
3058 measurement, since they provide a significant increase in the detectable parameter space  
3059 of CRES events, which allows for a better utilization of the larger detection volume.  
3060 While we have focused on the real-time detection of CRES signals from antenna arrays,  
3061 these same signal classifiers could be used in CRES experiments utilizing a different  
3062 detector technologies, since the same principles of signal detection will apply. For example,  
3063 previous CRES measurements by the Project 8 collaboration that utilized a waveguide  
3064 gas cell, could have improved their detection efficiency by employing a matched filter  
3065 or neural network classifier to identify trapped electrons with pitch angles that are too  
3066 small to be detected by the power threshold approach. Furthermore, alternative CRES  
3067 detector technologies such as resonant cavities [39] could also see similar improvements  
3068 in detection efficiency, which is of crucial importance to future efforts by the Project 8  
3069 collaboration to utilize CRES to measure the neutrino mass.

# **Chapter 5**

## **Antenna and Antenna Measurement System Development for the Project 8 Experiment**

### **5.1 Introduction**

The FSCD and antenna array CRES represent an innovative approach to beta-decay spectroscopy. While much can be learned from simulations about the systematics of CRES with antenna arrays, laboratory measurements and demonstrations provide critical inputs to sensitivity and simulation models as well as provide a means for calibration and commissioning of the experiment. Therefore, a robust program of antenna and antenna measurement hardware development is important to the success of the FSCD and the development of antenna array CRES more broadly.

In this chapter we summarize the development of an antenna measurement system at Penn State to implement and test the techniques of antenna array CRES on the bench-top, in order to support the efforts of the Project 8 collaboration. In Section 5.2 we provide an introduction to some fundamental parameters and concepts related to antenna measurements as well as an overview of the Penn State antenna measurement system hardware. In Section 5.3 we include the manuscript of a paper [79] which details the design and characterization of a specialized antenna developed to mimic the electric fields emitted by an electron in a CRES experiment. This antenna, called the Synthetic Cyclotron Antenna (SYNCA), is intended as a calibration tool for antenna arrays developed for CRES measurements. Lastly, in Section 5.4 we summarize a set of prototype FSCD antenna array measurements with the SYNCA [42], which we use to validate the simulated performance of the antenna array and estimate systematic errors associated with the antenna array.

## 3095 5.2 Antenna Measurements for CRES experiments

### 3096 5.2.1 Antenna Parameters

3097 Antenna characterization measurements are intended to validate simulations of the  
3098 antenna array performance, which ultimately informs the neutrino mass sensitivity of  
3099 the experiment. In this section, I shall summarize a few fundamental concepts relating  
3100 to antennas and antenna measurement, before introducing how Project 8 uses antenna  
3101 measurement for the development of antenna array CRES.

#### 3102 5.2.1.1 Radiation Patterns

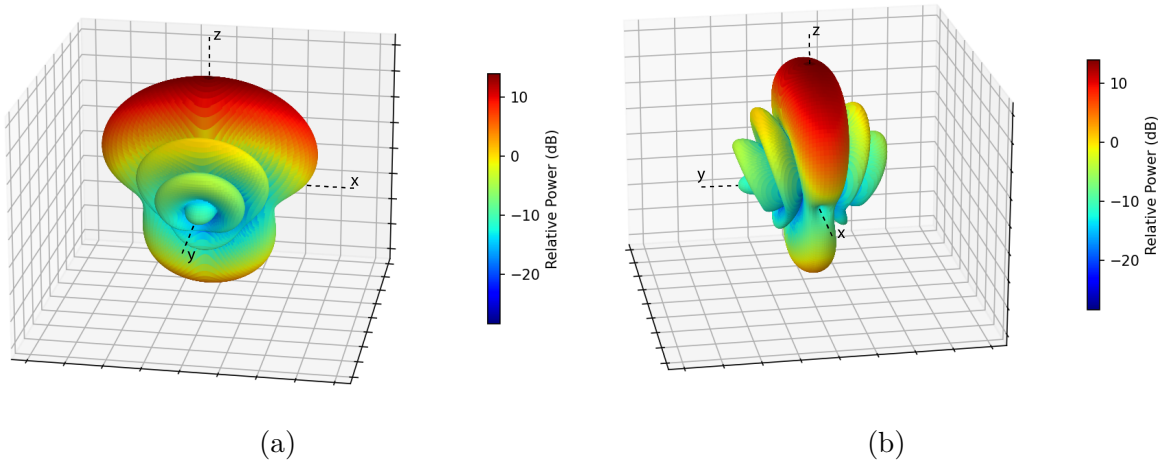


Figure 5.1: An example radiation pattern generated using HFSS simulations. The color and radial distance of the surface from the origin indicate the relative magnitude of radiation power emitted by the antenna in that direction. The primary goal of most antenna measurements is typically to measure the antenna pattern, which is used to derive many useful antenna performance parameters.

3103 Antennas are conductive structures designed to carry alternating electric currents  
3104 in order to transmit energy in the form of electro-magnetic (EM) waves [63]. Perhaps  
3105 the most fundamental way to characterize an antenna, is to map out the radiated power  
3106 density as a function of position, which is called the radiation pattern (see Figure 5.1).  
3107 We find the radiation power density by calculating the time-averaged Poynting vector for  
3108 all positions surrounding the antenna, which in equation form is

$$\mathbf{W}(x, y, z) = \langle \mathbf{E}(x, y, z, t) \times \mathbf{H}^*(x, y, z, t) \rangle_t, \quad (5.1)$$

3109 where  $\mathbf{E}(x, y, z, t)$  and  $\mathbf{H}(x, y, z, t)$  are the time-dependent electric and magnetic fields  
 3110 produced by the antenna [47]. The radiation power density has units of  $\text{W/m}^2$  and is  
 3111 more typically called the energy flux density in physics applications, since it is a measure  
 3112 of the amount of energy passing through a unit area over time.

3113 Because the radiation power density is a measure of power per unit area, its value  
 3114 in a particular direction will depend on the distance from the antenna at which we are  
 3115 measuring. This is undesirable for practical applications A related quantity, which is  
 3116 distance independent, is the energy flux per unit solid angle or radiation intensity, which  
 3117 is computed directly from the radition power density by multiplying by the squared  
 3118 distance from the antenna. Specifically,

$$U = r^2 W(x, y, z), \quad (5.2)$$

3119 where  $r$  is the distance from the antenna to the field measurement point. The radiation  
 3120 intensity is typically defined in regions where the Poynting vector consists only of a radial  
 3121 component where it is safe to treat as a scalar quantity.

### 3122 5.2.1.2 Directivity and Gain

3123 Since the radiation intensity is a measure of average power per unit solid angle, it is  
 3124 independent of distance and more useful as feature for antenna measurement. However,  
 3125 most antenna measurements are performed in terms of the directly related directivity  
 3126 and gain quantities. Directivity is defined as the ratio between the radiation intensity at  
 3127 particular point on the radiation pattern to the average radiation intensity computed  
 3128 over all solid angles [63]. The equation that relates the radiation intensity to directivity  
 3129 is

$$D = \frac{U}{U_0} = \frac{4\pi U}{P_{\text{rad}}}, \quad (5.3)$$

3130 where  $U_0$  is the average radiation intensity over all solid angles, which simply the total  
 3131 radiated power ( $P_{\text{rad}}$ ) divided by  $4\pi$ . Closely related to directivity is concept of gain,  
 3132 which accounts for energy losses that occur inside then antenna when attempting to  
 3133 transmit or receive a signal. The antenna gain is given by

$$G = \frac{4\pi U}{P_{\text{in}}}, \quad (5.4)$$

3134 where  $P_{\text{in}}$  is the total power delivered to the antenna. Gain can be thought of as the ratio  
 3135 of the antenna's radiation intensity to that of a hypothetical isotropic, lossless radiator.

<sup>3136</sup> The maximum values of gain and directivity exhibited by the main lobe of the antenna  
<sup>3137</sup> pattern as well as the ratio between the gain of the main lobe and any side-lobes are  
<sup>3138</sup> important figures of merit used to evaluate antenna designs.

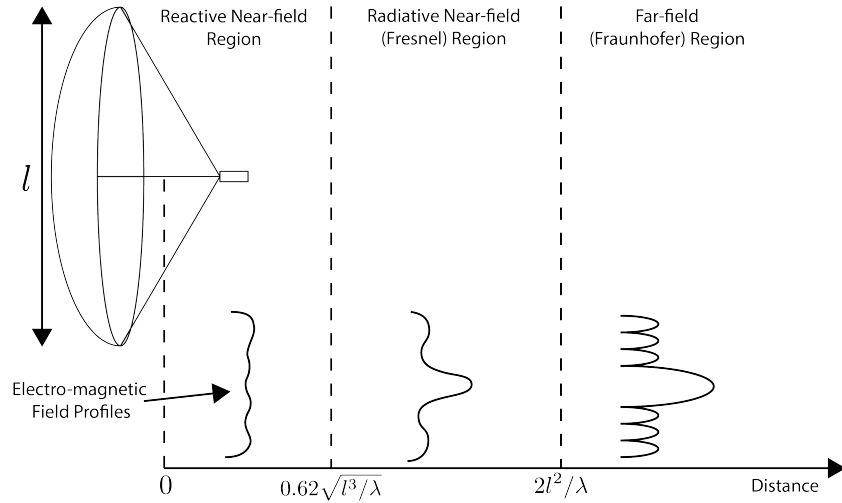


Figure 5.2: An illustration of the three field regions important for the analysis of an antenna system. Very close to the antenna the electric fields are primarily reactive so there is no radiation. If a receiving antenna were placed in this region most of the energy would be reflected back to the transmitter. Outside of the reactive near-field is the radiative near field. At these distances the antenna does radiate, but the radiation pattern is not well-defined since it changes based on the distance of the receiving antenna. It is only in the far-field region where the radiation pattern becomes constant as a function of distance, which is where the majority of antenna engineering is assumed to take place. The antenna arrays developed by Project 8 for CRES measurements operate in the radiative near-field due to the importance of limiting power loss from free-space propagation, which complicates the design of the antenna system.

### <sup>3139</sup> 5.2.1.3 Far-field and Near-field

<sup>3140</sup> Radiation patterns are only well-defined in regions where the shape of the radiation  
<sup>3141</sup> pattern is independent of distance. The region where this approximation is valid is called  
<sup>3142</sup> the "far-field", and in this region we can treat the EM fields from the antenna as spherical  
<sup>3143</sup> plane waves. A rule of thumb for antennas is that the far-field approximation is valid  
<sup>3144</sup> when the condition

$$R > \frac{2l^2}{\lambda} \quad (5.5)$$

<sup>3145</sup> is met. In this expression,  $R$  is the distance from the antenna,  $l$  is the largest characteristic  
<sup>3146</sup> dimension of the antenna, and  $\lambda$  is the wavelength of the radiation (see Figure 5.2).

3147        The region very close to the antenna is called the reactive near-field, because in this  
3148      region the reactive component of the EM field is dominant. Unlike radiative electric  
3149      fields, the reactive electric and magnetic fields are out of phase from each other by  
3150      90°, since they are the result of electrostatic and magnetostatic effects coming from the  
3151      self-capacitance and self-inductance of the antenna. The reactive fields are unable to  
3152      transfer energy a significant distance from the antenna and are thus completely negligible  
3153      for most antenna applications. The limit of the reactive near-field for an electrically-large  
3154      antenna is typically taken to be

$$R < 0.62\sqrt{l^3/\lambda}. \quad (5.6)$$

3155        The unique application of antennas by Project 8 is somewhat limited by reactive near-  
3156      field effects in the form of a maximum radial position for electrons inside the uniform  
3157      cylindrical antenna array. If electrons are too close to the edge of the array than reactive  
3158      near-field effects leads to a large reduction in the received power and consequently  
3159      detection efficiency. This leads to a significant volume inside of the antenna array that  
3160      is unsuitable for CRES lowering the volumetric efficiency of the antenna array CRES  
3161      technique relative to a cavity experiment.

3162        In between the reactive near-field and the far-field is the radiative near-field region.  
3163        In this region the fields are primarily radiative, however we are still too close to the  
3164      antenna for the spherical plane wave approximation to apply. Therefore, interference  
3165      effects between EM waves emitted from different points on the antenna occur causing the  
3166      shape of the radiation pattern to change as a function of distance from the antenna. If we  
3167      evaluate the far-field distance limit for the FSCD one finds an estimated far-field distance  
3168      of 43 cm, which is a factor of four larger than the radius of the antenna array designed for  
3169      the experiment. Consequently, we expect near-field effects to influence the performance  
3170      of the antenna array highlighting the importance of calibration and characterization  
3171      measurements.

#### 3172      **5.2.1.4    Polarization**

3173        The polarization of an EM wave defines the spatial orientation of the electric field  
3174      oscillations in the plane perpendicular to the direction of the propagation, and is defined  
3175      in terms of orthogonal polarization components. In our application, one analyzes the  
3176      properties of radiation propagating along the radial ( $\hat{r}$ ) direction away from the antenna,  
3177      which implies that the electric fields can be described as a linear combination of orthogonal

<sup>3178</sup> polarization components

$$\mathbf{E}_{\text{tot}} = E_x \hat{x} + E_y \hat{y} + E_z \hat{z}, \quad (5.7)$$

<sup>3179</sup> in Cartesian coordinates, or

$$\mathbf{E}_{\text{tot}} = E_\theta \hat{\theta} + E_\phi \hat{\phi}, \quad (5.8)$$

<sup>3180</sup> in spherical coordinates.

<sup>3181</sup> In general, one defines partial radiation patterns, directivities, and gains so that the  
<sup>3182</sup> performance of the antenna for the desired polarization can be analyzed. The radiation  
<sup>3183</sup> pattern defined in terms of partial patterns is

$$U_{\text{tot}} = U_\phi + U_\theta, \quad (5.9)$$

<sup>3184</sup> where  $U_\phi$  and  $U_\theta$  are the radiation intensities in a particular direction for the respective  
<sup>3185</sup> polarization components. Similarly, a quantity such as gain can be written in terms of  
<sup>3186</sup> partial gains,

$$G_{\text{tot}} = G_\phi + G_\theta = \frac{2\pi U_\phi}{P_{\text{in}}} + \frac{2\pi U_\theta}{P_{\text{in}}}. \quad (5.10)$$

<sup>3187</sup> If we view an electron performing a circular orbit in the XY-plane from the side, that  
<sup>3188</sup> is, along the X or Y axes, then we would observe the electron to be performing a linear  
<sup>3189</sup> oscillation perpendicular to the viewing axis. From this intuitive picture, we can predict  
<sup>3190</sup> that the primary polarization of electric fields from CRES events to be linearly polarized  
<sup>3191</sup> in the  $\hat{\phi}$  direction when viewed with an antenna positioned in the XY-plane.

### <sup>3192</sup> 5.2.1.5 Antenna Factor and Effective Aperture

<sup>3193</sup> A useful way to characterize the performance of an antenna is to measure the electric  
<sup>3194</sup> field magnitude required to produce a signal with an amplitude of one volt in the antenna  
<sup>3195</sup> terminals. This ratio between the magnitude of the incoming electric field and the  
<sup>3196</sup> magnitude of the signal produced by the antenna is called the antenna factor, which is  
<sup>3197</sup> written as

$$A_F = \frac{|\mathbf{E}_{\text{in}}|}{V_{\text{ant}}}, \quad (5.11)$$

<sup>3198</sup> where  $A_F$  is the antenna factor,  $E_{\text{in}}$  is the incoming electric field, and  $V_{\text{ant}}$  is the magnitude  
<sup>3199</sup> of the voltage produced by the antenna.

<sup>3200</sup> The antenna factor can be expressed in terms of the antenna's gain through a related  
<sup>3201</sup> quantity called the effective aperture. The effective aperture defines for a given incident  
<sup>3202</sup> radiation power density ( $\text{W/m}^2$ ) the power that is received by the antenna. Therefore,

3203 the effective aperture gives the equivalent area of the antenna,

$$A_{\text{eff}} = \frac{P_{\text{rec}}}{P_{\text{in}}} = \frac{\lambda^2}{4\pi} G, \quad (5.12)$$

3204 where the received power is  $P_r$  and the total incoming power is  $P_{\text{in}}$ .

3205 If we express the incident power in terms of the magnitude of the Poynting vector,  
3206 then

$$|\mathbf{S}_{\text{in}}| = |\mathbf{E}_{\text{in}}|^2 / \eta_0, \quad (5.13)$$

3207 where  $\eta_0$  is the impedance of free-space, which relates the magnitudes of the electric and  
3208 magnetic fields in a vacuum, and is defined by

$$\eta_0 = \frac{|\mathbf{E}|}{|\mathbf{H}|} = \sqrt{\frac{\epsilon_0}{\mu_0}}. \quad (5.14)$$

3209 The total received power by the antenna can therefore be expressed as

$$P_{\text{rec}} = |\mathbf{S}_{\text{in}}| A_{\text{eff}} = |\mathbf{S}_{\text{in}}| \frac{\lambda^2}{4\pi} G = \frac{|\mathbf{E}_{\text{in}}|^2 \lambda^2 G}{4\pi \eta_0}. \quad (5.15)$$

3210 To relate this to the antenna factor recall that we can relate the voltage produced by  
3211 the antenna to the received power with

$$P_{\text{rec}} = \frac{V_{\text{ant}}^2}{Z} = \frac{|\mathbf{E}_{\text{in}}|^2}{A_F^2 Z}, \quad (5.16)$$

3212 where  $Z$  is the system impedance. Setting Equations 5.15 and 5.16 equal to each other,  
3213 we obtain the following expression for antenna factor in terms of gain

$$A_F = \sqrt{\frac{4\pi\eta_0}{ZG\lambda^2}} = \frac{9.73}{\lambda\sqrt{G}}. \quad (5.17)$$

3214 The second expression in Equation 5.17 is obtained by evaluating the constant terms  
3215 assuming a system impedance of  $50 \Omega$ .

3216 We have gone through the effort of expressing the antenna factor in terms of gain  
3217 to highlight that the majority of antenna parameters that we care to measure for a  
3218 CRES experiment can be obtained from the radiation or gain pattern of the antenna.  
3219 The antenna factor is a particularly important parameter for CRES measurements  
3220 due to its relevance to antenna array simulations with the Locust software [60, 78].  
3221 Specifically, Locust simulates the trajectory of an electron in a magnetic trap by running

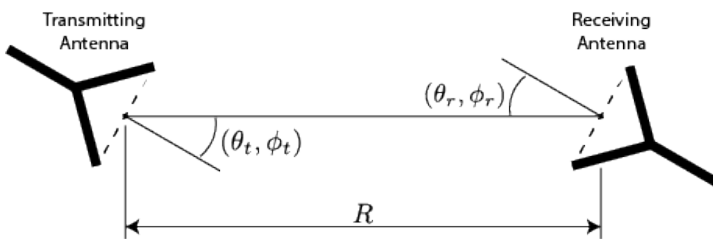
3222 the Kassiopeia software package [58] and then uses the Liénard-Wiechert equations [61, 62]  
3223 to calculate the electric fields that are incident on the antenna.

3224 To compute the response of the antenna to the electric field, Locust relies upon  
3225 linear time-invariant system theory, which computes the response of the antenna (i.e. the  
3226 voltage time series generated by the antenna) using a convolution between the electric field  
3227 time-series and the antenna impulse response. This approach is necessary for correctly  
3228 modeling the antenna response to the electric field due to the broadband and non-  
3229 stationary nature of the electric fields from CRES events. Since antenna measurements  
3230 take place under steady-state conditions, parameters such as the radiation pattern, gain,  
3231 and antenna factor are defined in the frequency domain. However, by performing an  
3232 inverse Fourier transform on the antenna factor we can obtain the antenna impulse  
3233 response, which allows us to simulate CRES events in the antenna array demonstrator  
3234 experiment.

### 3235 **5.2.2 Antenna Measurement Fundamentals**

#### 3236 **5.2.2.1 Friis Transmission Equation**

3237 The antenna factor, sometimes called the antenna transfer function, is used to model  
3238 how the antenna will respond to electric fields emitted from a CRES event. Therefore,  
3239 being able to measure the antenna transfer function of the antenna array is a key step  
3240 in the commissioning and calibration phases of an antenna array CRES experiment. A  
3241 common approach to antenna characterization is to perform a two antenna transmit-  
3242 receive measurement where an antenna with a known gain is used to characterize the  
3243 unknown gain of the antenna under test (see Figure 5.3).



3243 Figure 5.3: An illustration of the Friis measurement technique commonly used for antenna  
3244 characterization measurements.

3245 To analyze this two antenna setup we seek to calculate the amount of power from  
3246 the transmitting antenna that we will detect with the receiving antenna. Using our  
3247 understanding of antenna gain, we can calculate the power density transmitted by an

3247 antenna in a direction  $(\theta_t, \phi_t)$  at frequency  $f$  and distance  $R$ , which is given by

$$w_t = \frac{P_t}{4\pi R^2} G_t(\theta_t, \phi_t, f). \quad (5.18)$$

3248 Here,  $P_t$  is the total power delivered to the transmitting antenna and  $G_t(\theta_t, \phi_t, f)$  is  
3249 the value of the transmitting antenna gain. The power density is the power per unit  
3250 area, so to calculate the total power delivered to the receiving antenna we multiply the  
3251 transmitted power density by the effective area of the receiving antenna,

$$P_r = w_t A_{eff,r} = P_t \frac{G_t(\theta_t, \phi_t, f) G_r(\theta_r, \phi_r, f) c^2}{(4\pi R f)^2}, \quad (5.19)$$

3252 where  $G_r(\theta_r, \phi_r, f)$  is the gain of the receiving antenna. Equation 5.19 is called the Friis  
3253 transmission equation [84], which is of fundamental importance for antenna measurements,  
3254 since it allows one to measure the gain of an unknown antenna by measuring the power  
3255 received from an antenna with a known gain pattern. Alternatively, if no antenna with a  
3256 known gain pattern is available, two identical antennas with unknown gain patterns can  
3257 be used.

### 3258 5.2.2.2 S-Parameters and Network Analyzers

3259 Instead of directly measuring the power received by the antenna under test, it is more  
3260 common to measure the ratio of the received power to the transmitted power,

$$\frac{P_r}{P_t} = \frac{G_t(\theta_t, \phi_t, f) G_r(\theta_r, \phi_r, f) c^2}{(4\pi R f)^2}. \quad (5.20)$$

3261 This power ratio can be easily measured using a vector network analyzer (VNA), which  
3262 automates a significant fraction of the measurement process. Network analyzers are  
3263 used to measure the scattering or S-parameters of a multi-port RF device [85], which  
3264 describes how waves are scattered between the device ports. The antenna measurements  
3265 we have been considering can be modeled as a two-port microwave device that we can  
3266 characterize by measuring how incident voltage waves are transmitted or reflected (see  
3267 Figure 5.4). We can write the scattered waves ( $V_1^-$  and  $V_2^-$ ) in terms of the incident ( $V_1^+$   
3268 and  $V_2^+$ ) waves using the scattering matrix

$$\begin{pmatrix} V_1^- \\ V_2^- \end{pmatrix} = \begin{pmatrix} S_{11} & S_{12} \\ S_{21} & S_{22} \end{pmatrix} \begin{pmatrix} V_1^+ \\ V_2^+ \end{pmatrix}, \quad (5.21)$$

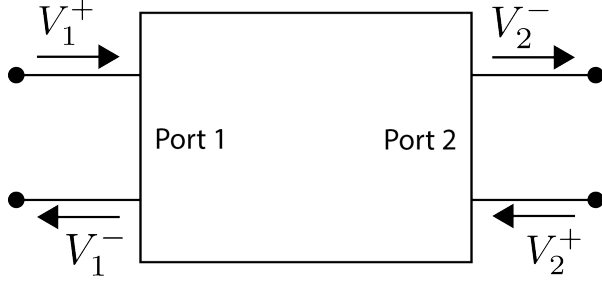


Figure 5.4: Illustration of a two-port S-parameter measurement setup. S-parameters characterize how incoming waves of voltage or power scatter off of the RF device under test. This allows you to measure important properties of the device. In particular, we can use this framework to model a two antenna radiation pattern measurement, which we can then automate using a VNA.

3269 where the elements of the matrix are the device S-parameters. It is assumed that,  
 3270 when exciting the device from a particular port, that all other ports in the network are  
 3271 terminated at the system impedance. This ensures that the incident waves from other  
 3272 ports in the network are zero. Therefore, the S-parameters are the ratios between the  
 3273 scattered and incident waves,

$$S_{ij} = \frac{V_i^-}{V_j^+}. \quad (5.22)$$

3274 Alternatively, S-parameters can be defined as the ratio of the scattered and incident  
 3275 power, which is proportional to the ratio of the squared voltage waves. Returning to  
 3276 our antenna measurement setup, we see that measuring the ratio of the received to the  
 3277 transmitted power is equivalent to measuring the ratio of power being scattered from port  
 3278 1 to port 2 in a RF network. Therefore, measuring an antenna's gain can be accomplished  
 3279 quite easily, by using a VNA to perform a two port  $S_{21}$  measurement.

### 3280 5.2.2.3 Antenna Array Commissioning and Calibration Measurements

3281 Up to this point we have been discussing calibration and commissioning measurements  
 3282 as they apply to a single antenna. While these measurements play an important role  
 3283 in validating the radiation patterns of the individual array elements, the ultimate goal  
 3284 is to use a phased array of these antennas. Therefore, we must also consider antenna  
 3285 measurement techniques that apply to the whole array system.

3286 By measuring the gain of each individual array element we can predict the features of  
 3287 the signals received during a CRES event using the antenna factor (see Section 5.2.1.5).  
 3288 However, unpredictable changes to the antenna performance can be introduced by the

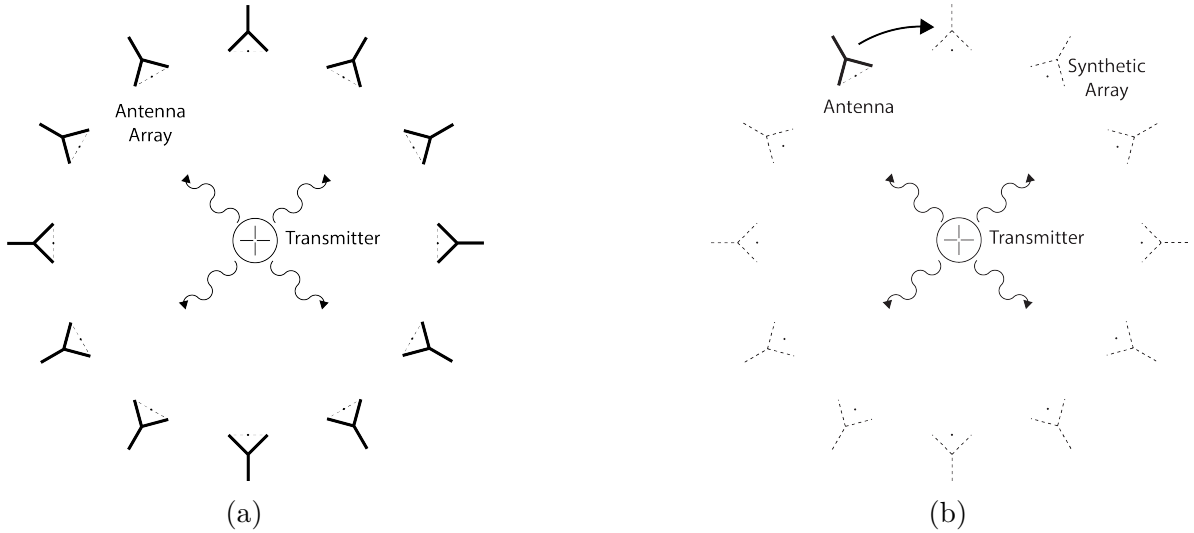


Figure 5.5: Two measurement approaches to characterize an antenna array for CRES measurements. The full-array approach (a) requires a complete antenna array with all the associated hardware. The synthetic array approach (b) utilizes a single antenna and a set of rotation/translation stages to reposition the transmitter or the receiving antenna to synthesize the signals that would be received by the full-array. This approach reduces the cost and complexity of array measurements. A down-side of the synthetic array approach is that multi-channel effects such as reflections cannot be measured. Utilizing both the full-array and the synthetic array is a powerful way to quantify the impact of errors from the multi-channel array.

incorporation of the antennas into the circular array geometry, therefore, we employ both individual antenna and full-array measurements in the commissioning of the FSCD to account for these effects.

There are two main approaches to array measurements that could be used for characterization and calibration (see Figure 5.5). One approach is to construct the complete array and use an omni-directional transmitting antenna to measure the power received by each channel in the antenna array. In Section 5.3 we describe the development of an omni-directional transmitter that also mimics the radiation phase characteristics of a CRES event, which is useful because the entire array can be tested without repositioning. Alternatively, a full antenna array can be synthesized by repeatedly moving and measuring a single array element. This approach is ideal for identifying if different channels in the antenna array are affecting each other through multi-path interference by comparing the measurement results of the synthetic array to the real array.

### **5.2.3 The Penn State Antenna Measurement System**

The development of antenna array based CRES requires the capability to test and calibrate different antenna array designs to validate the performance of the as-built antenna array before and during the experiment. With these aims in mind we developed an antenna measurement system at Penn State specifically designed to mimic the characteristics of the antenna experiment designed for demonstration of the antenna array CRES technique by the Project 8 collaboration.

The Penn State antenna measurement system utilizes a two antenna measurement configuration with a stationary reference antenna and a test antenna mounted on a set of motorized translation and rotation stages (see Figure 5.6). The antenna measurement system can be operated in two distinct modes, one focused on the characterization of the radiation patterns of prototype antennas and the other focused on the validation of data-acquisition (DAQ) and CRES signal reconstruction techniques to bridge the gap between real measurements and simulation. In both measurement configurations it is critical to isolate the antennas from the environment so that multi-path reflections do not negatively influence the measurement results. For this reason we surround the measurement volume with microwave absorber foam (AEMI AEC-1.5) specifically designed to attenuate microwave radiation near the 26 GHz measurement range of the system.

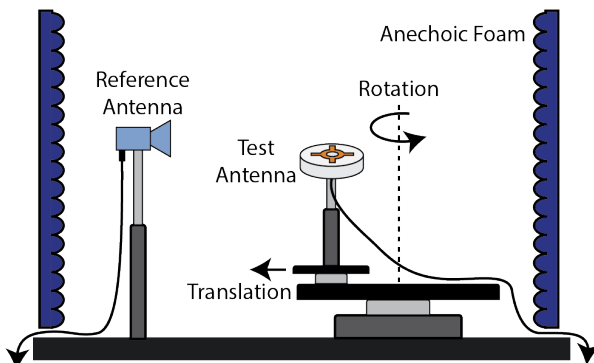


Figure 5.6: Illustration of the antenna measurement system developed for the Project 8 Collaboration. The reference and test antennas can be connected to different data acquisition configurations depending on the measurement goals. The reference antenna is typically a standard horn antenna and the test antenna is mounted on a set of translation stages for positioning. Automated translation stages allow for relatively painless data-taking enabling synthetic antenna array measurements using only a single receiving antenna. Anechoic form designed to mitigate RF reflections surrounds the setup.

In the first measurement configuration the reference antenna is typically a well-

characterized horn antenna as pictured, since horn antennas have well-known and stable radiation patterns making them ideal as standard references. For characterization measurements, the test antenna represents the antenna-under-test whose pattern we wish to characterize. Mounting the test antenna on motorized rotation and translation stages allows us to automate the procedure significantly speeding up the radiation pattern measurement process.

In the second measurement configuration one is interested in recreating the conditions of an antenna array CRES experiment as it concerns the antenna array and DAQ system. In this case, the reference antenna is a prototype FSCD antenna, which will be used to construct the antenna array in the FSCD experiment, and the test antenna is a specially designed synthetic cyclotron antenna (SYNCA) as picture in Figure 5.6. The SYNCA is designed such that the radiation pattern mimics that of a CRES electron so that the signals received by the prototype CRES array antenna mimic what is expected for a real CRES experiment.

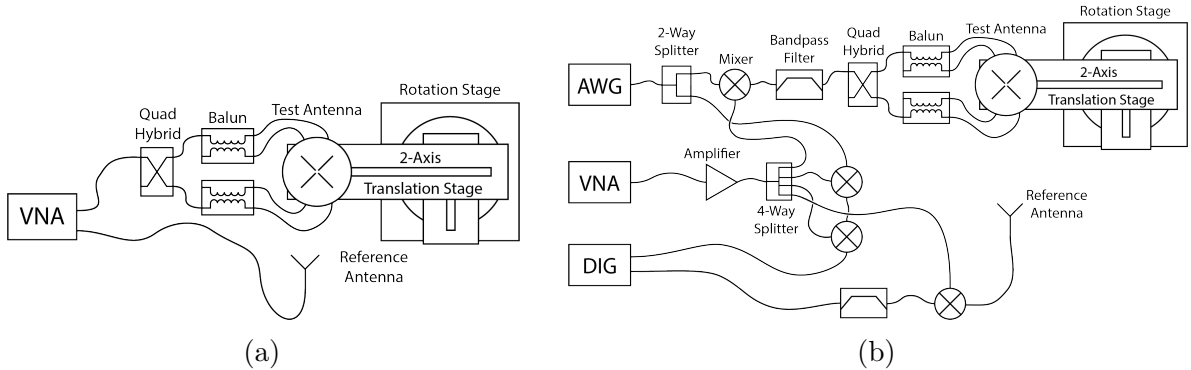


Figure 5.7: Diagrams of two measurement system configurations. Configuration (a) utilizes a VNA and is more suited to antenna characterization. Configuration (b) utilizes an AWG and VNA as a signal generation system and digitizer to collect measurement data, which is more suited to simulating CRES measurements. The transmission chain utilizes a quadrature hybrid and a pair of baluns to drive the cross-dipole variant test antenna developed for synthetic CRES measurements.

In Figure 5.7 we show two high-level system diagrams of the Penn State antenna measurement system that depict the important system components and the connections between them. The two configurations of the measurement system utilize different hardware. For characterization and radiation pattern measurements, one prefers the configuration shown in Figure ???. In this case a vector network analyzer (VNA) is used as both the transmission source and data acquisition system and it is relatively easy to calibrate over a wide range of frequencies. Whereas, if one is more interested in recreating

3343 what would take place in the FSCD experiment then the configuration shown in Figure  
3344 ?? is preferable, since this system effectively mimics the receiver chain envisioned for the  
3345 FSCD experiment.

3346 The characterization configuration utilizes a network analyzer (Keysight N5222A)  
3347 with two independent sources and four measurement ports as the primary measurement  
3348 tool. A standard reference antenna is connected to one measurement port, and the test  
3349 antenna is connected to a separate port. The typical reference antenna used for these  
3350 studies is a Pasternack PF9851 horn antenna . In the measurement shown, the test  
3351 antenna represents a SYNCA antenna, which requires a transmission chain consisting of  
3352 quadrature hybrid coupler (Marki QH-0226) connected to two baluns (Marki BAL-0026)  
3353 to generate feed signals with the appropriate phases. The VNA measures the radiation  
3354 pattern by performing a transmission S-parameter measurement, which can be used with  
3355 the knowledge of the reference antenna's radiation pattern to determine the radiation  
3356 pattern of the test antenna (see Section 5.2.1).

3357 The second configuration is more complicated and incorporates more hardware  
3358 components in order to more closely mimic the DAQ system envisioned for the FSCD  
3359 experiment. The basic approach is to produce CRES-like radiation and use an antenna  
3360 combined with a realistic RF receiver chain to acquire the signals. On the transmit side,  
3361 an arbitrary waveform generator (AWG, RIGOL DG5252) is used to generate a waveform  
3362 that mimics a CRES signal at a baseband frequency up to 250 MHz. This frequency is  
3363 then up-converted to the CRES signal frequency band of 25.8 to 26.0 GHz using a mixer  
3364 (Marki MM1-0832L) and a bandpass filter (K&L Microwave 3C62-25900/T200-K/K) to  
3365 reject unwanted mixing components outside out of the 200 MHz CRES signal band. The  
3366 local oscillator signal for mixing is provided by one of the VNA sources configured to run  
3367 in a continuous wave setting. On the receive side, a prototype antenna is used to detect  
3368 the radiation emitted by the test antenna, which is down-converted and filtered using  
3369 the same mixer and bandpass filter as the transmission chain. Lastly, data acquisition is  
3370 performed using a 14-bit ADC sampling at 500 MSa/s (CAEN DT530) to digitize the  
3371 down-converted signals.

3372 In order to distribute the LO to all mixers a 4-way power splitter (MiniCircuits  
3373 ZC4PD-18263-S+) along with an amplifier (Marki APM-6848) is used to drive the four  
3374 mixers used in the measurement system. A limitation of using the VNA as an LO source  
3375 is that there is no control of the LO phase when a measurement is triggered by the  
3376 control script, which leads to a random phase offset between acquisitions. This makes it  
3377 impossible to perform synthetic array measurements, which require strict control over

3378 the starting phase of the transmitted signal. In order to monitor the random phase of the  
3379 LO, a 2-way power splitter (MiniCircuits Z99SC-62-S+) is used to split the signal from  
3380 the AWG between the transmission path and a LO monitoring path. The LO monitoring  
3381 path consists of an up-conversion and down conversion using two mixers connected by a  
3382 coaxial cable, and monitors the relative phase of the LO using a channel on the digitizer  
3383 to sample this path. A phase shift in the LO will lead to a proportional phase shift in  
3384 the mixed signal, which is measured and removed from the received signals.

3385 The test antenna is mounted on a set of motorized stages, which are identical for  
3386 both measurement configurations. A rotational stage (ThorLabs PRMTZ8) is used as  
3387 the base layer with additional translation stages mounted on top of this. The rotational  
3388 stage is ideal for measuring a complete azimuthal scan of the test antenna's radiation  
3389 pattern as well as for moving a SYNCA antenna in circular motion to recreate the  
3390 symmetry of the FSCD antenna array. On top of the rotational stage we mount two  
3391 linear translation stages (ThorLabs MTS50-Z8 and MTS25-Z8) in a cross-wise manner  
3392 so that the test antenna can be moved along two perpendicular axes. Using the linear  
3393 stages in combination with the rotational stage allows one to fine-tune the positioning of  
3394 the test antenna so that it can be perfectly aligned with the central axis of the array.  
3395 A LabView script was developed to automate the measurement of a full 360° radiation  
3396 pattern and control the measurement electronics. Data from these acquisitions is stored  
3397 on university provided cloud storage.

## 3398 **5.3 Development of a Synthetic Cyclotron Antenna (SYNCA)** 3399 **for Antenna Array Calibration**

3400 This section is the manuscript of the publication [79] detailing the development of a  
3401 Synthetic Cyclotron Antenna (SYNCA) for antenna array characterization measurements  
3402 by the Project 8 collaboration.

### 3403 **5.3.1 Introduction**

3404 Neutrinos are the most abundant standard model fermions in our universe, but due to  
3405 weak interaction cross-sections with other particles, neutrinos are particularly difficult  
3406 to study. Consequently, many fundamental properties of neutrinos are still unknown  
3407 including the absolute scale of the neutrino mass [28]. Direct, kinematic measurements of  
3408 the neutrino mass are particularly valuable due to their model independent nature [35].

3409 To date the most sensitive direct neutrino mass measurements have been performed by  
 3410 the KATRIN collaboration [86], which measures the molecular tritium  $\beta$ -decay spectrum  
 3411 to infer the neutrino mass. Current data from neutrino oscillation measurements [28]  
 3412 allow for neutrino masses significantly smaller than the design sensitivity of the KATRIN  
 3413 experiment; therefore, there is a need for new technologies for performing direct neutrino  
 3414 mass measurements to probe lower neutrino masses.

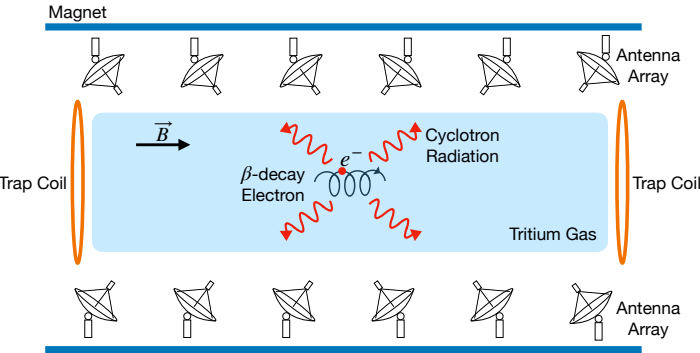


Figure 5.8: A sketch of an antenna array large-volume CRES experiment. Electrons from  $\beta$ -decays are confined in a magnetic field using a set of trap coils. The cyclotron radiation produced by the motion of the trapped electrons can be detected by a surrounding antenna array to determine the electron energies. Measuring the energies of many electrons produces a  $\beta$ -decay spectrum.

3415 The Project 8 collaboration is developing new methods for neutrino mass measurement  
 3416 based on Cyclotron Radiation Emission Spectroscopy (CRES) [54, 87–89], with the goal  
 3417 of measuring the absolute scale of the neutrino mass with a  $40 \text{ meV}/c^2$  sensitivity [?, 35].  
 3418 This sensitivity goal will require the development of two separate technical capabilities.  
 3419 First is the development of an atomic tritium source, which avoids significant spectral  
 3420 broadening due to molecular final states [53]. Second is the technology for performing  
 3421 CRES in a multi-cubic-meter experimental volume with high combined detection and  
 3422 reconstruction efficiency, which is required in order to obtain sufficient event statistics  
 3423 near the tritium spectrum endpoint.

3424 One approach for a large-volume CRES experiment is to use an array of antennas,  
 3425 which surrounds a volume of tritium gas, to detect the cyclotron radiation produced  
 3426 by the  $\beta$ -decay electrons when they are trapped in a background magnetic field using a  
 3427 set of magnetic trapping coils (see Figure 5.8). Project 8 has developed a conceptual  
 3428 experiment design to study the feasibility of this approach. The design consists of a  
 3429 single circular array of antennas with a radius of 10 cm and 60 independent channels  
 3430 positioned around the center of the magnetic trap. The motivation behind this antenna

array design is to first develop an understanding of the antenna array approach to CRES with a small scale experiment before attempting to scale the technique to large volumes by using multiple antenna rings to construct the full cylindrical array. The development of the antenna array approach to CRES has largely proceeded through simulations using the Locust software package [78, 90], which is used to model the fields emitted by CRES events and predict the signals received by the surrounding antenna array. To validate these simulations, a dedicated test stand is being constructed to perform characterization measurements of the prototype antenna array developed by Project 8 (see Figure 5.9) and benchmark signal reconstruction methods using a specially designed transmitting calibration probe antenna.

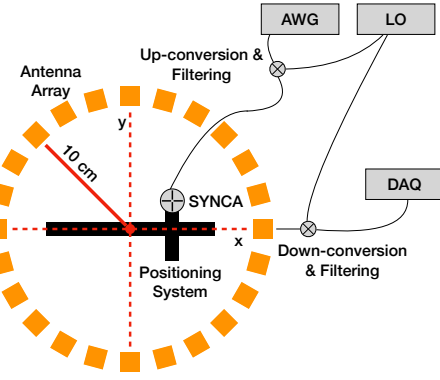


Figure 5.9: A schematic of the antenna array test stand. The circular antenna array has a radius of 10 cm with 60 independent channels (limited number shown for clarity). The test stand includes an arbitrary waveform generator (AWG), local oscillator (LO), and data acquisition (DAQ) hardware. Finally, a specialized Synthetic Cyclotron Antenna (SYNCA) is used to inject signals to test the antenna array.

We call this probe antenna the Synthetic Cyclotron Antenna or SYNCA. The SYNCA is a novel antenna design that mimics the cyclotron radiation generated by individual charged particles trapped in a magnetic field, which will be used in the antenna test stand to perform characterization measurements, simulation validation, and reconstruction benchmarking. This paper provides an overview of the design, construction, and characterization measurements of the SYNCA performed in preparation for its usage as a transmitting calibration probe.

In Section 5.3.2 we provide a description of the cyclotron radiation field characteristics that we recreate with the SYNCA. In Section 5.3.3 we give an overview of the simulations performed to develop an antenna design that mimics the characteristics of cyclotron radiation. In Section 5.3.4 we outline characterization measurements to validate that

3452 the fields generated by the SYNCA match simulation, and finally in Section 5.3.5 we  
3453 demonstrate an application of the SYNCA to test phased array reconstruction techniques  
3454 on the bench-top.

### 3455 5.3.2 Cyclotron Radiation Phenomenology

3456 To understand the cyclotron radiation phenomenology that the SYNCA should mimic,  
3457 we consider a charged particle moving at relativistic speed in the presence of an external  
3458 magnetic field (see Figure 5.10). In the special case we shall examine, the entirety of  
3459 the electron's momentum is directed perpendicular to the magnetic field; therefore, the  
3460 trajectory of the electron is confined to the cyclotron orbit plane. Because the momentum  
3461 vector is oriented perpendicular to the magnetic field, electrons with these trajectories  
3462 are said to have pitch angles of 90°.

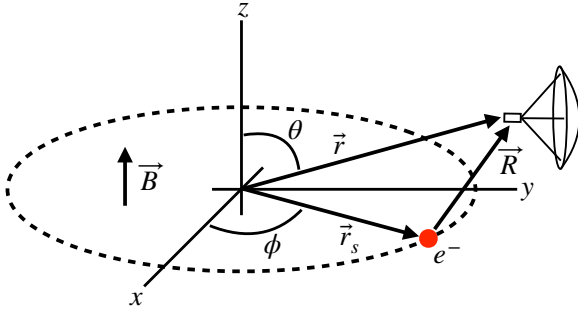


Figure 5.10: An electron (red dot) performing cyclotron motion in the x-y plane. The resulting cyclotron radiation is observed by an antenna located at the field point of interest.

3463 The cyclotron radiation fields generated by this circular trajectory are those which  
3464 we aim to reproduce with the SYNCA. We can describe the electromagnetic (EM) fields  
3465 using the Liénard-Wiechert equations [47, 78], which in non-covariant form express the  
3466 electric field as

$$\vec{E} = e \left[ \frac{\hat{n} - \vec{\beta}}{\gamma^2 (1 - \vec{\beta} \cdot \hat{n})^3 |\vec{R}|^2} \right]_{t_r} + \frac{e}{c} \left[ \frac{\hat{n} \times [(\hat{n} - \vec{\beta}) \times \dot{\vec{\beta}}]}{(1 - \vec{\beta} \cdot \hat{n})^3 |\vec{R}|} \right]_{t_r}, \quad (5.23)$$

3467 where  $e$  is the particle's charge,  $\hat{n} = (\vec{r} - \vec{r}_s)/|\vec{r} - \vec{r}_s|$  is the unit vector pointing from the  
3468 electron to the field measurement point,  $\vec{\beta} = \dot{\vec{r}}_s/c$  is the velocity of the particle divided  
3469 by the speed of light, and  $\gamma$  is the relativistic Lorentz factor. The equation is meant to  
3470 be evaluated at the retarded time as indicated by  $t_r = t - |\vec{R}|/c$ , which accounts for the

<sup>3471</sup> time delay due to the finite speed of light between the point where the field was emitted  
<sup>3472</sup> and the point where the field is detected.

<sup>3473</sup> We would like to simplify Equation 5.23 it at all possible. As a first step we analyze  
<sup>3474</sup> the relative magnitudes of the electric field polarization components. Consider an electron  
<sup>3475</sup> following a circular cyclotron orbit in a uniform magnetic field whose guiding center  
<sup>3476</sup> is positioned at the origin of the coordinate system. The equation of motion can be  
<sup>3477</sup> expressed as

$$\vec{r}_s = (r_c \cos \omega_c t_r) \hat{x} + (r_c \sin \omega_c t_r) \hat{y}. \quad (5.24)$$

<sup>3478</sup> For single antenna located along the y-axis at position  $\vec{r} = r_a \hat{y}$  we are interested in the  
<sup>3479</sup> incident electric fields from the electron. The electric field is given by Equation 5.23,  
<sup>3480</sup> which we evaluate in the regime where  $r_a \gg r_c$ . This limit can be justified by comparing  
<sup>3481</sup> the radius of the cyclotron orbit for an electron with the tritium beta-spectrum endpoint  
<sup>3482</sup> energy of 18.6 keV in a 1 T magnetic field to the typical ( $r_a \simeq 100$  mm) radial position  
<sup>3483</sup> of the receiving antenna. We find that the cyclotron orbit has a radius of 0.46 mm which  
<sup>3484</sup> is approximately a factor of 200 smaller than the typical antenna radial position. In this  
<sup>3485</sup> regime we can make the approximation  $\vec{R} \simeq r_a \hat{y}$  and the expression for the electric field  
<sup>3486</sup> at the antenna's position becomes

$$\vec{E} = \frac{e}{\gamma^2 r_a^2} \frac{\hat{x} \left( \frac{r_c \omega_c}{c} \sin \omega_c t_r \right) + \hat{y} \left( 1 - \frac{r_c \omega_c}{c} \cos \omega_c t_r \right)}{\left( 1 - \frac{r_c \omega_c}{c} \cos \omega_c t_r \right)^3} - \frac{e}{cr_a} \frac{\hat{x} \left( \frac{r_c^2 \omega_c^3}{c^2} - \frac{r_c \omega_c^2}{c} \cos \omega_c t_r \right)}{\left( 1 - \frac{r_c \omega_c}{c} \cos \omega_c t_r \right)^3}. \quad (5.25)$$

<sup>3487</sup> Since the receiving antenna is part of a circular array of antennas, it is useful to rewrite  
<sup>3488</sup> Equation 5.25 in terms of the azimuthal ( $\hat{\phi}$ ) and radial ( $\hat{r}$ ) polarizations. Making use of  
<sup>3489</sup> the fact that for an antenna located at  $R = r_a \hat{y}$  that  $\hat{\phi} = -\hat{x}$  and  $\hat{r} = \hat{y}$  we find

$$\vec{E} = \hat{\phi} E_\phi + \hat{r} E_r \quad (5.26)$$

$$E_\phi = \frac{e}{\left( 1 - \frac{r_c \omega_c}{c} \cos \omega_c t_r \right)^3} \left[ -\frac{\frac{r_c \omega_c}{c} \sin \omega_c t_r}{\gamma^2 r_a^2} + \frac{\omega_c \left( \frac{r_c^2 \omega_c^2}{c^2} - \frac{r_c \omega_c}{c} \cos \omega_c t_r \right)}{cr_a} \right] \quad (5.27)$$

$$E_r = \frac{e \left( 1 - \frac{r_c \omega_c}{c} \sin \omega_c t_r \right)}{\gamma^2 r_a^2 \left( 1 - \frac{r_c \omega_c}{c} \cos \omega_c t_r \right)^3}. \quad (5.28)$$

<sup>3490</sup> For the purposes of designing a synthetic cyclotron radiation antenna we are interested  
<sup>3491</sup> in the dominant electric field polarization emitted by the electron. The antenna is being  
<sup>3492</sup> designed to mimic the cyclotron radiation produced by electrons with kinetic energies of  
<sup>3493</sup> approximately 18.6 keV in a 1 T magnetic field [53]. Since the relativistic beta factor for

3494 an electron with this kinetic energy is  $|\vec{\beta}| \simeq \frac{1}{4}$ , the approximations  $\gamma \simeq 1$  and  $\frac{r_c \omega_c}{c} \simeq \frac{1}{4}$  are  
 3495 justified. Inserting these expressions into the equations for the electric field components  
 3496 above simplifies the comparison of the magnitudes of the two components. Additionally,  
 3497 we compare the time-averaged magnitudes to evaluate the root mean squared electric  
 3498 field ratio. The time-averaged ratio of the radial and azimuthally polarized electric fields  
 3499 with the above simplifications is given by

$$\frac{\langle |E_r| \rangle}{\langle |E_\phi| \rangle} = \frac{8 - \sqrt{2}}{\left| 1 - \frac{r_a}{r_c} \frac{1-2\sqrt{2}}{8} \right|} \simeq \frac{r_c}{r_a} \frac{8(8 - \sqrt{2})}{2\sqrt{2} - 1} = 0.13, \quad (5.29)$$

3500 where we have made use of the fact that for these magnetic fields and kinetic energies  
 3501 the cyclotron radius is much smaller than the radius of the antenna array.

3502 From Equation 5.29 we see that the time-averaged azimuthal polarization is larger than  
 3503 the radial polarization by about a factor of 8, which makes it the dominant contribution  
 3504 to the electric fields at the position of the antenna. We must also consider the directivity  
 3505 of the receiving antenna which can have a gain that is disproportionately large for a  
 3506 specific polarization component. Because the  $E_\phi$  component is dominant, the receiving  
 3507 antenna array is designed with an azimuthal polarization, which negates the voltages  
 3508 induced in the antenna from the radially polarized fields. Therefore, we conclude that  
 3509 for the purpose of designing the SYNCA antenna it is acceptable to approximate the  
 3510 electric fields from Equation 5.23 as purely azimuthally or  $\phi$ -polarized. The simplified  
 3511 expression for the electric field received by an antenna becomes

$$\vec{E} = E_\phi \hat{\phi} = \frac{e \frac{r_c \omega_c}{c}}{4r_a r_c} \left[ \frac{\frac{r_c \omega_c}{c} - \cos \omega_c t - \frac{4r_c}{r_a} \sin \omega_c t}{(1 - \frac{r_c \omega_c}{c} \cos \omega_c t)^3} \right]_{t_r} \hat{\phi}, \quad (5.30)$$

3512 where the radius of the cyclotron orbit is called  $r_c$ , the cyclotron frequency is called  $\omega_c$ ,  
 3513 and the radial position of the receiving antenna is called  $r_a$ . Equation 5.30 has been  
 3514 evaluated in the non-relativistic limit where  $\gamma \simeq 1$ , which is justified by the fact that  
 3515  $|\vec{\beta}| \simeq \frac{c}{4}$  for an electron with an 18.6 keV kinetic energy in a 1 T magnetic field.

3516 This rather complicated expression can be simplified using Fourier analysis. Assuming  
 3517 a background magnetic field of 1 T and a kinetic energy of 18.6 keV we calculate  
 3518 numerically the electric field using Equation 5.30 and apply a discrete Fourier Transform  
 3519 to visualize the frequency spectrum (see Figure 5.11).

3520 We observe that the azimuthally polarized electric field is periodic with a base cyclotron  
 3521 frequency of 25.898 GHz corresponding to the highest power frequency component in

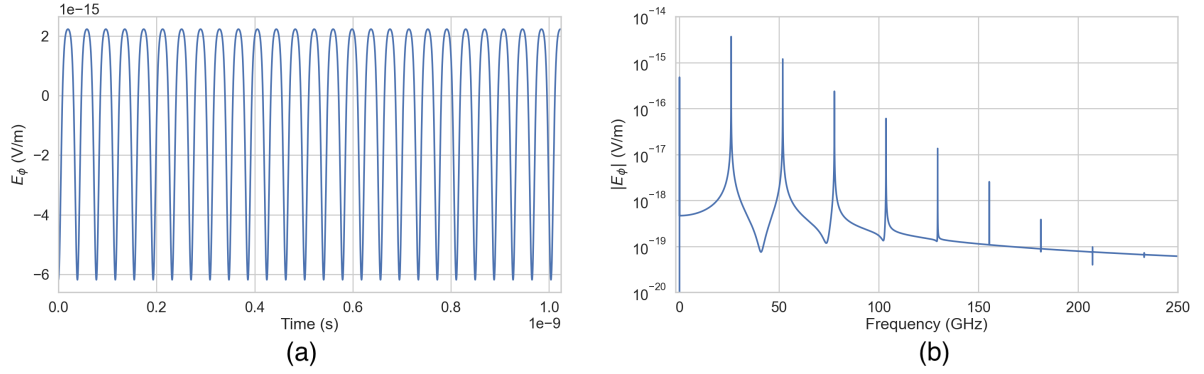


Figure 5.11: A plot of the numeric solution to Equation 5.31. The time-domain representation of the signal (a) is composed of a zero frequency term and a series of harmonics separated by the main cyclotron frequency as shown in the plot of the frequency spectrum (b). We can see that the relative amplitude of the harmonics beyond  $k = 7$  are smaller than the main carrier by a factor of about  $10^{-5}$  and are completely negligible.

3522 Figure 5.11. The frequency spectrum reveals that the signal is composed of a constant  
 3523 term with zero frequency and a series of harmonics separated by 25.898 GHz. Therefore,  
 3524 we can represent the azimuthal electric fields from the electron as a linear combination  
 3525 of pure sinusoids with frequencies given by  $\omega_k = k\omega_c$  ( $k \in 0, 1, 2, \dots$ ) and amplitudes  
 3526 extracted from the Fourier representation. Using this representation we can transform  
 3527 the equation for the azimuthally polarized electric fields in Equation 5.30 into

$$E_\phi = \frac{e^{\frac{r_c \omega_c}{c}}}{4r_a r_c} \sum_{k=0}^7 A_k e^{i\omega_k t_r}, \quad (5.31)$$

3528 where we have truncated the sum over harmonics at the 7th order for completeness. The  
 3529 amplitudes  $A_k$  are dimensionless complex numbers, which encode the relative powers of  
 3530 the harmonics as well as the starting overall phase of the cyclotron radiation. Because  
 3531 magnitude of the relative amplitudes exponentially decreases for higher harmonics, it is  
 3532 usually sufficient to consider only the terms up to  $k = 4$  where the relative amplitude  
 3533 of the harmonics has decreased from the main carrier by a factor of approximately 100.  
 3534 However, for completeness we include harmonics up to 7th order in Equation 5.31. The  
 3535 range of frequencies to which the receiving antenna array in the antenna test stand is  
 3536 sensitive is defined by the antenna's transfer function. The receptive bandwidth for  
 3537 the antennas used in the test stand is a range of frequencies with a bandwidth on the  
 3538 order of a few GHz centered around the main cyclotron carrier frequency of 25.898 GHz.  
 3539 Therefore, the higher order harmonics as well as the zero frequency term can be ignored

3540 when considering only the signals that will be received by the antenna array.

3541 Considering only the 1st order harmonic term from Equation 5.31, which represents  
3542 the portion of the electric field that will be detected by the array, and evaluating this at  
3543 the retarded time we obtain the following for the  $\phi$ -polarized electric fields

$$E_\phi \propto \cos \left( \omega_c \left( t - |\vec{R}|/c \right) - \Delta \right), \quad (5.32)$$

3544 where the arbitrary phase  $\Delta$  is defined by  $A_k = |A_k|e^{i\Delta}$ . We are interested in the  
3545 characteristics of the amplitude of the electric field as a function of the radial distance  
3546 component ( $|\vec{R}|$ ) of the retarded time. In particular, the maximum of  $E_\phi$  occurs when  
3547 the argument of the cosine function is equal  $n\pi$  where  $n \in \{0, \pm 2, \pm 4, \dots\}$ ; however, the  
3548 solutions where  $n$  is negative can be discarded since they represent unphysical negative  
3549 overall phases. Applying this condition to Equation 5.32 gives a condition on the radial  
3550 position of the maximum of  $E_\phi$

$$\omega_c(t - |\vec{R}|/c) - \Delta = n\pi, \quad (5.33a)$$

$$|\vec{R}| = \frac{c}{\omega_c} ((\omega_c t - \Delta) - n\pi), \quad (5.33b)$$

3551 which is a function of time in the frame of the moving electron ( $t$ ). Equation 5.33 can  
3552 be further simplified by noticing that the azimuthal position of the electron ( $\phi_e(t)$ ) as a  
3553 function of time is defined by  $\phi_e(t) = \omega_c t - \Delta$  which reduces Equation 5.33 to

$$|\vec{R}| = \frac{c}{\omega_c} (\phi_e(t) - n\pi). \quad (5.34)$$

3554 Equation 5.34 represents an archimedean spiral which is formed when plotting the  
3555 amplitude of  $E_\phi$  in the x-y plane. The solution where  $n = 0$  represents the leading edge  
3556 of the radiation spiral which propagates outward from the electron at the speed of light.  
3557 The additional solutions for  $n > 0$  represent the persistent spiral at radii inside the  
3558 leading edge of the radiated fields that have not yet been detected by the receiver at the  
3559 current time. In Figure 5.12a we show the expected spiral pattern for the maxima of the  
3560 cyclotron radiation.

3561 In particular, we note that for the circular array geometry of the test stand, depicted  
3562 as the series of circles in Figure 5.12a, each antenna receives a linearly polarized wave  
3563 with a phase offset that corresponds to the azimuthal angle for that antenna element.  
3564 Therefore, as we show in Figure 5.12b, when the relative phase of the received signal is  
3565 plotted as a function of the receiving antenna's azimuthal position the result is also an

3566 Archimedean spiral.

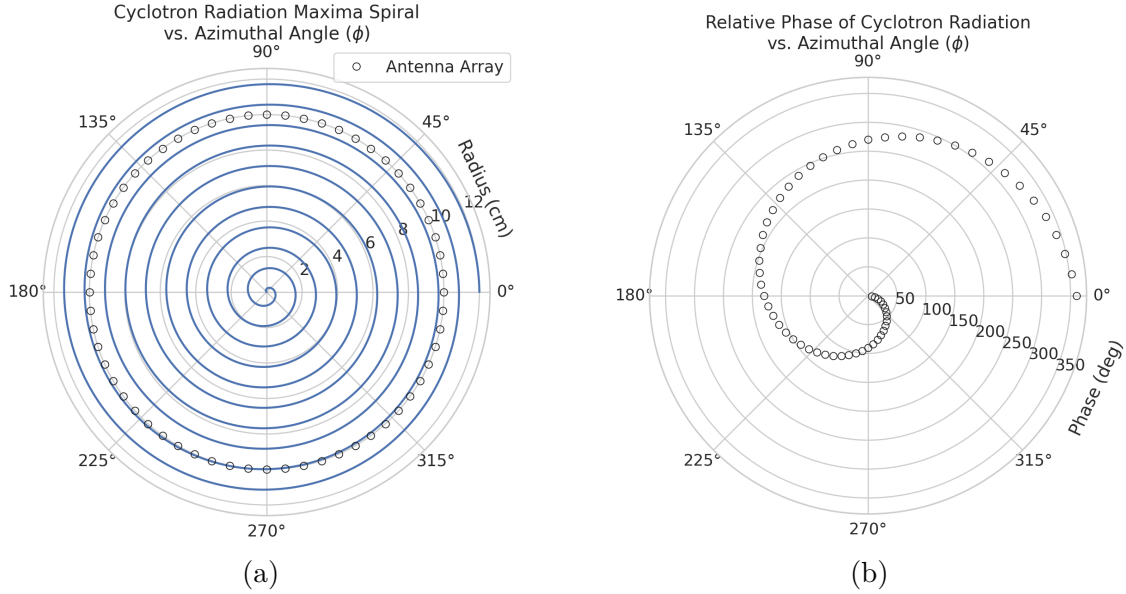


Figure 5.12: The amplitude maxima of the cyclotron radiation form an Archimedean spiral as the radiation propagates outward from the cyclotron orbit center (a). A circular antenna array located at a fixed radius from the orbit center will receive electric fields with equal magnitude in each of its channels, but the phase of the electric field incident on each array channel will be linearly out of phase from its neighbor antennas by an amount equal to the angular separation of the two channels (b).

3567 Based on these analytical calculations we can characterize the magnitude, polarization,  
 3568 and phase of the signals received by the antenna array using three criteria. These criteria  
 3569 are the basis of comparison for the radiation produced by the SYNCA and cyclotron  
 3570 radiation emitted by electrons and will be used to evaluate the performance of antenna  
 3571 designs. The criteria are:

- 3572 1. Electric fields that are  $\phi$ -polarized near  $\theta = 90^\circ$
- 3573 2. Uniform time-averaged electric field magnitudes around the circumference of a  
 3574 circle centered on the antenna
- 3575 3. Electric fields whose phase is equal to the azimuthal angle at the point of measure-  
 3576 ment plus a constant

3577 The Locust simulation package [90] can be used to directly simulate the EM fields  
 3578 generated by electrons performing cyclotron motion to validate the analytical calculations.  
 3579 Locust simulates the EM fields by first calculating the trajectory of the electrons in

3580 the magnetic trap using the Kassiopeia software package [91]. The trajectory can then  
 3581 be used to solve for the EM fields using the Liénard-Wiechert equations directly with  
 3582 no approximations. The resulting electric field solutions drive a receiving antenna by  
 3583 convolving the time-domain fields with the finite-impulse response filter of the antenna  
 3584 or they can be examined directly to study the field characteristics that the SYNCA must  
 3585 reproduce. In the next section we compare the radiation field patterns for electrons  
 3586 simulated with Locust to patterns from a SYNCA antenna design.

### 3587 5.3.3 SYNCA Simulations and Design

3588 One potential SYNCA design is the crossed-dipole antenna [92]. A crossed-dipole antenna  
 3589 consists of two dipole antennas, one of which is rotated 90° with respect to the other,  
 3590 which are fed with signals that are out of phase from the opposite dipole by 90° (see  
 Figure 5.13). This arrangement causes the signals fed to each arm of the dipole to be

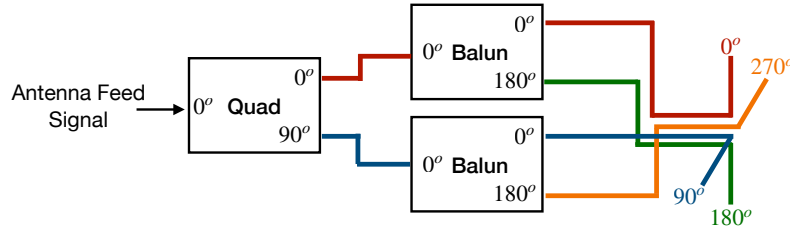


Figure 5.13: An idealized crossed-dipole antenna consists of two electric dipole antennas oriented perpendicular to each other and is fed with four signals with a quadrature phase relationship. An example antenna feed circuit is shown which is composed of a chained combination of a quadrature hybrid-coupler (Quad) and two baluns.

3591  
 3592 out of phase from each of the neighboring arms by 90°, which mirrors the spatial phase  
 3593 relationship of cyclotron radiation fields.

3594 A potential drawback of this design is that standard crossed-dipole antennas do not  
 3595 radiate uniform electric fields near the  $\theta = \pi/2$  plane. Typical crossed-dipole antennas  
 3596 use dipole arm lengths equal to  $\lambda/4$  or larger [92], where  $\lambda$  is the wavelength at the  
 3597 desired operating frequency. Such large arm lengths cause the electric field magnitude  
 3598 to vary significantly around the circumference of the antenna. However, making the  
 3599 antenna electrically small by shrinking the arm length can improve the antenna pattern  
 3600 uniformity.

3601 In general, the criterion for an electrically small antenna is that the largest dimension  
3602 of the antenna ( $D$ ) obey  $D \lesssim \lambda/10$  [63]. In our application, we are attempting to mimic  
3603 the cyclotron radiation emitted by electrons produced from tritium  $\beta$ -decay with energies  
3604 near the spectrum endpoint. For a background magnetic field of 1 T, the corresponding  
3605 cyclotron frequency of tritium endpoint electrons is approximately 26 GHz. Therefore, the  
3606 electrically small condition would require that the largest dimension of the crossed-dipole  
3607 antenna be smaller than 1.2 mm.

3608 A crossed-dipole antenna with an overall size of 1.2 mm is challenging to fabricate due  
3609 to the small dimensions of the dipole arms that, in practice, are fragile and unsuitable  
3610 for use as a calibration probe. To mitigate some of the challenges with the fabrication  
3611 of such a small antenna, a variant crossed-dipole antenna design using printed circuit  
3612 board (PCB) technology (see Figure 5.14) was developed in partnership with an antenna  
prototyping company, Field Theory Consulting <sup>1</sup>.

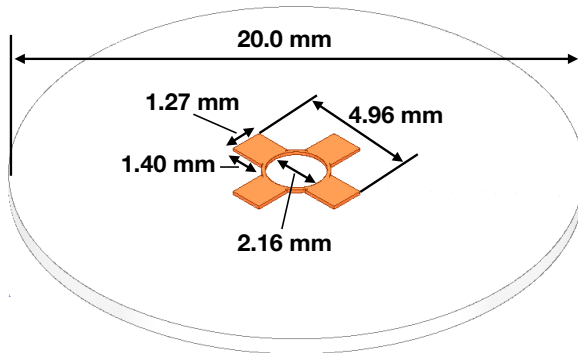


Figure 5.14: A model of the PCB crossed-dipole antenna with dimensions. The design has an inside diameter of 2.16 mm for the central circular trace, which is 0.13 mm wide. The dipole arms each have a width of 1.27 mm and protrude beyond the circular trace by 1.40 mm, which gives an overall width of 4.96 mm for the length of the antenna PCB trace from end-to-end. The overall size of the antenna is 20.0 mm the majority of which is the PCB dielectric material. This design was observed in simulation to maintain the field characteristics of the idealized crossed-dipole while being simpler to fabricate due to the increased size of the antenna.

3613  
3614 The PCB crossed-dipole design uses four rectangular pads to represent the dipole arms,  
3615 which are connected by a thin circular trace. The circular trace both adds mechanical  
3616 stability to the antenna and improves the azimuthal uniformity of the electric fields  
3617 compared to a more standard crossed-dipole geometry. Furthermore, the circular trace  
3618 allows for a greater separation between dipole arms than standard crossed-dipoles, which

---

<sup>1</sup><https://fieldtheoryinc.com/>

3619 is required to accommodate the coaxial connections to each pad. The pads each contain  
 3620 a through-hole solder joint to connect coaxial transmission lines using hand soldering.  
 3621 The antenna PCB has no ground plane on the bottom layer as this was observed in  
 3622 simulation to significantly distort the radiation pattern in the plane of the PCB. The  
 3623 only ground planes present in the model are the outer conductors of the four coaxial  
 3624 transmission lines which feed the antenna. These are left unterminated on the bottom of  
 3625 the PCB dielectric material.

3626 The antenna design development utilized a combination of Locust electron simula-  
 3627 tions and antenna simulations using ANSYS HFSS [64], a commercial finite-element  
 3628 electromagnetic simulation software. Two antenna designs were simulated: an idealized  
 3629 electrically small crossed-dipole antenna with an arm length of 0.40 mm and an arm  
 3630 separation of 0.05 mm, as well as a PCB crossed-dipole antenna with the dimensions  
 3631 shown in Figure 5.14. Plotting the magnitude of the electric fields generated by the  
 3632 antennas across a 10 cm square located in the same plane as the respective antennas  
 3633 reveals the expected cyclotron spiral pattern (see Figure 5.15) which closely matches  
 3634 the prediction for simulated electrons. The spiral pattern demonstrates that the electric  
 3635 fields have the appropriate phases to mimic cyclotron radiation, which fulfills SYNCA  
 criterion 3 identified in Section 5.3.2.

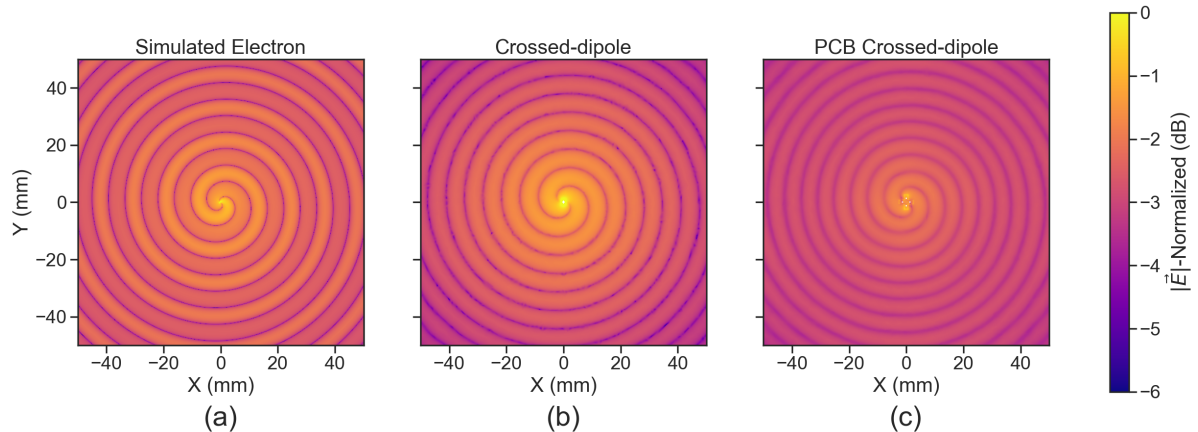


Figure 5.15: A comparison of the electric field magnitudes, normalized by the maximum value of the electric field in each simulation, plotted on a 10 cm square to visualize the Archimedean spirals formed by the electron (a), the crossed-dipole antenna (b), and a PCB crossed-dipole antenna (c). The matching patterns indicate that the electric fields have similar phase characteristics. These images were generated using Locust simulations for the electron and ANSYS HFSS for both antennas.

3636

3637 As we can see from Figure 5.16, the crossed-dipole antenna, which uses an idealized

3638 geometry, exhibits good agreement with simulation. The antenna has a maximum  
 3639 deviation from a simulated electron of approximately 0.5 dB in the total electric field, 1  
 3640 dB for the  $\phi$ -polarized electric field and 1 dB for the  $\theta$ -polarized electric field.

3641 In comparison, the pattern of the PCB crossed-dipole antenna, because the simulation  
 3642 incorporates the geometry of the coax transmission lines, exhibits some distortion from  
 3643 the idealized cross-dipole simulations. The vertically oriented ground planes of the coax  
 3644 lines introduce more  $\theta$ -polarized electric fields than are observed for simulated electrons  
 3645 near  $\theta = 90^\circ$ . The significant  $\theta$ -polarized field minimum is still present but shifted  
 to approximately  $\theta = 65^\circ$ . The  $\theta$ -polarized field deviations of the PCB crossed-dipole

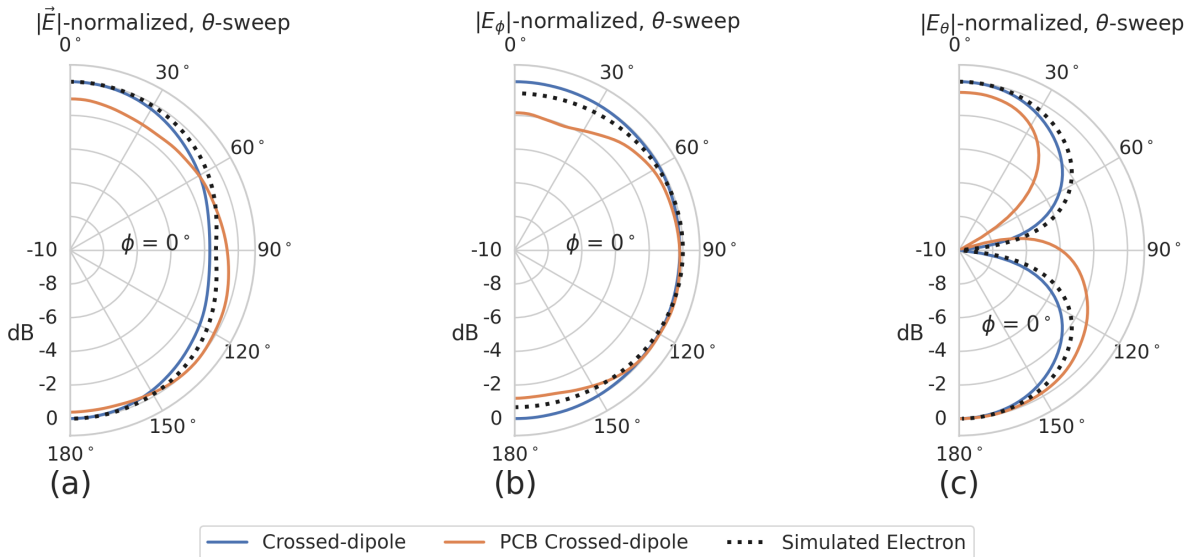


Figure 5.16: A comparison of the normalized electric field magnitudes for the ideal crossed-dipole, PCB crossed-dipole, and a simulated electron as a function of the polar angle ( $\theta$ ). (a) Shows the total electric field, (b) shows the  $\phi$ -polarized electric field component, and (c) shows the  $\theta$ -polarized electric field component. These images were generated using Locust simulations for the electron and ANSYS HFSS for both antennas.

3646  
 3647 antenna should not greatly impact the performance of the antenna because the receiving  
 3648 antenna array is primarily  $\phi$ -polarized. Therefore deviations in the  $\theta$ -polarized fields  
 3649 will be suppressed due to the polarization mismatch. More importantly, the  $\phi$ -polarized  
 3650 electric field pattern generated by the PCB crossed-dipole closely matches simulated  
 3651 electrons across the polar angle range of  $50^\circ < \theta < 150^\circ$ . In this region the PCB crossed-  
 3652 dipole differs by less than 0.5 dB from simulated electrons. This range greatly exceeds  
 3653 the beamwidth of the receiving antenna array which is designed to be most sensitive  
 3654 to fields produced near  $\theta = 90^\circ$ . Therefore, we conclude that the PCB crossed-dipole

3655 antenna generates a  $\phi$ -polarized radiation pattern that fulfills SYNCA criterion 1 from  
3656 Section 5.3.2.

3657 The final SYNCA criterion is related to the uniformity of the electric fields when  
3658 measured azimuthally around the antenna. As we saw for real electrons in Section 5.3.2  
3659 it is expected that the magnitude of the electric field be completely uniform as a function  
3660 of the azimuthal angle due to the symmetry of the cyclotron orbit. In Figure 5.17 we plot  
3661 the total electric field as a function of azimuthal angle for an electron, the crossed-dipole  
antenna, and the PCB crossed-dipole antenna. The crossed-dipole antenna exhibits

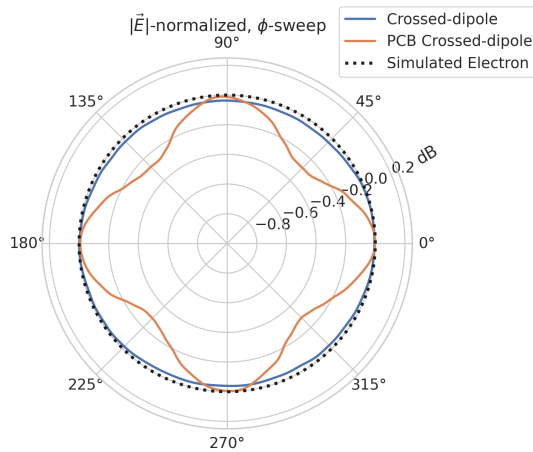


Figure 5.17: A comparison of the normalized electric field magnitudes for the crossed-dipole, PCB crossed-dipole, and a simulated electron as a function of the azimuthal angle ( $\phi$ ) evaluated at  $\theta = 90^\circ$ . This image was generated using Locust simulations for the electron and ANSYS HFSS for both antennas.

3662  
3663 perfect uniformity around the azimuthal angle, whereas the PCB crossed-dipole has a  
3664 small periodic deviation with a maximum difference of 0.3 dB caused by the coaxial  
3665 transmission lines below the PCB. Such a small deviation from uniformity is acceptable  
3666 since it is smaller than the expected variation in uniformity caused by imperfections in  
3667 the antenna fabrication process, which modifies the antenna shape in an uncontrolled  
3668 manner by introducing solder blobs with a typical size of a few tenths of a millimeter on  
3669 the dipole arms (see Figure 5.18). Additionally, the SYNCA will be separately calibrated  
3670 to account for azimuthal differences in the electric field magnitude. Therefore we see  
3671 from the simulated performance of the PCB crossed-dipole antenna that this antenna  
3672 design meets all three of the SYNCA criteria.

### 5.3.4 Characterization of the SYNCA

Two SYNCAs were manufactured using the PCB crossed-dipole design (see Figure 5.18). The antenna PCB (Matrix Circuit Board Materials, MEGTRON 6) is connected to four 2.92 mm coaxial connectors (Fairview Microwave, SC5843) using semi-rigid coax (Fairview Microwave, FMBC002), which also physically support the antenna PCB. The antenna PCB consists only of two layers which correspond to the copper antenna trace and the PCB dielectric. Each coax line is connected to the associated dipole arm using through-hole soldering and phase matched to ensure that the electrical length of each of the transmission lines is identical at the operating frequency. The antenna PCB is further reinforced using custom cut polystyrene foam blocks, which have an electrical permittivity nearly identical to air. A custom 3D printed mount is included at the base of the antenna to support the coax connectors and to provide a sturdy mounting base.

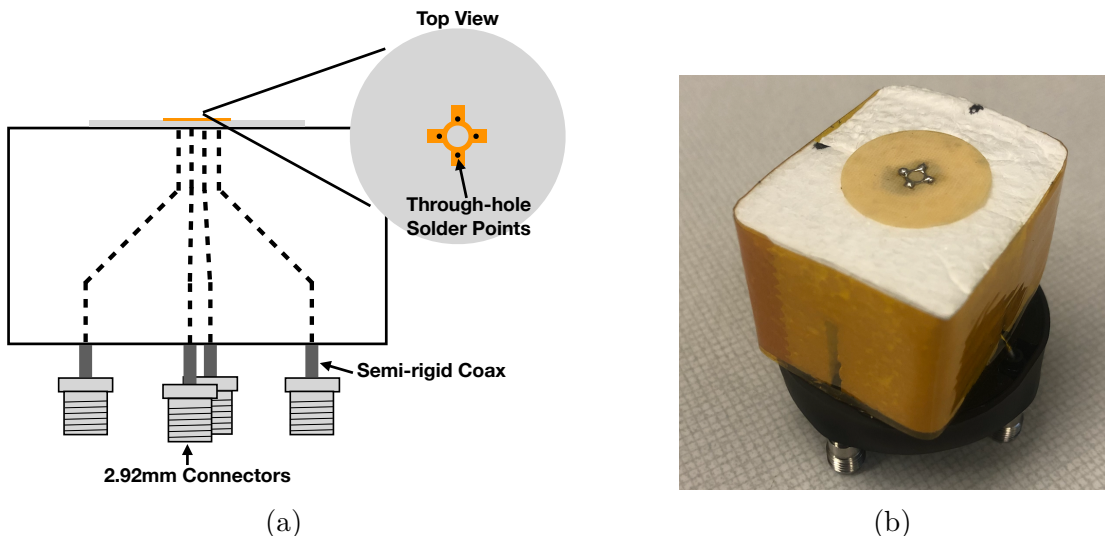


Figure 5.18: (a) A cartoon schematic which highlights the routing of the semi-rigid coax transmission lines. (b) A photograph of a SYNCA constructed using the modified crossed-dipole PCB antenna design. Visible in the photograph of the SYNCA are four blobs of solder which are an artifact of the SYNCA's hand-soldered construction. These solder blobs are the most significant deviation from the SYNCA design shown in Figure 5.14 and are responsible for a significant fraction of the irregularities seen in the antenna pattern.

Characterization measurements were performed using a Vector Network Analyzer (VNA) to measure the electric field magnitude and phase radiated by the SYNCA to verify the radiation pattern (see Figure 5.19). The VNA is connected to the SYNCA



Figure 5.19: A schematic of the VNA characterization measurements (a). This setup allows for antenna gain and phase measurements across a full  $360^\circ$  of azimuthal angles using a motorized rotation stage and control of the radial position of the SYNCA using a translation stage. A photo of the setup in the lab is shown in (b).

3688 at one port through a hybrid-coupler whose outputs are connected to two baluns to  
 3689 generate the signals with the appropriate phases to feed the SYNCA (see Figure 5.13).  
 3690 The other port of the VNA is connected to a single reference horn antenna that serves  
 3691 as a field probe. To position the SYNCA, a combination of translation and rotation  
 3692 stages are used to characterize the antenna's fields across the entire radiation pattern  
 3693 circumference. This measurement scheme is equivalent to measuring the fields generated  
 3694 by the SYNCA using a full circular array of probe antennas.

3695 The antenna measurement space is surrounded by RF anti-reflective foam to isolate  
 3696 the measurements from the lab environment (see Figure 5.19b) and remaining reflections  
 3697 are removed using the VNA's time-gating feature. The SYNCA is affixed to the stages  
 3698 by a custom RF transparent mount made of polystyrene foam. The coaxial cables deliver  
 3699 the antenna feed signals generated by the VNA to the SYNCA while still allowing  
 3700 unrestricted rotation. The horn antenna probe is nominally positioned in the plane  
 3701 formed by the antenna PCB ( $\theta = 90^\circ$  or  $z = 0$  mm) at a distance of 10 cm from the  
 3702 SYNCA, to match the expected position of the antenna array relative to the SYNCA in  
 3703 the antenna array test stand. The horn antenna can be manually raised or lowered to  
 3704 different relative vertical positions to characterize the radiation pattern at different polar  
 3705 angles.

3706 Several  $360^\circ$  scans were performed with probe vertical offsets of -10.0 mm, -5.0 mm,  
 3707 0.0 mm, 5.0 mm, and 10.0 mm relative to the antenna PCB plane. These probe offsets

3708 cover a 2 cm wide vertical region centered on the SYNCA PCB, approximately equal to  
 3709  $\pm 6$  degrees of polar angle. The measurements show that the SYNCA is generating fields  
 3710 with nearly isotropic magnitude across the probed region. The standard deviation of the  
 3711 electric field magnitude measured around the antenna circumference is approximately  
 3712 2.9 dB for a typical rotational scan. The presence of a significant pattern null is noted  
 3713 near 45° (see Figure 5.20), which we attribute to small imperfections in the antenna  
 3714 PCB that could be introduced from the hand soldered terminations connecting the coax  
 3715 cables to the antenna. There is no significant difference in the radiation pattern when  
 3716 measured across the 2 cm vertical range. The measured relative phases closely follow  
 3717 the expectation for an electron, being linear with the measurement rotation angle and  
 3718 forming the expected spiral pattern. Other than the small phase imperfections there is  
 3719 a slight sinusoidal bias to the phase data, which we determined is the result of a small  
 3720 ( $\lesssim 1$  mm) offset of the antenna's phase center from the rotation axis of the automated  
 3721 stages.

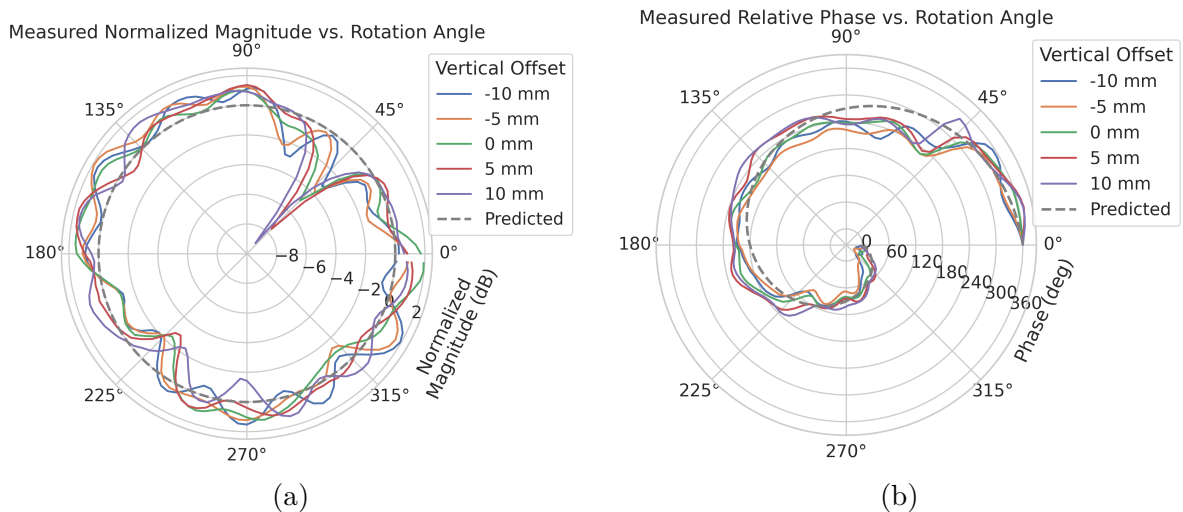


Figure 5.20: Linear interpolations of the measured electric field magnitude (a) and phase (b). The data was acquired using a VNA at 120 points spaced by 3 degrees from 0 to 357 degrees of azimuthal angle. The different color lines indicate the vertical offset of the horn antenna relative to the SYNCA PCB and the dashed line shows the expected shape from electron simulations. No significant difference in the antenna pattern is observed for the measured vertical offsets.

3722 The characterization measurements confirm the simulated performance of the SYNCA.  
 3723 As expected the fields generated by the antenna are nearly isotropic in magnitude,  $\phi$ -  
 3724 polarized, and are linearly out of phase around the circumference of the antenna as

3725 predicted for cyclotron radiation in Section 5.3.2. Small imperfections in the magnitude  
 3726 and phase of the antenna are expected, particularly at the antenna's high operating  
 3727 frequency of 26 GHz where small geometric changes can have significant impacts on  
 3728 electrical properties. However, calibration through careful characterization measurements  
 3729 can be used to remove the majority of these pattern imperfections, including the relatively  
 3730 large pattern null near 45°, which will allow for the usage of the SYNCA as a test source  
 3731 for free-space CRES experiments utilizing antenna arrays. In the next section we use the  
 3732 VNA measurements obtained here as a calibration for signal reconstruction using digital  
 3733 beamforming.

### 3734 **5.3.5 Beamforming Measurements with the SYNCA**

3735 Digital beamforming is a standard technique for signal reconstruction using a phased  
 3736 array [93]. The SYNCA, since it exhibits the same cyclotron phases as a trapped electron,  
 3737 can be used to perform simulated CRES digital beamforming reconstruction experiments  
 3738 on the bench-top without the need for the magnet, cryogenics, and vacuum systems  
 3739 required by a full CRES experiment. The fields received by the individual elements  
 3740 of the antenna array will have phases dependent on the spatial position of the source  
 3741 relative to the antennas. Therefore, a simple summation of the received signals will fail  
 3742 to reconstruct the signal due to destructive interference between the individual channels  
 3743 in the array. However, applying a phase shift associated with the source's spatial position

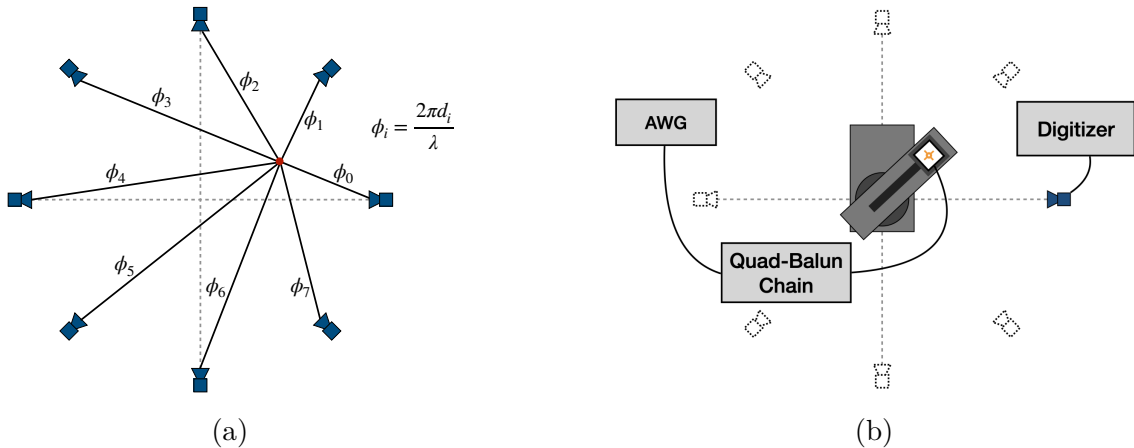


Figure 5.21: (a) A depiction of the relative phase differences for signals received by a circular antenna array from an isotropic source. The phases correspond to a unique spatial position. (b) A schematic of the setup used to perform digital beamforming.

<sup>3744</sup> removes phase differences and results in a constructive summation of the channel signals  
<sup>3745</sup> (see Figure 5.21). We can summarize the digital beamforming operation succinctly using  
<sup>3746</sup> the following equation

$$y[t_n] = \sum_{m=0}^{N-1} x_m[t_n] A_m e^{i\phi_m}, \quad (5.35)$$

<sup>3747</sup> where  $y[t_n]$  represents the summed array signal at time  $t_n$ ,  $x_m[t_n]$  is the signal received  
<sup>3748</sup> by channel  $m$  at time  $t_n$ ,  $\phi_m$  is the phase shift applied to the signal received at channel  
<sup>3749</sup>  $m$ , and  $A_m$  is an amplitude weighting factor that accounts for the different signal power  
<sup>3750</sup> received by individual channels. By changing the digital beamforming phases, the point  
<sup>3751</sup> of constructive interference can be scanned across the sensitive region of the array to  
<sup>3752</sup> search for the location of a radiating source, which is identified as the point of maximum  
<sup>3753</sup> summed signal power above a specified threshold. The digital beamforming phases consist  
<sup>3754</sup> of two components,

$$\phi_m = 2\pi d_m / \lambda + \theta_m, \quad (5.36)$$

<sup>3755</sup> where  $d_m$  is the distance from the  $m$ -th array element to the source, and  $\theta_m$  is the  
<sup>3756</sup> relative angle between the source position and the  $m$ -th antenna. The first component is  
<sup>3757</sup> the standard digital beamforming phase that corresponds to the spatial position of the  
<sup>3758</sup> source, and the second component is the cyclotron phase that corresponds to the relative  
<sup>3759</sup> azimuthal phase offset.

<sup>3760</sup> With a small modification to the hardware used to characterize the SYNCA (see  
<sup>3761</sup> Figure 5.19), we can perform a digital beamforming reconstruction of a synthetic CRES  
<sup>3762</sup> event. By replacing the VNA with an arbitrary waveform generator (AWG), the SYNCA  
<sup>3763</sup> can be used to generate cyclotron radiation with an arbitrary signal structure, which  
<sup>3764</sup> can then be detected by digitizing the signals received by the horn antenna. Rotational  
<sup>3765</sup> symmetry allows us to use the rotational stage of the positioning system to rotate the  
<sup>3766</sup> SYNCA to recreate the signals that would have been received by a complete circular  
<sup>3767</sup> array of antennas.

<sup>3768</sup> Using this setup, signals from a 60 channel circular array of equally spaced horn  
<sup>3769</sup> antennas were generated with the SYNCA positioned 10 mm off the central array axis,  
<sup>3770</sup> reconstructed using digital beamforming, and compared to Locust simulation (see Figure  
<sup>3771</sup> 5.22). When the cyclotron spiral phases are not used, which is equivalent to setting  $\theta_m$   
<sup>3772</sup> in Equation 5.36 to zero, the SYNCA's position is reconstructed as a relatively faint ring  
<sup>3773</sup> as predicted by simulation. However, when the appropriate cyclotron phases are used  
<sup>3774</sup> during the beamforming procedure, both the simulated electron and the SYNCA appear

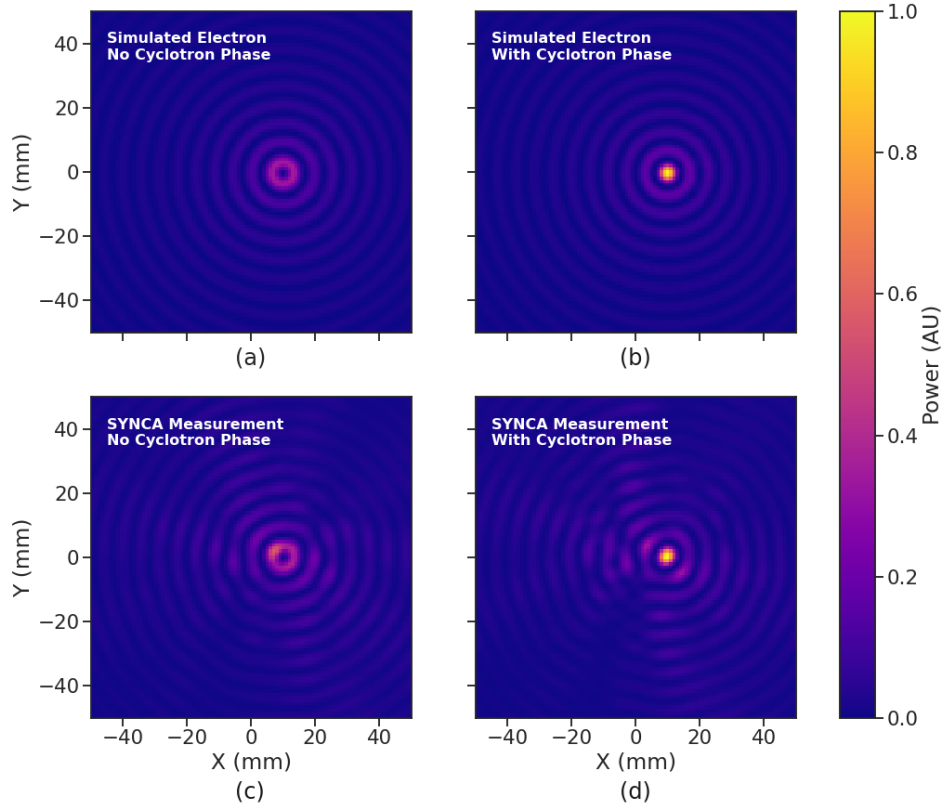


Figure 5.22: Digital beamforming maps generated using a simulated 60 channel array and electron simulated using the Locust package. (a) and (b) show the beamforming maps for simulated electrons without the cyclotron spiral phases and with the cyclotron spiral phases respectively. (c) and (d) show the beamforming maps produced from SYNCA measurements. We observe good agreement between simulated electrons and the SYNCA measurements.

as a single peak of high relative power corresponding to the source position. Therefore, we observe good agreement between the simulated and SYNCA reconstructions. While it may seem that for the case with no cyclotron phase corrections the ring reconstructs the position of the electron as effectively as beamforming with the cyclotron phase corrections, it is important to note that the simulations and measurements were generated without a realistic level of thermal noise. The larger maxima region and lower signal power, which occurs without the cyclotron phase corrections, significantly reduce the probability of detecting an electron in a realistic noise background.

To bound the beamforming capabilities of the synthetic array of horn antennas, we performed a series of beamforming reconstructions where the SYNCA was progressively moved off the central axis of the array (see Figure 5.23). To extract an estimate of the

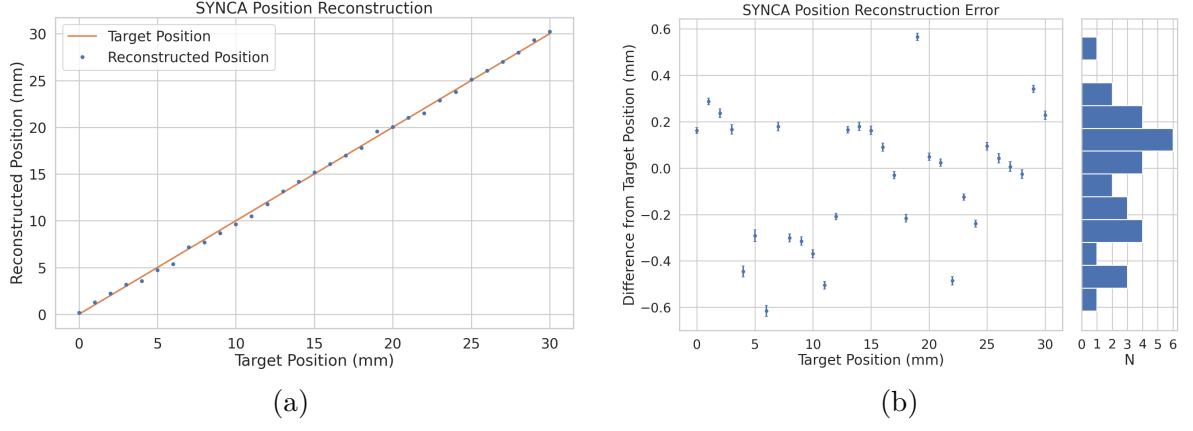


Figure 5.23: A plot of the SYNCA’s reconstructed position using the synthesized horn-antenna array and digital beamforming. (a) Shows the reconstructed position of the SYNCA compared with the target position indicated by the positioning system readout. (b) Shows the reconstruction error, which is the difference between the target and reconstructed positions. The error bars in (b) are the uncertainty in the mean position of the 2D Gaussian used to fit the digital beamforming reconstruction peak obtained from the fit covariance matrix. The mean fit position uncertainty of 0.02 mm is an order of magnitude smaller than the typical reconstruction error of 0.3 mm obtained by calculating the standard deviation of the difference between the reconstructed and target position.

position of the SYNCA using the digital beamforming image we apply a 2-dimensional (2D) Gaussian fit to the image data and extract the estimated centroid value. We find that the synthetic horn antenna array reconstructs the position of the SYNCA with a  $1\sigma$ -error of 0.3 mm with no apparent trend across the 30 mm measurement range. This reconstruction error is an order of magnitude larger than mean fit position uncertainty of 0.02 mm indicating that systematic effects related to the SYNCA positioning system could be contributing additional uncertainty to the measurements. Note that the current mean reconstruction error of 0.3 mm is a factor of 20 smaller than the full width at half maximum of the digital beamforming peak (6 mm), which could be interpreted as a naive estimate of the position reconstruction performance of this technique. Because these measurements are intended as a proof-of-principle demonstration, we do not investigate potential sources of systematic errors further; however, we expect that a similar and more thorough investigation will be performed using the Project 8 antenna array test stand, where typical reconstruction errors can be used to estimate the energy resolution limits of antenna array designs.

3801    **5.3.6 Conclusions**

3802    In this paper we have introduced the SYNCA, which is a novel antenna design that  
3803    emits radiation that mimics the unique properties of the cyclotron radiation generated by  
3804    charged particles moving in a magnetic field. The characterization measurements of the  
3805    SYNCA validated the simulated performance of the PCB crossed-dipole antenna design.  
3806    Additionally, the SYNCA was used to estimate the position reconstruction capabilities  
3807    of a synthesized array of horn antennas and experimentally reproduced the simulated  
3808    digital beamforming reconstruction of electrons.

3809    While the SYNCA performs well, there exist discrepancies in the phase and magnitude  
3810    of the radiation pattern compared to the simulated SYNCA design that are related to  
3811    the small geometric differences in the soldered connections. Future design iterations that  
3812    replace the soldered connections with a fully surface mount design could improve the  
3813    radiation pattern at the cost of some complexity and expense. Furthermore, improving  
3814    the design of the antenna PCB and mounting system would allow the antenna to be  
3815    inserted into a cryogenic and vacuum environment where in-situ antenna measurement  
3816    calibrations could be performed.

3817    The discrepancies in the radiation pattern and phases exhibited by the as-built  
3818    SYNCA should not greatly impact its performance as a calibration probe. Both magni-  
3819    tude and phase variations can be accounted by applying the SYNCA characterization  
3820    measurements as a calibration to the data collected by the antenna array test stand. The  
3821    separate calibration of the SYNCA radiation does not impact the primary goals for the  
3822    antenna array test stand which are array calibration and signal reconstruction algorithm  
3823    performance characterization, because it can be performed with standard reference horn  
3824    antennas with well understood characteristics.

3825    The SYNCA antenna technology advances the CRES technique by providing a  
3826    mechanism to characterize free-space antenna arrays for CRES measurements without  
3827    the need for a magnet and cryogenics system, which would be required for calibration  
3828    using electron sources. Both the Project 8 collaboration as well as future collaborations  
3829    which are developing antenna array based CRES experiments can make use of SYNCA  
3830    antennas as an important component of their calibration and commissioning phases.

## 3831 5.4 FSCD Antenna Array Measurements with the SYNCA

### 3832 5.4.1 Introduction

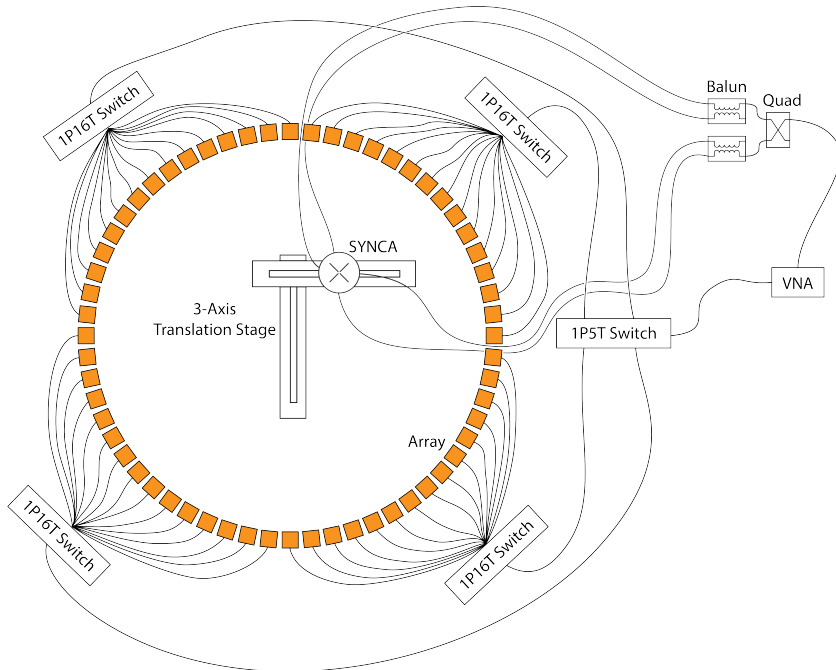


Figure 5.24: A diagram of the array measurement system used to test the prototype FSCD antenna array. A VNA is used as the primary measurement tool, which is connected to the array through a series of switches. The other port of the VNA connects to the SYNCA through the quad-balun chain used to provide the SYNCA feed signals. During measurements the SYNCA is positioned inside the center of the antenna array and translated to different radial and axial positions using a 3-axis manual translation stage setup.

3833 Using the SYNCA we can perform full-array measurements of prototype versions  
3834 of the FSCD antenna array to test its performance with a realistic cyclotron radiation  
3835 source (see Figure 5.24). The goal is to check how the measured power received by  
3836 the array compares to FSCD simulations as a function of the radial and axial position  
3837 of the SYNCA. These measurements are intended to validate the antenna research  
3838 and development by Project 8, which has been driven primarily by simulations with  
3839 Locust [60] and CRESana (see Section 4.2.3), and identify any discrepancies with these  
3840 simulations tools. This knowledge will provide confidence in the simulations necessary  
3841 for the analysis of the sensitivity of larger antenna array based CRES experiment designs  
3842 to the neutrino mass.

3843 As shown in Section 5.3, the SYNCA does have some radiation pattern imperfections  
3844 that complicate the comparison between measurement and simulation data. One way to  
3845 disentangle some of the effects of these imperfections is to perform an additional set of  
3846 measurements using a synthetic antenna array setup along with the SYNCA antenna.  
3847 Since the synthetic array setup uses only a single array antenna, the data should be  
3848 free of errors associated with individual antenna differences and multi-path interference,  
3849 which are two error sources being tested with the full-array setup. By comparing the  
3850 synthetic array data to the FSCD array data and to simulation data one can evaluate the  
3851 significance of these effects relative to the errors introduced by SYNCA imperfections.

### 3852 **5.4.2 Measurement Setups**

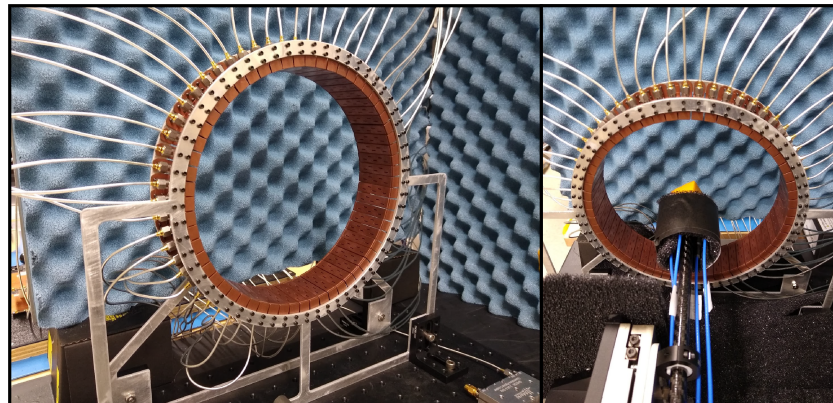
#### 3853 **5.4.2.1 FSCD Array Setup**

3854 The antenna design that composes the array is the 5-slot waveguide antenna developed  
3855 for the FSCD experiment (see Figure 5.25a). The antenna is 5 cm long and is constructed  
3856 out of WR-34 waveguide with a 2.92 mm coax connector located at the center of the  
3857 antenna. Copper flanges located on both ends of the antenna are used to mount the  
3858 antenna in the array support structure. The antennas are supported by two circular steel  
3859 brackets that can be bolted to both ends of the waveguide to construct the circular array  
3860 (see Figure 5.25b). The antenna array consists of sixty identical waveguide antennas  
3861 with a radius of 10 cm. The array is mounted perpendicular to an optical breadboard  
3862 surface using a pair of the steel brackets, which provide sufficient space for the coaxial  
3863 cable connections and allows for easy positioning of the SYNCA antenna. The SYNCA is  
3864 mounted on the end of a carbon fiber rod attached to a set of manual translation stages,  
3865 which are used to move the SYNCA antenna to different positions inside the array (see  
3866 Figure 5.25c). The stages allow for independent motion in three different axes and can  
3867 position the SYNCA at radial distances up to 5 cm from the center.

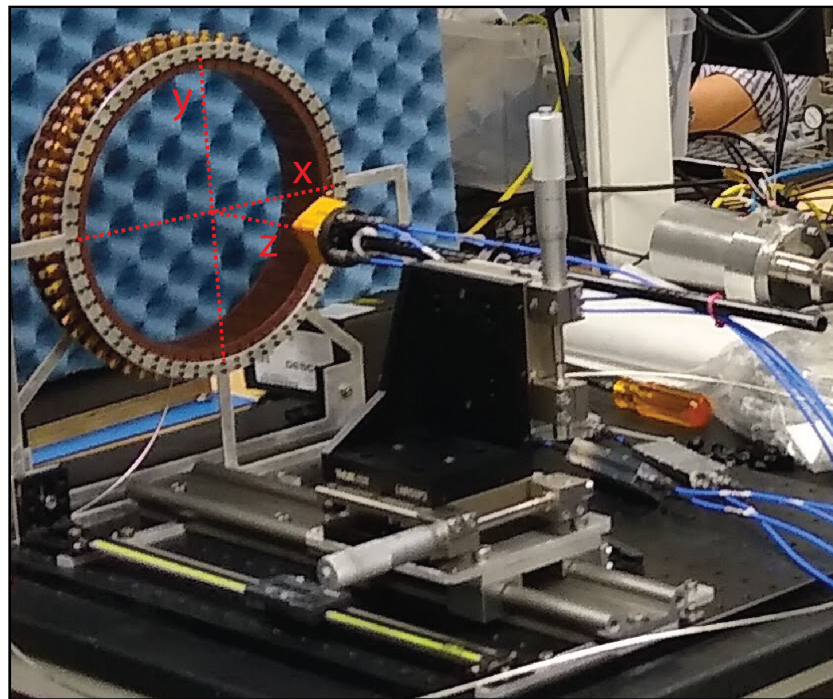
3868 Data acquisition is accomplished using a two-port VNA in combination with a series  
3869 of microwave switches that allow the VNA to connect to each channel in the array . The  
3870 first port of the VNA is connected to the quad-balun chain used to feed the SYNCA (see  
3871 Section 5.3), and the second port of the VNA connects to a 1P5T microwave switch. The  
3872 1P5T switch is connected to four separate 1P16T switch boards that connect directly  
3873 to the array. The data acquisition is controlled by a python script running on a lab  
3874 computer, which is connected to the VNA and an Arduino board programmed to control  
3875 the microwave switches. The script uses the switches to iteratively connect each of the



(a)



(b)



(c)

Figure 5.25: Photos of the prototype FSCD antenna (a), the FSCD array and SYNCA (b), and the translation stages and coordinate system used to position the SYNCA (c).

3876 antennas in the array to the VNA. The VNA is configured to load a specific calibration  
3877 file for each antenna channel and performs the measurements of all available S-parameters.  
3878 The separate calibration files is an attempt to remove phase and magnitude errors caused  
3879 by different propagation through the RF switches. Array measurements were performed  
3880 for the set of SYNCA positions consisting of radial (x-axis) positions from 0 to 50 mm in  
3881 5 mm steps and axial (z-axis) positions from 0 to 50 mm in 5 mm steps resulting in 121  
3882 array measurements. At each SYNCA position we measured the two-port S-parameter  
3883 matrix using a linear frequency sweep from 25.1 to 26.1 GHz with 101 discrete frequencies.

3884 **5.4.2.2 Synthetic Array Setup**

3885 A photograph of the setup used to perform the synthetic array measurements is shown  
3886 in Figure 5.26. One important difference between this setup and the FSCD array setup  
3887 is that the synthetic array measurements were performed with a waveform generator and  
3888 digitizer instead of a VNA. The electronics configuration is identical to the diagram in  
3889 Figure 5.7b. Despite the differences, one is still able to compare the measured phases of  
3890 the synthetic array and the relative magnitude of the power, since the digitized signal  
3891 power is directly proportional to S21.

3892 The arbitrary waveform generator in the setup is configured to produce a 64 MHz  
3893 sine wave signal that is up-converted to 25.864 GHz using a mixer and the VNA source.  
3894 This signal is passed through a bandpass filter and fed to the SYNCA quad-balun chain.  
3895 A single FSCD antenna is positioned 10 cm from the SYNCA and aligned vertically so  
3896 that the center of the 5-slot waveguide is in the plane of the SYNCA PCB (see Figure  
3897 5.26). This position corresponds to  $z = 0$  in Figure 5.25c. The SYNCA is rotated  
3898 in three degree steps to synthesize an antenna array with 120 channels. This channel  
3899 count is more than could physically fit in a 10 cm radius array, but there is no cost to  
3900 over-sampling. Additionally, over-sampling allows for a check of the smoothness of the  
3901 antenna array radiation pattern. The signals from the FSCD antenna are down-converted  
3902 using the second mixer connected to the VNA source before being digitized at 250 MHz  
3903 and saved to disk. Several synthetic array measurement scans were performed by using  
3904 the linear translation stage to change the radial position of the SYNCA. In total eight  
3905 scans were taken from 0 to 35 mm using a radial position step size of 5 mm.

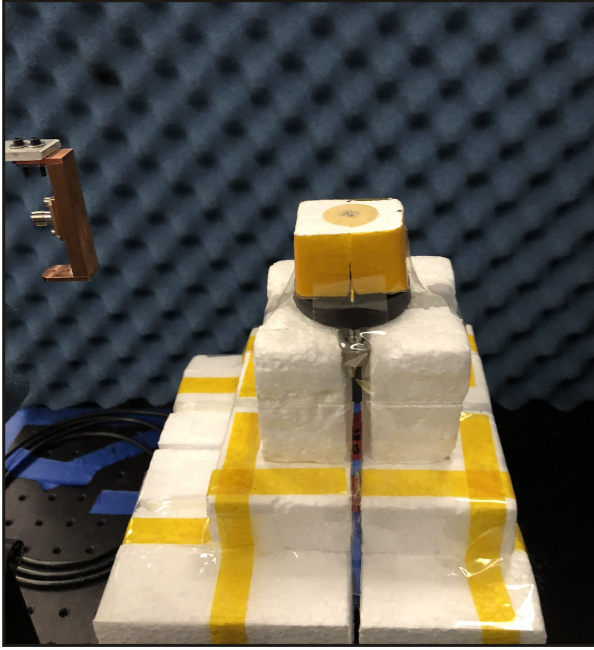


Figure 5.26: A photo of the FSCD antenna and the SYNCA in the synthetic array measurement setup at Penn State.

### 3906    5.4.3 Simulations, Analysis, and Results

3907    The Locust and CRESana simulation packages utilize the antenna transfer functions  
3908    to calculate the power that would be received by each antenna from a CRES electron.  
3909    The equivalent quantity in the measurement setup is the S21 matrix element, which  
3910    indicates the ratio of the power received by an antenna in the array to the amount of  
3911    power delivered to the SYNCA. Therefore, the analysis focuses on comparing the relative  
3912    magnitudes and phase of the S21 parameters measured by the VNA as a function of  
3913    the array channel and the SYNCA position. Additionally, we apply a beamforming  
3914    reconstruction to the S21 data to evaluate how the summed power and beamforming  
3915    images change as a function of the position of the SYNCA.

#### 3916    5.4.3.1 Simulations

3917    Simulations for the FSCD array measurements were performed using CRESana, which  
3918    performs analytical calculations of the EM-fields produced by an electron at the position  
3919    of the antennas. At each sampled time CRESana computes the electric field vector at the  
3920    antenna positions, which is projected onto the antenna polarization axis to obtain the  
3921    co-polar electric field. The magnitude of the co-polar electric field is then multiplied by

3922 a flat antenna transfer function to calculate the corresponding voltage signal. CRESana  
 3923 simulations exploit the flat transfer functions of the FSCD antennas, which allows the  
 3924 electric field to be multiplied by the antenna transfer function rather than performing  
 3925 the full FIR calculation. These calculations produce a voltage time-series for each of the  
 3926 antennas in the array that can be compared to the laboratory measurements.

3927 CRESana was configured to simulate a  $90^\circ$  electron in a constant background magnetic  
 3928 field of  $\approx 0.958$  T with a kinetic energy of 18.6 keV. These parameters were chosen  
 3929 in order to mimic a CRES event near the tritium beta-decay spectrum endpoint in  
 3930 the FSCD experiment. The constant background magnetic field guarantees that the  
 3931 guiding center of the electron is stationary across the duration of the simulation which is  
 3932 consistent with the SYNCA in the laboratory measurements. Simulations were performed  
 3933 with the electron's guiding center at radial positions from 0 to 45 mm in steps of 1 mm  
 3934 and axial positions from 0 to 30 mm in steps of 1 mm. The simulations generated time  
 3935 series consisting of 8192 samples at 200 MHz for the sixty channel FSCD antenna array  
 3936 geometry.

### 3937 5.4.3.2 Phase Analysis

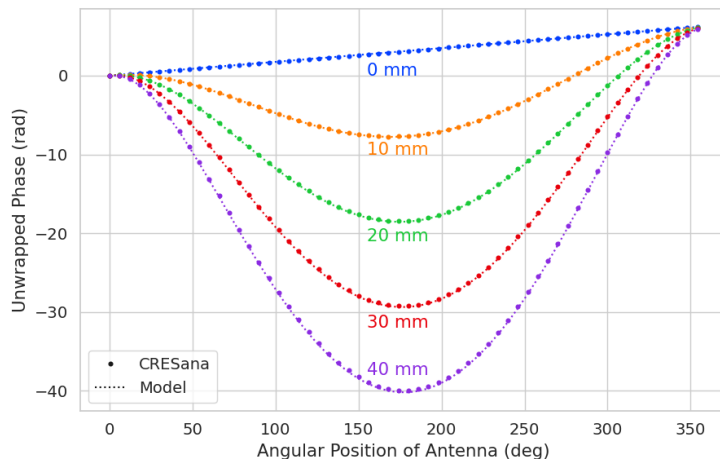


Figure 5.27: The unwrapped phases of signals received by the FSCD antenna array from an electron with a  $90^\circ$  pitch angle located in the plane of the antenna array. The data points indicated the phases extracted from simulation and the dashed lines show the model predictions.

3938 Correct modeling of the signal phases is fundamental to reconstruction for both  
 3939 beamforming and matched filter approaches. The beamforming reconstruction relies on

3940 a signal phase model developed from Locust simulations, which allows one to predict the  
3941 relative signal phases for a specific magnetic trap and electron position. The equation  
3942 for the model is

$$\phi_{ij}(t) = \frac{2\pi d_{ij}(t)}{\lambda} + \theta_{ij}(t), \quad (5.37)$$

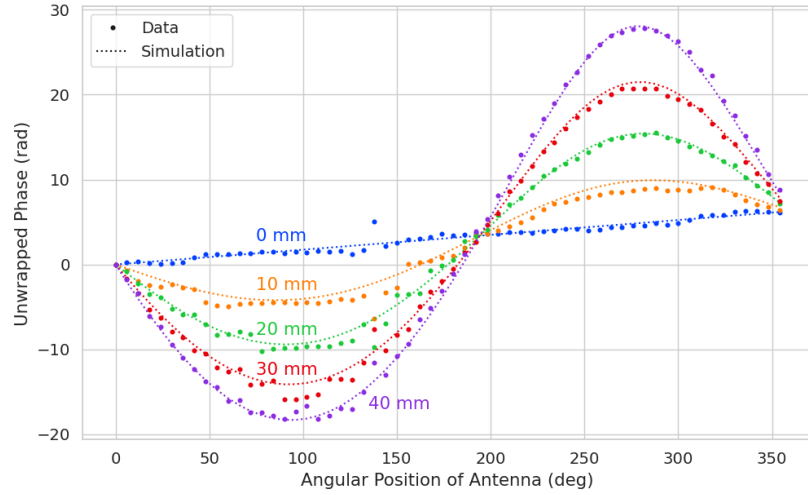
3943 where  $d_{ij}(t)$  is distance between the assumed electron position and the antenna position,  
3944 and  $\theta_{ij}(t)$  is the angular separation between the electron and antenna positions. For  
3945 details on the components of the phase model see Section 5.3.2. In Figure 5.27 we  
3946 compare the phases predicted by Equation 5.37 to phases extracted from CREsana  
3947 simulations of an electron located in the plane of the antenna array at a series of radial  
3948 positions. One observes excellent agreement between the model and simulation.

3949 The measured signal phases from the FSCD array and synthetic array are shown  
3950 in Figures 5.28a and 5.28b compared to the signal phase model. The axial position of  
3951 the SYNCA in both plots is  $z = 0$  mm, such that the plane of the PCB is aligned with  
3952 the center of the FSCD antenna. The data shown in Figure 5.28a corresponds to the  
3953 S-parameters measured at 25.80 GHz which is the frequency closest to the one used in  
3954 the synthetic array setup. The different slope and sinusoidal phases exhibited by Figure  
3955 5.28a and 5.28b reflects differences in the coordinate system for each setup. In general,  
3956 we see that the phase model predicts the large scale features of the phases quite well,  
3957 but there are some small scale deviations or errors from the phase model that do not  
3958 appear to be present in simulation.

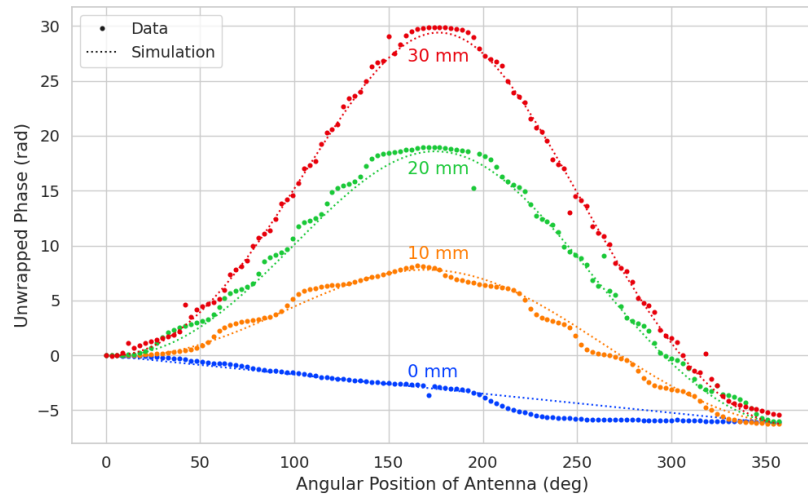
3959 A comparison of the phase errors, which are the difference between measurement and  
3960 model is shown in Figure 5.29. The FSCD array data is referred to as the JUGAAD  
3961 data in the plot legend, which is an alternative name for the FSCD array setup.

3962 The phase error at  $R = 0$  in Figure 5.29 forms a smooth curve, with the exception of  
3963 an outlier data point caused by a bug in the data acquisition script. One can attribute  
3964 the observed phase error at this position to imperfections in the antenna pattern of the  
3965 SYNCA. As the SYNCA is moved away from  $R = 0$  mm one observes that the phase  
3966 error exhibits oscillations whose frequency increases as a function of the radial position  
3967 of the SYNCA. These oscillations have the appearance of a diffraction pattern, which  
3968 is particularly clear for the radii  $\geq 15$  mm, due to the bilateral symmetry of the phase  
3969 error peaks around  $180^\circ$ .

3970 One can observe a higher average variance in the phase errors measured for the FSCD  
3971 array compared to the synthetic array. This is best seen by comparing the curves at  
3972  $R \leq 15$  mm where the smooth synthetic array curves are distinct from the relatively  
3973 noisy FSCD array errors. The extra noise in the FSCD array is most likely caused by



(a)



(b)

Figure 5.28: Plots of the measured unwrapped phases from the FSCD array (a) and the synthetic array (b) compared to the model predictions for a series of radial positions. The different phases of the sinusoidal phase oscillations in the two plots reflects differences in the coordinate systems of the measurements.

3974 differences in the radiation patterns of the antennas that make up the array as well as  
 3975 differences in the transmission lines through the switch network that introduce additional  
 3976 phase errors into the measurement. Since the synthetic array measurements use only  
 3977 a single antenna, these extra error terms are not present, which explains the relatively  
 3978 smoother phase error curves. Despite the extra phase errors in the FSCD array, it is still  
 3979 possible to observe a similar phase error oscillation effect as the SYNCA is moved away

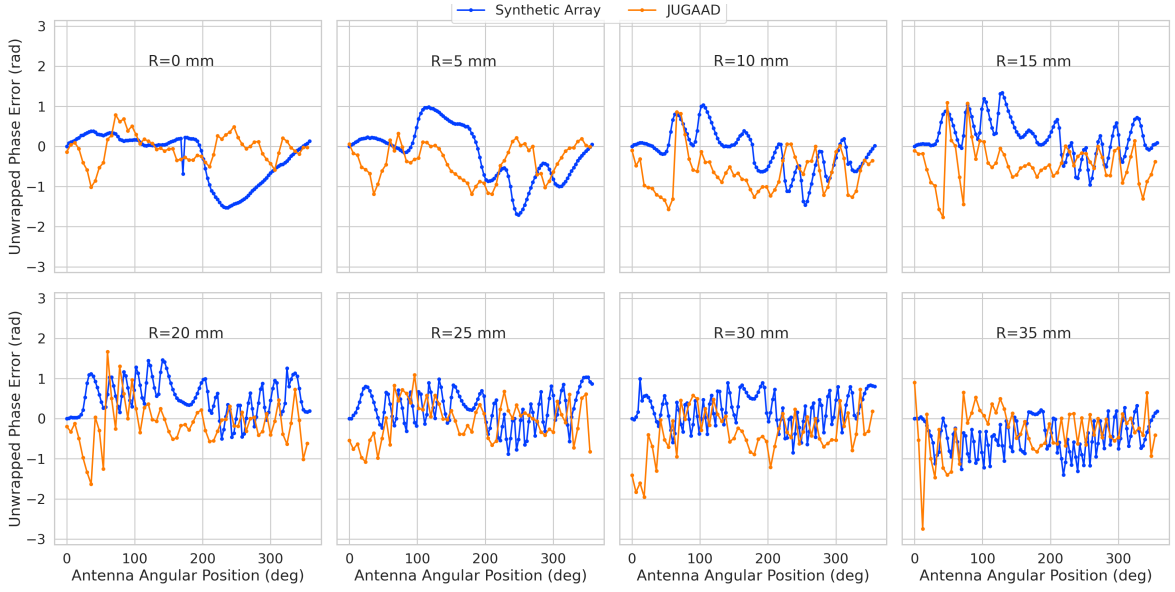
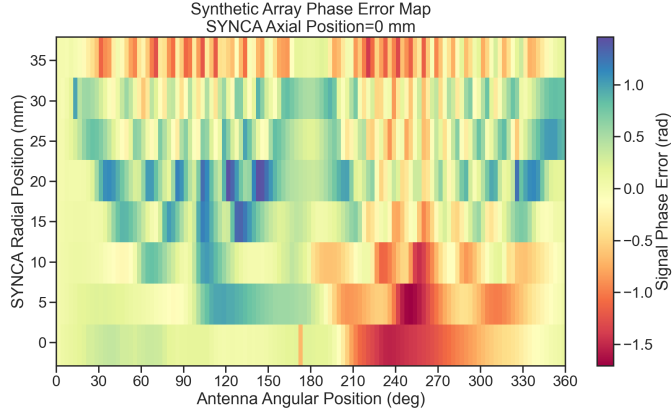


Figure 5.29: The phase errors between the measurement and model for the synthetic array (blue) and the FSCD array (orange) for a series of radial positions. The label JUGAAD refers to an alternative name for the FSCD array setup. As the SYNCA is translated off-axis phase errors with progressively higher oscillation frequency enter into the measurements.

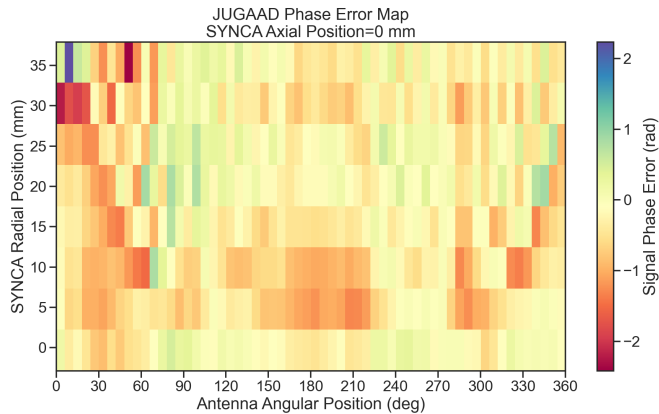
from  $R = 0$  mm.

The diffraction pattern exhibited by the phase error oscillations is more easily observed by plotting the phase errors in a two-dimensional map, which is done in Figures 5.30a and 5.30b. For the synthetic array data ones observes a relatively clear diffraction pattern that emerges as the SYNCA is moved radially. The bilateral symmetry of the diffraction patterns is due to the bilateral symmetry of the circular synthetic array around the translation axis of the SYNCA. A similar pattern is also visible in the FSCD array data, although, it is obscured by the additional phase error that results from the multi-channel array.

The physical origin of the phase error diffraction pattern is attributed to interference effects arising from path-length differences between the individual slots in the FSCD antenna and the SYNCA transmitter. Since we are operating in the radiative near-field of the FSCD antenna, the path length differences between the slots introduces a significant change in the summation of the signals that occurs inside the waveguide, which causes the radiation pattern of the antenna to change as a function of distance. Therefore, when the SYNCA is positioned off-axis the different path-lengths from the SYNCA to each antenna results in different radiation patterns leading to the observed diffraction pattern.



(a)



(b)

Figure 5.30: Two dimensional plots of the phase errors for the synthetic array (a) and the FSCD (JUGAAD) array (b). In both plots we observe evidence of a similar diffraction pattern with bilateral symmetry, but the FSCD array measurements have an additional phase error contribution from the different antennas and paths through the switch network.

This near-field effect is not present in simulations, because in order to simplify the calculations we assume that the far-field approximation can be applied to the FSCD antennas. This means that the radiation pattern and antenna transfer functions are independent of the distance between the transmitter and the receiving antenna. In principle, we can account for these near-field effects with a more detailed simulation of the FSCD antennas either in CRESana or Locust, which would result in an additional term in the beamforming phase model. However, this would increase the computational intensity of the simulation software. In the next section we briefly discuss the impact of

4005 these near-field effects on the measured magnitude of the signals.

#### 4006 5.4.3.3 Magnitude Analysis

4007 Exactly as for the signal phase, one can use simulations to construct a model that  
4008 describes the magnitude of the signals received by each channel in the antenna array.  
4009 By examining the results of simulations or by analyzing the Liénard-Wiechert equation  
4010 one can show that radiation pattern from a  $90^\circ$  pitch angle electron in a magnetic field  
4011 is omni-directional. Therefore the relative magnitudes of the signals received by each  
4012 channel will be determined by the free-space power loss, which is proportional to the  
4013 inverse distance between the assumed electron position and the antenna.

4014 A consequence of this is that the signals produced in the array for electrons off the  
4015 central axis will have larger amplitudes for the antennas closer to the electron compared  
4016 to those which are further away. The amplitudes of the signals received by the array  
from an electron located at a series of radial positions are shown in Figure 5.31.

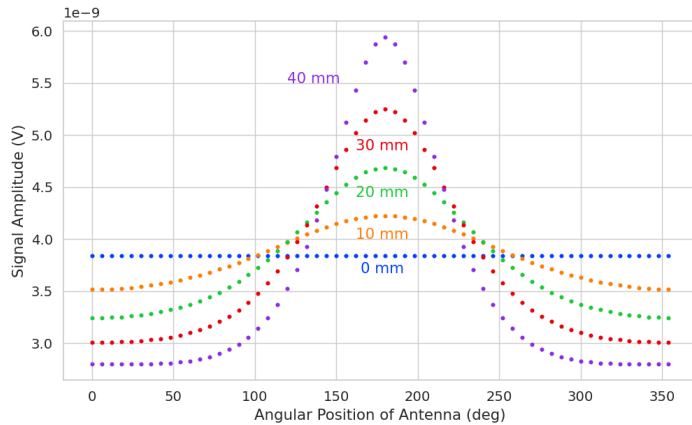


Figure 5.31: The amplitude of the signals from CREsana for the FSCD array from a  $90^\circ$  electron. As the electron is moved from  $R = 0$  the signals begin to have unequal amplitudes depending on the distance from the electron to the antenna.

4017  
4018 One expects to see a similar trend in the signal magnitudes in both the FSCD and  
4019 synthetic arrays. The normalized signal magnitudes extracted from the full and synthetic  
4020 array setups for a series of radial SYNCA positions are shown in Figure 5.32. The data  
4021 corresponds to a SYNCA axial position of  $z = 0$  mm and at a frequency 25.86 GHz. One  
4022 complication is that the radiation pattern of the SYNCA is not perfectly omni-directional,  
4023 which causes the measured magnitudes at  $R = 0$  mm to diverge from the perfectly flat  
4024 behavior exhibited by electrons.

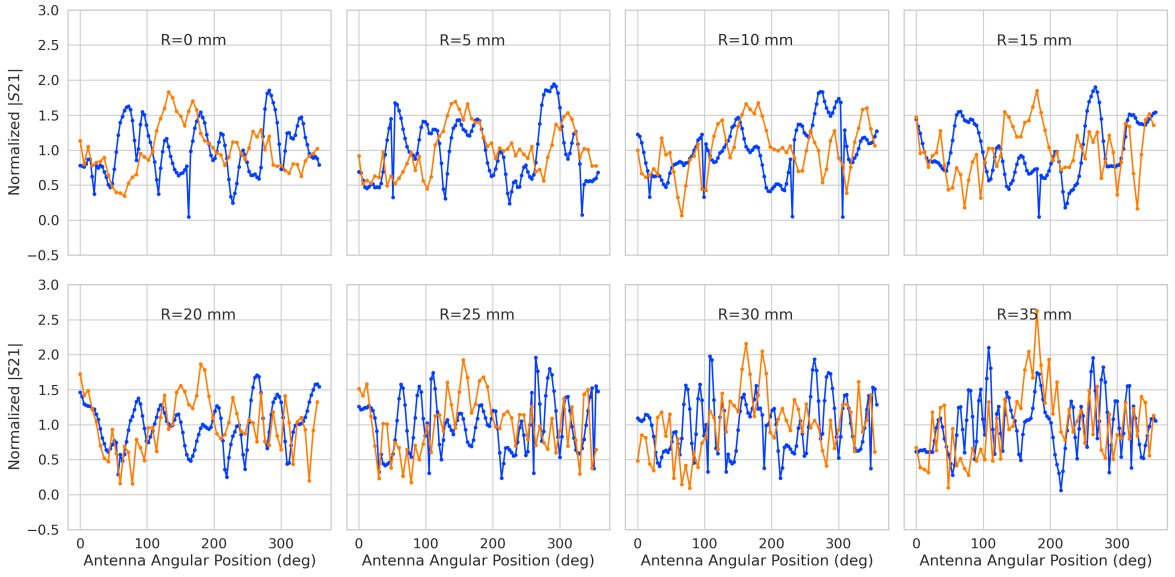
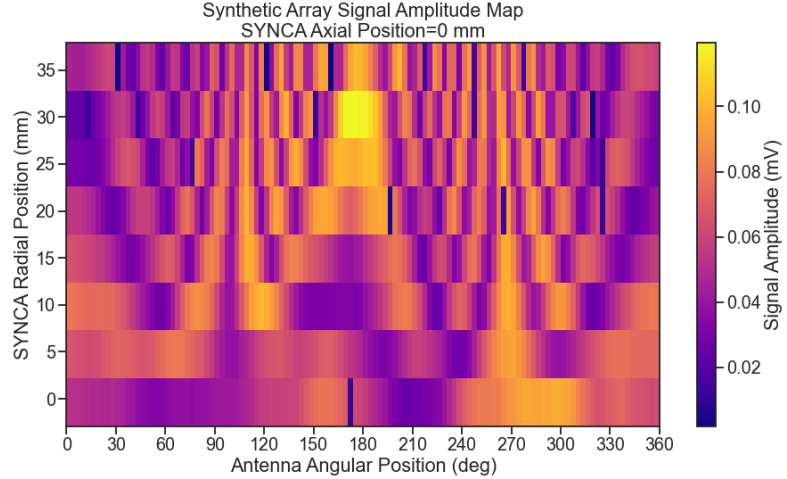


Figure 5.32: The normalized magnitudes of the S21 parameters measured in the FSCD (orange) and synthetic array (blue) setups. The dominant observed behavior as a function of radius is the increase in the number of magnitude peaks, which was noted in the phase error curves. There does not appear to be a strong change in the relative amplitude of a group of antennas as predicted by CREsana.

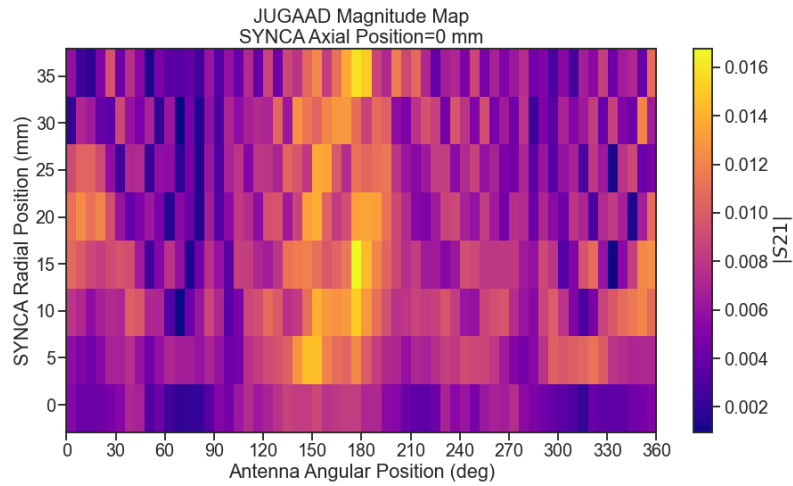
As the SYNCA is moved off-axis one observes a similar increase in the number of magnitude peaks in the synthetic array data that one would expect from a diffraction pattern, although this trend is not as stark compared to the phase data. Noticeably, there does not appear to be a set of channels with disproportionately larger amplitude at large  $R$ , which would be expected based on the trends from CREsana.

Comparing the magnitudes of the synthetic array to the FSCD array in Figure 5.32 we see that there is a similar amount of variability in the magnitudes at  $R = 0$  mm, although there is potentially more small scale error in the magnitude curve caused by channel differences in the FSCD array. We observe a similar trend in the number of magnitude error peaks in the FSCD array data to the synthetic array data, which mirrors the diffraction effect observed in the phase data. The diffraction effect can be visualized more clearly by plotting a similar two-dimensional map of the magnitudes (see Figure 5.33).

The fact that one observes a similar diffraction pattern in the signal magnitudes as a function the SYNCA position reinforces the conclusions from the phase analysis that near-field effects are having a significant impact on the radiation pattern of the FSCD array. These near-field effects lead to changes in the magnitude and phase of the



(a)



(b) The two-dimensional maps showing the diffractive pattern exhibited by the FSCD and synthetic array signal magnitudes.

Figure 5.33

4042 radiation pattern of the FSCD antenna as a function of distance. If left uncorrected these  
 4043 errors reduce detection efficiency by causing power loss in the beamforming or matched  
 4044 filter reconstruction due to phase mismatch. We explore the impact of these phase and  
 4045 magnitude errors on beamforming in the next section.

#### 4046 5.4.3.4 Beamforming Characterization

4047 Errors in the signal magnitudes and phases lead to errors in signal reconstruction. For  
 4048 example, a matched filter reconstruction requires accurate knowledge of the signals in

4049 each channel to achieve optimal performance. Uncorrected errors leads to mismatches  
 4050 between the template and signal, which reduces detection efficiency and introduces  
 4051 uncertainty in the parameter estimation. In this section, we analyze the beamformed  
 4052 signal amplitude as a function of the position of the SYNCA to quantify the impact of  
 4053 the phase and magnitude errors on signal reconstruction. Because of the imperfections  
 4054 in the SYNCA source, it is inappropriate to directly compare the beamformed signal  
 4055 amplitude of the FSCD array or synthetic array. Such a comparison would not allow  
 4056 one to disentangle losses that occur because of the antenna array from those that occur  
 4057 because of the source. Therefore, we focus on comparing the beamforming of the FSCD  
 4058 array to the synthetic array.

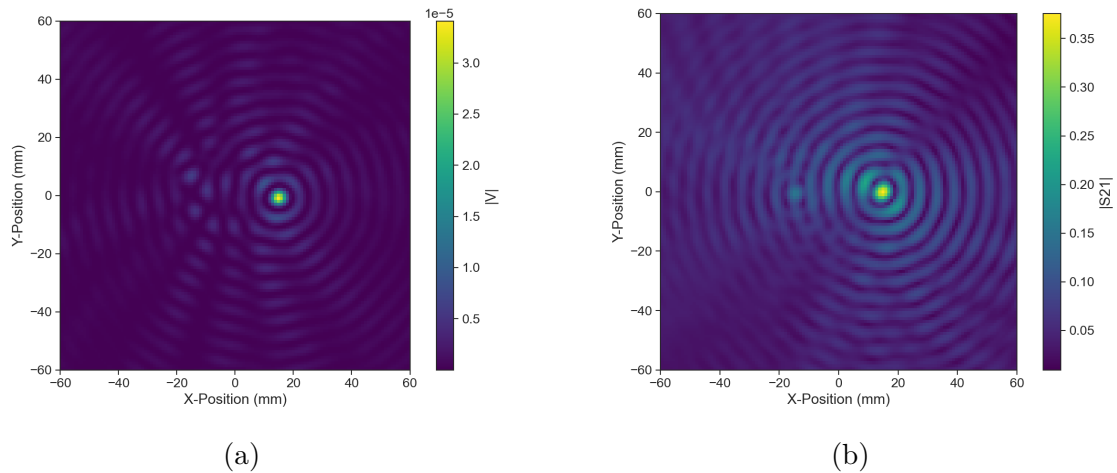


Figure 5.34: Beamforming images from the synthetic array (a) and FSCD array (b) setups with the SYNCA positioned 15 mm off the central axis. In both images we see a clear maxima that corresponds to the true SYNCA position. However, in the FSCD array there is an additional faint peak located at the opposite position of the beamforming maximum. This additional peak is the mirror of the true peak and is the result of reflections between antennas in the FSCD array.

4059 The first method of comparison is to analyze the images generated by applying the  
 4060 beamforming reconstruction specified in Section 4.3.1 to the FSCD and synthetic array  
 4061 data (see Figure 5.34). The beamforming grid consisting of a square  $121 \times 121$  grid  
 4062 spanning a range of -60-mm to 60 mm in the x and y dimensions. The beamforming  
 4063 images formed from the synthetic array produces a three-dimensional matrix where each  
 4064 grid position contains a summed time series. A single beamforming image is formed from  
 4065 this data matrix by taking the mean over the time dimension. In the case of the FSCD  
 4066 array, the VNA generates frequency domain data such that each grid position contains a  
 4067 summed frequency series produced by the VNA sweep. For this data a single image is

4068 formed by averaging in the frequency domain.

4069 There is a clear difference between the synthetic and FSCD array beamforming images,  
 4070 which is the additional faint beamforming maxima located directly opposite the maxima  
 4071 corresponding to the SYNCA position. The images in Figure 5.34 were generated with  
 4072 data collected at a SYNCA radial position of 15 mm, which agrees well with the observed  
 4073 beamforming maximum in both images. We observe that the faint beamforming peak is  
 4074 located directly opposite of the true beamforming maximum similar to a mirror image.  
 4075 Therefore, the origin of this additional feature appears to be reflections between the two  
 4076 sides of the circular antenna array that are not present for the synthetic array since only  
 4077 a single physical antenna is used.

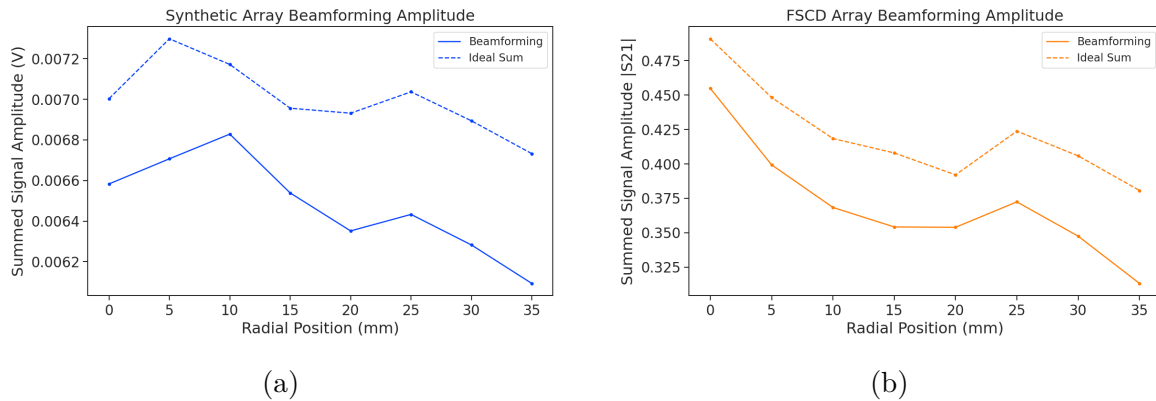


Figure 5.35: A comparison of the maximum signal amplitude obtained by beamforming to the signal amplitude obtained with an ideal summation as a function of the radial position of the SYNCA. The amplitudes for the synthetic array are shown in (a) and the FSCD array are shown in (b). In both setups we observe that the signal amplitudes obtained from beamforming are smaller than the signal amplitude that could be attained with the ideal summation without phase mismatch.

4078 From the beamforming images we extract the maximum amplitude, which we plot  
 4079 as a function of the radial position of the SYNCA (see Figure 5.35). The phase errors  
 4080 we observed in the FSCD and synthetic arrays leads to power loss at the beamforming  
 4081 stage due to phase mismatches between the signals at different channels. This power  
 4082 loss can be quantified by comparing the signal amplitude obtained from beamforming to  
 4083 the amplitude which would be obtained from an ideal summation. We perform the ideal  
 4084 summation by phase shifting each array channel to the same phase and then summing.  
 4085 The comparison between the beamforming and ideal sums is shown in Figure 5.35, where  
 4086 we observe that both the synthetic and FSCD arrays experience power losses from the  
 4087 beamforming summation.

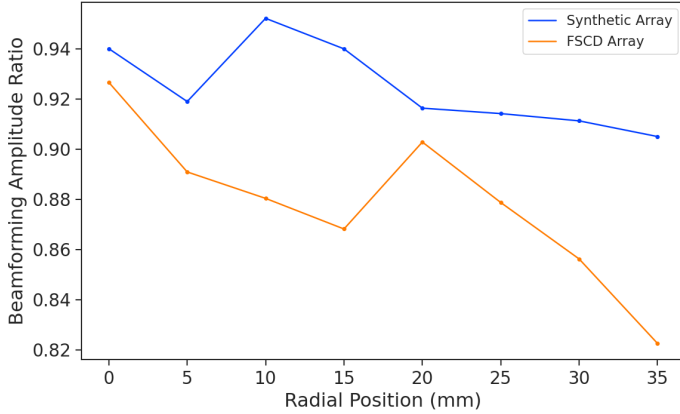


Figure 5.36: The ratio of the beamforming signal amplitude to the ideal signal amplitude for the FSCD and synthetic arrays. We see that the FSCD array has a larger power loss from phase error compare to the synthetic array which indicates that calibration errors associated with the multiple channels as well as reflections are impacting the signal reconstruction.

4088 The beamforming power loss can be quantified using the ratio of the beamforming to  
 4089 ideal signal amplitudes. Computing this ratio as a function of SYNCA radial position  
 4090 radius for the FSCD and synthetic arrays we find that the FSCD array has a uniformly  
 4091 smaller beamforming amplitude ratio, which means that the FSCD array has a larger  
 4092 beamforming power loss (see Figure 5.36). The primary contributions to the beamforming  
 4093 power loss in the synthetic array are phase errors from the SYNCA and phase errors  
 4094 from the FSCD antenna near-field. Both of these phase errors contribute to beamforming  
 4095 losses in the FSCD array, but there are clearly additional phase errors in the FSCD array  
 4096 measurements contributing to the smaller ratio. Two potential error sources include phase  
 4097 differences in the different antenna channels that could not be corrected by calibration as  
 4098 well as reflections between antennas in the array. The total effect of these additional phase  
 4099 errors is to reduce the beamforming amplitude ratio by about 5% from the beamforming  
 4100 ratio of the synthetic array. Therefore, we estimate that if no effort is made to correct  
 4101 these phase errors in an FSCD-like experiment, then we expect approximately a 10%  
 4102 total signal amplitude loss from a beamforming signal reconstruction.

#### 4103 5.4.4 Conclusions

4104 The estimated power loss of a beamforming reconstruction obtained from this analysis  
 4105 provides valuable inputs to sensitivity calculations of a FSCD-like antenna array exper-  
 4106 iment to measure the neutrino mass, since it helps to bound systematic uncertainties

4107 from the antenna array and reconstruction pipeline. This power loss lowers the estimated  
4108 detection efficiency of the experiment since some of the signal power is lost due to  
4109 improper combining between channels and also increases the uncertainty in the electron's  
4110 kinetic energy by contributing to errors in the estimation of the electron's cyclotron  
4111 frequency.

4112 If these reconstruction losses prove unacceptable there are steps that can be taken  
4113 to mitigate their effects. Some examples include the development of a more accurate  
4114 antenna simulation approach that can reproduce the observed near-field interference  
4115 patterns of the FSCD antennas and the implementation of a calibration approach that  
4116 allows for the relative phase delays of the array to be measured without changing or  
4117 disconnecting the antenna array configuration.

4118 **Chapter 6 |**

4119 **Development of Resonant Cavities for Large**

4120 **Volume CRES Measurements**

4121 **6.1 Introduction**

4122 The cavity approach was originally an alternative CRES measurement technology under  
4123 consideration by the Project 8 collaboration for the Phase IV experiment. After pursuing  
4124 an antenna array based CRES demonstrator design for several years, the increasing costs  
4125 and complexity of the antenna arrays led to a reconsideration of the baseline technology  
4126 for the ultimate CRES experiment planned by Project 8. Currently, a cavity based CRES  
4127 experiment is the preferred technology choice for future experiments by the Project 8  
4128 collaboration including the Phase IV experiment.

4129 In this chapter I provide a brief summary of resonant cavities and sketch out the key  
4130 features of a cavity based CRES experiment. In Section 6.2 I provide a brief introduction  
4131 to cylindrical resonant cavities and the solutions for the electromagnetic fields in the  
4132 cavity volume.

4133 In Section 6.3 I describe the main components of a cavity based CRES experiment,  
4134 including the background and trap magnets, cavity geometry and design, and cavity  
4135 coupling considerations. I also discuss some relevant trade-offs between an antenna array  
4136 and cavity CRES experiment, and highlight some reasons for the transition of Project 8  
4137 to the development of a cavity based experiment.

4138 Finally, in Sections 6.4 and 6.5, I present the design and development of an open  
4139 mode-filtered cavity that could be used in a cavity based CRES experiment with atomic  
4140 tritium. The results of the cavity simulations are confirmed by laboratory measurements  
4141 of a proof-of-principle prototype that demonstrates key features of the design.

## 4142 6.2 Cylindrical Resonant Cavities

4143 Resonant cavities are sealed conductive containers, which allows us to describe the  
4144 electromagnetic (EM) fields contained in the cavity volume as a superposition of resonant  
4145 modes [85]. The field shapes of the resonant modes are determined by Maxwell's equations  
4146 and the boundary conditions enforced by the cavity geometry. Of interest to Project 8  
4147 for CRES measurements are cylindrical cavities due to their ease of construction and  
4148 integration with atom and electron trapping magnets.

### 4149 6.2.1 General Field Solutions

4150 Consider a long segment of conducting material with a cylindrical cross-section (see  
4151 Figure 6.1). A geometry such as this can be used as a waveguide transmission line to  
4152 transfer EM energy from point to point, or, if conducting shorts are inserted on both  
4153 ends of the cylinder, the waveguide becomes a resonant cavity.

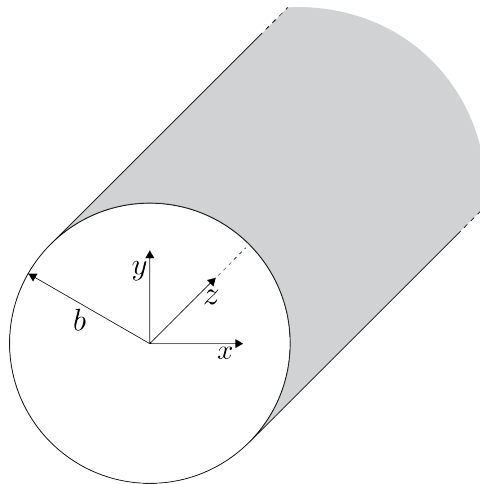


Figure 6.1: Geometry of a cylindrical waveguide with radius  $b$ .

4154 The fields allowed inside a cylindrical cavity are determined by the boundary conditions  
4155 of the cylindrical geometry. The general approach to solving the fields begins by assuming  
4156 solutions to Maxwell's equations of the form

$$\mathbf{E}(x, y, z) = (\mathbf{e}(x, y) + \hat{z}e_z(x, y))e^{-i\beta z}, \quad (6.1)$$

$$\mathbf{H}(x, y, z) = (\mathbf{h}(x, y) + \hat{z}h_z(x, y))e^{-i\beta z}. \quad (6.2)$$

4157 The solutions assume a harmonic time dependence of the form  $e^{i\omega t}$  and propagation

4158 along the positive z-axis. The functions  $\mathbf{e}(x, y)$  and  $\mathbf{h}(x, y)$  represent the transverse  
 4159  $(\hat{x}, \hat{y})$  components of the electric and magnetic fields respectively, and  $e_z(x, y)$ ,  $h_z(x, y)$   
 4160 represent the longitudinal components. The version of Maxwell's equations in the case  
 4161 where there are no source terms can be written as a pair of coupled differential equations,

$$\nabla \times \mathbf{E} = -i\omega\mu\mathbf{H}, \quad (6.3)$$

$$\nabla \times \mathbf{H} = i\omega\epsilon\mathbf{E}, \quad (6.4)$$

4162 where  $\epsilon$  and  $\mu$  are the permittivity and permeability of the material inside the waveguide  
 4163 or cavity. Using the field solutions from Equations 6.1 and 6.2 one can solve for the  
 4164 transverse components of the fields in terms of the longitudinal fields. Because we  
 4165 are interested in cylindrical cavities it is advantageous to write the field solutions in  
 4166 cylindrical coordinates. After performing this transformation the set of four equations  
 4167 for the transverse field components are,

$$H_\rho = \frac{i}{k_c^2} \left( \frac{\omega\epsilon}{\rho} \frac{\partial E_z}{\partial\phi} - \beta \frac{\partial H_z}{\partial\rho} \right), \quad (6.5)$$

$$H_\phi = \frac{-i}{k_c^2} \left( \omega\epsilon \frac{\partial E_z}{\partial\rho} + \frac{\beta}{\rho} \frac{\partial H_z}{\partial\phi} \right), \quad (6.6)$$

$$E_\rho = \frac{-i}{k_c^2} \left( \beta \frac{\partial E_z}{\partial\rho} + \frac{\omega\mu}{\rho} \frac{\partial H_z}{\partial\phi} \right), \quad (6.7)$$

$$E_\phi = \frac{i}{k_c^2} \left( \frac{-\beta}{\rho} \frac{\partial E_z}{\partial\phi} + \omega\mu \frac{\partial H_z}{\partial\rho} \right), \quad (6.8)$$

4168 where  $k_c$  is the cutoff wavenumber defined by  $k_c^2 = k^2 - \beta^2$  with  $k = \omega\sqrt{\mu\epsilon}$  being the  
 4169 wavenumber of the EM radiation.

4170 This set of equations can be used to solve for a variety of different modes that can be  
 4171 obtained by setting conditions on  $E_z$  and  $H_z$ . For cylindrical cavities two types of modes  
 4172 are allowed, which correspond to solutions where  $E_z = 0$  and  $H_z = 0$  respectively.

### 4173 6.2.2 TE and TM Modes

4174 The TE family of modes corresponds to the case where  $E_z = 0$ . This implies that  $H_z$  is  
 4175 a solution to the Helmholtz wave equation

$$(\nabla^2 + k^2)H_z = 0. \quad (6.9)$$

4176 For solutions of the form  $H_z(\rho, \phi, z) = h_z(\rho, \phi)e^{-i\beta z}$ , Equation 6.9 can be solved using  
4177 the standard technique of separation of variables. Rather than reproduce the derivation  
4178 here we shall simply quote the solutions for the transverse fields [85], which are

$$H_\rho = \frac{-i\beta}{k_{c_{nm}}} (A \sin n\phi + B \cos n\phi) J'_n(k_{c_{nm}}\rho) e^{-i\beta_{nm}z}, \quad (6.10)$$

$$H_\phi = \frac{-i\beta n}{k_{c_{nm}}^2 \rho} (A \cos n\phi - B \sin n\phi) J_n(k_{c_{nm}}\rho) e^{-i\beta_{nm}z}, \quad (6.11)$$

$$E_\rho = \frac{-i\omega\mu n}{k_{c_{nm}}^2 \rho} (A \cos n\phi - B \sin n\phi) J_n(k_{c_{nm}}\rho) e^{-i\beta_{nm}z}, \quad (6.12)$$

$$E_\phi = \frac{i\omega\mu}{k_{c_{nm}}} (A \sin n\phi + B \cos n\phi) J'_n(k_{c_{nm}}\rho) e^{-i\beta_{nm}z}. \quad (6.13)$$

4179 One can observe that the solutions have a periodic dependence on  $\phi$ , and radial profiles  
4180 given by the Bessel functions of the first kind. The integer indices  $n$  and  $m$  arise from  
4181 continuity conditions on the EM fields in the azimuthal and radial directions. For the  
4182 TE modes  $n \geq 0$  and  $m \geq 1$ .  $k_{c_{nm}}$  is the cutoff wavenumber for the  $\text{TE}_{nm}$  mode given by

$$k_{c_{nm}} = \frac{p'_{nm}}{b}, \quad (6.14)$$

4183 where  $b$  is the radius of the cavity or waveguide and  $p'_{nm}$  is the  $m$ -th root of the derivative  
4184 of the  $n$ -th order Bessel function (see Table 6.1).

Table 6.1: A table of the values of  $p'_{nm}$ .

$n$	$p'_{n1}$	$p'_{n2}$	$p'_{n3}$
0	3.832	7.016	10.174
1	1.841	5.331	8.536
2	3.054	6.706	9.970

4185 The TM mode family corresponds to the case where  $H_z = 0$ , and  $(\nabla^2 + k^2)E_z = 0$ .  
4186 Again, we assume solutions of the form  $E_z(\rho, \phi, z) = e_z(\rho, \phi)e^{-i\beta z}$ , for which the general  
4187 form of the solutions is the same as for the TE modes. However, the different boundary  
4188 conditions for the TM modes results in particular solutions with a different from, which  
4189 we shall quote here without derivation. The transverse fields of the TM modes are given  
4190 by

$$H_\rho = \frac{-i\omega\epsilon n}{k_{c_{nm}}^2 \rho} (A \cos n\phi - B \sin n\phi) J_n(k_{c_{nm}}\rho) e^{-i\beta_{nm}z}, \quad (6.15)$$

$$H_\phi = \frac{-i\omega\epsilon}{k_{c_{nm}}}(A \sin n\phi + B \cos n\phi) J'_n(k_{c_{nm}}\rho) e^{-i\beta_{nm}z} \quad (6.16)$$

$$E_\rho = \frac{-i\beta}{k_{c_{nm}}}(A \sin n\phi + B \cos n\phi) J'_n(k_{c_{nm}}\rho) e^{-i\beta_{nm}z}, \quad (6.17)$$

$$E_\phi = \frac{-i\beta n}{k_{c_{nm}}^2 \rho}(A \cos n\phi - B \sin n\phi) J_n(k_{c_{nm}}\rho) e^{-i\beta_{nm}z}, \quad (6.18)$$

<sup>4191</sup> which one may notice are the same solutions as the TE modes with  $H$  and  $E$  flipped.  
<sup>4192</sup> The cutoff wavenumber for the TM modes is given by,  $k_{c_{nm}} = p_{nm}/b$ , where the values of  
<sup>4193</sup>  $p_{nm}$  correspond to the  $m$ -th zero of the  $n$ -th order Bessel function (see Table 6.2).

Table 6.2: A table of the values of  $p_{nm}$ .

$n$	$p_{n1}$	$p_{n2}$	$p_{n3}$
0	2.405	5.520	8.654
1	3.832	7.016	10.174
2	5.135	8.417	11.620

### <sup>4194</sup> 6.2.3 Resonant Frequencies of a Cylindrical Cavity

<sup>4195</sup> A cylindrical cavity is constructed by taking a section of cylindrical waveguide and  
<sup>4196</sup> shorting both ends with conductive material. This means that the electric fields inside  
<sup>4197</sup> a cylindrical cavity are exactly those we derived in Section 6.2.2 with the additional  
condition that the electric fields must go to zero at  $z = 0$  and  $z = L$  (see Figure 6.2).

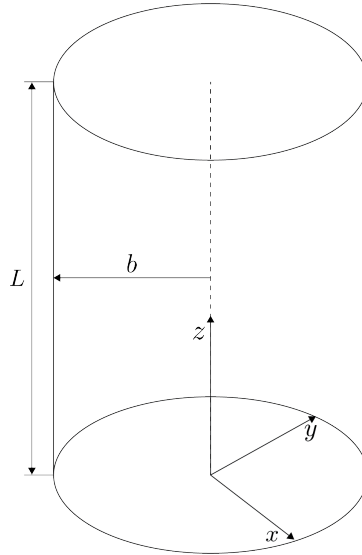


Figure 6.2: The geometry of a cylindrical cavity with length  $L$  and radius  $b$ .

4198

4199 The transverse electric field solutions for a cylindrical waveguide are of the form

$$\mathbf{E}(\rho, \phi, z) = \mathbf{e}(\rho, \phi) (A_+ e^{-i\beta_{nm}z} + A_- e^{i\beta_{nm}z}), \quad (6.19)$$

4200 where  $A_+$  and  $A_-$  are arbitrary amplitudes of forward and backward propagating waves.

4201 In order to enforce that  $\mathbf{E}$  is zero at both ends of the cavity we require that

$$\beta_{nm}L = 2\pi\ell, \quad (6.20)$$

4202 where  $\ell = 0, 1, 2, 3, \dots$ . Using this constraint on the propagation constant we can solve

4203 for the resonant frequencies of the  $\text{TE}_{nml}$  and the  $\text{TM}_{nml}$  modes in a cylindrical cavity.

4204 For the TE modes the resonant frequencies are

$$f_{nml} = \frac{c}{2\pi\sqrt{\mu_r\epsilon_r}} \sqrt{\left(\frac{p'_{nm}}{b}\right)^2 + \left(\frac{\ell\pi}{L}\right)^2}, \quad (6.21)$$

4205 and the frequencies of the TM modes are

$$f_{nml} = \frac{c}{2\pi\sqrt{\mu_r\epsilon_r}} \sqrt{\left(\frac{p_{nm}}{b}\right)^2 + \left(\frac{\ell\pi}{L}\right)^2}. \quad (6.22)$$

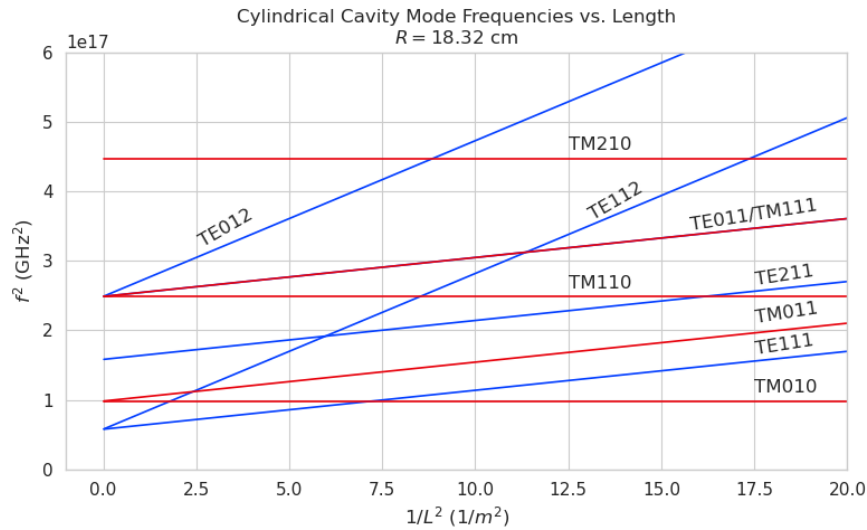


Figure 6.3: Relation of mode frequency to cavity length for a cylindrical cavity with a radius of 18.32 cm.

## 4206 6.2.4 Cavity Q-factors

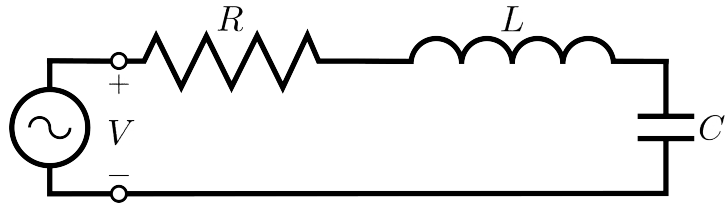


Figure 6.4: A series RLC circuit.

4207 The resonant behavior of cylindrical cavities can be modeled as a series RLC circuit  
 4208 (see figure 6.4). The input impedance of the circuit can be obtained by applying  
 4209 Kirchhoff's laws to calculate the impedance of the equivalent circuit. For a series RLC  
 4210 circuit the input impedance is

$$Z_{\text{in}} = \left( \frac{1}{R} + \frac{1}{i\omega L} + i\omega C \right). \quad (6.23)$$

4211 The resistance in the circuit represents all sources of loss in the cavity, which is primarily  
 4212 caused by the finite conductivity of the cavity walls. The inductor and capacitor represent  
 4213 the energy stored in the cavity in the form of electric and magnetic fields. If the circuit  
 4214 is being driven by an external power source we can write the input power in terms of the  
 4215 circuit input impedance and the source voltage

$$P_{\text{in}} = \frac{1}{2} Z_{\text{in}} |I|^2 = \frac{1}{2} |I|^2 \left( \frac{1}{R} + \frac{1}{i\omega L} + i\omega C \right). \quad (6.24)$$

4216 The resistor introduces a loss into the system with a power given by

$$P_{\text{loss}} = \frac{1}{2} |I|^2 R, \quad (6.25)$$

4217 and the capacitor and inductor store energies given by

$$W_e = \frac{1}{4} \frac{|I|^2}{\omega^2 C}, \quad (6.26)$$

$$W_m = \frac{1}{4} |I|^2 L, \quad (6.27)$$

4218 respectively. Using these expressions we can write the input power and input impedance

4219 expressions in terms of the lost power and stored energy

$$P_{\text{in}} = P_{\text{loss}} + 2i\omega(W_m - W_e), \quad (6.28)$$

$$Z_{\text{in}} = \frac{P_{\text{loss}} + 2i\omega(W_m - W_e)}{\frac{1}{2}|I|^2}. \quad (6.29)$$

4220 The condition for resonance in the RLC circuit is that the stored magnetic energy  
4221 is equal to the stored electric energy ( $W_e = W_m$ ). When this occurs  $Z_{\text{in}} = R$ , which is a  
4222 purely real impedance, and  $P_{\text{in}} = P_{\text{loss}}$ . The resonant frequency of the circuit can be  
4223 determined from the condition  $W_e = W_m$  from which one finds that

$$\omega_0 = \frac{1}{\sqrt{LC}}. \quad (6.30)$$

4224 An important performance parameter for any resonant system is the Q-factor, which  
4225 quantifies the quality of the resonator as the ratio of the stored energy multiplied by the  
4226 resonant frequency to the average energy lost per second. For the series RLC circuit, the  
4227 Q-factor is given by the expression

$$Q_0 = \omega \frac{W_e + W_m}{P_{\text{loss}}} = \frac{1}{\omega_0 RC}, \quad (6.31)$$

4228 from which one observes that as the resistance of the RLC circuit is decreased the quality  
4229 factor of the resonator increases. From the perspective of cylindrical cavities this implies  
4230 that as one decreases the resistance of the cavity walls it is expected that the Q-factor of  
4231 the cavity should increase, which is indeed the case. In certain applications where a high  
4232 Q is desireable it is possible to manufacture a cavity out of superconducting materials in  
4233 order to minimize the power losses of the system.

4234 The Q-factor of the resonator also determines with bandwidth (BW) of the system.  
4235 A cavity with a high Q-factor will resonant with a smaller range of frequencies than a  
4236 cavity with a low Q-factor. To see this we can examine the behavior of the RLC circuit  
4237 when driven by frequencies near the resonance. For a frequency  $\omega = \omega_0 + \Delta\omega$ , where  
4238  $\Delta\omega = \omega - \omega_0 \ll \omega_0$ , we can write the input impedance as

$$Z_{\text{in}} = R + i\omega L \left( \frac{\omega^2 - \omega_0^2}{\omega^2} \right), \quad (6.32)$$

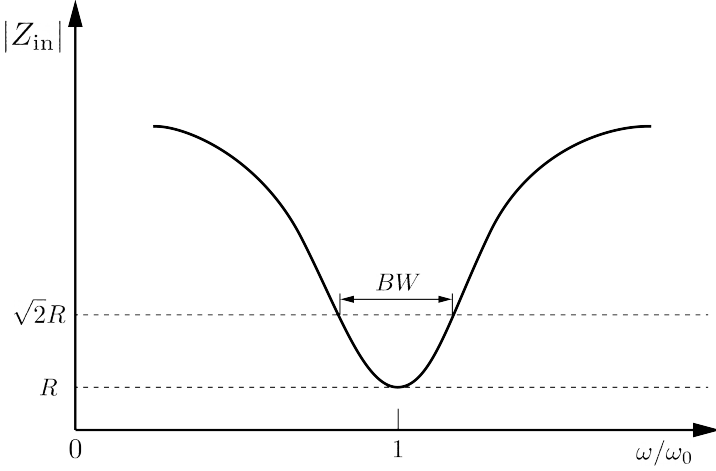


Figure 6.5: Illustration of the behavior of the input impedance of the series RLC circuit as a function of the driving frequency. The BW is proportion to the width of the resonance, which is inversely proportional to Q.

<sup>4239</sup> and by expanding  $(\omega^2 - \omega_0^2)/\omega^2$  to first order in  $\Delta\omega$ , we obtain

$$Z_{\text{in}} \approx R + i \frac{2RQ_0\Delta\omega}{\omega_0}. \quad (6.33)$$

<sup>4240</sup> Therefore, the magnitude of the input impedance near the resonance is given by

$$|Z_{\text{in}}| = R \sqrt{1 + 4Q_0^2 \frac{\Delta\omega^2}{\omega^2}}, \quad (6.34)$$

<sup>4241</sup> from which we observe that for the series RLC circuit the input impedance is minimized  
<sup>4242</sup> at the resonant frequency, which corresponds to the maximum input power (see Figure  
<sup>4243</sup> 6.5). The half-power BW is the range of frequencies over which the input power drops to  
<sup>4244</sup> half the input power on resonance. This occurs when  $|Z_{\text{in}}| = \sqrt{2}R$ , which corresponds to  
<sup>4245</sup>  $\Delta\omega/\omega = \text{BW}/2$ . Using Equation 6.34 one can find that

$$2R^2 = R^2(1 + Q_0^2\text{BW}^2), \quad (6.35)$$

<sup>4246</sup> which implies

$$\text{BW} = \frac{1}{Q_0} \quad (6.36)$$

<sup>4247</sup> It is important to emphasize that the Q-factor defined here,  $Q_0$ , is technically the  
<sup>4248</sup> unloaded Q. It reflects the quality of the cavity or resonant circuit without the influence  
<sup>4249</sup> of any external circuitry. In practice, however, a cavity is invariably coupled to an

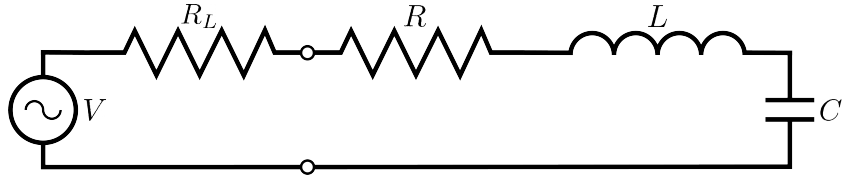


Figure 6.6: A series RLC circuit coupled to an external circuit with input impedance  $R_L$ .

external circuit to drive a cavity resonance or to measure the energy of a resonant mode. Coupling a cavity to an external circuit changes the Q by loading the equivalent cavity RLC circuit (see Figure 6.6). The Q-factor of the cavity when it is loaded by an external circuit is called the loaded Q, which is the quantity that one actually measures when exciting a resonance in the cavity. Using the series RLC circuit model one can see that the load resistor in Figure 6.6 will add in series with the resistor in the circuit for a total equivalent resistance of  $R + R_L$ . Therefore, the loaded Q is given by

$$Q_L = \frac{1}{\omega_0(R + R_L)C}, \quad (6.37)$$

from which one observes that the loaded Q is always less than the intrinsic Q of the cavity.

The amount of coupling that is desireable depends on the specific application of the resonator. If one wants a resonator that is particular frequency selective than it makes sense to limit the amount of coupling to the cavity to maintain a small BW, alternatively, if a larger BW is need one can increase the cavity coupling by tuning the input impedance of the external circuit. The critical point, where maximum power is transferred between the cavity and the external circuit, occurs when the input impedance of the cavity matches the input impedance of the external transmission line. For the series RLC circuit on resonance, this matching condition corresponds to

$$Z_0 = Z_{in} = R, \quad (6.38)$$

where  $Z_0$  is the impedance of the transmission line. The loaded Q at this critical point is, therefore,

$$Q_L = \frac{1}{2\omega_0 Z_0 C} = \frac{Q_0}{2}. \quad (6.39)$$

One can described the degree of coupling between the cavity and an external circuit by

4270 defining a coupling factor,  $g$ , such that,

$$g = \frac{Q_0}{Q_L} - 1. \quad (6.40)$$

4271 When  $g = 1$  then  $Q_L = Q_0/2$ , and the cavity is said to be critically coupled as we  
4272 described. If  $Q_L < Q_0/2$ , then the cavity is undercoupled to the transmission line,  
4273 corresponding to  $g < 1$ . Alternatively, if  $Q_L > Q_0/2$ , then  $g > 1$ , and the cavity is  
4274 overcoupled to the transmission line. Various specialized circuits can be used to tune the  
4275 input impedance of the external circuit as seen by the cavity to achieve a wide range of  
4276 different coupling factors based on the desired application of the cavity.

## 4277 6.3 The Cavity Approach to CRES

### 4278 6.3.1 A Sketch of a Molecular Tritium Cavity CRES Experiment

4279 Resonant cavities can be used to perform CRES measurements, and they represent the  
4280 current preferred technology by the Project 8 collaboration. The basic approach to a  
4281 neutrino mass measurement using a resonant cavity and molecular tritium beta-decay  
source is illustrated by Figure 6.7.

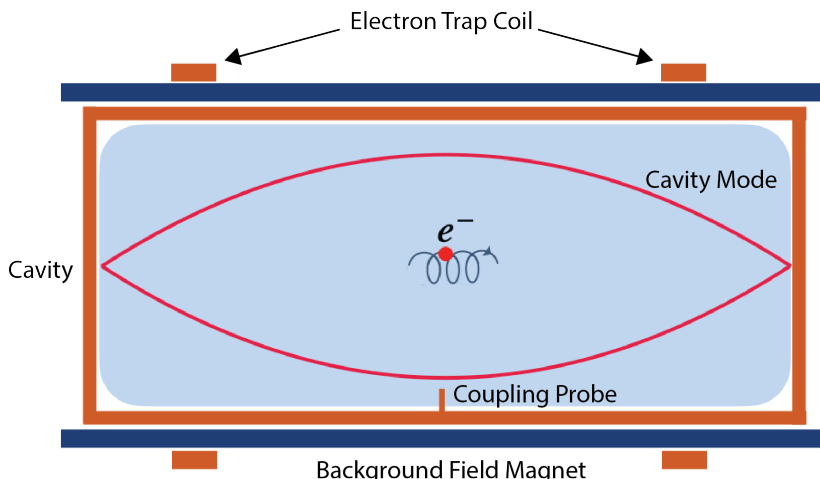


Figure 6.7: A cartoon depiction of a cavity CRES experiment. A metallic cavity filled with tritium gas is inserted into a uniform background magnetic field to perform CRES measurements. Electrons from beta-decays inside the cavity can be trapped and used to excite a resonant mode(s). By coupling to the cavity mode with a suitable probe one can measure the cyclotron frequency of the electron and perform CRES.

4282

4283 At the core of the experiment is a large resonant cavity filled with tritium gas. The  
4284 filled cavity is then placed in a uniform magnetic field provided by a primary magnet  
4285 that provides the background magnetic field. The value of the background magnetic field  
4286 sets the range of cyclotron frequencies for electrons emitted near the tritium spectrum  
4287 endpoint. When a beta-decay electron is produced in the cavity it is trapped using a set  
4288 of magnetic pinch coils that keep electrons inside the cavity volume.

4289 Electrons trapped inside the cavity do not radiate in the same way as electrons  
4290 in free-space. Effectively, the same boundary conditions that were used to derive the  
4291 resonant modes of a cylindrical cavity in Section 6.2 apply to the radiation of the electron  
4292 as well. The coupling of an electron performing cyclotron motion in a cavity has been  
4293 studied in detail for measurements of the electron’s magnetic moment [94–96] If an  
4294 electron is emitted with a kinetic energy that corresponds to a cyclotron frequency that  
4295 matches a resonant frequency of the cavity, then energy radiated by the electron excites  
4296 a corresponding resonance in the cavity. The strength of the electron’s coupling to the  
4297 cavity is given to first order by the dot product between the electrons trajectory and  
4298 the electric field vector of the resonant mode. Additional effects, such as the Purcell  
4299 enhancement [97], alter the emitted power from the free-space Larmor equation [48]. If an  
4300 electron is moving with a cyclotron frequency that is far from any resonant modes in the  
4301 cavity, then radiation from the electron is suppressed. One can interpret this somewhat  
4302 surprising effect as the metallic walls of the cavity reflecting the radiated energy back to  
4303 the electron.

4304 Detecting an electron in the cavity is accomplished by coupling the cavity to an  
4305 external transmission line that leads to an amplifier and RF receiver chain [98]. The  
4306 coupling of the cavity resonance to the amplifier occurs through a coupling probe or  
4307 aperture designed to read-out the excitation of the mode(s) excited by the electron. For  
4308 CRES measurements, the placement of a wire antenna coupling probe inside the cavity  
4309 volume leads to unacceptable losses of tritium atoms due to recombination to molecular  
4310 tritium on the antenna surface, therefore, apertures are the preferred coupling method  
4311 for cavity CRES experiments.

4312 One of the attractive features of the CRES technique for neutrino mass measurement  
4313 is the gain in statistics that comes from the differential nature of the tritium spectrum  
4314 measurement. Initially, this seems incompatible with cavities, due to the narrow reso-  
4315 nances of cavity modes giving relatively small bandwidth. However, by intentionally  
4316 over-coupling to a single cavity mode one can achieve bandwidths of a few 10’s of MHz  
4317 (see Section 6.2), which is sufficient for a measurement of the tritium spectrum endpoint

4318 region.

### 4319 **6.3.2 Magnetic Field, Cavity Geometry, and Resonant Modes**

#### 4320 **Magnetic Field and Volume Scaling**

4321 For a CRES experiment, cylindrical cavities are a natural choice since they match  
4322 the geometry of standard solenoid magnets, which are needed in order to produce the  
4323 background magnetic field for CRES measurements. Furthermore, the cylindrical shape is  
4324 compatible with a Halbach array, which is the leading choice of atom trapping technology  
4325 for future atomic tritium experiments by the Project 8 collaboration. Cylindrical  
4326 cavities also benefit from well-established machining practices that are able to achieve  
4327 high geometric precision at large lengths scales. More exotic cavity designs are under-  
4328 consideration and there are on-going efforts to investigate the potential advantages these  
4329 may have over the standard cylindrical geometry.

4330 As we saw in Section 6.2, the physical dimensions of the cavity are directly coupled  
4331 to the resonant frequencies of the cavity. This dependency links the size of the cavity to  
4332 the magnitude of the background magnetic field, because the magnetic field determines  
4333 the cyclotron frequencies of trapped electrons. Specifically, as the size of the cavity is  
4334 increased to accommodate larger volumes of tritium gas, the frequencies of the resonant  
4335 modes decrease proportionally. This requires that the magnetic field also decrease in  
4336 order to maintain coupling between electrons and the desired cavity mode.

4337 The required cavity size is ultimately determined by the required statistics in the  
4338 tritium spectrum endpoint region. Because the gas density must be kept below a certain  
4339 level to ensure that electrons have sufficient time to radiate before scattering, larger  
4340 volumes become the only way to achieve higher event statistics. To achieve the sensitivity  
4341 goals of Phase III and IV cavity volumes on the order of several cubic-meters are required,  
4342 which pushes one towards frequencies in the range of 100's of MHz.

#### 4343 **Single-mode Cavity CRES**

4344 It is tempting to consider maintaining a high magnetic field, while still increasing the size  
4345 of the cavity, in order to increase the radiated power from trapped electrons for better  
4346 SNR. However, if one were to maintain the same magnetic field while increasing the  
4347 size of the cavity, the electrons would begin to couple to higher order modes with more  
4348 complicated transverse geometries. The danger with this approach is that a complicated  
4349 mode structure could introduce systematic errors into the CRES signals. Example

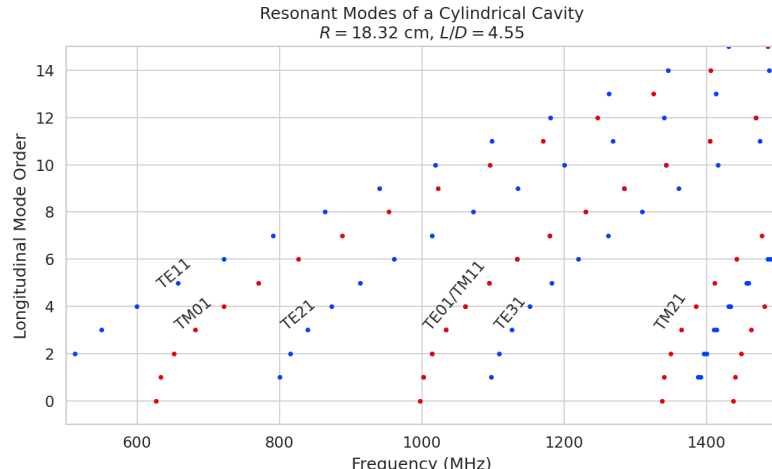
4350 systematics include unpredicted mode hybridization or changes in the mode shapes from  
4351 imperfections in the cavity construction, which would prevent reconstruction of the  
4352 electron's starting kinetic energies with adequate resolution. For this reason, it is ideal  
4353 to operate with magnetic fields that give cyclotron frequencies near the fundamental  
4354 frequency of the cavity, where the mode structure is relatively simple (see Figure 6.8).  
4355 In this frequency region it is possible to perform CRES by coupling to only a single  
4356 resonant mode, however, it is currently an open question if a single mode measurement  
4357 will provide enough information about an individual electron's position to reconstruct  
4358 the full event. Regardless, developing a solid understanding of the CRES phenomenology  
4359 when an electron is coupling to a single mode will be a necessary step towards a future  
4360 multi-mode cavity experiment.

#### 4361 Considerations for Resonant Mode Selection

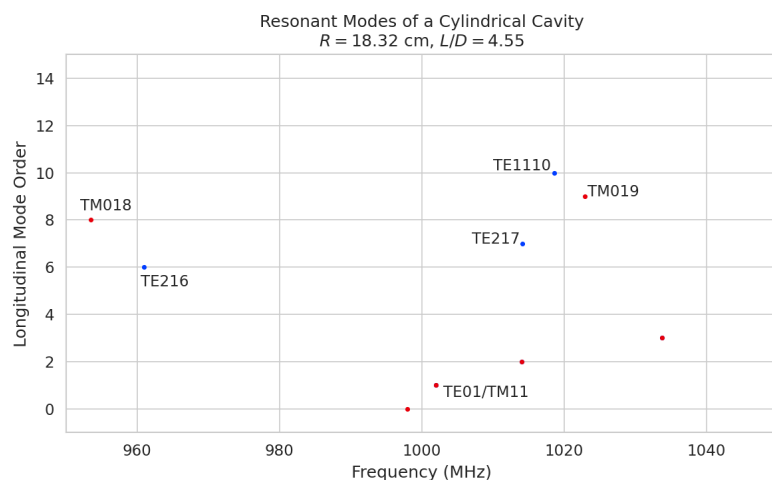
4362 A single-mode cavity experiment begs the question, which resonant mode is best for  
4363 CRES measurements? There is an immediate bias towards low order  $TE_{nm}$  and  $TM_{nm}$   
4364 modes due to the multi-mode considerations discussed above. Additionally, there is a  
4365 preference towards modes with longitudinal index  $\ell = 1$  with a single antinode along the  
4366 vertical axis of the cylindrical cavity. The reason for this is that there is a phase change  
4367 in the electric fields between antinodes that leads to modulation effects that destroy the  
4368 carrier frequency signal information.

4369 A second consideration for mode selection is the volumetric efficiency of the mode.  
4370 Volumetric efficiency can be thought of as an integral over the volume of the cavity  
4371 weighted by the relative amplitude of the mode. From the perspective of simply maximiz-  
4372 ing the volume useable for CRES measurements this integral would be as close to unity  
4373 as possible. However, there is a requirement to reconstruct the position of the electrons  
4374 inside the cavity volume so that the local magnetic fields can be used to convert the  
4375 measured cyclotron frequency to a kinetic energy. With a single mode this necessarily  
4376 requires a variable transverse mode amplitude, which lowers the volumetric efficiency, so  
4377 that position of the electron in the cavity can be estimated from the average amplitude  
4378 of the CRES signal. Longitudinal indices of  $\ell = 1$  have an advantage in volumetric  
4379 efficiency over higher order  $\ell$  modes, since there are only two longitudinal nodes, one at  
4380 each end of the cavity. Therefore, the average coupling strength of trapped electrons as  
4381 they oscillate axially is higher for  $\ell = 1$  modes.

4382 The longitudinal variation in the mode strength is ultimately critical for achieving the  
4383 energy resolution required for neutrino mass measurements. Correcting for the change in



(a)



(b)

Figure 6.8: Examples of the resonant mode frequencies of a cylindrical cavity. This cavity has a radius of 18.32 cm and a length to diameter ratio of 4.55.

4384 the average magnetic fields experienced by electrons with different pitch angles requires  
 4385 that information on the axial motion of the electron be encoded into the CRES signal.  
 4386 The longitudinal variation in the mode amplitude leads to amplitude modulation of the  
 4387 CRES signal with a frequency proportional to the electron's pitch angle.

4388 An additional factor for mode selection is the intrinsic or unloaded Q of the mode. In  
 4389 terms of SNR it is advantageous to use a mode with a very high  $Q_0$ , which is then highly  
 4390 overcoupled to achieve the necessary bandwidth to cover the tritium endpoint spectrum.  
 4391 This scheme leads to a decoupling of the physical cavity temperature from the effective  
 4392 noise temperature after the amplifier, which allows us to achieve adequate SNR without

4393 the requirement of cooling the entire cavity to single Kelvin temperatures.

4394 An example of a resonant mode that exhibits these traits is the TE<sub>011</sub> mode. At present  
4395 the TE<sub>011</sub> mode is the preferred resonance for a single-mode cavity CRES experiment  
4396 by the Project 8 collaboration. TE<sub>011</sub> is a low order mode located in a region relatively  
4397 far from other cavity modes. Furthermore, the separation of the TE<sub>011</sub> mode can be  
4398 improved by various mode-filtering techniques discussed in Section 6.4.2 below. TE<sub>011</sub>  
4399 consists of a single longitudinal antinode that can provide pitch angle information in the  
4400 form of amplitude modulation, and has an electric field with a radial profile given by the  
4401  $J'_0$  Bessel function allowing for radial position estimation. Lastly, the TE<sub>011</sub> mode has a  
4402 relatively high intrinsic Q compared to nearby modes, which helps with SNR. Unloaded  
4403 Q's greater than 80000 are achievable for a 1 GHz TE<sub>011</sub> resonance using a copper walled  
4404 cavity.

#### 4405 **6.3.3 Trade-offs Between the Antenna and Cavity Approaches**

4406 The choice between cavities and antennas for large-scale CRES measurements is not  
4407 without trade-offs. Both the antenna array and cavity approaches are relatively immature  
4408 techniques, at present there are no known obstacles that would prevent either approach  
4409 from being used for a large scale neutrino mass experiment. The preference for cavities  
4410 is largely driven by important practical considerations that could make a cavity based  
4411 experiment significantly cheaper than an antenna experiment of similar size and scope.  
4412 However, the switch to cavities also introduces new challenges less relevant to the  
4413 antenna array, which must be solved in order for Project 8 to achieve its neutrino mass  
4414 measurement goals.

4415 One of the major relative drawbacks of the antenna array approach is the size and  
4416 complexity of the data-acquisition system. A large-scale antenna array experiment  
4417 requires  $O(100)$  antennas independently digitized at rates of  $O(10)$  to  $O(100)$  MHz. Since  
4418 there is insufficient information in a single antenna channel to detect or reconstruct the  
4419 CRES signal, the entire array output must be processed during the signal reconstruction.  
4420 Because data storage becomes an issue with these data volumes, there is a real-time  
4421 signal reconstruction requirement that allows one to detect CRES signals buried in the  
4422 thermal noise. As we discuss in Section 4.4, the computational cost of these real-time  
4423 detection algorithms are potentially quite large for even a small scale antenna array  
4424 experiment. However, the operating principle of a cavity experiment allows the CRES  
4425 signal to be detected using only a single read-out channel digitized at rates of  $O(10)$  MHz,  
4426 which reduces the cost of the data acquisition system by many orders of magnitude.

4427 From an engineering perspective, the simple geometry and thin-walls of a cylindrical  
4428 cavity are simpler to interface with the cryogenic and magnetic subsystems needed for a  
4429 CRES experiment. Whereas, the antenna array requires careful design and engineering  
4430 to accommodate the antenna array and receiver electronics in proximity to the trapping  
4431 magnets. Additionally, due to near-field interference effects, the antenna array is unable  
4432 to reconstruct CRES events within the reactive near-field distance of the antennas.  
4433 Because atom trapping requirements require magnetic fields which correspond to cyclotron  
4434 frequencies for endpoint electrons less than 1 GHz, the required stand-off distance leads to  
4435 a significant loss in useable experiment volume, necessitating larger and more expensive  
4436 magnets.

4437 Another advantage to the cavity approach is the relatively compact sideband structure,  
4438 which is a result of the low modulation index for cavity CRES signals. The axial motion  
4439 in an antenna array experiment leads to frequency modulation and sidebands. The shape  
4440 of the sideband structure is determined by the modulation index,  $h = \frac{\Delta f}{f_a}$ , where  $\Delta f$   
4441 is the size of the frequency deviation and  $f_a$  is the axial frequency. The large electron  
4442 traps required for a cubic-meter-scale experiment leads to high modulation indices, which  
4443 causes the signal spectrum to be made up of numerous low power sidebands that make  
4444 reconstruction and detection challenging. This behavior was observed in simulations  
4445 of the FSCD in which carrier power decreased with pitch angle due to the increase in  
4446 modulation index (see Figure 4.31). For cavities, however, the modulation index remains  
4447 near  $h = 1$  even for very long magnetic traps due to the high phase velocity in cavities  
4448 relative to the axial velocity of the electron. This results in an almost ideal spectrum  
4449 shape that has a strong carrier frequency with a few sidebands whose relative amplitudes  
4450 encode pitch angle information.

4451 A downside of the cavity approach is the apparent difficulty of estimating the position  
4452 of the electron using only the coupling of the electron to a single mode. The amplitude of  
4453 the TE<sub>011</sub> mode is completely independent of the azimuthal coordinate, therefore, position  
4454 reconstruction using the TE<sub>011</sub> mode is only able to estimate the radial position of the  
4455 electron. This position degeneracy may lead to magnetic field uniformity requirements  
4456 that are too challenging to meet due to mechanical uncertainties in cavity and magnet  
4457 construction, as well as uncertainties caused by nuisance external magnetic fields such  
4458 as the Earth's field and magnetic fields from building materials. A multi-mode cavity  
4459 experiment may provide a way to extract more precise information on the position of  
4460 the electron by analyzing the coupling of the electron to several modes that overlap in  
4461 different ways.

## 4462 **6.4 Single-mode Resonant Cavity Design and Simulations**

4463 The single-mode cylindrical cavities envisioned for the Phase III and IV experiments must  
4464 be carefully engineered in order to measure the neutrino mass with the desired sensitivity.  
4465 In this section I summarize some simulation studies performed to analyze early design  
4466 concepts for a single-mode cavity. The primary tool for these investigations was Ansys  
4467 HFSS, which was also used for the development of the SYNCA antenna described in  
4468 Section 5.3.

### 4469 **6.4.1 Open Cylindrical Cavities with Coaxial Terminations**

#### 4470 **Design Concept**

4471 A basic cavity design question relevant to Project 8's ultimate goal of an atomic tritium  
4472 CRES experiment is how to build a cavity that can be efficiently filled with atomic  
4473 tritium. To keep the rate of atom loss from recombination on surfaces it is ideal if the  
4474 ends of the cylindrical cavity are as open as possible so that tritium atoms can flow  
4475 inside unimpeded. Additionally, one of the primary calibration techniques planned for  
4476 future CRES experiments involves CRES measurements using electrons injected from  
4477 an electron gun source, which also requires an opening at the cavity end. Cylindrical  
4478 cavities with open ends can be manufactured, however, the intrinsic Q-factors of these  
4479 cavities are orders of magnitude less than their sealed counterparts, which reduces the  
4480 signal-to-noise ratio when that cavity is used for CRES measurement.

4481 Cylindrical cavities with mostly open ends that also exhibit Q values for the  $TE_{01\ell}$   
4482 modes similar to sealed cavities can be built by using coaxial endcaps to terminate  
4483 the cavity. Cavities of this type have been manufactured for specialized applications  
4484 related to the measurements of the dielectric constants of liquefied gasses (see Figure  
4485 6.9) [99,100]. This cavity design leaves the ends of the cavity wide open, but retains high  
4486 Q-values for the  $TE_{01\ell}$  modes due to the coaxial endcap, which are designed to perfectly  
4487 reflect the electric fields of  $TE_{01\ell}$  modes. Coupling to the  $TE_{01\ell}$  mode is achieved via an  
4488 aperture located at the center of the cavity wall.

4489 A cavity similar to Figure 6.9 is a candidate design for the future CRES experiments  
4490 by Project 8, since it appears to elegantly solve many practical issues that arise when  
4491 combining cavity CRES and atomic tritium. The coaxial endcaps leave significant regions  
4492 of the cavity ends completely open, which allows for the entrance of atomic tritium as  
4493 well as the pumping away of molecular tritium that has recombined on the cavity walls.

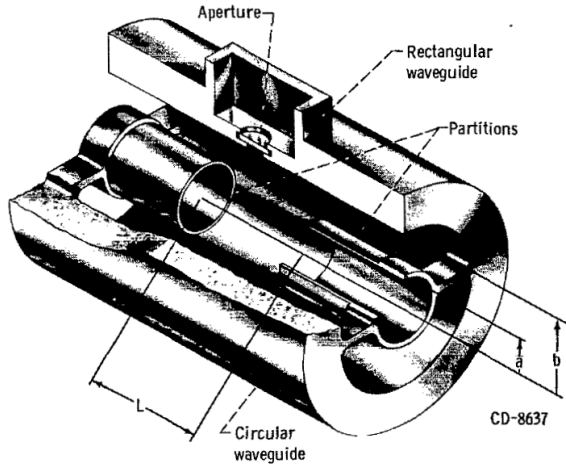


Figure 6.9: An image of an open cavity with coaxial terminations used for dielectric constant measurements. Figure from [100].

4494 These open ends are achieved while preserving the high Q-values of the  $TE_{01\ell}$  modes,  
 4495 which is important for extracting as much signal power from the electron as possible. In  
 4496 subsequent sections we shall analyze this cavity design in more detail, primarily by using  
 4497 HFSS simulations to analyze the resonant mode structure of this cavity geometry.

#### 4498 Coaxial Terminator Constraints

4499 The reason that coaxial endcaps can be used to achieve high Q-values for the  $TE_{01\ell}$   
 4500 modes is that the electric fields for these modes are purely azimuthally polarized (see  
 4501 Equations 6.12 and 6.13). Therefore, the boundary conditions that require the electric  
 4502 field to go to zero at the cavity ends can be supplied using a coaxial partition of the  
 4503 correct radius (see Figure 6.10). Because the cylindrical shape enforced by the partition  
 4504 does not match the boundary conditions of other cavity modes, these terminations also  
 4505 significantly suppress the Q-factors of non- $TE_{01\ell}$  modes, which is potentially beneficial  
 4506 for a single-mode cavity CRES experiment.

4507 The correct radius of the cylindrical partition is derived by setting up the boundary  
 4508 value problem in Figure 6.10, and analyzing the reflection and transmission coefficients  
 4509 for waves incident on the coaxial terminators. The basic problem is to identify the radius  
 4510  $a$  where the reflection coefficient for the  $TE_{01\ell}$  modes becomes equal to 1. One can show  
 4511 that if the coaxial partitions are made sufficiently long relative to the wavelength of the  
 4512  $TE_{01}$  modes than perfect reflection can be achieved. This derivation is quite lengthy  
 4513 and complex and is presented in full in [99]. Here, we shall simply explain the resulting

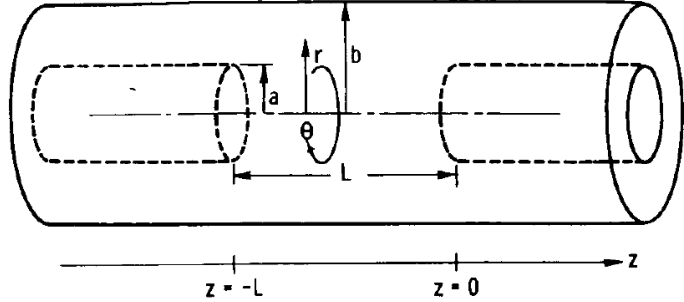


Figure 6.10: The simplified geometry of an open cavity with coaxial terminations. Figure from [99].

4514 conditions on the partition radius for perfect reflection.

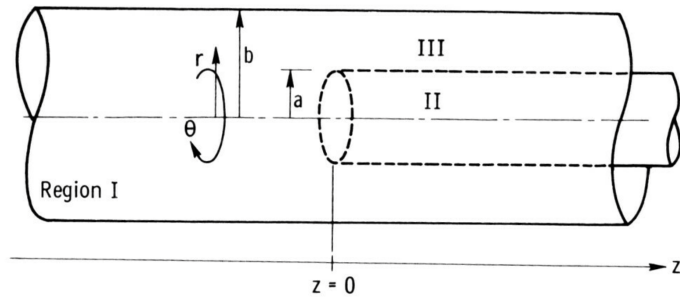


Figure 6.11: Electric field regions for the open cavity boundary value problem. Figure from [99].

4515 The open cavity boundary value problem is solved by expressing the forms of the  
 4516 electric fields in the different regions of the cavity and requiring that the electric fields are  
 4517 continuous. There are effectively three distinct regions in the open cavity corresponding  
 4518 to the central cavity volume, the inner coaxial volume, and the outer coaxial volume (see  
 4519 Figure 6.11).

4520 In Region I, the boundary conditions are those of a cylindrical waveguide, and we  
 4521 require that  $E_\phi$  for the  $TE_{0m}$  modes go to zero at the cavity wall ( $r = b$ ). This requires  
 4522 that  $J'_{0m}(k_{c0m} b) = 0$ . We aim to solve for the radius  $a$  in the specific situation where the  
 4523  $TE_{01}$  mode can propagate but all other  $TE_{0m}$  modes are below the cutoff frequency for  
 4524 the circular waveguide. This is equivalent to requiring

$$3.832 < k_{c0m} b < 7.016, \quad (6.41)$$

4525 where the numbers 3.832 and 7.016 correspond to the first and second zeros of the Bessel

4526 function (see Table 6.1).

4527 In Region II the boundary conditions are those of a cylindrical waveguide, but with  
4528 a smaller radius. The condition that  $E_\phi = 0$  at the cylindrical partition radius is that  
4529  $J'_{0m}(k_{c0m}a) = 0$ . To ensure perfect reflection, we want all modes in Region 1 of the cavity  
4530 to be below the cutoff frequency of the circular waveguide formed by the inner volume of  
4531 the coaxial terminator. Therefore, we consider the solutions where

$$k_{c0m}a < 3.832. \quad (6.42)$$

4532 Finally, in Region III the boundary condition are those of a coaxial waveguide. We  
4533 need to guarantee that  $E_\phi = 0$  at both  $r = b$  and  $r = a$ , which involves finding the  
4534 eigenvalues of the following equation

$$J'_0(k_{c0m}a)Y'_0(k_{c0m}b) - J'_0(k_{c0m}b)Y'_0(k_{c0m}a) = 0, \quad (6.43)$$

4535 where  $Y'_0$  the zeroth-order derivatives of the Bessel function of the second kind. The  
4536 solutions to this equation depend on the value of the ratio  $b/a$ . The approximate solution  
4537 is given by

$$\delta_n a \simeq \frac{n\pi}{b/a - 1}, \quad (6.44)$$

4538 where  $\delta_n$  are eigenvalues of Equation 6.43. Similar to Region II, we are interested in  
4539 solutions for which the TE<sub>01</sub> modes of Region I are below the cutoff of Region III.  
4540 Therefore, we require that

$$k_{c0m} < \delta_1. \quad (6.45)$$

4541 In general, one has some freedom in specifying the value of  $b/a$ . A value typically used  
4542 in practice is  $b/a = 2.082$ , which corresponds to positioning the radius of the cylindrical  
4543 partition at the maxima of the TE<sub>01</sub> electrical fields.

4544 Using the constraints from the three field regions one can develop a coaxial terminator  
4545 that acts as a virtual perfectly conducting surface for the TE<sub>01</sub> modes. The only required  
4546 inputs are the desired frequency of the TE<sub>011</sub> mode and a choice for the value of  $b/a$ .

#### 4547 6.4.2 Mode Filtering

4548 The general case of an electron coupling to a resonant cavity is complicated. This is  
4549 because cavities contain an infinite number of resonant modes, which for higher order  
4550 modes, have couplings to the electron with a complex spatial dependence. The danger is

4551 that improper modeling of the electron's coupling to the cavity can lead to systematic  
4552 errors in the CRES measurements that prevent a high-resolution measurement of the  
4553 electron's kinetic energy. This in part drives the preference for a single-mode cavity  
4554 experiment that uses only the electron's coupling to the TE<sub>011</sub> mode to perform CRES,  
4555 assuming that sufficient information on the electron's position can be obtained with a  
4556 single mode.

4557 The TE<sub>011</sub> mode is in a region where there are relatively few other modes to which  
4558 the electron could couple(see Figure 6.8). However, one can see that the frequency of  
4559 the TE<sub>011</sub> is perfectly degenerate with the TM<sub>111</sub> mode, which means that electrons will  
4560 inevitably couple to both modes if they have the correct cyclotron frequency.

4561 The magnitude of the impact of the electron coupling to both TE<sub>011</sub> and TM<sub>111</sub> is  
4562 currently unknown. To first order an electron coupling to more both modes will lose more  
4563 energy overtime, which can be measured by observing the frequency chirp rate of the  
4564 signal. This effect may be small enough to be negligible or simple enough to model that  
4565 the cavity can be treated as an effective single-mode cavity. Alternatively, the one could  
4566 consider devising a coupling scheme that is sensitive to both the TE<sub>011</sub> and the TM<sub>111</sub>  
4567 modes. By measuring the coupling of the electron to both modes more information on  
4568 the position of the electron could be obtained, which could improve the position and  
4569 energy resolution of the CRES measurements.

4570 A different approach is the mode filtering approach, which seeks to obtain a single  
4571 TE<sub>011</sub> mode cavity using perturbations to the cavity walls that selectively impede the  
4572 TM modes, while leaving the TE modes mostly unperturbed. The type of perturbations  
4573 required can be determined by visualizing the surface currents induced in the cavity  
4574 walls by each type of mode (see Figure 6.12). By definition, all TM have electric fields  
4575 directed along the vertical axis of the cylindrical cavity, which means that perturbations  
4576 that impede currents in this direction will modify TM resonances. On the other hand,  
4577 the TE<sub>01</sub> modes induce azimuthal currents in the cavity walls, therefore, it is possible to  
4578 break the degeneracy between TE<sub>01</sub> and TM<sub>11</sub> using a cavity perturbation that impedes  
4579 axial currents, but does not affect the flow of azimuthal currents.

4580 Figure 6.12 shows two cavity design concepts that achieve this selective current  
4581 perturbation. The resistive approach inserts a series of thin dielectric rings into the walls  
4582 of the cavity that introduces a resistive and capacitive impedance to the longitudinal  
4583 currents, while leaving azimuthal current paths intact. Cavities of this type with high  
4584 TE<sub>01</sub> Q's have also been constructed by tightly wrapping a thin, dielectric coated wire  
4585 around a mold to form the cavity wall. An alternative method is to introduce an inductive

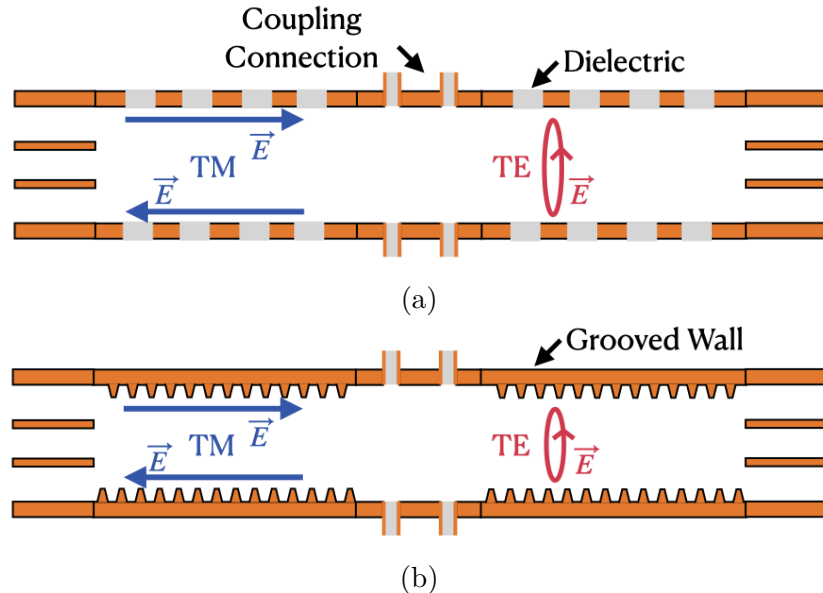


Figure 6.12: Two mode filtering concepts to break the degeneracy of  $\text{TE}_{01}$  and  $\text{TM}_{11}$  modes. The resistive approach uses dielectric materials to impede currents that travel vertically along the cavity while leaving azimuthal currents unperturbed. An alternative approach is to impede the currents using grooves cut into the cavity wall, which achieve the same effect with an inductive impedance.

4586 impedance by cutting grooves or a thread pattern on the inside wall of the cavity. For  
 4587 reasons of manufacturability and compatibility with tritium the grooved cavity approach  
 4588 is the preferred method for mode-filtered cavity construction by Project 8.

#### 4589 6.4.3 Simulations of Open, Mode-filtered Cavities

4590 A candidate design for a single  $\text{TE}_{011}$  mode CRES experiment is a cavity that utilizes  
 4591 the coaxial terminations combined with a mode-filtering wall. The first step towards  
 4592 validating that a cavity that combines these two design features will operate as expected  
 4593 is a thorough simulation effort for which finite element method (FEM) simulation software  
 4594 is invaluable. The primary tool for electromagnetic FEM calculations inside Project 8 is  
 4595 Ansys HFSS, which has a robust and well-established eigenmode solver that can identify  
 4596 the resonant frequencies and associated Q-factors for given structure.

4597 Four variations of a cavity design with a  $\sim 1$  GHz  $\text{TE}_{011}$  resonance were implemented  
 4598 in HFSS (see Figure 6.13). The four designs include a standard cylindrical cavity, an  
 4599 open cavity with smooth walls, an open cavity with resistive walls, and an open cavity  
 4600 with grooved walls. The relevant design parameters are summarized in Table 6.3. All

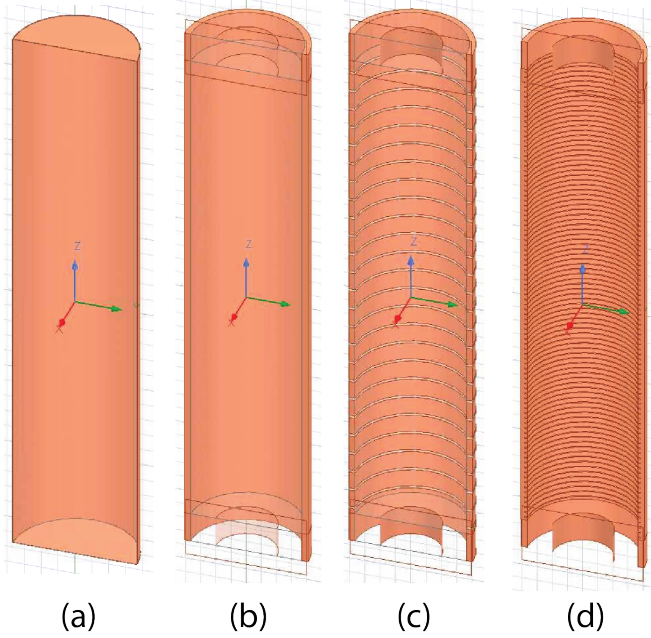


Figure 6.13: Four cavity design variations. (a) is a standard sealed cylindrical cavity, (b) is an open cavity with smooth walls, (c) is an open cavity with resistive walls, and (d) is an open cavity with grooved walls. The main cavity and coaxial terminator parameter are identical for all four cavities.

4601 cavities were simulated using copper walls and filled with a vacuum dielectric. The  
 4602 identities of the resonant modes found by HFSS were validated by visual inspection of  
 4603 the electric and magnetic field patterns and by comparison to analytical calculations of  
 4604 the mode frequencies.

Table 6.3: A table of cavity design parameters used for HFSS simulations.

Name	Qty.	Unit	Description
$D_{\text{cav}}$	326.4	mm	Cavity diameter
$L_{\text{cav}}$	1668.0	mm	Cavity length
$D_{\text{term}}$	200.2	mm	Inner diameter of coaxial terminator
$L_{\text{term}}$	100.0	mm	Terminator length
$l_{\text{die}}$	8.3	mm	Dielectric spacer thickness
$\Delta l_{\text{die}}$	66.7	mm	Distance between dielectric spacers
$l_{\text{groove}}$	3.0	mm	Groove height
$d_{\text{groove}}$	9.0	mm	Groove depth
$\Delta l_{\text{groove}}$	18.3	mm	Distance between grooves

4605 The results of the HFSS simulations validate our predictions of the resonant behavior  
 4606 of an open, mode-filtered cavity developed in the preceding sections (see Figure 6.14) One

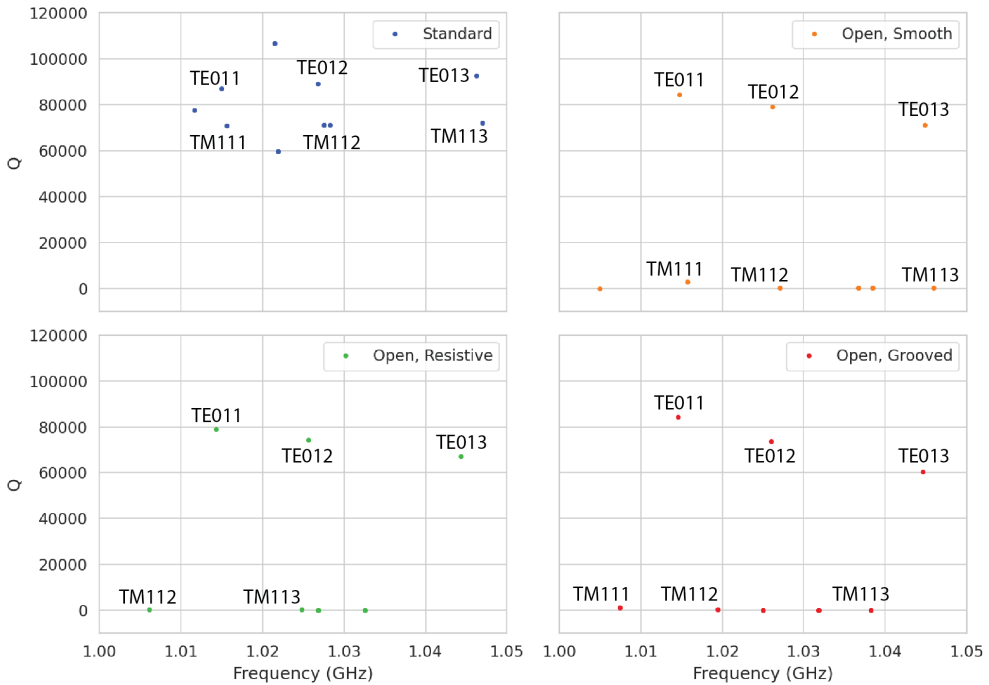


Figure 6.14: The frequencies and Q-factors of the resonant modes identified by HFSS for the cavity variations shown in Figure 6.13. The fully-sealed cavity with smooth walls has several high-Q modes near the  $TE_{01}$  resonance. Introducing the open-termination preserves the Q-factors of the  $TE_{01\ell}$  modes and suppresses the Q-factors of the modes whose boundary conditions do not match the cylindrical partition. Both the resistive and grooved wall perturbations shift the resonant frequencies of the TM modes away from the  $TE_{011}$  mode. By properly tuning the geometry of the grooves or the resistive spacers several MHz of frequency separation can be achieved.

can see that for a standard cavity the  $TE_{01}$  and the  $TM_{11}$  are degenerate in frequency with relatively high Q-factors. The open-ended cavity preserves the high Q-factors of the  $TE_{01}$  modes, while the other modes, since their boundary conditions do not match the coaxial geometry, have their Q-factors suppressed. One can see that the effect of the resistive and inductive mode-filtering schemes is to effectively shift the resonant frequencies of the  $TM_{11}$  modes below those of the associated  $TE_{01}$  modes, which breaks the degeneracy. Optimization of the dielectric spacer or groove parameters can ensure that the  $TE_{011}$  mode is isolated from other modes by  $O(10)$  MHz, which provides sufficient bandwidth for a measurement of the tritium spectrum endpoint.

Further optimization of the cavity design requires a more detailed cavity simulation that includes the cavity coupling mechanism as well as other geometry modifications required for integration into the magnetic and tritium gas subsystems. Perhaps more

4619 important is the development of the capability to simulate the interaction of electrons  
4620 with the cavity so that simulated CRES signals can be generated using cavities designed  
4621 for CRES measurements. Simulated CRES signals can then be used to estimate the  
4622 neutrino mass sensitivity of the experiment, which allows for the optimization of the cavity  
4623 design towards the configuration that provides the best measurement of the neutrino  
4624 mass.

## 4625 **6.5 Single-mode Resonant Cavity Measurements**

4626 Measurement test stands play an important role in the research and development process  
4627 that cannot be replaced by simulations. For example, constructing a prototype CRES  
4628 cavity forces one to consider important practical issues such as manufacturability and  
4629 machine tolerances that may require modifications to the design. Furthermore, by  
4630 comparing laboratory measurements of a real cavity to simulations, one can quantify  
4631 the impact of imperfections and real-life measurement systematics, which allows for  
4632 more accurate sensitivity estimates of the experiment. Lastly, the development of these  
4633 prototypes helps to build the necessary experience and expertise within the collaboration  
4634 required for more complicated experiments to succeed.

4635 In this spirit a prototype cavity was constructed to demonstrate the open, mode-  
4636 filtered cavity concept explored in the previous sections. The primary goal of the  
4637 measurements was to validate that an open, mode-filtered cavity suppressed the  $\text{TM}_{11}$   
4638 modes as predicted by HFSS simulations.

### 4639 **6.5.1 Cavities and Setup**

4640 Two rudimentary, cavities were constructed using segments of copper pipe available from  
4641 McMaster-Carr (see Figure 6.15). The design consists of copper pipes of two diameters.  
4642 The larger diameter pipe forms the main cavity wall and the smaller diameter pipe is  
4643 used to create a coaxial termination. The diameter of the outer pipe was chosen to  
4644 produce a  $\text{TE}_{011}$  resonance of approximately 6 GHz, while the diameter of the smaller  
4645 pipe was selected based on the open termination criteria introduced in Section 6.4.1. The  
4646 approximate diameters and lengths of the copper pipe are summarized in Table 6.4.

4647 Coupling to the cavity was achieved using a hand-formable segment of coaxial cable  
4648 stripped at one end to form a loop antenna. This was inserted into a small hole located  
4649 at the center of the main cavity wall. The coaxial terminators were supported inside the

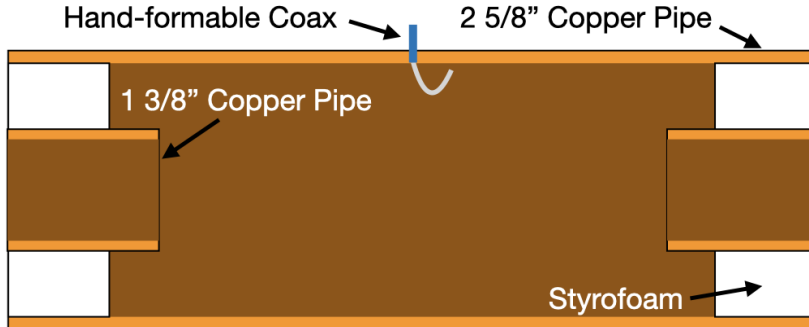


Figure 6.15: A cartoon depicting the design of the open-ended cavity prototype designed to operate at approximately 6 GHz. The main cavity wall was composed of a single copper pipe. A mode-filtered version of this cavity was constructed by

<sup>4650</sup> main cavity by carving a spacer from polystyrene foam (styrofoam) so that they could  
<sup>4651</sup> be easily inserted into the cavity and repositioned. The dielectric constant of styrofoam  
<sup>4652</sup> is quite close to air at microwave frequencies so this is expected to have minimal impact  
<sup>4653</sup> on the resonant properties of the cavity.

Table 6.4: A table of parameters describing the cavity prototypes. Certain values such as the cavity length and the distance between dielectric spacers are approximate due to variation in the machining of the copper. In particular, the filtered cavity was constructed from conducting copper segments that varied in size from 1.50" to 1.85".

Name	Qty.	Unit	Description
$D_{\text{cav}}$	2.625	in	Cavity diameter
$L_{\text{cav}}$	$\approx 13$	in	Cavity length
$D_{\text{term}}$	1.375	in	Inner diameter of coaxial terminator
$L_{\text{term}}$	1.575	in	Terminator length
$l_{\text{die}}$	0.75	in	Dielectric spacer thickness
$\Delta l_{\text{die}}$	$\approx 1.50$ to $1.85$	in	Distance between dielectric spacers

<sup>4654</sup> The actual length of the cavity is given by the distance between the inner edges of the  
<sup>4655</sup> coaxial terminators. The length of the outer section of pipe that forms the main wall of  
<sup>4656</sup> the cavity is approximately 16" in length which leads to a cavity length of  $\approx 13"$  when  
<sup>4657</sup> both terminators are inserted in the cavity. Because the terminators were not rigidly  
<sup>4658</sup> mounted this distance is only approximate, however, the uncertain length of the cavity  
<sup>4659</sup> will not prevent us from validating the open cavity design.

<sup>4660</sup> Along with the smooth-walled open cavity a resistively mode-filtered cavity was  
<sup>4661</sup> constructed by creating dielectric spacers out of segments of clear PVC pipe (see Figure  
<sup>4662</sup> 6.16). The spacers were machined such that the conductive segments of the cavity would

4663 be separated by 0.75" when the cavity was fully assembled. Due to variations in the  
 4664 lengths of the copper segments that make up the cavity wall the distance between spacers  
 4665 has significant variation with average value of about 1.7". Eight total spacers were used  
 4666 to build the cavity, which when assembled was approximately 16" in total length similar  
 to the non-filtered cavity.

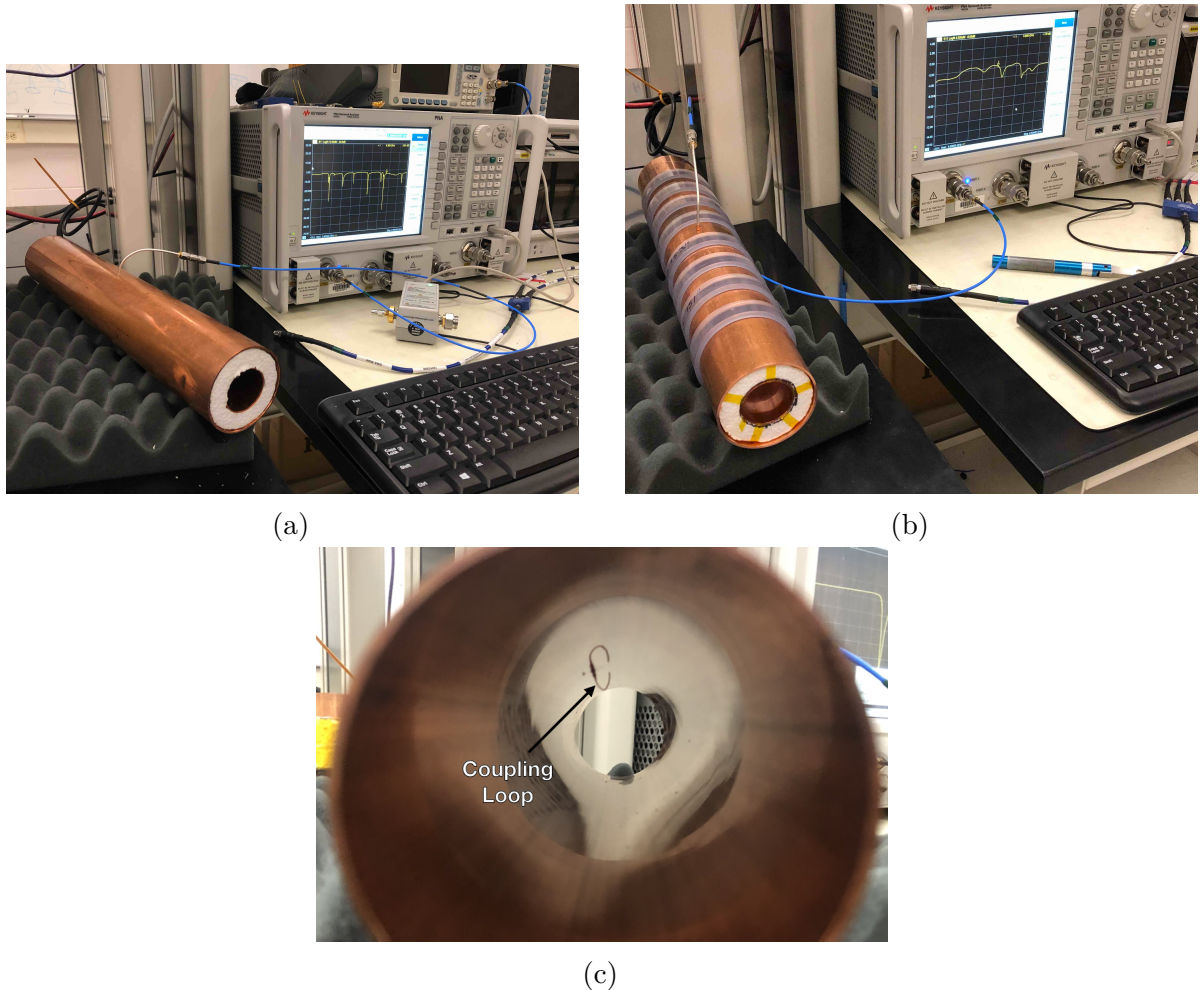


Figure 6.16: Images depicting the measurement of the filtered and non-filtered open cavities using the VNA. The coupling loop in the figure is shown in the TE orientation.

4667 Measurements of both cavities were performed using a VNA connected to the cavity  
 4668 coupling probe (see Figure 6.16). By measuring the return loss over a range of frequencies  
 4669 one can measure the frequencies and relative Q-factors of the resonant modes in the  
 4670 cavity. Due to the opposite polarity of the electric fields for the TE and TM modes,  
 4671 the loop coupling probe must be rotated 90° to change the polarity of the loop antenna.  
 4672 When the antenna is oriented such that the loop opening faces the ends of the cavity, it  
 4673

4674 couples primarily to the TE modes which have magnetic fields directed along the long  
 4675 axis of the cavity (see Figure 6.16). If the coupling loop is turned by  $90^\circ$  from where  
 4676 it is shown in the image then it will couple to the TM modes which have azimuthally  
 4677 directed magnetic fields. In this way both the TE and TM resonances can be measured  
 4678 independently.

## 4679 **6.5.2 Results and Discussion**

4680 The primary analysis method for the prototype cavities involved simply visualizing the  
 4681 return loss measured by the VNA and comparing between the filtered and non-filtered  
 4682 cavities. Since the resonances measured by the VNA are not labeled, there is some  
 4683 uncertainty about the true identities of the modes measured by the VNA. To help with  
 4684 this we performed a simulation of the simplest possible cavity that could be created from  
 4685 the prototype components, which is a fully open cavity created by simply removing the  
 4686 coaxial inserts from the non-filtered cavity configuration. The fully open cavity with the  
 4687 as-built dimensions was simulated in HFSS to get estimates on the positions of the  $\text{TE}_{011}$   
 4688 and  $\text{TM}_{111}$  modes (see Figure 6.17).

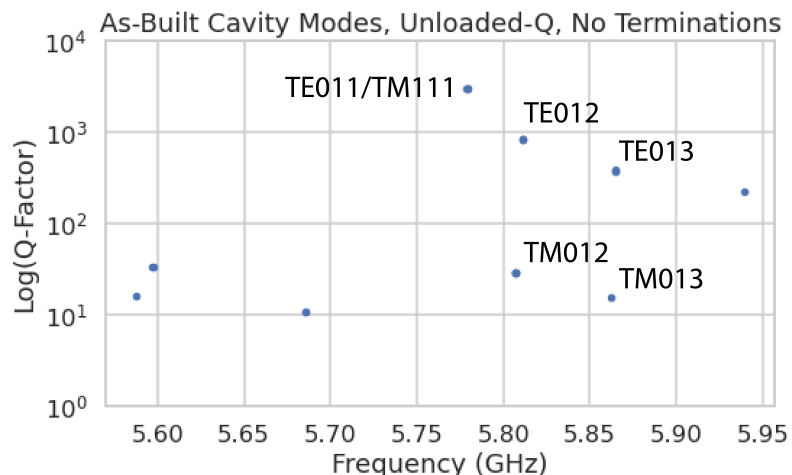


Figure 6.17: HFSS simulation results for a the as-built cavity with the coaxial terminators removed. The  $\text{TE}_{011}/\text{TM}_{111}$  frequency is approximately 5.78 GHz.

4689 Simulation of the fully open cavity shows that the  $\text{TE}_{011}/\text{TM}_{111}$  modes have a  
 4690 frequency of approximately 5.78 GHz in the fully open cavity. If the frequency of this  
 4691 mode is compared to the measurments of the fitered and non-filtered cavities with the  
 4692 terminators removed we can easily identify the  $\text{TE}_{011}$  mode at approximately 5.75 GHz

4693 (see Figure 6.18).

4694 For the non-filtered cavity one sees that the  $TE_{011}$  mode is degenerate in frequency  
 4695 with what appears to be a doublet of TM modes located at the  $TM_{111}$  frequency position.  
 4696 This doublet is actually the  $TM_{111}$  mode, which has two polarizations with opposite  
 4697 polarizations. Because the pipe used to construct the cavity is not perfectly round, the  
 4698 frequency degeneracy between the two polarizations is broken producing the doublet  
 peak. In the case of the filtered cavity with no terminators there is an isolated TE

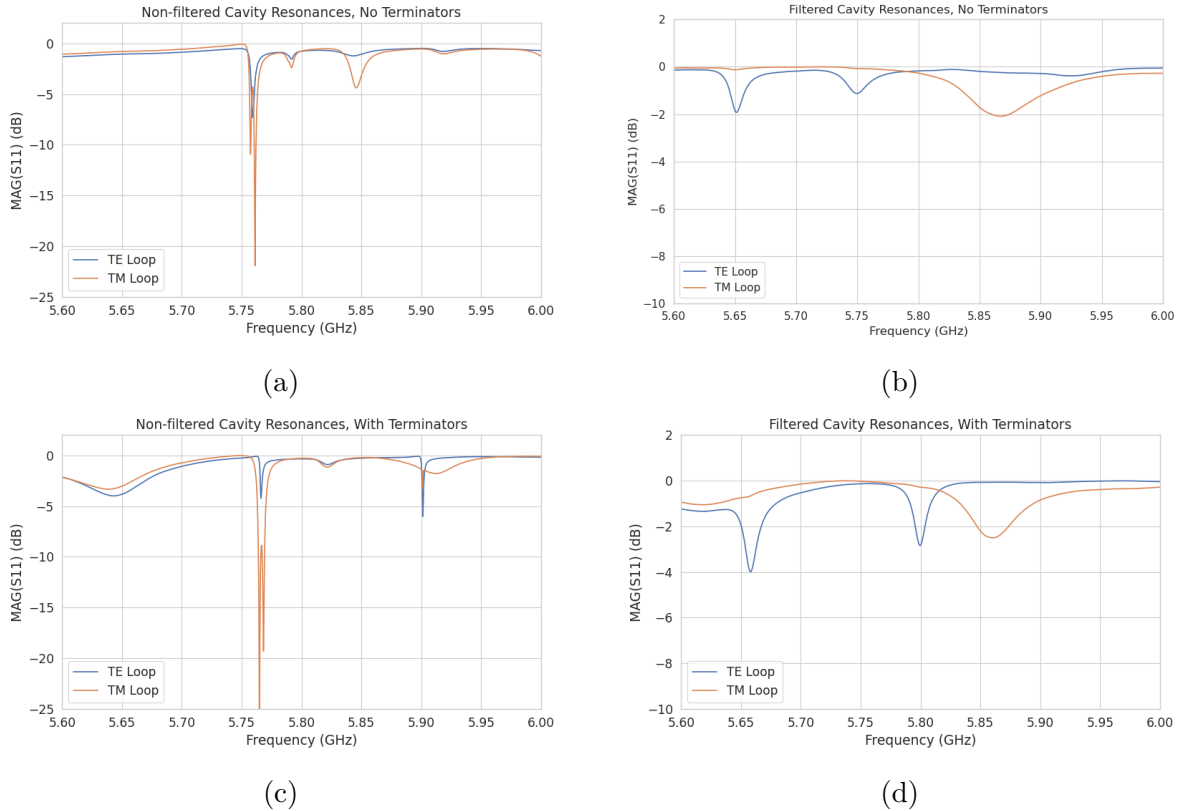


Figure 6.18: Measurements of the filtered and non-filtered prototype cavities acquired with the VNA.

4699  
 4700 resonance at 5.75 GHz that appears to be the  $TE_{011}$ , however, there is no apparent  $TM_{111}$   
 4701 doublet at the same frequency. This is what one would expect if the mode-filtering was  
 4702 effective at suppressing the TM modes. There is a notable difference in the Q of the  
 4703  $TE_{011}$  resonance for the non-filtered and filtered cavities indicated by the relative widths  
 4704 of the resonances. This is likely caused by the large width of the dielectric spacers that  
 4705 are partially impeding the TE modes. When the terminators are inserted into the cavity  
 4706 one sees that Q-factors of the modes improves as expected, by noticing the narrowing of  
 4707 the peaks compared to the no terminator plots.

<sup>4708</sup> In conclusion, one can see from these cavity measurements that, in principle, mode-  
<sup>4709</sup> filtering can be used to separate the TE<sub>011</sub> resonance from the degenerate TM<sub>111</sub> mode  
<sup>4710</sup> in combination with the an open cavity design. The next step would be to construct a  
<sup>4711</sup> prototype cavity that could be used to perform CRES measurements and measure its  
<sup>4712</sup> mode-structure using a technique such as a bead-puller [101] to study the coupling of an  
<sup>4713</sup> electron to a more realistic cavity mode structure.

4714 **Chapter 7 |**

4715 **Conclusion and Future Prospects**

4716 In this dissertation we have discussed research and development efforts towards the  
4717 development of a scalable CRES measurement technology that can be used to build a  
4718 CRES experiment at cubic-meter scales with sensitivity to neutrino masses of 40 meV.  
4719 The primary contributions of my dissertation are the development and analysis of signal  
4720 reconstruction algorithms for an antenna array based CRES experiment [102], which leads  
4721 to estimates of the neutrino mass sensitivity; the development of a synthetic cyclotron  
4722 radiation antenna (SYNCA) [79], which allowed for laboratory validation of antenna  
4723 array CRES simulation models [42]; and the development of an open-ended cavity design  
4724 compatible with atomic tritium for a cavity based CRES experiment. A measurable  
4725 impact of this work is the transition of the Project 8 collaboration’s experimental plan  
4726 from an antenna array based approach to a cavity based approach, where my work played  
4727 a key role in demonstrating the significantly higher cost and complexity of the antenna  
4728 array experiment.

4729 The transition from antenna arrays to cavities requires a new set of demonstrator  
4730 experiments to make incremental progress towards a 40 meV measurement of the neutrino  
4731 mass. At the time of writing, the near-term plan of Project 8 is to design and construct a  
4732 small-scale cavity CRES experiment utilizing the 1 T magnet installed in the UW-Seattle.  
4733 This cavity is designed to have a TE011 resonance with a frequency of about 26 GHz with  
4734 a length-to-diameter ratio that mimics the larger cavities intended for the pilot-scale and  
4735 Phase IV experiments. The goal of this experiment is to demonstrate cavity CRES as  
4736 well as validate models of CRES systematics using electrons from  $^{83m}\text{Kr}$  and an electron  
4737 gun. Though the primary goal is demonstration, near-term physics measurements are  
4738 available in the form of high-resolution measurements of the  $^{83m}\text{Kr}$  conversion spectrum  
4739 of interest to the KATRIN collaboration.

4740 Furthermore, Project 8 is currently constructing a low-frequency CRES setup located  
4741 at Yale University to better understand the principles of cavity based CRES at lower

4742 magnetic fields. The Low, UHF Cavity Krypton Experiment at Yale (LUCKEY) is  
4743 a 1.5 GHz cavity CRES experiment the will use conversion electrons from  $^{83m}\text{Kr}$  to  
4744 perform CRES measurements at the lowest frequencies ever attempted with the technique.  
4745 LUCKEY will validate frequency scaling models developed by Project 8 and will pave  
4746 the way for the future Low-Frequency Apparatus (LFA), which will be a larger, 1 GHz  
4747 cavity CRES experiment that includes a molecular tritium source. The target for the  
4748 LFA is a measurement of the neutrino mass with a sensitivity of approximately 0.2 eV,  
4749 which will build towards the atomic pilot-scale CRES experiment.

4750 In parallel to the development of cavity CRES is the development of the atomic  
4751 tritium source. Recent demonstrations of the production of atomic hydrogen are excellent  
4752 steps towards the atomic tritium production needed for the pilot-scale experiment. One  
4753 area of future study includes the development of a more detailed unstanding of the  
4754 efficiency of atomic hydrogen production. Near-term plans include the development of a  
4755 magnetic, evaporatively cooled beamline, as well as the prototyping of a Halbach array  
4756 atoms trap. Nearly all of the components of the atomic tritium system will require  
4757 demonstration before the complete system can be built. The long-term goal of the  
4758 atomic tritium work is to construct a full atomic tritium prototype that demonstrates  
4759 the production, cooling, trapping, and recycling of tritium at the rates needed for the  
4760 pilot-scale experiment.

4761 More broadly, the long-term goal of the Project 8 collaboration is to fully develop  
4762 both the atomic tritium and cavity CRES technologies so that both can be combined in  
4763 a pilot-scale CRES experiment. It is envisioned that this process will take approximately  
4764 10 years for both atomic tritium and cavity CRES. After these developments comes  
4765 the pilot-scale experiment which will be the first CRES experiment that simultaneously  
4766 demonstrates all the required technologies for Phase IV. Scaling to Phase IV with cavity  
4767 CRES will require the construction of multiple copies (approximately 10) of the pilot-scale  
4768 experiment to obtain sufficient statistics for 40 meV sensitivity.

4769 Development of the CRES experimental technique by Project 8 has led to new  
4770 experiments utilizing the CRES technique for basic physics research, such as the  $^6\text{He}$ -  
4771 CRES collaboration [103], and has also found applications as a new approach to x-ray  
4772 spectroscopy [104]. Recently, a new experimental effort called CRESDA has begun in  
4773 the UK to develop new quantum technologies applied to CRES measurements for the  
4774 neutrino mass [105]. This flourishing of new experimental efforts based on the CRES  
4775 technique is likely to continue as Project 8 continues to develop the technique towards  
4776 its neutrino mass measurement goal.

# Bibliography

- [1] DAS, A. and T. FERBEL (2003) *Introduction to Nuclear and Particle Physics*, World Scientific.
- [2] CURIE, P. (1898) “Sur une nouvelle substance fortement radioactive, contenue dans la pechblende,” *Comptes rendus de l’Academie des Sciences, Paris*, **127**, pp. 1215–1217.
- [3] RUTHERFORD, E. (1899) “Uranium radiation and the electrical conduction produced by it,” *Philos. Mag.*, **47**, p. 109.  
URL <https://cds.cern.ch/record/261896>
- [4] GERWARD, L. (1999) “Paul Villard and his Discovery of Gamma Rays,” *Physics in Perspective*, **1**, pp. 367–383.
- [5] BECQUEREL, H. (1900) “Deviation du rayonnement du radium dans un champ électrique,” *C.R.*, **130**, pp. 809–815.
- [6] D.Sc., E. R. M. and F. S. B.A. (1902) “XLI. The cause and nature of radioactivity.—Part I,” *The London, Edinburgh, and Dublin Philosophical Magazine and Journal of Science*, **4**(21), pp. 370–396, <https://doi.org/10.1080/14786440209462856>.  
URL <https://doi.org/10.1080/14786440209462856>
- [7] CHADWICK, J. (1914) *Intensitätsverteilung im magnetischen Spektrum der  $\beta$ -Strahlen von Radium B+C*, Druck von Friedr. Vieweg und Sohn.  
URL <https://books.google.com/books?id=8s8UmQEACAAJ>
- [8] BROWN, L. M. (1978) “The idea of the neutrino,” *Physics Today*, **31**(9).
- [9] PAULI, W. (1978) “Dear radioactive ladies and gentlemen,” *Phys. Today*, **31N9**, p. 27.
- [10] AMALDI, E. (1984) “From the discovery of the neutron to the discovery of nuclear fission,” *Physics Reports*, **111**(1), pp. 1–331.  
URL <https://www.sciencedirect.com/science/article/pii/037015738490214X>

- 4805 [11] CHADWICK, J. (1932) “The existence of a neutron,” *Proceedings of the Royal*  
4806 *Society of London. Series A, Containing Papers of a Mathematical and Physical*  
4807 *Character*, **136**(830), pp. 692–708, <https://royalsocietypublishing.org/doi/pdf/10.1098/rspa.1932.0112>.  
4809 URL <https://royalsocietypublishing.org/doi/abs/10.1098/rspa.1932.0112>
- 4811 [12] WILSON, F. L. (1968) “Fermi’s Theory of Beta Decay,” *American Journal of*  
4812 *Physics*, **36**(12), pp. 1150–1160, [https://pubs.aip.org/aapt/ajp/article-pdf/36/12/1150/11891052/1150\\_1\\_online.pdf](https://pubs.aip.org/aapt/ajp/article-pdf/36/12/1150/11891052/1150_1_online.pdf).  
4814 URL <https://doi.org/10.1119/1.1974382>
- 4815 [13] CRANE, H. R. and J. HALPERN (1938) “New Experimental Evidence for the  
4816 Existence of a Neutrino,” *Phys. Rev.*, **53**, pp. 789–794.  
4817 URL <https://link.aps.org/doi/10.1103/PhysRev.53.789>
- 4818 [14] COWAN, C. L., F. REINES, F. B. HARRISON, H. W. KRUSE, and A. D.  
4819 MC GUIRE (1956) “Detection of the Free Neutrino: a Confirmation,” *Science*,  
4820 **124**(3212), pp. 103–104, <https://www.science.org/doi/pdf/10.1126/science.124.3212.103>.  
4822 URL <https://www.science.org/doi/abs/10.1126/science.124.3212.103>
- 4823 [15] ANICIN, I. V. (2005) “The Neutrino - Its Past, Present and Future,” *arXiv e-prints*,  
4824 physics/0503172, [physics/0503172](https://arxiv.org/abs/physics/0503172).
- 4825 [16] DAVIS, R. (2003) “Nobel Lecture: A half-century with solar neutrinos,” *Rev. Mod.*  
4826 *Phys.*, **75**, pp. 985–994.
- 4827 [17] McDONALD, A. B. ET AL. (2002) “Direct evidence for neutrino flavor transfor-  
4828 mation from neutral-current interactions in SNO,” *AIP Conf. Proc.*, **646**(1), pp.  
4829 43–58.
- 4830 [18] FUKUDA, Y. ET AL. (1998) “Evidence for oscillation of atmospheric neutrinos,”  
4831 *Phys. Rev. Lett.*, **81**, pp. 1562–1567, [hep-ex/9807003](https://arxiv.org/abs/hep-ex/9807003).
- 4832 [19] GIGANTI, C., S. LAVIGNAC, and M. ZITO (2018) “Neutrino oscillations: The rise  
4833 of the PMNS paradigm,” *Prog. Part. Nucl. Phys.*, **98**, pp. 1–54, [1710.00715](https://arxiv.org/abs/1710.00715).
- 4834 [20] AN, F. ET AL. (2016) “Neutrino Physics with JUNO,” *J. Phys. G*, **43**(3), p. 030401,  
4835 [1507.05613](https://arxiv.org/abs/1507.05613).
- 4836 [21] BIAN, J. ET AL. (2022) “Hyper-Kamiokande Experiment: A Snowmass White  
4837 Paper,” in *Snowmass 2021*, [2203.02029](https://arxiv.org/abs/2203.02029).
- 4838 [22] ABI, B. ET AL. (2020) “Long-baseline neutrino oscillation physics potential of the  
4839 DUNE experiment,” *Eur. Phys. J. C*, **80**(10), p. 978, [2006.16043](https://arxiv.org/abs/2006.16043).

- 4840 [23] WORKMAN, R. L. ET AL. (2022) “Review of Particle Physics,” *PTEP*, **2022**, p.  
4841 083C01.
- 4842 [24] ZUBER, K. (2020) *Neutrino Physics*, CRC Press.
- 4843 [25] XING, Z. Z. and S. ZHOU (2011) *Neutrinos in Particle Physics, Astronomy and*  
4844 *Cosmology*, Springer.
- 4845 [26] MOHAPATRA, R. N. ET AL. (2007) “Theory of neutrinos: A White paper,” *Rept.*  
4846 *Prog. Phys.*, **70**, pp. 1757–1867, hep-ph/0510213.
- 4847 [27] DE GOUVÉA, A. (2016) “Neutrino Mass Models,” *Ann. Rev. Nucl. Part. Sci.*, **66**,  
4848 pp. 197–217.
- 4849 [28] WORKMAN, R. L. and OTHERS (2022) “Review of Particle Physics,” *PTEP*, **2022**,  
4850 p. 083C01.
- 4851 [29] WONG, Y. Y. Y. (2011) “Neutrino mass in cosmology: status and prospects,”  
4852 *Ann. Rev. Nucl. Part. Sci.*, **61**, pp. 69–98, 1111.1436.
- 4853 [30] ADE, P. A. R. ET AL. (2016) “Planck 2015 results. XIII. Cosmological parameters,”  
4854 *Astron. Astrophys.*, **594**, p. A13, 1502.01589.
- 4855 [31] CARLSTROM, J., K. ABAZAJIAN, G. ADDISON, P. ADSHEAD, Z. AHMED,  
4856 S. W. ALLEN, D. ALONSO, M. ALVAREZ, A. ANDERSON, K. S. ARNOLD,  
4857 C. BACCIGALUPI, K. BAILEY, D. BARKATS, D. BARRON, P. S. BARRY, J. G.  
4858 BARTLETT, R. BASU THAKUR, N. BATTAGLIA, E. BAXTER, R. BEAN, C. BE-  
4859 BEK, A. N. BENDER, B. A. BENSON, E. BERGER, S. BHIMANI, C. A. BISCHOFF,  
4860 L. BLEEM, S. BOCQUET, K. BODDY, M. BONATO, J. R. BOND, J. BOR-  
4861 RILL, F. R. BOUCHET, M. L. BROWN, S. BRYAN, B. BURKHART, V. BUZA,  
4862 K. BYRUM, E. CALABRESE, V. CALAFUT, R. CALDWELL, J. E. CARLSTROM,  
4863 J. CARRON, T. CECIL, A. CHALLINOR, C. L. CHANG, Y. CHINONE, H.-  
4864 M. S. CHO, A. COORAY, T. M. CRAWFORD, A. CRITES, A. CUKIERMAN,  
4865 F.-Y. CYR-RACINE, T. DE HAAN, G. DE ZOTTI, J. DELABROUILLE, M. DE-  
4866 MARTEAU, M. DEVLIN, E. DI VALENTINO, M. DOBBS, S. DUFF, A. DUIVEN-  
4867 VOORDEN, C. DVORKIN, W. EDWARDS, J. EIMER, J. ERRARD, T. ESSINGER-  
4868 HILEMAN, G. FABBIAN, C. FENG, S. FERRARO, J. P. FILIPPINI, R. FLAUGER,  
4869 B. FLAUGHER, A. A. FRAISSE, A. FROLOV, N. GALITZKI, S. GALLI, K. GANGA,  
4870 M. GERBINO, M. GILCHRIESE, V. GLUSCEVIC, D. GREEN, D. GRIN, E. GROHS,  
4871 R. GUALTIERI, V. GUARINO, J. E. GUDMUNDSSON, S. HABIB, G. HALLER,  
4872 M. HALPERN, N. W. HALVERSON, S. HANANY, K. HARRINGTON, M. HASEGAWA,  
4873 M. HASSELFIELD, M. HAZUMI, K. HEITMANN, S. HENDERSON, J. W. HEN-  
4874 NING, J. C. HILL, R. HLOŽEK, G. HOLDER, W. HOLZAPFEL, J. HUBMAYR,  
4875 K. M. HUFFENBERGER, M. HUFFER, H. HUI, K. IRWIN, B. R. JOHNSON,  
4876 D. JOHNSTONE, W. C. JONES, K. KARKARE, N. KATAYAMA, J. KERBY,  
4877 S. KEROVSKY, R. KESKITALO, T. KISNER, L. KNOX, A. KOSOWSKY, J. KO-  
4878 VAC, E. D. KOVETZ, S. KUHLMANN, C.-L. KUO, N. KURITA, A. KUSAKA,

- A. LAHTEENMAKI, C. R. LAWRENCE, A. T. LEE, A. LEWIS, D. LI, E. LINDER,  
 M. LOVERDE, A. LOWITZ, M. S. MADHAVACHERIL, A. MANTZ, F. MATSUDA,  
 P. MAUSKOPF, J. MCMAHON, P. D. MEERBURG, J. MELIN, J. MEYERS,  
 M. MILLEA, J. MOHR, L. MONCELSI, T. MROCKOWSKI, S. MUKHERJEE,  
 M. MUNCHMEYER, D. NAGAI, J. NAGY, T. NAMIKAWA, F. NATI, T. NATOLI,  
 M. NEGRELLO, L. NEWBURGH, M. D. NIEMACK, H. NISHINO, M. NORDBY,  
 V. NOVOSAD, P. O'CONNOR, G. OBIED, S. PADIN, S. PANDEY, B. PARTRIDGE,  
 E. PIERPAOLI, L. POGOSIAN, C. PRYKE, G. PUGLISI, B. RACINE, S. RAGHU-  
 NATHAN, A. RAHLIN, S. RAJAGOPALAN, M. RAVERI, M. REICHANADTER, C. L.  
 REICHARDT, M. REMAZEILLES, G. ROCHA, N. A. ROE, A. ROY, J. RUHL,  
 M. SALATINO, B. SALIWANCHIK, E. SCHAAN, A. SCHILLACI, M. M. SCHMITT-  
 FULL, D. SCOTT, N. SEHGAL, S. SHANDERA, C. SHEEHY, B. D. SHERWIN, E. SHI-  
 ROKOFF, S. M. SIMON, A. SLOSAR, R. SOMERVILLE, S. T. STAGGS, A. STARK,  
 R. STOMPOR, K. T. STORY, C. STOUGHTON, A. SUZUKI, O. TAJIMA, G. P.  
 TEPLY, K. THOMPSON, P. TIMBIE, M. TOMASI, J. I. TREU, M. TRISTRAM,  
 G. TUCKER, C. UMLITA, A. VAN ENGELEN, J. D. VIEIRA, A. G. VIEREGG,  
 M. VOGELSBERGER, G. WANG, S. WATSON, M. WHITE, N. WHITEHORN, E. J.  
 WOLLACK, W. L. K. WU, Z. XU, S. YASINI, J. YECK, K. W. YOON, E. YOUNG,  
 and A. ZONCA (2019) "CMB-S4," in *Bulletin of the American Astronomical Society*,  
 vol. 51, p. 209, 1908.01062.
- [32] ELLIOTT, S. R. and P. VOGEL (2002) "Double beta decay," *Ann. Rev. Nucl. Part. Sci.*, **52**, pp. 115–151, hep-ph/0202264.
- [33] DOLINSKI, M. J., A. W. P. POON, and W. RODEJOHANN (2019) "Neutrinoless Double-Beta Decay: Status and Prospects," *Ann. Rev. Nucl. Part. Sci.*, **69**, pp. 219–251, 1902.04097.
- [34] AGOSTINI, M., G. BENATO, and J. DETWILER (2017) "Discovery probability of next-generation neutrinoless double-  $\beta$  decay experiments," *Phys. Rev. D*, **96**(5), p. 053001, 1705.02996.
- [35] FORMAGGIO, J. A., A. L. C. DE GOUVÊA, and R. G. H. ROBERTSON (2021) "Direct measurements of neutrino mass," *Physics Reports*, **914**, pp. 1–54, direct measurements of neutrino mass.  
 URL <https://www.sciencedirect.com/science/article/pii/S0370157321000636>
- [36] AKER, M. ET AL. (2022) "New Constraint on the Local Relic Neutrino Background Overdensity with the First KATRIN Data Runs," *Phys. Rev. Lett.*, **129**(1), p. 011806, 2202.04587.
- [37] FORMAGGIO, J. A., A. L. C. DE GOUVÊA, and R. G. H. ROBERTSON (2021) "Direct Measurements of Neutrino Mass," *Phys. Rept.*, **914**, pp. 1–54, 2102.00594.

- 4917 [38] MONREAL, B. and J. A. FORMAGGIO (2009) “Relativistic cyclotron radiation  
 4918 detection of tritium decay electrons as a new technique for measuring the neutrino  
 4919 mass,” *Phys. Rev. D*, **80**, p. 051301.  
 4920 URL <https://link.aps.org/doi/10.1103/PhysRevD.80.051301>
- 4921 [39] ESFAHANI, A. A., S. BÖSER, N. BUZINSKY, M. C. CARMONA-BENITEZ,  
 4922 C. CLAESSENS, L. DE VIVEIROS, P. J. DOE, S. ENOMOTO, M. FERTL, J. A.  
 4923 FORMAGGIO, J. K. GAISON, M. GRANDO, K. M. HEEGER, X. HUYAN, A. M.  
 4924 JONES, K. KAZKAZ, M. LI, A. LINDMAN, C. MATTHÉ, R. MOHIUDDIN, B. MON-  
 4925 REAL, R. MUELLER, J. A. NIKKEL, E. NOVITSKI, N. S. OBLATH, J. I. PEÑA,  
 4926 W. PETTUS, R. REIMANN, R. G. H. ROBERTSON, G. RYBKA, L. SALDAÑA,  
 4927 M. SCHRAM, P. L. SLOCUM, J. STACHURSKA, Y. H. SUN, P. T. SURUKUCHI,  
 4928 J. R. TEDESCHI, A. B. TELLES, F. THOMAS, M. THOMAS, L. A. THORNE,  
 4929 T. THÜMMLER, W. V. D. PONTSEELE, B. A. VANDEVENDER, T. E. WEISS,  
 4930 T. WENDLER, and A. ZIEGLER (2022) “The Project 8 Neutrino Mass Experiment,”  
 4931 2203.07349.
- 4932 [40] ESFAHANI, A. A., S. BÖSER, N. BUZINSKY, M. C. CARMONA-BENITEZ,  
 4933 C. CLAESSENS, L. DE VIVEIROS, P. J. DOE, M. FERTL, J. A. FORMAG-  
 4934 GIO, J. K. GAISON, L. GLADSTONE, M. GUIQUE, J. HARTSE, K. M. HEEGER,  
 4935 X. HUYAN, A. M. JONES, K. KAZKAZ, B. H. LAROQUE, M. LI, A. LIND-  
 4936 MAN, E. MACHADO, A. MARSTELLER, C. MATTHÉ, R. MOHIUDDIN, B. MON-  
 4937 REAL, R. MUELLER, J. A. NIKKEL, E. NOVITSKI, N. S. OBLATH, J. I. PEÑA,  
 4938 W. PETTUS, R. REIMANN, R. G. H. ROBERTSON, D. R. D. JESÚS, G. RYBKA,  
 4939 L. SALDAÑA, M. SCHRAM, P. L. SLOCUM, J. STACHURSKA, Y. H. SUN, P. T.  
 4940 SURUKUCHI, J. R. TEDESCHI, A. B. TELLES, F. THOMAS, M. THOMAS, L. A.  
 4941 THORNE, T. THÜMMLER, L. TVRZNIKOVA, W. V. D. PONTSEELE, B. A. VAN-  
 4942 DEVENDER, J. WEINTROUB, T. E. WEISS, T. WENDLER, A. YOUNG, E. ZAYAS,  
 4943 and A. ZIEGLER (2023) “Cyclotron Radiation Emission Spectroscopy of Electrons  
 4944 from Tritium Beta Decay and  $^{83m}\text{Kr}$  Internal Conversion,” 2303.12055.
- 4945 [41] ESFAHANI, A. A., S. BÖSER, N. BUZINSKY, M. C. CARMONA-BENITEZ,  
 4946 C. CLAESSENS, L. DE VIVEIROS, P. J. DOE, M. FERTL, J. A. FORMAG-  
 4947 GIO, J. K. GAISON, L. GLADSTONE, M. GRANDO, M. GUIQUE, J. HARTSE,  
 4948 K. M. HEEGER, X. HUYAN, J. JOHNSTON, A. M. JONES, K. KAZKAZ, B. H.  
 4949 LAROQUE, M. LI, A. LINDMAN, E. MACHADO, A. MARSTELLER, C. MATTHÉ,  
 4950 R. MOHIUDDIN, B. MONREAL, R. MUELLER, J. A. NIKKEL, E. NOVITSKI,  
 4951 N. S. OBLATH, J. I. PEÑA, W. PETTUS, R. REIMANN, R. G. H. ROBERT-  
 4952 SON, D. R. D. JESÚS, G. RYBKA, L. SALDAÑA, M. SCHRAM, P. L. SLOCUM,  
 4953 J. STACHURSKA, Y. H. SUN, P. T. SURUKUCHI, J. R. TEDESCHI, A. B. TELLES,  
 4954 F. THOMAS, M. THOMAS, L. A. THORNE, T. THÜMMLER, L. TVRZNIKOVA,  
 4955 W. V. D. PONTSEELE, B. A. VANDEVENDER, J. WEINTROUB, T. E. WEISS,  
 4956 T. WENDLER, A. YOUNG, E. ZAYAS, and A. ZIEGLER (2023) “Tritium Beta Spec-  
 4957 trum and Neutrino Mass Limit from Cyclotron Radiation Emission Spectroscopy,”  
 4958 2212.05048.

- 4959 [42] “Antenna Arrays for Physics Measurements with Large-scale CRES Detectors,” *In  
4960 preparation.*
- 4961 [43] NICHOLSON, T. ET AL. (2015) “Systematic evaluation of an atomic clock at 2 x  
4962 10-18 total uncertainty,” *Nature Communications*, **6**(6896).
- 4963 [44] HÄNSCH, T. W. (2006) “Nobel Lecture: Passion for precision,” *Rev. Mod. Phys.*,  
4964 **78**, pp. 1297–1309.  
4965 URL <https://link.aps.org/doi/10.1103/RevModPhys.78.1297>
- 4966 [45] GABOR, D. (1946) “Theory of communication. Part 1: The analysis of information,”  
4967 *Journal of the Institution of Electrical Engineers-part III: radio and communication  
4968 engineering*, **93**(26), pp. 429–441.
- 4969 [46] ESFAHANI ASHTARI, A. ET AL. (2022) “Viterbi decoding of CRES signals in  
4970 Project 8,” *New J. Phys.*, **24**(5), p. 053013, 2112.05265.
- 4971 [47] JACKSON, J. D. (1999) *Classical electrodynamics*, 3rd ed., Wiley, New York, NY.  
4972 URL <http://cdsweb.cern.ch/record/490457>
- 4973 [48] F.R.S., J. L. D. (1897) “LXIII. On the theory of the magnetic influence on  
4974 spectra; and on the radiation from moving ions,” *The London, Edinburgh, and  
4975 Dublin Philosophical Magazine and Journal of Science*, **44**(271), pp. 503–512,  
4976 <https://doi.org/10.1080/14786449708621095>.  
4977 URL <https://doi.org/10.1080/14786449708621095>
- 4978 [49] ESFAHANI, A. A. ET AL. (2022) “The Project 8 Neutrino Mass Experiment,” in  
4979 *2022 Snowmass Summer Study*, 2203.07349.
- 4980 [50] KRAUS, C. ET AL. (2005) “Final results from phase II of the Mainz neutrino mass  
4981 search in tritium beta decay,” *Eur. Phys. J. C*, **40**, pp. 447–468, [hep-ex/0412056](#).
- 4982 [51] ASEEV, V. N. ET AL. (2011) “An upper limit on electron antineutrino mass from  
4983 Troitsk experiment,” *Phys. Rev. D*, **84**, p. 112003, 1108.5034.
- 4984 [52] SAENZ, A., S. JONSELL, and P. FROELICH (2000) “Improved Molecular Final-  
4985 State Distribution of HeT+ for the  $\beta$ -Decay Process of T2,” *Phys. Rev. Lett.*, **84**(2),  
4986 p. 242.
- 4987 [53] BODINE, L. I., D. S. PARNO, and R. G. H. ROBERTSON (2015) “Assessment  
4988 of molecular effects on neutrino mass measurements from tritium  $\beta$  decay,” *Phys.  
4989 Rev. C*, **91**(3), p. 035505, 1502.03497.
- 4990 [54] ASNER, D. M. ET AL. (2015) “Single electron detection and spectroscopy via  
4991 relativistic cyclotron radiation,” *Phys. Rev. Lett.*, **114**(16), p. 162501, 1408.5362.
- 4992 [55] VÉNOS, D., J. SENTKERESTIOVÁ, O. DRAGOUN, M. SLEZÁK, M. RYŠAVÝ, and  
4993 A. ŠPALEK (2018) “Properties of 83mKr conversion electrons and their use in the  
4994 KATRIN experiment,” *JINST*, **13**(02), p. T02012.

- 4995 [56] LAGENDIJK, A., I. F. SILVERA, and B. J. VERHAAR (1986) “Spin exchange and  
 4996 dipolar relaxation rates in atomic hydrogen: Lifetimes in magnetic traps,” *Phys.  
 4997 Rev. B*, **33**, pp. 626–628.  
 4998 URL <https://link.aps.org/doi/10.1103/PhysRevB.33.626>
- 4999 [57] SILVERA, I. and J. WALRAVEN (1986) “Spin-polarized atomic hydrogen,” *Prog.  
 5000 Low Temp. Phys.*, **X**, pp. 139–370.
- 5001 [58] FURSE, D. ET AL. (2017) “Kassiopeia: a modern, extensible C++ particle tracking  
 5002 package,” *New Journal of Physics*, **19**(5), p. 053012.  
 5003 URL <https://doi.org/10.1088/1367-2630/aa6950>
- 5004 [59] ESFAHANI, A. A., V. BANSAL, S. BÖSER, N. BUZINSKY, R. CERVANTES,  
 5005 C. CLAESSENS, L. DE VIVEIROS, P. J. DOE, M. FERTL, J. A. FORMAGGIO,  
 5006 L. GLADSTONE, M. GUIGUE, K. M. HEEGER, J. JOHNSTON, A. M. JONES,  
 5007 K. KAZKAZ, B. H. LAROQUE, M. LEBER, A. LINDMAN, E. MACHADO, B. MON-  
 5008 REAL, E. C. MORRISON, J. A. NIKKEL, E. NOVITSKI, N. S. OBLATH, W. PET-  
 5009 TUS, R. G. H. ROBERTSON, G. RYBKA, L. SALDAÑA, V. SIBILLE, M. SCHRAM,  
 5010 P. L. SLOCUM, Y.-H. SUN, J. R. TEDESCHI, T. THÜMMLER, B. A. VAN-  
 5011 DEVENDER, M. WACHTENDONK, M. WALTER, T. E. WEISS, T. WENDLER,  
 5012 and E. ZAYAS (2019) “Electron radiated power in cyclotron radiation emission  
 5013 spectroscopy experiments,” *Phys. Rev. C*, **99**, p. 055501.  
 5014 URL <https://link.aps.org/doi/10.1103/PhysRevC.99.055501>
- 5015 [60] ASHTARI ESFAHANI, A. ET AL. (2019) “Locust: C++ software for simulation of  
 5016 RF detection,” *New J. Phys.*, **21**, p. 113051, 1907.11124.
- 5017 [61] WIECHERT, E. (1901) “Elektrodynamische Elementargesetze,” .  
 5018 URL <https://doi.org/10.1002/andp.19013090403>
- 5019 [62] LIÉARD, A. (1898) “Champ électrique et Magnétique,” *Léclairage électrique*, **16**(27-  
 5020 29).
- 5021 [63] BALANIS, C. (2015) *Antenna Theory: Analysis and Design*, Wiley.  
 5022 URL <https://books.google.com/books?id=PTFcCwAAQBAJ>
- 5023 [64] <https://www.ansys.com/products/electronics/ansys-hfss>.
- 5024 [65] [https://en.wikipedia.org/wiki/Linear\\_time-invariant\\_system](https://en.wikipedia.org/wiki/Linear_time-invariant_system).
- 5025 [66] NYQUIST, H. (1928) “Certain Topics in Telegraph Transmission Theory,” *Transac-  
 5026 tions of the American Institute of Electrical Engineers*, **47**(2), pp. 617–644.
- 5027 [67] BRUN, R. and F. RADEMAKERS (1997) “ROOT: An object oriented data analysis  
 5028 framework,” *Nucl. Instrum. Meth. A*, **389**, pp. 81–86.

- 5029 [68] ASHTARI ESFAHANI, A. ET AL. (2021) “Bayesian analysis of a future  $\beta$  decay  
 5030 experiment’s sensitivity to neutrino mass scale and ordering,” *Phys. Rev. C*, **103**,  
 5031 p. 065501.  
 5032 URL <https://link.aps.org/doi/10.1103/PhysRevC.103.065501>
- 5033 [69] KAY, S. (1998) *Fundamentals of Statistical Signal Processing: Detection Theory, Volume II*, Pearson.  
 5034
- 5035 [70] NEYMAN, J. and E. PEARSON (1933) “On the problem of the the most efficient  
 5036 tests of statistical hypotheses,” *Phil. Trans. R. Soc. Lond. A*, **231**.  
 5037
- 5038 [71] STUMPF, M. (2018) *Electromagnetic Reciprocity in Antenna Theory*, Wiley.  
 5039
- 5040 [72] BISHOP, C. (2016) *Pattern Recognition and Machine Learning*, Springer.  
 5041
- 5042 [73] PLEHN, T., A. BUTTER, B. DILLON, and C. KRAUSE (2022) “Modern Machine  
 5043 Learning for LHC Physicists,” 2211.01421.  
 5044
- 5045 [74] GEORGE, D. and E. A. HUERTA (2018) “Deep Learning for Real-time Gravitational  
 5046 Wave Detection and Parameter Estimation: Results with Advanced LIGO Data,”  
 5047 *Phys. Lett. B*, **778**, pp. 64–70, 1711.03121.  
 5048
- 5049 [75] GABBARD, H., C. MESSENGER, I. S. HENG, F. TONOLINI, and R. MURRAY-  
 5050 SMITH (2022) “Bayesian parameter estimation using conditional variational au-  
 5051 toencoders for gravitational-wave astronomy,” *Nature Phys.*, **18**(1), pp. 112–117,  
 5052 1909.06296.  
 5053
- 5054 [76] REIMANN, R. (2022) “Project 8: R&D for a next-generation neutrino mass experi-  
 5055 ment,” *PoS*, **PANIC2021**, p. 283.  
 5056
- 5057 [77] LAROQUE, B. (2020) “Zero-deadtime processing in beta spectroscopy for measure-  
 5058 ment of the non-zero neutrino mass,” *EPJ Web Conf.*, **245**, p. 01014.  
 5059
- 5060 [78] BUZINSKY, N. (2021) *Statistical Signal Processing and Detector Optimization in*  
 5061 *Project 8*, Ph.D. thesis, Massachusetts Institute of Technology.  
 5062
- 5063 [79] ESFAHANI, A. A., S. BÖSER, N. BUZINSKY, M. CARMONA-BENITEZ,  
 5064 C. CLAESSENS, L. DE VIVEIROS, M. FERTL, J. FORMAGGIO, L. GLADSTONE,  
 5065 M. GRANDO, J. HARTSE, K. HEEGER, X. HUYAN, A. JONES, K. KAZKAZ,  
 5066 M. LI, A. LINDMAN, C. MATTHÉ, R. MOHIUDDIN, B. MONREAL, R. MUELLER,  
 5067 J. NIKKEL, E. NOVITSKI, N. OBLATH, J. PEÑA, W. PETTUS, R. REIMANN,  
 5068 R. ROBERTSON, L. SALDAÑA, P. SLOCUM, J. STACHURSKA, Y.-H. SUN, P. SU-  
 5069 RUKUCHI, A. TELLES, F. THOMAS, M. THOMAS, L. THORNE, T. THÜMM-  
 5070 LER, L. TVRZNKOVA, W. V. D. PONTSEELE, B. VANDEVENDER, T. WEISS,  
 5071 T. WENDLER, E. ZAYAS, A. ZIEGLER, and P. . COLLABORATION (2023) “SYNCA:  
 5072 A Synthetic Cyclotron Antenna for the Project 8 Collaboration,” *Journal of In-*  
 5073 *strumentation*, **18**(01), p. P01034.  
 5074 URL <https://dx.doi.org/10.1088/1748-0221/18/01/P01034>

- 5066 [80] <https://www.nvidia.com/en-us/data-center/v100/>.
- 5067 [81] <https://www.nvidia.com/en-us/data-center/h100/>.
- 5068 [82] HE, K., X. ZHANG, S. REN, and J. SUN (2016) “Deep Residual Learning for  
5069 Image Recognition,” in *2016 IEEE Conference on Computer Vision and Pattern  
5070 Recognition (CVPR)*, pp. 770–778.
- 5071 [83] SIMONYAN, K. and A. ZISSERMAN (2015) “Very Deep Convolutional Networks  
5072 for Large-Scale Image Recognition,” in *3rd International Conference on Learning  
5073 Representations, ICLR 2015, San Diego, CA, USA, May 7-9, 2015, Conference  
5074 Track Proceedings* (Y. Bengio and Y. LeCun, eds.).  
5075 URL <http://arxiv.org/abs/1409.1556>
- 5076 [84] FRIIS, H. (1946) “A Note on a Simple Transmission Formula,” *Proceedings of the  
5077 IRE*, **34**(5), pp. 254–256.
- 5078 [85] POZAR, D. M. (2005) *Microwave engineering*; 3rd ed., Wiley, Hoboken, NJ.  
5079 URL <https://cds.cern.ch/record/882338>
- 5080 [86] AKER, M. ET AL. (2022) “Direct neutrino-mass measurement with sub-electronvolt  
5081 sensitivity,” *Nature Physics*, **18**(2), pp. 160–166.  
5082 URL <https://doi.org/10.1038/s41567-021-01463-1>
- 5083 [87] MONREAL, B. and J. A. FORMAGGIO (2009) “Relativistic Cyclotron Radiation  
5084 Detection of Tritium Decay Electrons as a New Technique for Measuring the  
5085 Neutrino Mass,” *Phys. Rev. D*, **80**, p. 051301, 0904.2860.
- 5086 [88] ASHTARI ESFAHANI, A. ET AL. (2017) “Determining the neutrino mass with  
5087 cyclotron radiation emission spectroscopy—Project 8,” *J. Phys. G*, **44**(5), p. 054004,  
5088 1703.02037.
- 5089 [89] ESFAHANI, A. A. ET AL. (2022) “The Project 8 Neutrino Mass Experiment,” in  
5090 *2022 Snowmass Summer Study*, 2203.07349.
- 5091 [90] ASHTARI ESFAHANI, A. ET AL. (2019) “Locust: C++ software for simulation of  
5092 RF detection,” *New Journal of Physics*, **21**(11), p. 113051.  
5093 URL <https://doi.org/10.1088/1367-2630/ab550d>
- 5094 [91] FURSE, D. ET AL. (2017) “Kassiopeia: a modern, extensible C++ particle tracking  
5095 package,” *New Journal of Physics*, **19**(5), p. 053012.  
5096 URL <https://doi.org/10.1088/1367-2630/aa6950>
- 5097 [92] BALANIS, C. (2011) *Modern Antenna Handbook*, Wiley.  
5098 URL <https://books.google.com/books?id=UYpV8L8GNcWc>
- 5099 [93] WIRTH, W. (2001) *Radar Techniques Using Array Antennas*, Institution of Engi-  
5100 neering and Technology.  
5101 URL <https://books.google.com/books?id=ALht42gkzLsC>

- 5102 [94] BROWN, L. S., G. GABRIELSE, K. HELMERSON, and J. TAN (1985) “Cyclotron  
 5103 motion in a microwave cavity: Lifetime and frequency shifts,” *Phys. Rev. A*, **32**,  
 5104 pp. 3204–3218.  
 5105 URL <https://link.aps.org/doi/10.1103/PhysRevA.32.3204>
- 5106 [95] HANNEKE, D., S. FOGWELL HOOGERHEIDE, and G. GABRIELSE (2011) “Cavity  
 5107 control of a single-electron quantum cyclotron: Measuring the electron magnetic  
 5108 moment,” *Phys. Rev. A*, **83**, p. 052122.  
 5109 URL <https://link.aps.org/doi/10.1103/PhysRevA.83.052122>
- 5110 [96] HANNEKE, D. A. (2007) *Cavity control in a single-electron quantum cyclotron: an*  
 5111 *improved measurement of the electron magnetic moment*, Ph.D. thesis, Harvard U.
- 5112 [97] PURCELL, E. (1946) “Spontaneous Emission Probabilities at Radio Frequencies,”  
 5113 *Phys. Rev.*, **69**, pp. 674–674.  
 5114 URL <https://link.aps.org/doi/10.1103/PhysRev.69.674>
- 5115 [98] MOSKOWITZ, B. E. and J. ROGERS (1988) “ANALYSIS OF A MICROWAVE  
 5116 CAVITY DETECTOR COUPLED TO A NOISY AMPLIFIER,” *Nucl. Instrum.*  
 5117 *Meth. A*, **264**, pp. 445–452.
- 5118 [99] WENGER, N. (1967) “Resonant Frequency of Open-Ended Cylindrical Cavity,”  
 5119 *IEEE Transactions on Microwave Theory and Techniques*, **15**(6), pp. 334–340.
- 5120 [100] WENGER, N. C. and J. SMETANA (1972) “Hydrogen Density Measurements Using  
 5121 an Open-Ended Microwave Cavity,” *IEEE Transactions on Instrumentation and*  
 5122 *Measurement*, **21**(2), pp. 105–114.
- 5123 [101] RAPIDIS, N. M. (2018) “Application of the Bead Perturbation Technique to a  
 5124 Study of a Tunable 5 GHz Annular Cavity,” *Springer Proc. Phys.*, **211**, pp. 45–51,  
 5125 1708.04276.
- 5126 [102] “Real-time Signal Detection for Cyclotron Radiation Emission Spectroscopy Mea-  
 5127 surements using Antenna Arrays,” *In preparation*.
- 5128 [103] BYRON, W. ET AL. (2022) “First observation of cyclotron radiation from MeV-scale  
 5129  $e^{pm}$  following nuclear beta decay,” 2209.02870.
- 5130 [104] KAZKAZ, K. and N. WOOLLETT (2021) “Using Cyclotron Radiation Emission  
 5131 for Ultra-high Resolution X-Ray Spectroscopy,” *New J. Phys.*, **23**(3), p. 033043,  
 5132 1911.05869.
- 5133 [105] CANNING, J. A. L., F. F. DEPPISCH, and W. PEI (2023) “Sensitivity of future  
 5134 tritium decay experiments to New Physics,” *JHEP*, **03**, p. 144, 2212.06106.